Forward Modelling of Multifrequency SAR Backscatter of Snow-Covered Lake Ice: Investigating Varying Snow and Ice Properties Within a Radiative Transfer Framework

by

Justin Charles Murfitt

A thesis

presented to the University of Waterloo

in fulfillment of the

thesis requirement for the degree of

Doctor of Philosophy

in

Geography

Waterloo, Ontario, Canada, 2022

Examining Committee Membership

The following served on the Examining Committee for this thesis. The decision of the Examining Committee is by majority vote.

External Examiner	Dr. Benoit Montpetit Physical Scientist (ECCC)
Supervisor(s)	Dr. Claude Duguay Professor
Internal Member	Dr. Grant Gunn Assistant Professor
Internal-external Member	Dr. Andrea Scott Associate Professor
Other Member(s)	Dr. Richard Kelly Professor

Author’s Declaration

I hereby declare that I am the sole author of this thesis. This is a true copy of the thesis, including any required final revisions, as accepted by my examiners.

I understand that my thesis may be made electronically available to the public.

Abstract

Lakes are a key feature in the Northern Hemisphere landscape. The coverage of lakes by ice cover has important implications for local weather conditions and can influence energy balance. The presence of lake ice is also crucial for local economies, providing transportation routes, and acting as a source of recreation/tourism and local customs. Both lake ice cover, from which ice dates and duration can be derived (i.e., ice phenology), and ice thickness are considered as thematic variables of lakes as an essential climate variable by the Global Climate Observing System (GCOS) for understanding how climate is changing. However, the number of lake ice phenology ground observations has declined over the past three decades. Remote sensing provides a method of addressing this paucity in observations. Active microwave remote sensing, in particular synthetic aperture radar (SAR), is popular for monitoring ice cover as it does not rely on sunlight and the resolution allows for the monitoring of small and medium-sized lakes. In recent years, our understanding of the interaction between active microwave signals and lake ice has changed, shifting from a double bounce mechanism to single bounce at the ice-water interface. The single bounce, or surface scattering, at the ice-water interface is due to a rough surface and high dielectric contrast between ice and water. However, further work is needed to fully understand how changes in different lake ice properties impact active microwave signals. Radiative transfer modelling has been used to explore these interactions, but there are a variety of limitations associated with past experiments. This thesis aimed to faithfully represent lake ice using a radiative transfer framework and investigate how changes in lake ice properties impact active microwave backscatter. This knowledge was used to model backscatter throughout ice seasons under both dry and wet conditions. The radiative transfer framework used in this thesis was the Snow Microwave Radiative Transfer (SMRT) model.

To investigate how broad changes in ice properties impact microwave backscatter, SMRT was used to conduct experiments on ice columns representing a shallow lake with tubular bubbles and a deep lake without tubular bubbles at L/C/X-band frequencies. The Canadian Lake Ice Model

(CLIMo) was used to parameterize SMRT. Ice properties investigated included ice thickness, snow ice bubble radius and porosity, root mean square (RMS) height of the ice-water interface, correlation length of the ice-water interface, and tubular bubble radius and porosity. Modelled backscatter indicated that changes in ice thickness, snow ice porosity, and tubular bubble radius and porosity had little impact on microwave backscatter. The property that had the largest impact on backscatter was RMS height at the ice-water interface, confirming the results of other recent studies. L and C-band frequencies were found to be most sensitive to changes in RMS height. Bubble radius had a smaller impact on backscatter, but X-band was found to be most sensitive to changes in this property and would be a valuable frequency for studying surface ice conditions.

From the results of these initial experiments, SMRT was then used to simulate the backscatter from lake ice for two lakes during different winter seasons. Malcolm Ramsay Lake near Churchill, Manitoba, represented a shallow lake with dense tubular bubbles and Noell lake near Inuvik, Northwest Territories, represented a deep lake with no tubular bubbles. Both field data and CLIMo simulations for the two lakes were used to parameterize SMRT. Because RMS height was determined to be the ice property that had the largest impact on backscatter, simulations focused on optimizing this value for both lakes. Modelled backscatter was validated using C-band satellite imagery for Noell Lake and L/C/X-band imagery for Malcolm Ramsay Lake. The root mean square error values for both lakes ranged from 0.38 to 2.33 dB and Spearman's correlation coefficient (ρ) values >0.86. Modelled backscatter for Noell Lake was closer to observed values compared to Malcolm Ramsay Lake. Optimized values of RMS height provided a better fit compared to a stationary value and indicated that roughness likely increases rapidly at the start of the ice season but plateaus as ice growth slows.

SMRT was found to model backscatter from ice cover well under dry conditions, however, modelling backscatter under wet conditions is equally important. Detailed field observations for Lake Oulujärvi in Finland were used to parameterize SMRT during three different conditions. The first was lake ice with a dry snow cover, the second with an overlying layer of wet snow, and the third was when a slush layer was present on the ice surface. Experiments conducted under dry

conditions continued to support the dominance of scattering from the ice-water interface. However, when a layer of wet snow or slush layer was introduced the dominant scattering interface shifted to the new wet layer. Increased roughness at the boundary of these wet layers resulted in an increase in backscatter. The increase in backscatter is attributed to the higher dielectric constant value of these layers. The modelled backscatter was found to be representative of observed backscatter from Sentinel-1.

The body of work of this thesis indicated that the SMRT framework can be used to faithfully represent lake ice and model backscatter from ice covers and improved understanding of the interaction between microwave backscatter and ice properties. With this improved understanding inversion models can be developed to retrieve roughness of the ice-water interface, this could be used to build other models to estimate ice thickness based on other remote sensing data. Additionally, insights into the impact of wet conditions on radar backscatter could prove useful in identifying unsafe ice locations.

Acknowledgements

First, and foremost, I would like to acknowledge Dr. Claude Duguay for his support, insight, opinions, and advice throughout the writing, researching, and development of this thesis. I appreciate all the opportunities that you provided me with through my time in 'Team Duguay'.

The Natural Science and Engineering Research Council of Canada and the University of Waterloo are acknowledged for the financial support provided during competition of this thesis. I would also like to acknowledge the staff of the Aurora College Western Arctic Research Centre for their support during field work in 2019.

I would like to recognize and express my appreciation to Dr. Richard Kelly (University of Waterloo – Geography and Environmental Management), Dr. Grant Gunn (University of Waterloo – Geography and Environmental Management), and Dr. Andrea Scott (University of Waterloo – Systems Design Engineering) for serving on my thesis examination committee.

I would also like to acknowledge Dr. Ghislain Picard for his support on using SMRT. A big thanks to Yusof Ghiasi and Mark Wu for the company in the office and on trips across Central Ontario. Also, a thank you to others who have helped me throughout my graduate school experience, Dr. Nastaran Saberi, Dr. Aaron Thompson, the CTE Team, Dr. Laura Brown, Alexis Robinson, and Dr. Yuhong He.

Finally, I would like to acknowledge my friends and family for always being there to listen and act as a sounding board throughout my many years of schooling. Could not have done it without any of you.

Dedication

This thesis is dedicated to my wife, Rosalie Ruthart, and son, Arthur Murfitt.

Table of Contents

List of Figures

List of Tables

List of Symbols

α	Surface Albedo
c	Speed of Light (299 792 458 m/s)
C_p	Specific Heat Capacity
dB	Decibel
ε - CLIMo	Emissivity
ε_r	Real Component of Complex Relative Permittivity
ε_i	Imaginary Component of Complex Relative Permittivity
eps_r	Permittivity Ratio at an Interface
f	Frequency
F_{lat}	Downward latent heat flux
F_{lw}	Downwelling Long Wave Radiative Flux
F_o	Net Downward Heat Flux
F_{sens}	Downward Sensible Heat Flux
F_{sw}	Downwelling Short Wave Radiative Energy Flux
F_{qp}	Complementary Field Coefficient
f_{qp}	Field Scattering Coefficient
I_o	Fractional Short Wave Radiation Flux
K - CLIMo	Bulk Extinction Coefficient
k - CLIMo	Thermal Conductivity
k_0	Wavenumber
K_s	Scattering Coefficient

K_a	Absorption Coefficient
L	Correlation Length - Roughness
θ_i	Incidence Angle
p_{ex}	Correlation Length - Microstructure
ρ - CLIMo	Density
ρ_{ice}	Ice Density
ρ_s	Snow Density
σ - CLIMo	Stefan-Boltzmann Constant
σ	Fraunhoffer Criterion
σ°	Sigma-naught Backscatter
R_o	Optical Radius
$R_{V,H}(\theta_i)$	Fresnel Coefficients at Incidence Angle
$R_{V,H}(\theta_{spec})$	Fresnel Coefficients at Specular Angle
τ	Stickiness
λ	Wavelength

List of Abbreviations

AIEM	Advanced Integral Equation Model
ALOS-PALSAR	Advanced Land Observing Satellite Phased Array Type L-band Synthetic Aperture Radar
ASF	Alaska Satellite Facility
AMSR-E/2	Advanced Microwave Scanning Radiometer – Earth Observing System
ASAR	Advanced Synthetic Aperture Radar
CAA	Canadian Arctic Archipelago
CLIMo	Canadian Lake Ice Model
CIS	Canadian Ice Service
CRISTAL	Copernicus Polar Ice and Snow Topography Altimeter
DDM	Delay-Doppler Maps
DMRT	Dense Media Radiative Transfer Model
DM-PACT	Dense Medium Phase and Amplitude Correction
DORT	Discrete Ordinate and Eigenvalue
ECCC	Environment Climate Change Canada
ECMWF	European Centre for Moderate Range Weather Forecasting
ECV	Essential Climate Variable
EODMS	Earth Observation Data Management System
ERA	ECMWF Re-Analysis
ERS-1	European Remote Sensing Satellite-1
ESA	European Space Agency

EW	Extra Wide
FM-CW	Frequency Modulated Continuous Wave
FMI	Finnish Meteorological Institute
FQ	Fine Beam Quad Mode
GCOS	Global Climate Observation System
GDP	Gross Domestic Product
GNSS-R	Global Navigation Satellite System Reflectometry
HIRLAM	High Resolution Limited Area Model
HUT	Helsinki University of Technology
IBA	Improved Born Approximation
IEEE	Institute of Electrical and Electronics Engineers
IEM	Integral Equation Model
InSAR	Interferometric Synthetic Aperture Radar
IOP	Intensive Operation Period
IRGS	Iterative Region Growing and Semantics
IW	Interferometric Wide
MAE	Mean Absolute Error
MAGIC	Map-Guided Ice Classification System
MEaSUREs	Making Earth System Data Records for Use in Research Environments
MEMLS	Microwave Emission Model of Layered Snowpacks
MODIS	Moderate Resolution Imaging Spectroradiometer

NPC	Normalized Percentage Change
NSIDC	National Snow and Ice Data Centre
QCAP	Quasi-crystalline Approximation
Radar	Radio Detection and Ranging
RAR	Real Aperture Radar
RCM	RADARSAT Constellation Mission
RMSE	Root Mean Square Error
RMS Height / RMSH / *s*	Root Mean Square Height
RTM	Radiative Transfer Modelling
SAR	Synthetic Aperture Radar
SLAR	Side Looking Airborne Radar
SMMR	Scanning Multichannel Microwave Radiometer
SMRT	Snow Microwave Radiative Transfer Model
SNAP	Sentinel Application Platform
SHS	Sticky Hard Spheres
SSA	Specific Surface Area
SSM/I	Special Sensor Microwave/Imagery
SWE	Snow Water Equivalency
SWOT	Surface Water and Ocean Topography
VMC	Volumetric Water Content
WMO	World Meteorological Organization

Chapter 1
Introduction and Motivation

1.1 Motivation

Freshwater waterbodies (lakes and rivers) across the Northern Hemisphere experience substantial ice cover throughout the winter season, with peak area coverage reaching 1.71x106 km^2 of which the majority, 1.5x106 km^2, is lake ice (Brooks et al., 2013). Freshwater lakes are an important physical feature and can cover 15 to 40% of the land surface at Subarctic and Arctic latitudes (Duguay et al., 2003). Lakes play an important role in local climate and weather. For example, 2-m temperature variations observed in January 2012 near Lake Ladoga in Finland were modelled with the lowest bias ($\leq$ -0.5 °C) by the High Resolution Limited Area Model, a Numerical Weather Prediction Model, when ice concentration was correctly considered (Eerola et al., 2014). Lake ice also plays an important role in freshwater ecosystems and there is increasing interest in the role that ice growth has in under-ice biology (Hampton et al., 2017). Social and economic systems are impacted by the presence and absence of lake ice as the formation of ice creates crucial ice road networks that allow for the transportation of goods to northern communities as well as travel between local communities (Mullan et al., 2017; Knoll et al., 2019). Recreation and tourism at mid-latitudes rely on the formation of lake ice as it allows for the establishment of extensive snowmobile trails in provinces such as Ontario, and the northern United States. According to a recent study on the economic impact of snowmobiling, the Haliburton/Pembroke region of Ontario saw a gross domestic product (GDP) of greater than $60 million due to the operation of these trail systems (Cummings et al., 2019).

These uses of lake ice are impacted by a warming climate, which is changing the timing and duration of lake ice cover across the Northern Hemisphere. Recent research predicts that warming winters will lead to a larger number of lakes experiencing ice-free years (Filazzola et al., 2020). Recent trends in Arctic lakes support this, showing a shift towards earlier break-up (Šmejkalová et al., 2016), while studies of lakes at mid-latitudes and across the Northern Hemisphere have revealed a north-south divide in the patterns of lake ice phenology during the early 21st century (Du et al., 2017; Murfitt & Brown, 2017). Lakes at lower latitudes appear to be trending towards a mix of earlier(later) freeze-up(break-up) dates connected to cooling temperatures (Murfitt & Brown, 2017) whereas lakes at higher latitudes are trending towards

earlier break-up dates due to warming temperatures (Šmejkalová et al., 2016; Surdu et al., 2016). This diversity in lake ice phenology patterns makes it increasingly important to observe changes in lake ice. However, the "Global Lake and River Ice" database has declined from more than 1000 observations of river and lake ice events in the 1980s to an average of 165 observations per year between 2010 and 2020 (Benson et al., 2013), making it difficult to monitor these events during recent decades using in situ data. These data are needed as lake ice cover and thickness are named as thematic products of lakes as an essential climate variable under the Global Climate Observation System (GCOS), requiring lake ice thickness at a 1-15 cm accuracy and ice cover at 10% accuracy (World Meteorological Organization, 2022). These accuracies are necessary to establish a climate record for understanding how climate change will impact lake systems (Belward et al., 2016).

However, due to the volume of lakes in the Subarctic and Arctic as well as at more southern locations of some northern countries, such as Canada, consistent monitoring is difficult. Therefore, there has been an increasing reliance on remote sensing for the study of lake ice (Duguay et al., 2015). Optical remote sensing (i.e., satellite imagery and aerial photographs) provides an easy to access view of lakes and has been used successfully to monitor ice cover and phenology (i.e., Latifovic & Pouliot, 2007; Arp et al., 2013). However, these methods are restricted by cloud cover and the occurrence of polar darkness; this can limit the capture of crucial lake ice events such as the timing of full ice cover and the start of the break-up process. Passive microwave data addresses these limitations and can provide more consistent monitoring of lake ice. These data have been used to effectively estimate both ice thickness (Kang et al., 2014) and the timing of ice phenology events (Kang et al., 2012; Du et al., 2017; Cai et al., 2021). However, each data point is associated with a large footprint (>10 km at high frequencies) limiting the application to large lakes. The most common remote sensing data used for lake ice observation since the 1970s has been active microwave (Murfitt & Duguay, 2021), and in recent years there has been extensive application of synthetic aperture radar (SAR). Active microwave addresses the limitations associated with optical remote sensing and SAR has a finer spatial resolution relative to passive microwave data, typically less than 100 m. Ground-based scatterometer measurements have been used to study the impact of changes in ice properties on microwave signals (Gunn, Brogioni, et al., 2015) and estimate lake ice thickness (Gunn, Duguay, et al., 2015). Recently spaceborne SAR has been used to classify ice covers (K. A. Scott et al., 2020) and explore scattering mechanisms within lake ice (Engram et al., 2013).

While there has been extensive use of imaging SAR, recent research has challenged past understanding on how SAR signals interact with lake ice. Early research using X-band Side Looking Airborne Radar (SLAR) identified a connection between higher backscatter from frozen lakes and the presence of tubular-shaped bubbles within the ice (Weeks et al., 1981). This was further supported by a combination of C-band VV-polarized satellite images and in situ data that related thickening ice cover and development of tubular bubbles to increasing backscatter (Jeffries et al., 1994). However, recent research conducted using quad-pol SAR data and decomposition techniques has indicated that surface scattering is the dominant mechanism for lake ice (Engram et al., 2013; Gunn et al., 2018). Surface scattering is a result of roughness at the ice-water interface that is attributed to the extrusion of tubular bubbles (Gunn et al., 2018) or development of methane ebullition bubbles (Engram et al., 2012, 2013). Additional experiments have been conducted using backscatter models that have confirmed the importance of ice-water interface roughness (Atwood et al., 2015; Tian et al., 2015).

Although these experiments highlight the importance of roughness at the ice-water interface, ranges used in sensitivity experiments have been limited and focused on small scale variations in roughness and other ice properties. Additionally, the majority of lake ice forward modelling has been conducted using C-band data with limited exploration of other frequencies. Finally, deeper lakes or deeper sections of lakes (≥4 m in depth, Mellor, 1982) where the formation of tubular bubbles is absent have been largely ignored and the impact of changing properties on backscatter from these lakes has not been explored. Due to these limitations exploration of the impact of changing ice properties on microwave backscatter through a faithful representation of ice covers is needed.

1.2 Objectives

This thesis looks to address these gaps in representation and understanding by conducting forward modelling experiments using the snow microwave radiative transfer (SMRT) model (Picard et al., 2018) to address three main objectives: 1) explore differences in how backscatter from shallow and deep lakes respond to changes in lake ice properties; 2) investigate the impact that changing properties have on different SAR frequencies; and 3) determine appropriate representations of lake ice in SMRT under different conditions (cold dry and warmer wet). SMRT was selected as the modelling framework for this thesis as it helps address limitations of past

studies. This includes allowing for roughness at multiple interfaces, parameterization of snow microstructure, and inclusion of multilayer snowpacks and ice columns. Furthermore, the Canadian Lake Ice Model (CLIMo) will be used to parameterize SMRT to produce more realistic representations of ice columns compared to previous modelling studies.

1.3 Structure

This thesis is structured in a manuscript format and contains a total of seven chapters. This first chapter highlights the relevant motivations of the thesis in relation to the remote sensing of lake ice as well as why understanding how to represent lake ice in the SMRT framework is important. Chapter 2 of the thesis goes into further details around the basics of the interaction between lake ice and active microwave signals and provides further details of the basics of SMRT. Chapter 2 also provides information on the different electromagnetic, microstructure, and interface models used in this thesis to parameterize SMRT.

Chapter 3 provides a detailed review of lake ice active microwave research over the last 50 years, providing context to the studies conducted in the other chapters. This review explores the interaction between microwave signals and lake ice as well as the mechanisms responsible for these interactions. Additionally, the review explores how active microwave data have been used to obtain lake ice properties (phenology, cover, and thickness). The review concludes by proposing future avenues of research and identifies key needs within the field of lake ice remote sensing. The chapter was published in the peer-reviewed journal *Remote Sensing of Environment*:

Murfitt, J., Duguay, C.R., 2021. 50 years of lake ice research from active microwave remote sensing: Progress and prospects. Remote Sens. Environ. 264, 1–21. https://doi.org/10.1016/j.rse.2021.112616

Chapter 4 addresses the first and second objectives of thesis which are to investigate how changes in ice properties for shallow and deep lakes impact microwave response at different frequencies. This is the first published work that applies SMRT for lake ice. Various ice properties (ice thickness, bubbles radius, ice layer porosity, and roughness) are iterated to explore how these changes impact microwave backscatter. The modelled backscatter provides insight into which properties have a greater impact on backscatter from lake ice covers. This chapter was published in the peer-reviewed journal *IEEE Transactions on Geoscience and Remote Sensing*:

Murfitt, J., Duguay, C.R., Picard, G., Gunn, G.E., 2022. Investigating the Effect of Lake Ice Properties on Multifrequency Backscatter Using the Snow Microwave Radiative Transfer (SMRT) Model. IEEE Trans. Geosci. Remote Sens. 60, 1–26. https://doi.org/10.1109/TGRS.2022.3197109

Chapter 5 addresses one aspect of the third objective of this thesis by simulating microwave backscatter throughout an ice season for two Canadian Subarctic lakes. SMRT is parameterized through a combination of field data and outputs of a thermodynamic lake ice model. This chapter focuses on forward modelling of backscatter under dry conditions and identifies limitations in the representation of ice covers within SMRT. This chapter is currently under revision for the journal *Remote Sensing of Environment*.

Chapter 6 addresses another aspect of the third objective of the thesis by simulating microwave backscatter for a lake in Finland, however, focuses on simulations conducted under wet conditions. Field data collected during the winter of 2021 is used to parameterize SMRT and investigate how microwave response changes when surface conditions are altered due to warmer temperatures and the presence of saturated layers. This chapter is planned for submission to *Remote Sensing*.

Chapter 7 is a summary of the findings presented in the previous chapters and outlines limitations of the work as well as highlights areas of future study. Chapters that contain published material or material that is currently under review are provided in their original format and are subject to copyright. The manuscripts are included in their original format, resulting in some duplication of equations, sensor descriptions and methodologies between chapters.

Chapter 2
Active Microwave, Lake Ice, and SMRT Fundamentals

2.1 Introduction

This chapter provides a brief review of the interaction between active microwave signals and lake ice. This chapter also details past experiments conducted for forward modelling of microwave signals from lake ice, highlighting the different models that have been used and identifying weaknesses of the different approaches. Finally, the chapter outlines the basics of the snow microwave radiative transfer model, including the parameterization of lake ice. Additionally, this section addresses the electromagnetic, microstructure, and surface scattering models used throughout the experiments performed in this thesis.

2.2 Active Microwave Interactions with Lake Ice

The evolution of backscatter from lake ice has been covered in several publications from the late 1970s (side looking airborne radar, SLAR) and more frequently since the launch of ERS-1 in 1991. Early formation of a thin layer of ice results in low backscatter as the ice suppresses wave action of the lake creating a smooth surface (Jeffries et al., 1994). For Arctic lakes this has been identified as a drop in backscatter compared to open water values due to wind action creating a rougher surface. However, for small/medium-sized lakes in mid-latitudes this impact is reduced (Murfitt et al., 2018b). As ice thickens backscatter increases until it reaches a plateau where values remain relatively consistent throughout the ice season (Duguay et al., 2002). These high backscatter values are caused by strong reflection of microwave signals due to the ice dielectric contrast between ice (dielectric constant of 3.17) and water (dielectric constant >10 at 0 ◦C between 1 and 37 GHz) as well as roughness at the ice-water interface (Mätzler & Wegmüller, 1987; Engram et al., 2013; Ulaby & Long, 2014). However, if the lake is shallow enough for the ice cover to freeze to the lakebed, known as grounded (or bedfast) ice cover, there is a decrease in backscatter due to the low dielectric contrast between the ice and soil mediums (dielectric constant <8 between 0.01 and 10 GHz at -10 ◦C (P. Hoekstra & Delaney, 1974)). When temperatures increase in the spring, fluctuations in backscatter are observed with a general decreasing trend in backscatter values. For floating ice covers that did not freeze to the lakebed, this decrease is due to the increase in water content of the overlying snowpack or due to the formation of melt ponds

on the ice surface (Morris et al., 1995; Duguay et al., 2002). Increases in backscatter for floating ice covers during ice decay can be attributed to increased roughness of the snow surface or ice surface due to multiple melt/refreeze events or candling at the ice surface (Duguay et al., 2002; Antonova et al., 2016). On the other hand, with increasing temperatures a backscatter reversal is noted initially for grounded ice covers. This reversal has been attributed to the draining of the ice surface and creation of a wet reflective rough ice surface (Jeffries et al., 1994; Wakabayashi et al., 1999). Following this initial reversal backscatter values also decrease for grounded ice covers. Further discussion on these processes for backscatter evolution can be found in Chapter 3 of this thesis.

The initial increase in backscatter from lake ice was traditionally associated with the thickening of a layer of tubular bubbles at the ice-water interface that forms due to the lake water becoming saturated with gas (Bari & Hallett, 1974). Early support for this mechanism was made by connecting observations in X-band side looking aperture radar (SLAR) to ground observations of ice stratigraphy (Weeks et al., 1981). The presence of the tubular bubbles was thought to create a double bounce scattering mechanism as the incoming microwave signal first bounced off the vertically oriented bubble and then the ice-water interface where there was a high dielectric contrast (Weeks et al., 1981). This theory was further supported when increasing backscatter from calibrated ERS-1 C-band was found to correspond to thickening of these tubular bubble layers for lakes on the North Slope of Alaska (Jeffries et al., 1994).

With the advent of fully polarimetric data new active microwave processing techniques allowed for interpretation of the contribution of difference scattering mechanisms within an area of study. Using techniques such as polarimetric decomposition, co-pol phase difference, and microwave modelling, there can be a clearer understanding of the contributions of scattering mechanisms, surface, volume, and double bounce scattering, from lake ice covers (Atwood et al., 2015). Through these analysis it has been demonstrated that the largest contributor to backscatter from lake ice cover is a surface or single bounce scattering mechanism, not double bounce as previously thought (Engram et al., 2012; Atwood et al., 2015; Gunn et al., 2018). The surface scattering is a result of roughness at the ice-water interface and observed using various frequencies (L, C, and X-band). There are different explanations for the cause of this roughness including, the presence of methane ebullition bubbles, tubular bubbles extruding from the bottom of the ice, and variations in the growth rate of the ice (Engram et al., 2012; Gunn et al., 2018). Though modern

remote sensing techniques have led to these conclusions, it was suggested in earlier research that the roughness of the ice-water interface could be responsible for the backscatter observed from lake ice covers (Jirberg et al., 1974; Weeks et al., 1977). The research on early and newer theories of scattering mechanisms for lake ice is also further explored in Chapter 3 of this thesis.

2.3 Lake Ice and Microwave Modelling

As noted above, modelling of microwave signals from lake ice has been used to better understand the mechanisms for the observed returns from lake ice covers. Early modelling of active microwave data from the well-studied lakes of the North Slope of Alaska used numerical modelling to determine backscatter and allowed for the inclusion of layers of varying ice thickness, varying layers of bubble types, and a slightly rough or smooth ice-water interface (Wakabayashi et al., 1994). The modelled backscatter was used to confirm early theories concerning active microwave signals from lake ice, for example, demonstrating that backscatter increases as ice thickens with bubbles present, and was validated using ERS-1 backscatter measurements (R^2 of 0.97) (Wakabayashi et al., 1994). Further exploration of these lakes was conducted using a single scattering model, the integral equation model (IEM) (Fung et al., 1992; Wakabayashi et al., 1999). This model was used to explore the scattering mechanisms associated with floating and grounded ice during spring melt. Forward modelling demonstrated that increases in backscatter from grounded ice covers in the spring are associated with increases in ice surface roughness. Alternatively, decreases in backscatter from floating ice covers for the same period were associated with the presence of water on the ice surface. More recent experiments have used IEM in combination with volume scattering models to explore how the dominant interface changes during surface freezing and melt (Han & Lee, 2013). For this experiment a snow-free ice surface was flooded, and backscatter was measured over an hour and a half using a C-band scatterometer. Using a genetic algorithm for inversion, the RMS height and correlation length were retrieved as well as the contributions from different interfaces (air-ice and ice-water). Results indicated that when the ice surface was flooded, the air-ice interface was the dominant scattering interface due to the higher dielectric constant; this is similar to the results obtained by Wakabayashi et al. (1999) for floating ice cover on the North Slope of Alaska lakes. However, as the water froze, the response from the ice-water interface increased in strength due to the higher transmissivity of the frozen surface (Han & Lee, 2013). The contribution of the air-ice interface increased later during the

freeze process as crystallization raised the RMS height of the ice surface (Han & Lee, 2013). Numerical modelling was also used to explore the role of bubbles as scatterers in lake and sea ice in Hokkaido, Japan (Matsuoka et al., 1999). The model determined backscatter through a summation of the total contributions of bubbles to scattering within the ice column, but made assumptions different to existing field observations from prior research such as smooth interfaces and only allowed for spherical bubbles in the ice (Jeffries et al., 1994; Matsuoka et al., 1999). Recently, the impact of ice-water boundary roughness was studied using numerical modelling (Atwood et al., 2015). The numerical model solved for the propagation and scattering of microwave signals through an ice medium, both with and without tubular bubbles (Atwood et al., 2015). Model results demonstrated that smooth ice-water interfaces were not able to replicate backscatter from floating ice covers (Atwood et al., 2015). Additionally, numerical experiments showed that backscatter from an ice column with ice-water interface roughness parameterized using a root means square (RMS) height of 5 mm and correlation length of 50 mm was similar with and without a layer of tubular shaped bubbles. This indicates that the presence of these bubbles has little impact on the backscatter returned from lake ice.

Radiative transfer models are also an effective way of modelling backscatter as this approach addresses the energy transmitted through a medium and assumes that fields scattered by the particles in the medium are not correlated (Ulaby & Long, 2014). Because of this assumption, the radiative transfer theory states that particles in the medium should be randomly distributed and that the spacing between adjacent particles is sufficient to not allow coupling between them (Ulaby & Long, 2014). The modified HUT model is one example of a radiative transfer theory-based model that can be used to determine brightness temperature from multiple layers of a snowpack and allows for the inclusion of underlying ice layers (Lemmetyinen et al., 2010, 2011). Scattering and emission properties for each layer are determined using the single-layer HUT model formulations of the radiative transfer equation (Pulliainen et al., 1999; Lemmetyinen et al., 2010). The interaction of emitted energy at the interfaces between layers is determined using transmission/reflection coefficients and the refraction angle from the Fresnel equations (Lemmetyinen et al., 2010). Studies that have used the modified HUT model for brightness temperature from lake ice modified the rough soil reflection coefficient used in the model (Wegmüller & Mätzler, 1999) to a simpler relationship following Choudhury et al. (1979) that is valid when bottom-interface roughness is small relative to wavelength (Gunn et al., 2011). The

modified HUT model was used for both Arctic and Subarctic lakes (Gunn et al., 2011; Kang et al., 2014) within Canada, with both studies showing the best results when a roughness of 1 mm was used at the ice-water interface. According to model results, the highest sensitivity of brightness temperature to ice thickness was at approximately 15 GHz (Kang et al., 2014).

Another model based in radiative transfer theory, the dense media-radiative transfer (DMRT) model with quasi-crystalline approximation (QCA), and an empirical model, the Oh Model, were used to demonstrate the sensitivity of active Ku and X-band to ice properties (Gunn, Brogioni, et al., 2015). DMRT-QCA was selected due to its ability to represent volume scattering from densely packed spheres within a medium (i.e. snow ice) (Tsang et al., 2007) and the Oh model was used to represent surface scattering at different interfaces, such as ice-water or ice-ground (Oh et al., 2002; Gunn, Brogioni, et al., 2015). When compared to ground-based scatterometer measurements, modelled backscatter was found to be within 5 dB of the observed values. Additionally, these modelling experiments demonstrated that while overlying snow cover has little impact on X-band backscatter, the removal of snow by lake ice can result in a decrease of up to 6.17 dB for co-pol and 7.96 dB for cross-pol for Ku-band (Gunn, Brogioni, et al., 2015). Radiative transfer modelling was also used to test the sensitivity of VV polarized backscatter to lake ice properties (i.e. thickness, temperature, bubble size, and roughness) from lakes on the Qinghai-Tibet Plateau (QTP) (Tian et al., 2015). Backscatter was modelled using the dense medium phase and amplitude correction (DM-PACT) method (Ewe et al., 1998), this model considers a dense medium with spherical inclusions bounded by rough surfaces, for the lakes on the QTP the Advanced Integral Equation Model (AIEM) was used to represent these surfaces (Chen et al., 2003; Tian et al., 2015). The results of these experiments for the QTP indicated that the key properties impacting backscatter and lake ice were RMS height at the ice-water interface and bubble radius. This supports the results of previously mentioned numerical studies and more recent polarimetric decomposition experiments that show surface scattering is the primary scattering mechanism for lake ice (Engram et al., 2013; Gunn et al., 2018). Radiative transfer modelling has also been performed for river ice, which does share similarities with lake ice, however different physical processes exist for the two types of ice (Gherboudj et al., 2010). This modelling approach presents volume, surface, and total scattering components using a combination of DM-PACT (Chuah et al., 1996), Mie and Rayleigh modelling, and IEM. The experiments presented in this research evaluated how changes in properties (roughness components, bubble

size, and ice type) impacted the backscatter from river ice columns. Results indicate increasing roughness at both snow-ice and ice-water interfaces increase backscatter and that the presence of air inclusions in the ice leads to an increase in backscatter, particularly at high frequencies (Gherboudj et al., 2010).

Forward modelling of lake ice has primarily focused on the role of ice thickness, bubbles within the ice, and the presence of snow. With more recent findings indicating the importance of surface scattering from the ice-water interface, modelling has shifted to focusing on exploring the sensitivity of microwave signals to varying roughness (Han & Lee, 2013; Atwood et al., 2015; Tian et al., 2015). However, there are limitations associated with these modelling approaches taken to date. Several modelling experiments have ignored the presence of snow properties. While dry snow cover will have little impact on the backscatter from lower frequencies (i.e., L, C, and X-band), wet snow during mid-winter melt event and melt onset has been shown to decrease the backscatter returned from lake ice covers (Duguay et al., 2002; Antonova et al., 2016). Furthermore, some modelling approaches have treated ice cover as a homogenous medium, for example, assuming the ice column is only clear ice or only contains one size of air inclusions. Ice cores from various locations indicate that this is not an appropriate representation of ice covers and that most contain layers of snow/grey ice, clear ice, and layers containing vertically oriented tubular bubbles (Hall et al., 1994; Jeffries et al., 1994; Gunn et al., 2018). Therefore, backscatter from lake ice should be modelled using an approach that allows for the inclusion of multiple layers. Additionally, it is important that roughness be included for the different interfaces present within the ice column (e.g., snow-ice and ice-water). Modelling approaches have also focused primarily on shallower lakes where layers of tubular bubbles are common, but the deeper lakes where these bubbles are absent have been largely ignored. Forward modelling has also been conducted primarily looking at C-band backscatter, however, other frequencies can also have important applications for lake ice. Finally, modelling experiments that explore the impact of varying ice properties on backscatter have used synthetic data to represent ice thickness, ice temperature, and other properties. The various limitations discussed above demonstrate that, to date, models have not provided faithful representations of ice covers. However, the recent publication of the Snow Microwave Radiative Transfer Model (SMRT) (Picard et al., 2018) provides a solution to these gaps within the field of lake ice forward modelling.

2.4 Snow Microwave Radiative Transfer Model

The snow microwave radiative transfer (SMRT) model is an active-passive model that allows users to produce both backscatter and brightness temperature primarily for snow mediums (Picard et al., 2018). However, recent updates to the model include the addition of both saline and freshwater ice mediums (Murfitt et al., 2022; Soriot et al., 2022). The model is designed with user flexibility in mind allowing for the selection of different electromagnetic theories and microstructure models and exploration of different representations of snow and ice layers (Picard et al., 2018). The model is also continuously updated and developed through an active community, identifying issues, and proposing needed approaches to better represent observed conditions. SMRT computes the scattering, absorption, and phase matrix for each layer using the selected electromagnetic model, which includes improved Born approximation (IBA) and dense media radiative transfer (DMRT) theory, and user-defined snow/ice layer properties (Picard et al., 2018). Reflectivity and transmissivity coefficients are calculated for interfaces between layers and at the substrate (i.e., soil, ice, or water) (Picard et al., 2018). In the current version of SMRT, roughness can be added to the interfaces and substrate in active mode using two surface scattering models, the integral equation model (IEM, Fung et al., 1992), that is most applicable for small roughness values, and geometrical optics (Tsang & Kong, 2001). Once all components within the model are specified, the underlying equations are solved through the radiative transfer equation component, the discrete ordinate and eigenvalue (DORT) method is used in SMRT, which provides the user with the intensity from the given medium (Picard et al., 2018). The main assumption of SMRT is that microstructure and medium layers are considered isotropic. Additionally, SMRT assumes that there are no horizontal variations in layer properties. It is also assumed that dry snow grains are pure ice and air scatterers are pure air. All bubbles within freshwater layers for SMRT are assumed to be spherical. Additional assumptions depend on the selected electromagnetic and microstructure models within SMRT that are discussed further in the following sections.

2.4.1 Layer Dielectrics

Within SMRT ice and snow layers are represented as mirror opposites. Snow layers are represented as ice inclusions in an air medium while ice layers are represented as air inclusions in an ice medium. The permittivity of the layers is used to determine the Ks, Ka, phase function and effective permittivity with the electromagnetic models which will be discussed in Section 2.4.2.

Air within both snow and ice has a set permittivity of 1. The permittivity of ice for both layers is solved using the formulation presented in Mätzler et al. (2006). Through this formula the permittivity of layers is temperature dependent and determined via the following equations,

$$\varepsilon_r = 3.1884 + 9.1 * 10^{-4} * (T_K - 273.16) \quad (2.1)$$

$$\varepsilon_i = \frac{a_0}{f + \beta_0 * f} \quad (2.2)$$

where ε_r is the real permittivity, T_K is the temperature of the layer in Kelvins, ε_i is the imaginary permittivity or dielectric loss, f is the frequency in GHz. For ε_i, a_0 and β_0 are semiempirical expressions which are calculated through equations 2.3 and 2.4,

$$a_0 = (0.00504 + 0.0062\theta) * \exp(-22.1\theta), \text{units are GHz} \quad (2.3)$$

$$\beta_0 = \frac{B_1}{T_K} \frac{\exp(b/T_K)}{[\exp(b/T_k - 1]^2} + B_2 f^2 + \exp[-9.963 + 0.0372(T_K - 273.16)], \text{units are GHz}^{-1} \quad (2.4)$$

where,

$$\theta = \frac{300}{T_K} - 1, \text{units are in K}$$

$$B_1 = 0.0207 \text{ K/GHz}, b = 335\ K, \text{and } B_2 = 1.16 * 10^{-11} \text{ GHz}^{-3}$$

This permitivity model holds true for dry conditions, however, when considering wet snow conditions other models are necessary. This is because wet snow conditions must consider layers that contain a mix of air, ice, and water. The most recent version of SMRT includes a number of models to address the mixing of water into snowpacks. While the formulation of permitivity for these models differs, all models follow the same pattern which is an increase in both real and imaginary permitvity with increasing liquid water content (Picard, Leduc-Leballeur, et al., 2022). However, the differences in calculations between these models does result in differences in the real and imaginary permitivity values as shown in **Figure 2.1** from Picard, Leduc-leballeur, et al.

(2022). below.

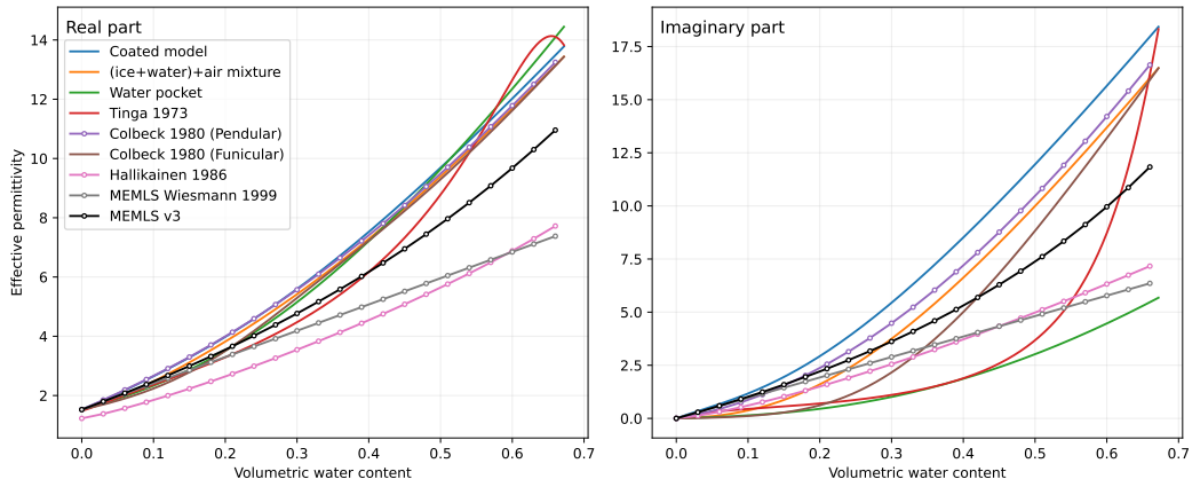

Figure 2.1 Permitivity values for snow cover using different mixed medium models. The plot on the left shows the real part of the effective permitivity and the right plot shows the imaginary part. Source: Picard, Leduc-leballeur, et al. (2022).

For the purposes of this thesis, specifically, Chapter 6, the MEMLS v3 permittivity model is selected to calculate permitivity for wet snow (Mätzler & Wiesmann, 2007). This model was selected following Picard, Leduc-Leballeur, et al. (2022), which states that the MEMLS permitivity is based on ground measurments and behaves more realistically for higher water content even though it is not optimized for this range. Furthermore, in Chapter 6 of this thesis, experiments conducted using other wet snow perimitivity models (i.e. Hallikainen et al., 1986) resulted in underestimated HH-pol backscatter while HH backscatter under MEMLS was found to be closer to observed backscatter from Sentinel-1.

2.4.2 Electromagnetic Models

One of the key features within SMRT is the user flexibility to select different electromagnetic models for solving the radiative transfer equation through DORT. This thesis makes use of this flexibility and works with two of the electromagnetic models within the SMRT framework, the dense media radiative transfer (DMRT) theory with Quasi-Crystalline Approximation-Coherent Potential (QCACP) short range (Tsang et al., 1985; Picard et al., 2013) and the improved Born approximation (IBA) (Mätzler, 1998; Picard et al., 2018). DMRT QCACP has been used in past lake ice modelling experiments (Gunn, Brogioni, et al., 2015) while IBA is a common electromagnetic model in cryosphere radiative transfer modelling. The electromagnetic

models within SMRT are key for determining the scattering and absorption coefficients and the phase matrix for solving the radiative transfer equation. These models are parameterized using microstructure parameters and layer permittivity.

DMRT QCACP requires the sticky hard sphere (SHS) microstructure model (summarized in section 2.4.3). Full formulation of the DMRT QCACP within the SMRT framework can be found in Picard et al. (2018). The multilayer DMRT within SMRT follows the formulation noted by Picard et al. (2013) and the effective permittivity as well as scattering and extinction coefficients are calculated according to Shih et al. (1997) and Tsang et al. (1985). The effective permittivity of the layer refers to the permittivity of the layer when both the background and scatterers are considered. For DMRT QCACP, effective permittivity is solved considering the fractional volume of scatterers, the dielectric constants for background and scatterers, the wavenumber, and stickiness parameter (Picard et al., 2018). There are key limitations of this model that must be noted. First, the current implementation of this model within SMRT does not allow for the inclusion of cylinder air inclusions. This is an issue for proper representation of air bubbles within lake ice as tubular bubbles are a key feature within ice columns for shallow lakes. This issue is addressed in both Chapters 4 and 5 where smaller spherical bubbles are used as an approximation for tubular bubbles. As explained within these chapters, while it is possible this may result in errors with the modelling, past research has indicated that it is likely these bubbles play a minor role in the scattering of active microwave signals by lake ice (Atwood et al., 2015). Therefore, this approximation should have little impact on the results. The second limitation of DMRT QCACP is the validity range. DMRT QCACP in SMRT is implemented as a short-range electromagnetic model. Because of this implementation the model is only valid for smaller snow grains and lake ice bubble radius. Comparison between DMRT QCACP and other electromagnetic models indicate that it is valid up to $k_0a < 0.6$, where k_0 is the wavenumber and a is the radius of the snow grain or air bubble (Picard, Löwe, & Mätzler, 2022). Beyond this range there is a divergence of the resulting backscatter from the short-range model and long-range models that are appropriate for large snow grains and bubbles.

To address the limitations of DMRT QCACP when performing sensitivity experiments the improved Born approximation (IBA) is used. The implementation of IBA in SMRT follows closely to the formulation presented in Mätzler (1998). IBA is a long-range electromagnetic model and therefore does not encounter the same limitation as DMRT QCACP, except when values of

k_0a exceed 1.5 (Picard, Löwe, & Mätzler, 2022). **Figure 2.2** shows the divergence of modelled backscatter for these two electromagnetic models for a lake ice column with varying bubble radius. Unlike DMRT QCACP, IBA can be parameterized with both SHS and other microstructure models such as the exponential correlation length model in SMRT. However, similar to DMRT QCACP, current implementation of the model within SMRT only allows for the inclusion of spherical bubbles in lake ice and does not allow for vertical tubular bubbles to be added. IBA is also used in Chapter 6 as this is required when modelling mediums that contain ice, air, and water in SMRT. The effective permittivity of layers in IBA is calculated using the Polder-van Santen mixing formula (Sihvola, 1999). The effective permittivity is crucial in IBA for determining the microstructure term, given as $M(|k_d|)$, which is used to determine the phase function (Picard et al., 2018). Additionally, calculation of the effective permittivity is important for computing the absorption coefficient and the boundary conditions within SMRT (Picard et al., 2018). SMRT also includes an electromagnetic model named 'original IBA' which determines the absorption coefficient not using the effective permittivity as in the radiative transfer model MEMLS, however, this must be set by the user and is not the default (Picard et al., 2018).

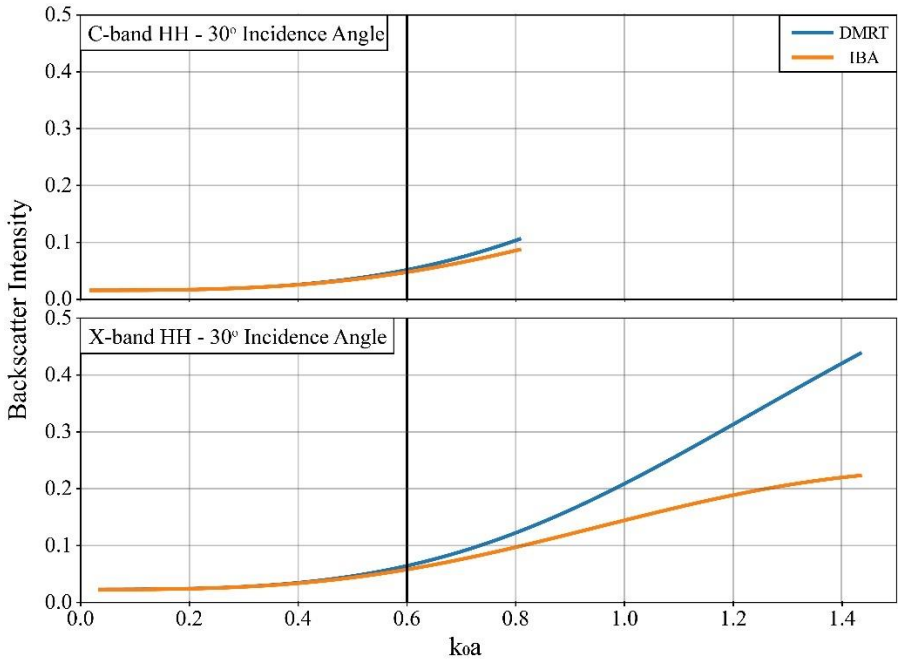

Figure 2.2 Comparison of linear intensity between DMRT and IBA with increasing k_0a. The vertical black line indicates a k_0a of 0.6 where values start to diverge.

2.4.3 Microstructure Models

In selecting the microstructure model for experiments and applications throughout this thesis, the flexibility of SMRT was utilized. As discussed in section 2.4.2, this thesis utilizes the electromagnetic models, DMRT QCACP and IBA. While DMRT must be parameterized using the SHS microstructure model, IBA can be parameterized with other microstructure models, for the purposes of this thesis the exponential correlation length microstructure model. A brief description of these two models will be given below.

The Sticky Hard Spheres microstructure model represents scattering medium as spherical grains or air inclusions depending on whether it is ice or snow. One key feature of the SHS model is that it can be used to change the relative position of grains without modifying the diameter or volume fraction (Löwe & Picard, 2015). The microstructure model is parameterized through the stickiness and grain size/bubble radius settings. Higher values of the stickiness parameter indicate that there is a lower tendency for the spheres in the medium to stick together while lower values of stickiness indicate a higher tendency for the spheres to stick together (Löwe & Picard, 2015). SHS was utilized in Chapters 4 – 6 of this thesis. For Chapters 4 and 5, SHS was used because the selected electromagnetic model was DMRT QCACP as in past lake ice modelling experiments (Gunn, Brogioni, et al., 2015). Additionally, information on effective correlation length for snow grains and SSA was limited to estimates based on terrestrial snow cover for the study sites used in these chapters (Vargel et al., 2020). For Chapter 6, SHS is used for ice layers in combination with IBA due to this chapter focusing on wet snow conditions. One limitation of using SHS for the SMRT experiments in this thesis was the lack of available in situ measurements. While there are methods for obtaining stickiness from micro-computed tomography (Löwe & Picard, 2015), these measurements have not been acquired for snow over lake ice. Therefore, for the purposes of Chapter 4 and 5 in this thesis, past determined values of 0.1 for terrestrial snow cover in the Canadian Subarctic and Artic were used (Vargel et al., 2020). SHS was used as the microstructure model for all lake ice experiments as this is likely the best representation or the spherical bubbles present in the snow ice layers. For snow ice and clear ice covers, a value of 0.4 and 1.0 were used respectively throughout all experiments in the thesis. A value of 0.4 was used for snow ice to represent the moderate tendency of spherical bubbles in snow ice layers to stick together, while a value of 1.0 was used for clear ice due to the limited number of air inclusions present in these layers. **Figure 2.3** shows a comparison between these types illustrating this difference.

Figure 2.3 Difference between air inclusions for snow ice (left) and clear ice (right).

For Chapter 6 of the thesis, the exponential microstructure model is used for the overlying snowpack on the ice. This model is parameterized using the exponential correlation length which is a way of representing the relative position of snow grains to each other within the snow medium (Mätzler, 2002). In Chapter 6, field data collected from overlying snow cover on lake ice was collected during the 2021 ice season at Lake Oulujärvi by the Finnish Meteorological Institute (FMI). These data included detailed measurements of snow properties including SSA and snow density. Following the parameterization of SMRT in Rutter et al. (2019), these values can be used to determine exponential correlation length following equations 9 and 10 in Mätzler (2002), which can be calculated using equation 2.5 below:

$$p_{ex} = 0.75\ (\frac{4 * \left(1 - \frac{\rho}{\rho_{ice}}\right)}{SSA * \ \rho_{ice}})$$

(2.5)

where ρ_{ice} is the density of the ice, assumed to be 916.7 kg m^{-3}, ρ is the density of the snow layer, and SSA is the specific surface area (m^2 kg^{-1}). This provides a better representation of the snow microstructure compared to SHS used in other experiments as it is determined from collected field data. However, it could not be used for the experiments conducted in Chapters 4 and 5 due to the lack of field data as mentioned above.

2.4.4 Interface and Substrate Roughness

The interaction of microwave signals at substrates or interfaces in SMRT are determined through the user selected interface model. SMRT currently has several models implemented for interface and substrate interactions; however, many are not applicable for active mode simulations. For active mode, there are three options for modelling these interactions, flat, integral equation model (IEM) (Fung et al., 1992; Fung & Chen, 2010), and geometrical optics (Tsang & Kong, 2001). The default in SMRT is to treat the interface or substrate as flat and the reflectivity and transmittivity are determined through the Fresnel coefficients. However, based on the recent findings of polarimetric decomposition, modelling, and co-pol phase difference analysis highlighting the importance of roughness at the ice-water interface (Engram et al., 2012; Atwood et al., 2015; Gunn et al., 2018), this is not a suitable approach for lake ice. Therefore, roughness must be varied at the ice-water interface using one of the two other models. Both models are parameterized using root mean square height or *s*, which is the approximation of the vertical variation of surface roughness, and correlation length or *l*, which is the horizonal variation in roughness or displacement between two points on the surface (Ulaby & Long, 2014). Additionally, to produce a faithful representation of the ice column, roughness at the snow-ice and air-snow interfaces should be considered (Wakabayashi et al., 1999; Han & Lee, 2013), particularly when exploring varying water content in the overlying snow layers. Geometrical optics is valid when the $k_0 s >> 1$ and $k_0 l >> 1$, typically this occurs for large values of *s* and *l* meaning that geometrical optics is applicable for large scale roughness values. IEM is valid when k_0*RMSH < 2 and $k_0^2 * RMSH * Correlation\ Length < \sqrt{eps_r}$, where eps_r is the ratio between the permittivity of the mediums at the interface (Fung et al., 1992; Fung & Chen, 2010). SMRT allows for an extension of this final limitation using the formulas stated in Brogioni et al. (2010), where the Fresnel coefficients are determined using either the incidence angle ($k_0^2 * RMSH * Correlation\ Length < \sqrt{eps_r}$) or an angle of 0° ($k_0^2 * RMSH * Correlation\ Length > \sqrt{eps_r}$). IEM is therefore more applicable for small scale roughness. Measurements of roughness at the lake ice-water interface are limited, if non-existent, however, measurements for the underside roughness of smooth congelation river ice can provide a proxy. According to measurements of this ice type, roughness values likely range from 0.1 to 10 mm (Gherboudj et al., 2010). Due to these small roughness values, IEM was selected as the model for representing both interface and substrate roughness throughout this thesis. Additionally, IEM and advanced IEM (not available in SMRT)

have been used in past lake ice modelling experiments (Wakabayashi et al., 1999; Gherboudj et al., 2010; Han & Lee, 2013; Tian et al., 2015).

The purpose of IEM in SMRT is to solve for the reflection coefficients at each relevant interface where the model is implemented. This is achieved in SMRT by solving equation 82 in Fung et al. (1992) resulting in the single scattering component for the interface,

$$\sigma_{qp}^{S}(S) = \frac{k^2}{2} \exp\left(-2k_z^2\sigma^2\right) \sum_{n=1}^{\infty} \sigma^{2n} \left|I_{qp}^{n}\right|^2 \frac{W^n(-2k_x, 0)}{n!}$$

where σ^2 is the RMS height squared, W represents the autocorrelation function/Fourier transform with n being the nth power. I_{qp}^{n} is defined as,

$$I_{qp}^{n} = (2k_z)^n f_{qp} \exp(-\sigma^2 k_z^2) + \frac{k_z^n [F_{qp}(-k_x,0) + F_{qp}(k_x,0)]}{2}$$

where F_{qp} is a complementary field coefficient and f_{qp} is a scattered field (Fung et al., 1992). The behaviour of IEM results in a bell-shaped pattern where increasing *s* results in an initial increase in backscatter which then peaks and decreases as *s* continues to increase (Fung & Chen, 2010). The point at which this peak in backscatter is reached will depend on incidence angle, with backscatter continuing to increase at larger incidence angles (Fung & Chen, 2010). Additionally, it should be noted that VV-pol is more sensitive to *s* than HH-pol resulting in higher backscatter for the same medium (Fung & Chen, 2010). While IEM can reproduce cross-polarized backscatter, in SMRT cross-pol data is underestimated and therefore not modelled throughout the experiments conducted in this thesis.

2.5 CLIMo Integration

One key limitation of past lake ice modelling experiments has been the use of synthetic values for ice properties, for example ice temperature and ice thickness. To make the sensitivity experiments conducted throughout this thesis better reflect true conditions, SMRT was integrated with the Canadian Lake Ice Model (CLIMo). CLIMo is a 1-D thermodynamic lake ice model that has been used across the Northern Hemisphere in both field and remote sensing studies (add citations). A full description of the model can be found in Duguay et al. (2003). The model is based on a one-dimensional thermodynamic sea-ice model (see Flato & Brown, 1996), which makes use of the one-dimensional unsteady heat conduction equation (Maykut & Untersteiner, 1971) (2.6),

where ρ (kg m^{-3}) is the density, C_p (J kg^{-1} K^{-1}) is the specific heat capacity, T (K) is the temperature of ice or snow, t (s) is the time, k (W m^{-1} K^{-1}) is the thermal conductivity, z (m) is the distance from the surface (positive if in the downward direction), F_{sw} (W m^{-2}) is the downwelling short wave radiative energy flux, I_o (W m^{-2}) is the fraction of short wave radiation flux that penetrates the surface layer, α is the surface albedo, and K is the bulk extinction coefficient for shortwave radiation (Duguay et al., 2003),

$$\rho C_p \frac{\partial T}{\partial t} = \frac{\partial}{\partial z} k \frac{\partial T}{\partial z} + F_{sw} I_o (1 - \alpha) K e^{-kz}$$

(2.6)

Following this, the surface energy budget can be solved from equation 2.7, where F_o (W m^{-2}) is the net downward heat flux absorbed at the surface, ε is the emissivity, σ is the Stefan-Boltzmann constant, F_{lw} is the downwelling long wave radiative flux, F_{lat} is the downward latent heat flux, and F_{sens} is the downward sensible heat flux,

$$F_o = F_{lw} - \varepsilon \sigma T_s^4(0,t) + (1 - \alpha)(1 - I_o) F_{sw} + F_{lat} + F_{sens}$$

(2.7)

Surface type (ice, snow, or open water), surface temperature, and ice thickness are used to determine how albedo is parameterized (Duguay et al., 2003). For CLIMo to produce a yearly ice-on and off cycle a fixed-depth mixed layer is included (Duguay et al., 2003). If there is ice cover on the lake, the temperature of the mixed layer is set to the freezing point (0 °C), however, if the lake is ice free the temperature is set from the surface energy budget; thereby serving as a measure of heat storage within the lake (Duguay et al., 2003).

Surface type (ice, snow, or open water), surface temperature, and ice thickness are used to determine how albedo is parameterized (Duguay et al., 2003). For CLIMo to produce a yearly ice-on and off cycle a fixed-depth mixed layer is included (Duguay et al., 2003). If there is ice cover on the lake, the temperature of the mixed layer is set to the freezing point (0 °C), however, if the lake is ice free the temperature is set from the surface energy budget; thereby serving as a measure of heat storage within the lake (Duguay et al., 2003).

The key outputs from CLIMo used in this thesis were ice and snow temperatures, snow depth, and ice thickness. These outputs were used to parameterize SMRT during the different experiments. To run CLIMo, meteorological data are required including, air temperature,

humidity, cloud cover, wind speed, and snow accumulation. Due to the remote locations of some of the lakes in this study and due to inconsistencies in available climate data, ERA5 reanalysis data (Hersbach et al., 2020) were used to parameterize these meteorological variables for input into CLIMo. For Chapters 4 and 5, the same ERA5 data were used, with one 30 x 30 km ERA5 grid cell covering Noell Lake and two grid cells covering the area of Malcolm Ramsay Lake. For Chapter 6, the ERA5 grid cell that overlapped the locations of obtained field data was used to determine the CLIMo inputs. Additionally, due to the size of Lake Oulujärvi studied in Chapter 6, snow accumulation data from a nearby weather station was used as an alternative to ERA5 data. Following successful CLIMo runs, results were validated using available ice thickness and snow depth data to select the best settings for each lake. **Table 2.1** provides the values used as constant inputs for each CLIMo simulation based on the results of this validation. Values were either obtained from past applications of CLIMo or based on values obtained during respective field campaigns.

Table 2.1 Parameterization of CLIMo for the study lakes in this thesis.

		Value	Reference
Noell Lake	Mixing Depth	6 m	Ogbebo et al., 2009
	Snow Density	283 kg m^{-3}	Field Campaign March 2019
	On-ice Snow Depth	35%	
Malcolm Ramsay Lake	Mixing Depth	2 m	Gunn et al., 2015b
	Snow Density	276 kg m^{-3}	Brown and Duguay, 2011b
	On-ice Snow Depth	50%	
Lake Oulujärvi	Mixing Depth	10 m	
	Snow Density	150 kg m^{-3}	

On-ice Snow Depth	50%

After the CLIMo results were obtained they were translated into a usable format for SMRT. The largest modification made was to average the interface temperatures from CLIMo to create layer temperatures for use in SMRT. **Figure 2.4** provides a simple representation of how the interface temperatures were translated to layer temperatures. While CLIMo did provide thicknesses for the different layers, total ice thickness from CLIMo was instead divided into equal amount for use in SMRT and reflected what was produced by CLIMo. This also allowed for the inclusion of a more reflective snow ice layer based on recorded field observations. Details of the specific inclusion of CLIMo outputs for SMRT analysis are included with each respective chapter.

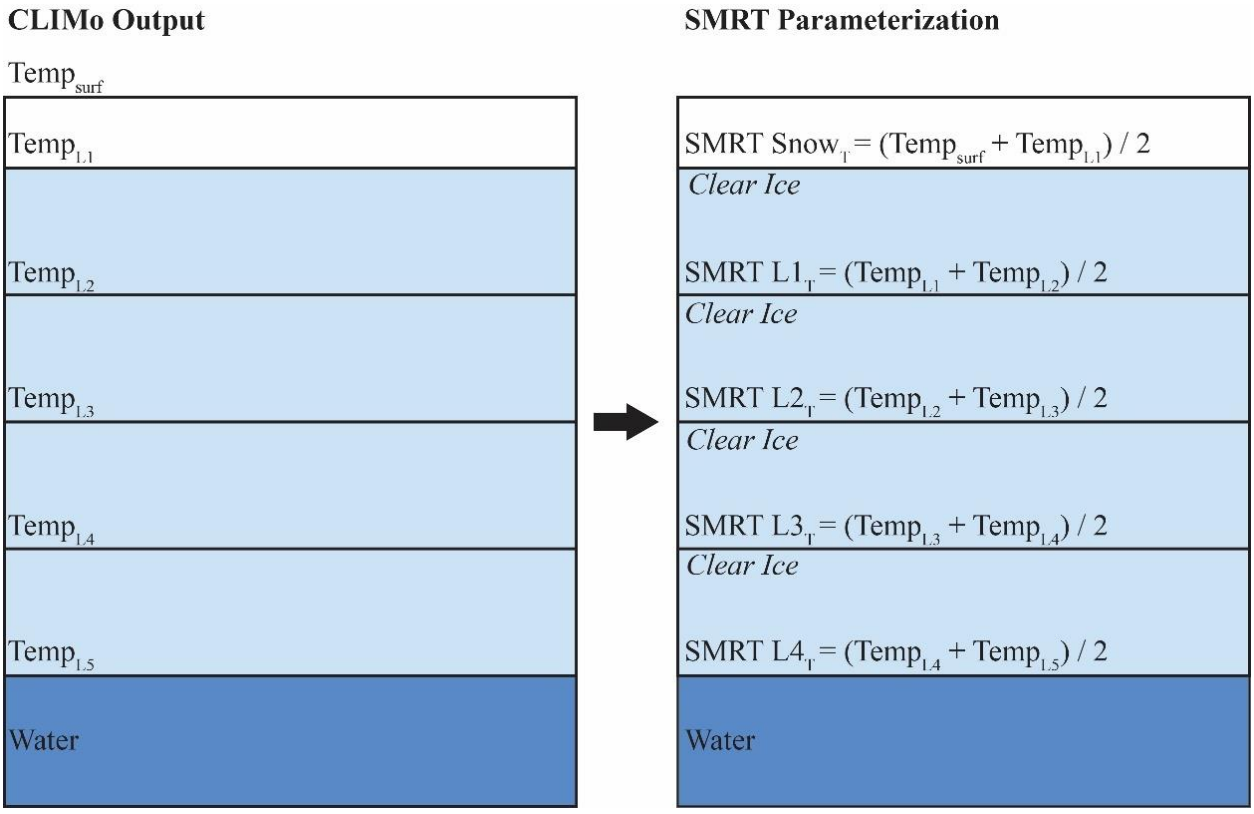

Figure 2.4 Translation of CLIMo output temperatures to SMRT layer temperatures.

2.6 Summary

This chapter provides a brief review of the response of microwave signals to lake ice throughout the ice season and recent changes in the primary scattering mechanism for lake ice.

Through modelling, polarimetric decomposition, and co-pol phase difference analysis, surface scattering as a result of roughness at the ice-water interface has been noted as the dominant mechanism (Engram et al., 2012; Atwood et al., 2015; Gunn et al., 2018). The next chapter of this thesis will explore the interaction between lake and microwave further by reviewing active microwave and lake ice literature over the past fifty years. Furthermore, it will highlight key areas of future research in the field of active microwave and lake ice.

While modelling has been used to explore how changing ice properties impact backscatter response, this chapter notes that there are limitations associated with these approaches and a more faithful representation of lake ice covers from a modelling standpoint can be achieved through the snow microwave radiative transfer (SMRT) model. This chapter discusses how lake ice and the overlying snow layers are represented in the different chapters of this thesis as well as provides background on the different electromagnetic, microstructure, and interface models. Chapters 4 – 6 of this thesis will use SMRT to investigate the impact of changing ice properties on microwave backscatter as well as apply the model to conduct forward modelling under both wet and dry conditions. This will help address gaps in the representation of lake ice in the modelling literature to date, provide insight into understanding various interactions, and detail areas that require further exploration.

Chapter 3
50 Years of Lake Ice Research from Active Microwave Remote Sensing: Progress and Prospects

3.1 Introduction

Global lake coverage is reported at 3.7% of non-glaciated area with areal coverage between 45 and 75 °N (aggregated for 3° of latitude) ranging from 100 to >300 x 10^3 km^2 (Verpoorter et al., 2014). Lakes at mid and high latitudes go through cycles associated with the formation and decay of lake ice, with an estimated extent of 1.59 x 10^6 km^2 at peak ice thickness across the Northern Hemisphere (Brooks et al., 2013). The presence of lakes and lake ice plays an important role in the regulation of local climate and weather. As an example, temperature fluctuations in southern Finland during January 2012 were most accurately reproduced using the High Resolution Limited Area Model (HIRLAM) Numerical Weather Prediction model when ice cover extent conditions were properly represented (Eerola et al., 2014). Reduced ice cover on the Laurentian Great Lakes can result in intense lake-effect snow events; however, it has also been noted that warmer temperatures may result in a decrease in sensible heat flux, limiting precipitation amounts (Notaro et al., 2015; Baijnath-Rodino et al., 2018). High snowfall events from the Great Lakes can have severe consequences for high population areas such as Southern Ontario (Canada) and the North-Eastern United States. For example, in November 2014, Buffalo (New York, USA) experienced over 1.5 m of snow accumulation within 48 hours which resulted in 13 casualties, and severe structural and tree damage (National Weather Service, 2014). Beyond the impact on climate and weather, the presence and thickness of lake ice also has an important role in local economies, recreation, and culture. Northern communities rely on the presence of lake ice and river ice for the operation of ice roads throughout the winter season and for travel between communities (Mullan et al., 2017; Knoll et al., 2019). Additionally, lake ice provides recreation for both residents and tourists in areas such as Southern-Central Ontario (Canada) as it helps establish recreational snowmobile trails. According to a recent report, the estimated economic impact of snowmobiling in the Huntsville region of Ontario resulted in a gross domestic product (GDP) of over $50 million (Cummings et al., 2019). The Tibbitt to Contwoyto winter road is made up of 85% of ice crossings (over 400 km) and services three diamond mines north of Yellowknife, Northwest Territories (Canada) (Tibbitt to Contwoyto Winter Road Joint Venture, 2020). In 2019, 4700 tonnes of

material was hauled on this road everyday of operation (Tibbitt to Contwoyto Winter Road Joint Venture, 2020).

The economic and recreational benefits of lake ice are being threatened due to the impact of climate change on lake ice phenology and thickness. Recent long-term trends in ice freeze-up from 75 lakes in the United States, Sweden, Finland, and Russia, show average shifts of 1.5 days later per decade from 1950 to 2013, while trends in break-up for Canada, the United States, Switzerland, Sweden, Finland, and Russia, show average shifts of 1.2 days earlier per decade from 1951 to 2014 (n=152 lakes) (Hewitt, 2019; Lopez et al., 2019). These changes are expected to continue as modelled ice phenology for 2040-2079 shows a shift towards shorter ice cover duration by up to 50 days compared to averages from 1960-1990 (Dibike et al., 2011). Recent short-term trends, 2000-2013, in lake ice phenology for the Canadian Arctic remain consistent with long-term observations, showing an earlier end to the break-up period by 0.3 days per year (Šmejkalová et al., 2016). Lake ice cover is a robust climate change proxy (Magnuson et al., 2000), making it important to understand and monitor these changes. The Global Climate Observation System (GCOS) of the World Meteorological Organization (WMO) identifies lake ice cover and thickness as Essential Climate Variables (ECVs) (Belward et al., 2016). GCOS requirements state that lake ice cover should be available daily with a maximum uncertainty of 10% and lake ice thickness is needed monthly with an uncertainty of 1-2 cm. These requirements are set to establish a sufficient data record for understanding variability in lake systems within a changing climate (Belward et al., 2016). However, the number and density of lakes makes manual measurements of these properties difficult to sustain over time. This is reflected in the global number of ice event observations (ice-on and ice-off dates) in the "Global Lake and River Ice Phenology" database (Benson et al., 2013), which had a maximum of 1046 observations in 1980 but averaged 165 observations per year between 2010 and 2018 (**Figure 3.1**).

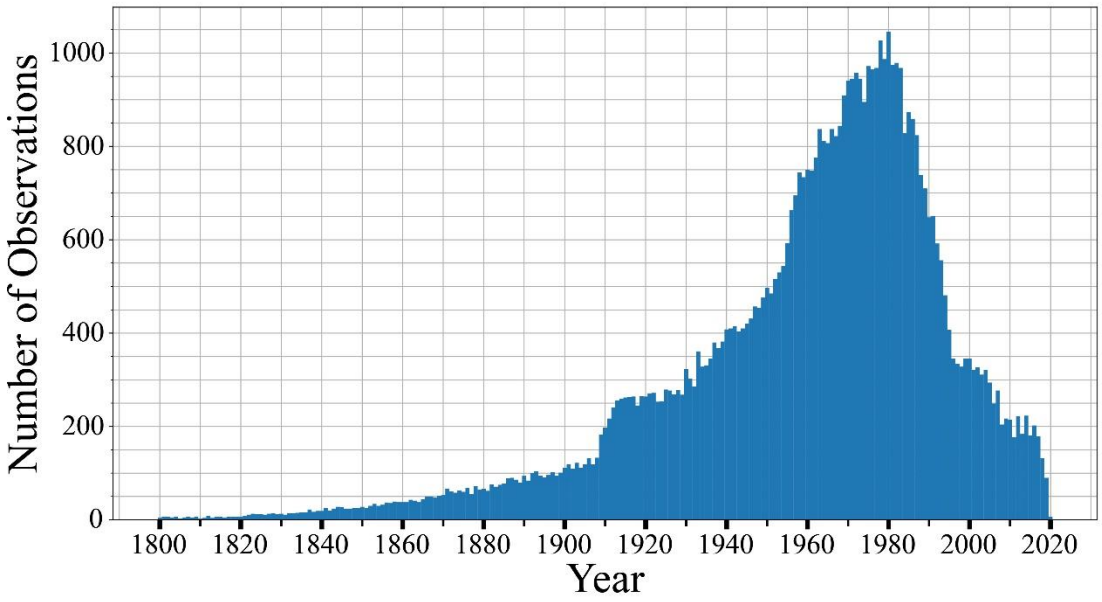

Figure 3.1 Yearly ground-based ice phenology observations from 1800 to 2020 reported in the "Global Lake and Rive Ice Phenology" database (Benson et al., 2013). Ice-on and ice-off were counted as unique observations. Observations between 1444 and 1799 are not displayed due to the low counts during those years; the total number of observations during that time is 599.

To address the decline of in-situ lake ice monitoring there has been a shift towards the increased use of remote sensing technology (Duguay et al., 2015). Remote sensing observations provide capability for frequent monitoring in areas of high-density lake coverage at medium (250-500 m) to high spatial (<10 to 100 m) resolutions. The application of this technology for monitoring lake ice cover and thickness can help to expand existing records of ice properties. Radar remote sensing is an ideal choice for this because it can view ice during any weather condition and time of day. It provides high spatial resolution, and the penetration of signals through the ice can help study ice structural properties. This paper reviews how our understanding of lake ice has evolved using active microwave data and the development of monitoring methods over the past 50 years. The primary focus of this review will be on synthetic aperture radar (SAR) as 70% of published active microwave literature over the last five decades have used these radar systems to study lake ice, however, other active microwave systems such as scatterometers and radar altimetry will be mentioned. **Section 3.2** of this review will briefly discuss the existing literature on lake ice remote sensing since 1971, focusing on research using active microwave data. **Section 3.3** of the review will highlight our current understanding of the interaction between active microwave signals and lake ice. **Section 3.3.1** focuses on what we have learned regarding the

evolution of backscatter from lake ice while **Section 3.3.2** highlights how our understanding of scattering mechanisms has changed. **Section 3.3.3** and **3.3.4** highlight current methods of monitoring lake ice phenology, thickness, and differing regimes. Finally, **Section 3.4** will identify future directions and provide suggestions for further research.

3.2 Overview of Remote Sensing of Lake Ice

The importance of lake ice to both local/regional weather (i.e., temperature fluctuations and lake-effect snow) as well as its connection to economic activities and recreation (ice roads and snowmobiling) have been highlighted above. Lake ice is also an important indicator of climate change and has been identified as an ECV (Belward et al., 2016). Yet, within the broader context of cryosphere research it remains an understudied topic. Between the period of 1994 and 2003 there was consistently less research published on freshwater ice (both lake and river) compared to other cryosphere topics (Jeffries et al., 2012). However, research using remote sensing for the study of lake ice is increasing in popularity because it successfully addresses some of the knowledge gaps in the important study of freshwater ice. Additionally, while remote sensing is dependent on field measurements for validation, lake ice science is no longer dependent solely on a small number of point field measurements but can use remote sensing to extrapolate these measurements across the landscape. This is particularly helpful in unpopulated areas where infrequent field measurements can be supplemented by frequent remote sensing observations of ice phenology. Furthermore, remote sensing images allow us to monitor and study lakes in remote areas where field campaigns can be logistically challenging or dangerous (e.g., the High Arctic). Remote sensing of lake ice can be broadly categorized into three groups, active microwave remote sensing (i.e., real aperture/synthetic aperture radar (RAR/SAR), radar altimeters, ground penetrating radar, and short pulse radar), passive microwave remote sensing (radiometers), and optical remote sensing (airborne/spaceborne optical and thermal imagery). These broad categories have seen various research applications that include tracking ice phenology, estimating ice thickness, and understanding the interaction between microwave signals and ice structural properties.

3.2.1 Optical Remote Sensing

Optical remote sensing is an important tool for determining the presence of ice cover, particularly for large mid-latitude water bodies such as the Great Lakes. Large collections of

optical images are made easily accessible with no external processing through web applications such the National Aeronautics and Space Agency's Worldview website (https://worldview.earthdata.nasa.gov/). Other large databases of optical images, such as the United States Geologic Survey's Earth Explorer (https://earthexplorer.usgs.gov/), allow for the free-download of consistent image time series (e.g., Landsat). **Table 3.1** lists common optical satellites used for lake ice monitoring and details the number of channels, repeat cycle, and spatial resolution. However, optical remote sensing is a passive system that relies on the Sun's reflected energy from the Earth's surface, and its use is therefore limited by cloud cover and to daylight hours. Large cloud systems in areas of dense lake coverage can obscure the timing of key lake ice events (i.e. break-up and freeze-up) (Arp et al., 2013). The presence of cloud cover can also affect the accuracy of pre-classified products as there is noted confusion between ice and cloud in current algorithms (Riggs et al., 2019). This makes the accurate delineation of cloud cover important for optical image analysis. Observation of lake ice at Arctic latitudes is limited by the occurrence of polar darkness and high solar zenith angles particularly during freeze-up (Šmejkalová et al., 2016).

Table 3.1 Common optical sensors used for lake ice monitoring. Repeat cycles are given for the equator but are more frequent at higher latitudes.

	Operating Period	Number of Channels	Repeat Cycle (days)	Spatial Resolution (m)
Landsat MSS	1972 to 1995	4	18	60
Landsat TM	1982 to 2012	7	16	30
Landsat ETM+	1999 to present (Scan Line Corrector failed 2003)	8	16	30 (15 for panchromatic band)
Landsat OLI/TIRS	2013 to present	11	16	30 (15 for panchromatic band)
Sentinel-2	2015 to present	12	10	10 to 60
MODIS	1999 to present	36	1 to 2	250 to 1000
AVHRR	1979 to present	6	1	1000

VIIRS	2011 to present	5	16	375 to 750

Moderate Resolution Imaging Spectroradiometer (MODIS) data are a popular choice for lake ice monitoring over large lakes. Visual interpretation of these images has been used to interpret patterns in break-up across Alaska (Reed et al., 2009; Arp et al., 2013) and time series of reflectance data have been used to monitor trends in ice phenology across the Arctic (Šmejkalová et al., 2016). Calibrated radiance data from MODIS are used to develop the snow and ice product (currently version 6.1, Riggs et al., 2019), providing daily global land cover mapping of snow cover percentage and lake ice pixels. This product has been used to extract ice phenology dates from lakes in Ontario, Manitoba, and Quebec (L. C. Brown & Duguay, 2012; Murfitt & Brown, 2017), and in recent years to monitor lake ice on the Tibetan Plateau (Cai et al., 2019; Qiu et al., 2019). MODIS reflectance data are also used to generate two recently released products, the Copernicus Lake Ice Extent (Heinilä et al., 2017) and the European Space Agency (ESA) CCI Lakes Lake Ice product (Crétaux et al., 2020). The Copernicus product covers central and northern Europe with classifications for open water, partially and fully snow covered ice, and cloud cover using top of atmosphere (TOA) reflectance products at a resolution of 250 m (Heinilä et al., 2017). The CCI Lakes product provides classification for open water, ice, and clouds for selected lakes across the Northern Hemisphere using surface reflectance data at a spatial resolution of 1/120° (Crétaux et al., 2020). Although MODIS data are the most utilized product, the coarser spatial resolution (250-1000 m) limits the observation of lake ice patterns on small and medium sized lakes (Murfitt & Brown, 2017). Higher resolution imagery, e.g., Landsat and Sentinel-2 (10-30 m), can provide additional detail for these smaller lakes but lack the consistent daily global coverage of the coarser MODIS data.

3.2.2 Passive Microwave Remote Sensing

Passive microwave remote sensing, unlike optical data, can be used to observe lake ice under most atmospheric conditions, regardless of time of day and cloud cover, because passive microwave sensors measure the emission of energy (6.6 to 91 GHz) from the earth and do not depend on solar illumination. Passive microwave sensors commonly used for lake ice monitoring include the Scanning Multichannel Microwave Radiometer (SMMR) (e.g. Cai et al., 2017), the Special Sensor Microwave/Imagery (SSM/I) (e.g. Ke et al., 2013), and the Advanced Microwave

Scanning Radiometer – Earth Observing System (AMSR-E/2) (e.g. Kang et al., 2012; Du et al., 2017). The frequency and available polarizations of these systems are summarized in **Table 3.2**. The multiple passive microwave datasets (e.g. SMMR, SSM/I, SSMIS, and AMSR-E) are available as one collection, the 'Making Earth System Data Records for Use in Research Environments' (MEaSUREs) Calibrated Enhanced-Resolution Passive Microwave Daily EASE-Grid 2.0 Brightness Temperature Earth System Data Record (ESDR), from the National Snow and Ice Data Centre (NSIDC) (Brodzik & Long, 2018). These data are provided at grid spacings between 3.125 km and 25 km from 1978 to 2019. For lake ice monitoring (phenology and thickness) the key piece of information provided by passive microwave systems is brightness temperatures. Brightness temperatures observed from passive microwave systems are shown to increase with thickening lake ice due to the lessening influence of the lower emissivity of the underlying water and emission of microwave energy from the ice cover (Lemmetyinen et al., 2009). Lower frequency observations (ca. 19 GHz) have shown the best success for monitoring ice thickness (Kang et al., 2014). However, the shallower emission depths of higher frequency passive microwave data (ca. 37 GHz) are useful for measuring the thickness of thinner ice covers (Kang et al., 2012). Higher frequencies (ca. 36.5 GHz) were also shown to successfully detect patterns in lake ice phenology across the Northern Hemisphere (Du et al., 2017). In addition, methods have been developed to use a combination of both passive microwave and data from various altimeter satellite missions (i.e., Jason-1, TOPEX/Poseidon, and ENVISAT) to classify ice cover (Kouraev et al., 2007); this method will be further discussed in **Section 3.3.3**. Although these data address the issues associated with cloud cover and polar darkness, the application of these data is restricted due to coarse spatial resolution (3 to 120 km). The coarser resolutions of the datasets mentioned above are more suitable for monitoring the largest lakes of the globe and care must be taken to avoid land contamination of shoreline pixels.

Table 3.2 Common passive microwave systems used for lake ice monitoring.

	SMMR	SSM/I	SSMIS	AMSR-E	AMSR-2
Operating Period	1978 to 1987	1987 to 2008	2000-present	2002 to 2011	2012-present
Frequency					
6.6 GHz	**H, V**				
6.9 GHz				**H, V**	**H, V**
7.3 GHz					**H, V**
10.7 GHz	**H, V**			**H, V**	**H, V**
18 GHz	**H, V**				
18.7 GHz				**H, V**	**H, V**
19 GHz		**H, V**	**H, V**		
21 GHz	**H, V**				
22 GHz		**V**	**V**		
23.8 GHz				**H, V**	**H, V**
37 GHz	**H, V**	**H, V**	**H, V**	**H, V**	**H, V**
85 GHz		**H, V**			
89 GHz				**H, V**	**H, V**
91 GHz			**H, V**		

3.2.3 Active Microwave Remote Sensing

The limitations of passive microwave and optical remote sensing can be addressed using active microwave remote sensing. Active microwave data can be acquired in any weather condition or time of day. Unlike optical imagery that is easily obscured by clouds, active microwave systems can effectively 'see' the ice conditions below the cloud cover. Additionally, SAR, the most common type of active microwave data that has been used in 70% of active

microwave lake ice publications in the last 50 years, is available at comparable resolutions to optical remote sensing. SAR data resolution can range from ca. 3 m for fine resolution data to 100 m for images that cover larger swaths. This allows for varying lake sizes to be resolved in radar imagery. Furthermore, calibrated SAR data has allowed researchers to understand changes in backscatter, which has become the key piece of information for studying lake ice, throughout the ice season and relate this to *in situ* observations (e.g. Jeffries et al., 1994; Morris et al., 1995). Continued advancement in SAR data through diversity of wavelength/frequency (**Table 3.3**) and the launch of multiple satellite systems (**Table 3.4**) with diverse polarizations has allowed for further investigation of lake ice type (surface ice type) and ice structure (roughness, bubble content) (e.g. Atwood et al., 2015; Gunn et al., 2017). Diverse software platforms (**Table 3.5**) have also increased accessibility for processing these images and allowed for detailed analysis of time series and pixel values in GIS software (e.g. Surdu et al., 2015; Murfitt et al., 2018b).

While these advantages and technological developments have shaped lake ice research over the last 50 years, there remain trade-offs associated with these data. The preprocessing steps for active microwave data are more complex compared to other forms of remote sensing. Also, infrequent revisit times, reduced spatial coverage, and selected beam modes can limit these data for certain geographical areas, however, availability of these data has increased in recent years.

Table 3.3 Common radar bands for lake ice research.

Radar Band	Wavelength (cm)	Frequency (GHz)
L-band	~25 cm	~1.2 GHz
C-band	~5.6 cm	~5.4 GHz
X-band	~3.1 cm	~9.6 GHz
Ku-band	~2.2 cm	~13.4 GHz

Table 3.4 Common satellite SAR systems for lake ice research.

	Operating Period	Band	Polarizations	Repeat Cycle (days)	Pixel Spacing (m)
European Space Agency Missions					
ERS-1	1991 to 2000	C-band	VV	35	12.5
ERS-2	1995 to 2011	C-band	VV	35	12.5
ENVI-SAT ASAR	2002 to 2012	C-band	VV+HH/HH+HV/ VV+VH	35	12.5 to 1000
Sentinel-1	2014	C-band	HH+HV/VV+VH	12	1.5 to 49
Canadian Space Agency Missions					
RADARSAT-1	1995 to 2013	C-band	HH	24	4.6 to 50
RADARSAT-2	2007-present	C-band	FP*	24	0.5 to 50
RADARSAT Constellation	2019-present	C-band	FP*/CP**	4	1 to 100
German Aerospace Center Missions					
TerraSAR-X	2007-present	X-band	FP*	11	0.2 to 15
TanDEM-X	2010-present	X-band	FP*	11	0.2 to 15
Japan Aerospace Exploration Agency Missions					
JERS-1	1992 to 1998	L-band	HH	44	18
PALSAR	2006 to 2011	L-band	FP*	46	6.25 to 500
PALSAR-2	2014-present	L-band	FP*/CP**	14	1 to 300
Italian Space Agency					
COSMO-SkyMed	2007-present	X-band	HH/VV/HV/VH	16	1 to 100
National Aeronautics and Space Administration					
SeaSat	June 1978 to Oct. 1978	L-band	HH	17	25

Argentina National Space Activities Commission				
SAOCOM-1	2018-present	HH+HV/VV+VH	16	10 to 100

*FP indicates the SAR system is fully polarimetric
**CP indicates the SAR system has an operational (RCM) or experimental (PALSAR-2) circular polarization mode

Table 3.5 Common platforms for SAR image processing.

Software Name	Publisher	Most Recent Release	Cost Associated
PCI Geomatica	CATALYST *https://www.pcigeomatics.com/software/geomatica/professional*	2020	Commercial
Sentinel Application Platform	ESA *https://step.esa.int/main/toolboxes/snap/*	2020	Free Access
PolSARpro	ESA *https://step.esa.int/main/toolboxes/polsarpro-v6-0-biomass-edition-toolbox/*	2019	Free Access
Gamma Processing Software	Gamma Remote Sensing *https://www.gamma-rs.ch/software*	2020	Commercial
MapReady	ASF *https://asf.alaska.edu/how-to/data-tools/data-tools/*	2013	Free Access
ENVI	Harris Geospatial *https://www.l3harrisgeospatial.com/Software-Technology/ENVI*	2020	Commercial
ERDAS IMAGINE	Hexagon Geospatial *https://www.hexagongeospatial.com/products/power-portfolio/erdas-imagine*	2020	Commercial

To understand how the literature on active microwave sensing of lake ice has developed, a broad search was conducted to collect research items that mentioned lake ice and remote sensing from 1971 to September 2020. This search was conducted using the terms “lake ice”, “radar”, “microwave”, “MODIS”, and “Optical”, returning over 4000 results from the Google Scholar database (https://scholar.google.ca). The search was performed using the ‘Publish or Perish’ software available for free download at https://harzing.com/resources/publish-or-perish (Harzing, 2020). These 4000 results were filtered manually to remove duplicates and identify papers that primarily focused on studying lake ice with the use of remote sensing. From these 506 items, the type of remote sensing (active, passive, or optical) was identified for 471 (review papers were removed from analysis) and 55% of all entries from this collection used active microwave sensors (SAR, RAR, short-wave impulse radar, ground penetrating radar, or frequency modulated continuous wave (FM-CW) radar). This subset of research material was sorted to determine the medium of publication, including theses, conference papers/abstracts, technical reports, preprints, and journal articles. The material was further analyzed to improve our understanding of study locations, radar frequency, and radar polarization.

3.2.3.1 Incidence Angle and Lake Ice

Incidence angle is a key element of radar geometry and the size of the angle has an impact on the observed radar response from lake ice surfaces. Incidence angle is defined as the angle between the incident radar beam and a vector perpendicular to the ground surface. Investigations of C-band SAR HH polarized data over floating lake ice (i.e., not frozen to the lakebed) near Churchill, Manitoba found that at varying incidence angles there could be differences of 1 to 7 dB (Duguay et al., 2002). Steeper incidence angles resulted in higher backscatter from ice while shallower angles resulted in lower backscatter, the magnitude of these differences was found to be influenced by the bubble content within the ice (Duguay et al., 2002). Differences in backscatter of a smaller magnitude (1 to 3 dB) were also identified for grounded ice cover that contained a large concentration of bubbles (Duguay et al., 2002). This pattern of decreasing backscatter with increasing incidence angle has been noted in other literature on floating ice cover using both HH and VV polarizations (Geldsetzer et al., 2010; Surdu et al., 2015).

Studies that have investigated the application of SAR for monitoring lake ice rely on dense time series of imagery from a variety of SAR orbits which results in data being acquired at

varying incidence angles. To counter the problem of varying incidence angles, several normalization procedures have been developed. Both linear (Murfitt et al., 2018b; Murfitt and Duguay, 2020) and polynomial (Pointner et al., 2019, 2021) approaches have been used to normalize backscatter for varying orbits, allowing for the creation of a more consistent record of backscatter.

3.2.3.2 Metanalysis of Active Microwave Publications: Study Sites and Publication Format

The diversity of study locations and publication types for active microwave research has evolved since the 1970s (**Figure 3.2**). Between 1971 and 1990, research using active microwave remote sensing focused primarily on the Great Lakes and Alaskan lakes. The focus of these studies was on connecting observed tones in radar return to field observations (e.g. Elachi, Bryan, & Weeks, 1976; Weeks, Sellmann, & Campbell, 1977) and exploring the use of radar as a Great Lakes monitoring tool (Larrowe, 1971; Leshkevich, 1977). Since 1991, there has been an increased diversity of study site locations across the Northern Hemisphere (High Arctic, mid-latitudes, and Eurasia).

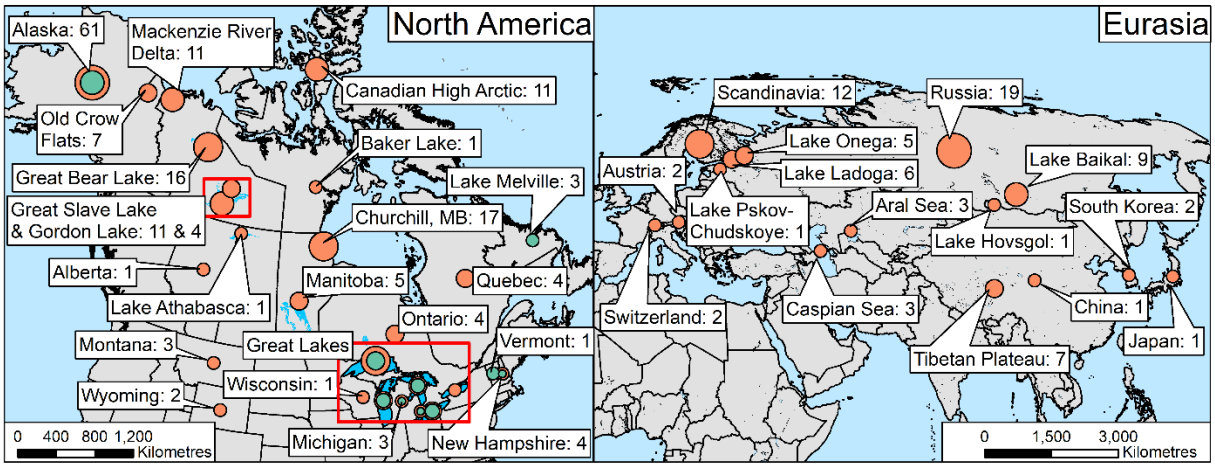

Figure 3.2 Study locations of active microwave research between 1971 and first three quarters of 2020. The upper left map shows studies conducted in North America, the upper right shows studies conducted in Europe and Asia. Green circles indicate locations where studies occurred prior to 1990 and orange circles indicate locations where studies occurred after 1991.

Additionally, the formats of publications for lake ice research using active microwave data have changed over the past 50 years (**Figure 3.3**). During the 1970s technical reports were a popular form of publication but in recent years have declined with peer reviewed articles and conference abstracts/proceedings becoming dominant. There has also been an increase in the number of publicly available theses. The diversity of study site locations and growing number of lake ice focused publications can be attributed to active microwave data, specifically SAR data, becoming increasingly available. For example, Sentinel-1 via the ESA's Copernicus program and through ASF, and more recently historical RADARSAT-1 through Natural Resource Canada's Earth Observation Data Management System (EODMS).

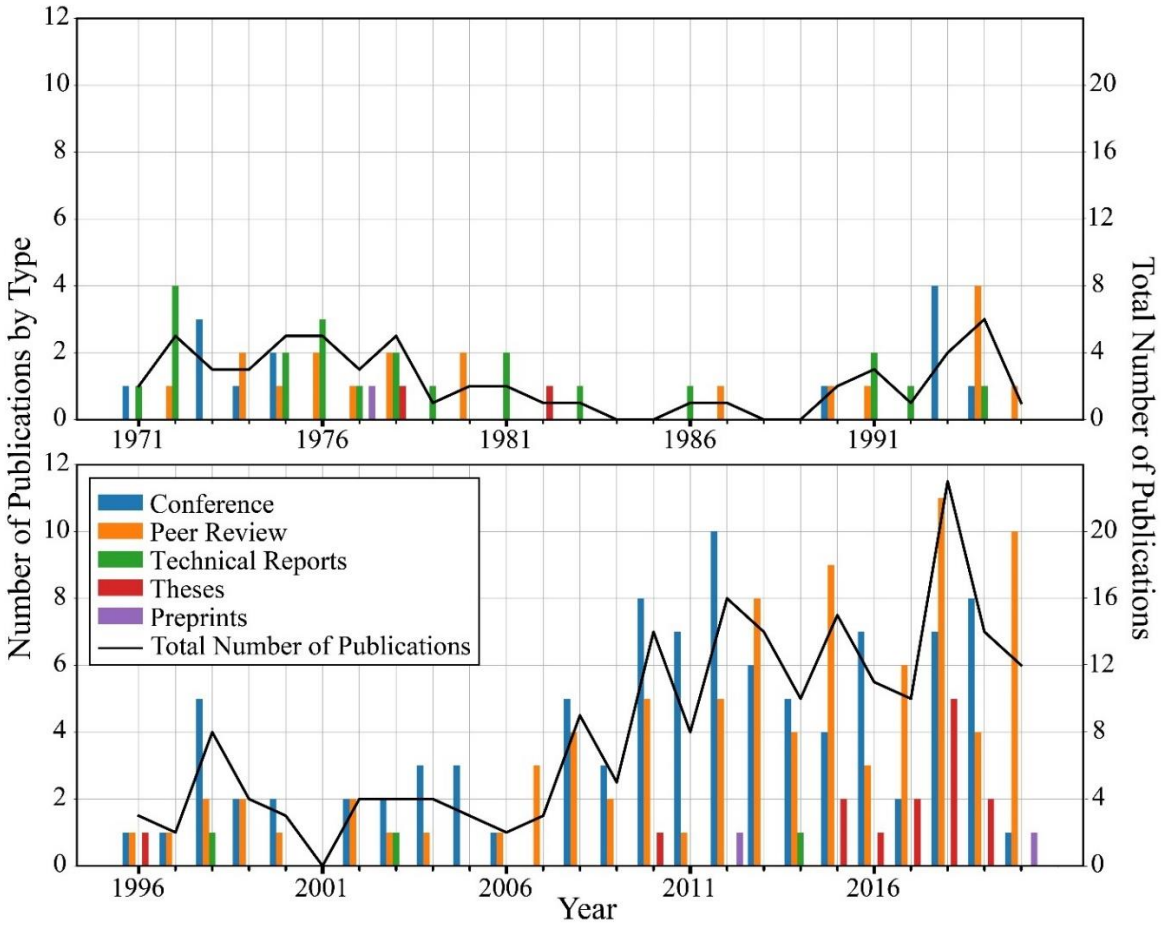

Figure 3.3 The proportion of research classified by type between 1971 and first three quarters of 2020. The top plot shows papers from 1971 – 1995 and the bottom plot shows papers from 1996 – 2020. The solid black line shows the total number of publications throughout the same timespan.

3.2.3.3 Radar Frequency

Radar system frequencies are typically designated as different bands as seen in **Table 3**. The frequency and wavelength of the radar system can influence how it interacts with different mediums and what size of target is detected. For lake ice this is important to consider as different frequencies will be appropriate for monitoring different properties such as bubble size/density, cracks, and interface roughness. Frequency and wavelength also determine the penetration depth of signals, with smaller frequencies having greater penetration depth through materials. The analysis of literature reveals that although a wide number of radar bands were used to monitor lake ice between 1971 and 2020, the most selected radar frequency was C-band (55% of publications). However, C-band has not always been the historic choice for lake ice monitoring, as the bulk of research was conducted using X-band airborne radar prior to 1987 (**Figure 3.4**). The launch of ERS-1 by ESA in 1991 allowed for wider access to spaceborne C-band radar (VV polarization), and since 1993 C-band data has been used for 64% of the research published on active microwave sensing of lake ice. This is due to its continued usage in sensors such as the RADARSAT systems and Sentinel-1, which are becoming more widely available due to data distribution platforms such as the Copernicus Open Access Hub (https://scihub.copernicus.eu/), Canada's EODMS (https://www.eodms-sgdot.nrcan-rncan.gc.ca/index_en.jsp), and the ASF's Vertex Data Search (https://search.asf.alaska.edu/).

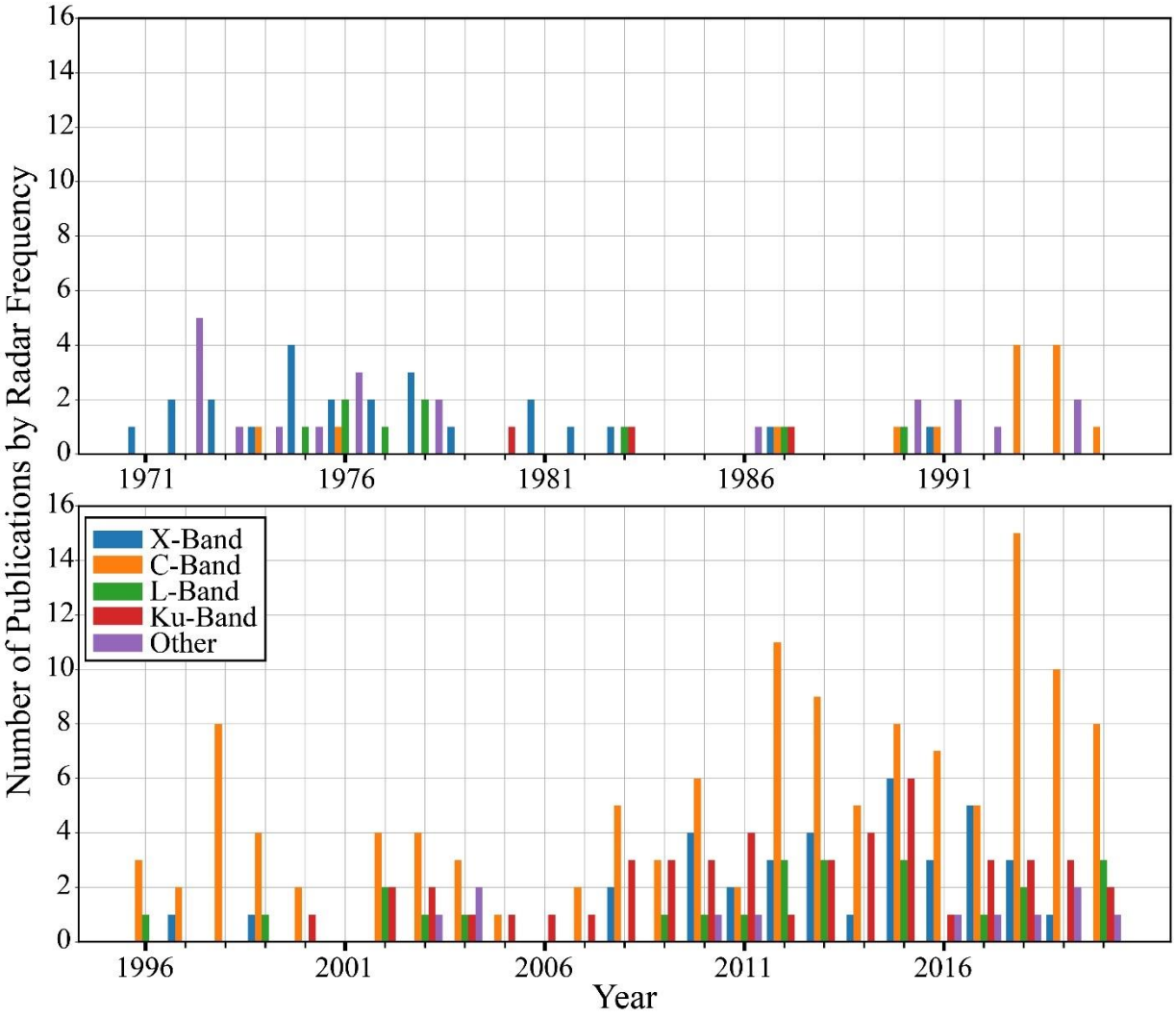

Figure 3.4 The proportion of different radar frequencies used between 1971 and first three-quarters of 2020. The top plot shows papers from 1971 – 1995 and the bottom plot shows papers from 1996 – 2020.

3.2.3.4 Radar Polarization

Polarization is a key component of active microwave data and refers to the orientation of transmitted and received radar waves, the two primary orientations are horizontal and vertical. **Table 3.6** summarizes radar system configurations.

Table 3.6 Radar system configurations.

Polarization	Orientation of Radar Waves	Examples
Co-Polarized	Transmit and Receive Identical	HH or VV
Cross-Polarized	Transmit and Receive Opposite	HV or VH
Dual-Polarized	Both Co- and Cross-Polarized	HH + HV
Fully Polarimetric or Quad-Polarized	All Combinations of Co- and Cross-Polarized	HH/VV/HV/VH

Compact polarimetry is a new orientation for radar data and was made operationally available with the launch of RADARSAT Constellation, here data is transmitted circularly polarized (Right or Left) and received as a linear polarization (H or V) (Raney, 2019). Trends in the use of radar polarization are more difficult to analyze as it is commonly omitted from publications. From the filtered active microwave documents, 48%[1] did not clearly report the polarization used. Polarizations were most frequently omitted from conference abstracts and research items that used ground penetrating radar (GPR), radar altimetry, or shortwave impulse radars. In recent research, a wide variety of polarizations have been used. This can be attributed to the diversity in polarizations available on current satellite missions. Sentinel-1 (C-band, launched 2014) and TerraSAR-X (X-band, launched 2007) support single or dual polarizations (TerraSAR-X has an experimental quad-pol mode). RADARSAT-2 (C-band, launched 2007), RADARSAT Constellation (C-band, launched 2019), and ALOS-PALSAR-2 (L-band, launched 2014) have single, dual, and quad-pol modes with PALSAR-2 including an experimental compact-pol mode and RCM offering operational compact-pol. Some temporal patterns do stand out in polarizations, particularly the dominance of VV-pol data after the launch of ERS-1 in 1991 (**Figure 3.5**). However, after the launch of RADARSAT-1 in 1995 HH experiences similar usage. Overall VV and HH polarizations (co-polarized) are the most common type used for active microwave remote

[1]Excluded documents include those that used a system with a single polarization (e.g. RADARSAT-1: HH and ERS-1/2: VV) but did not explicitly state the polarization. However, because we can easily identify the polarization for these documents, they were included in the final counts for polarizations between 1971 - 2020.

sensing studies of lake ice and in the last decade 74% of research where polarizations can be identified have used one of these two types.

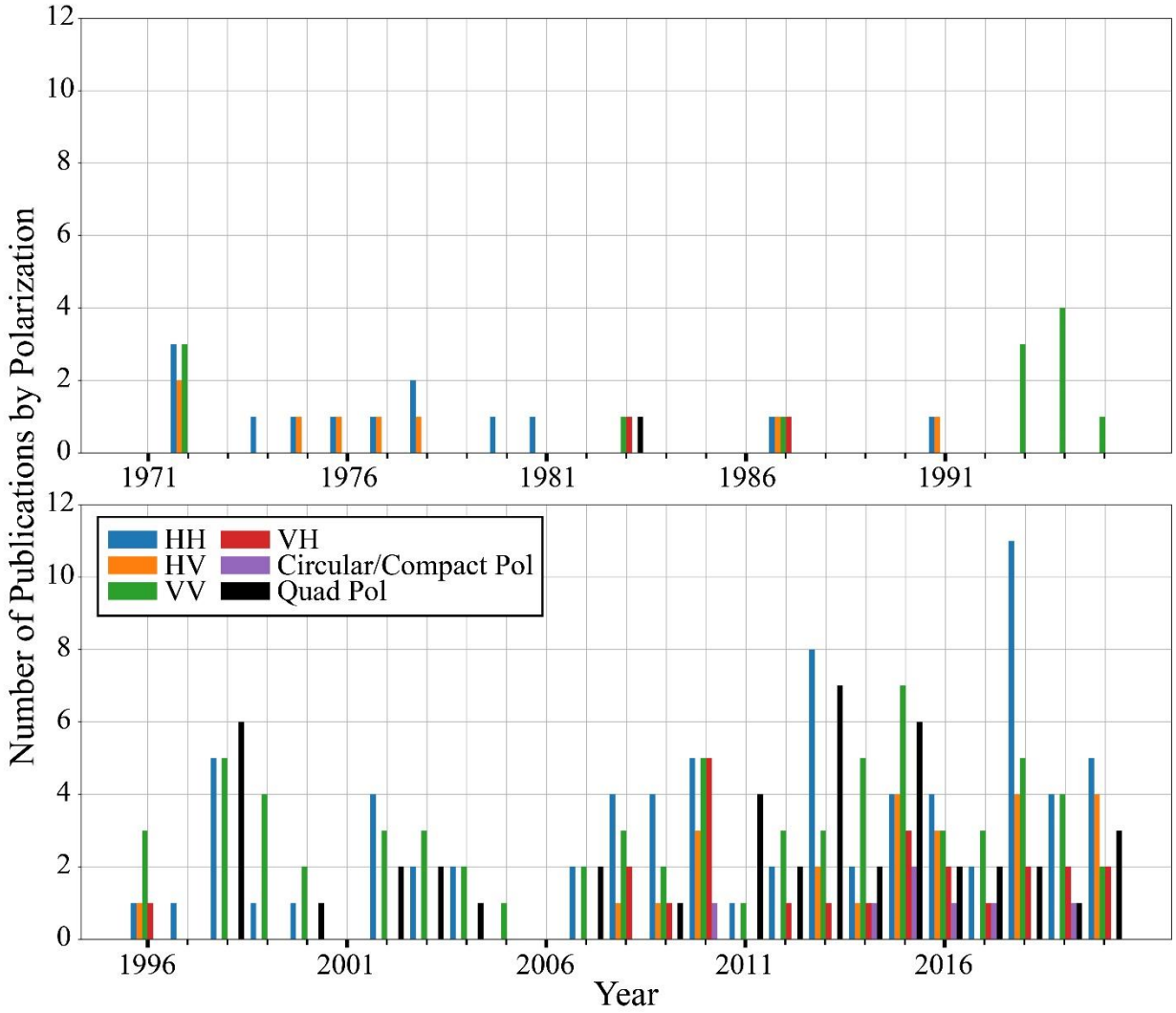

Figure 3.5 The proportion of different polarizations used between 1971 and first three-quarters of 2020 for studies where it could be determined. The top plot shows papers from 1971 – 1995 and the bottom plot shows papers from 1996 – 2020.

3.3 Advances in Active Microwave Remote Sensing of Lake Ice

3.3.1 Patterns in Backscatter Evolution from Floating and Grounded Ice Cover

Reported patterns in backscatter evolution during freeze-up, ice growth, and break-up have remained consistent between studies at various latitudes. This section will summarize the observed backscatter patterns and identify commonalities and differences between published

literature. Early radar observations of lake ice focused on the use of X and L-band SLAR on the North Slope of Alaska (Sellmann et al., 1975; Elachi et al., 1976; Weeks et al., 1981). Visual analysis of these images connected ice properties to radar return and identified differences between floating and grounded (bedfast) ice covers. Over the last three decades calibrated SAR has allowed for quantitative analysis of the evolution in backscatter from both floating and grounded ice covers.

Prior to the formation of ice for both regimes (floating and grounded ice), calm and windy days result in a combination of high and low backscatter values from lakes due to Bragg scattering from the rough lake surface (Jeffries et al., 1994). These fluctuations have been observed at Ku, X, and C-band frequencies in Arctic latitudes (Morris et al., 1995; Howell et al., 2009; Antonova et al., 2016). On the other hand, smaller lakes at mid-latitudes may not experience these variations due to trees acting as wind blocks around the perimeter of the lake (Murfitt et al., 2018b). **Table 3.7** summarizes the expected ranges of backscatter prior to ice formation and during maximum ice thickness. Backscatter ranges during freeze-up and break-up are not included due to the increased variability in backscatter during these periods.

Table 3.7 Summary of expected backscatter ranges for different ice covers. References provided are a sample of publications where these values are reported.

	Open Water	Maximum Ice Thickness	Observed Frequencies	Sample References
Shallow Arctic/Subarctic Lakes – Floating Ice	-2 to -25 dB	-5 to -17 dB	X/C/L-band	Jeffries et al., 1994; Morris et al., 1995; Duguay et al., 2002; Antonova et al., 2016; Engram et al, 2013, 2018
Shallow Arctic/Subarctic Lakes – Grounded Ice	-2 to -25 dB	-13 to -20 dB	X/C/L-band	Jeffries et al., 1994; Duguay et al., 2002; Antonova et al., 2016; Engram et al, 2013, 2018
Deep Arctic/Subarctic Lakes – Floating Ice	-5 to -30 dB	-10 to -15 dB	Ku-band Scatterometer/C-band SAR	Morris et al., 1995; Howell et al., 2009; Murfitt and Duguay, 2020

Small/Medium Temperate Lakes – Floating Ice	-20 to -25 dB	-10 to -20 dB	C-band	Murfitt et al., 2018b

The initial skim ice that forms on lakes is thin and smooth (Schwarz et al., 1986); the smooth ice-water interface present during this time acts as a specular reflector resulting in low backscatter (Jeffries et al., 1994; Duguay et al., 2002). This can also affect visual identification of early freeze-up due to the noted similarity between initial ice cover and calm water surfaces (Antonova et al., 2016). During ice formation cracks and deformations can occur in the ice surface. Research on Arctic lakes using satellite C-band SAR data has shown backscatter values 10 dB higher for these features compared to non-deformed ice (Morris et al., 1995), therefore these features can be helpful in visually identifying the formation of ice and can be seen in **Figure 3.6A** and **3.6B**. These cracks have also been noted in X-band imagery for lakes in the Lena Delta (Antonova et al., 2016). The impact of cracks on backscatter disappears as ice thickens.

For floating ice covers, backscatter increases until it reaches a plateau (**Figure 3.6C** and **3.6D** show the increase, **Figure 3.6E** and **3.6F** show the plateau). This plateau has been reported in backscatter evolution profiles for lakes at C, X, and Ku-band over a range of latitudes (Duguay et al., 2002; Howell et al., 2009; Antonova et al., 2016; Murfitt et al., 2018b). Discontinuity between dielectric constants, the real part of the relative permittivity of a material, results in the reflection of radar signals at the interface between two layers, this is commonly referred to as a dielectric contrast (Richards, 2009). Due to the large difference in dielectric constant values for ice, approximately 3.17 (Mätzler & Wegmüller, 1987), and water, >10 at 0 °C between 1 and 37 GHz (Ulaby and Long, 2014), there is a strong reflection at the ice-water interface. This combined with roughness at the ice-water interface causes strong radar return (Engram et al., 2013).

However, if the ice is thick enough to freeze to the lake bed a decrease in backscatter is observed (**Figure 3.6C**) (Weeks et al., 1977, 1981)**.** This decrease in backscatter has been noted at X, C, and L-band frequencies through both visual and quantitative analysis of backscatter (Elachi et al., 1976; Jeffries et al., 1996; Antonova et al., 2016). Dissimilar to floating ice cover where there is a large dielectric discontinuity between ice and water, there is little difference between the values of ice (dielectric constant of 3.17) and frozen soil (dielectric constant <8 between 0.01 and

10 GHz at -10 °C (P. Hoekstra & Delaney, 1974)). This lack of contrast results in transmission of the radar energy from ice to soil with little reflection resulting in a low return (Elachi et al., 1976).

When temperatures begin to increase during the spring, backscatter from the ice cover starts to decrease due to the overlying wet snow cover and pooling of melt water (Morris et al., 1995; Duguay et al., 2002). Melt onset is noted by a decrease in backscatter at all frequencies due to increased water content. Ku-band backscatter should have a higher sensitivity as the higher frequency will be more affected by the introduction of water into the overlying snowpack, if present (Howell et al., 2005, 2009).

Increases and fluctuations in backscatter from ice covers during melt can be attributed to wind-action on melt ponds or increase in open-water surface. Additionally, increased roughness of the snow surface or ice surface, if lacking snow cover, due to multiple melt/refreeze events or candling at the ice surface can cause higher backscatter due to higher reflection from a wet ice surface (Duguay et al., 2002; Howell et al., 2009; Antonova et al., 2016; Murfitt & Duguay, 2020). Backscatter increase is observed between **Figure 3.6F** and **3.6H**, dark areas in the ice cover of **Figure 3.6H** are likely small melt ponds or holes in the ice cover. The draining of the ice surface and creation of a slightly wet, higher reflection, rough air-ice interface results in an increase in backscatter and backscatter reversal for grounded ice cover (Jeffries et al., 1994; Wakabayashi et al., 1999). Observations of X-band backscatter evolution for grounded lakes in the Lena Delta show a mix of both increases and decreases in backscatter around the first reported positive temperature (Antonova et al., 2016). The backscatter reversal can be observed between **Figure 3.6E** and **3.6G** where an increase in backscatter occurs for previously grounded pixels.

To monitor these transitions in ice conditions, it is common to use co-polarized signals (HH and VV). Cross-polarized signals (HV and VH) respond to deformations in the ice surface (cracks and rafting) and the presence of varying surface ice types, such as snow ice (Gunn et al., 2017, 2018). Snow ice is a layer of white ice containing spherical bubbles that forms on top of congelation/clear ice; it most commonly forms when snow cover on thin ice decompresses the ice resulting in water flooding the surface through cracks or holes leading to the formation of slush that then freezes (Schwarz et al., 1986). Formation can also occur if rain or melting snow causes the formation of slush in the lower levels of a snow pack (Schwarz et al., 1986). These features

are more likely to cause depolarization and an increase in the cross-polarization signals (Gunn et al., 2017).

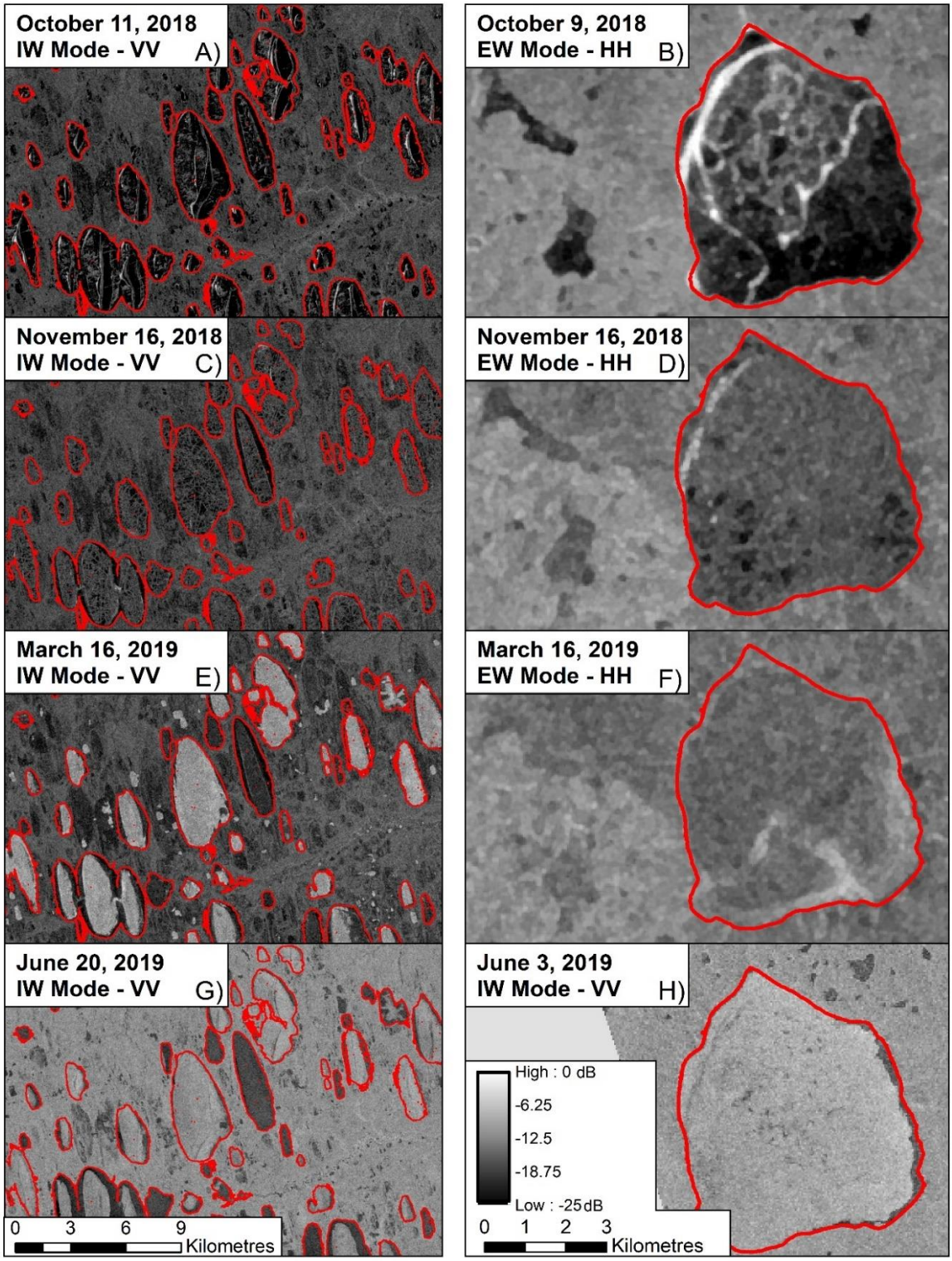

Figure 3.6 C-band backscatter evolution for lake ice from two locations, the red outline indicates the location of lakes. The left column illustrates evolution for shallow Arctic lakes near Wainwright, Alaska (70.67°, -158.34°), USA. The decrease associated with grounded ice cover is demonstrated by the darker tones observed in the March 16, 2019 image. The right column shows evolution for a deep Arctic lake, Noell Lake (68.53°, -133.57°), near Inuvik, Northwest Territories, Canada. These images highlight the high backscatter from deformation features in the ice (October 9, 2018) and increasing radar return throughout the ice season. All Images have been scaled so that values range from 0 to -25 dB as shown in the legend in the lower right panel. All images are from Sentinel-1, IW mode images are resampled to a resolution of 10 m and EW mode images are resampled to a resolution of 40 m. Copernicus Sentinel-1 imagery 2018/2019, processed by ESA.

3.3.2 Lake Ice Scattering Mechanisms: Evolution in Understanding

This section will discuss how our understanding of scattering mechanisms for lake ice has changed over the last 50 years. The primary focus of this section will be on early theories concerning the role of a double bounce mechanism caused by tubular bubbles within the ice column (Section 3.2.1) and recent research that has shifted the focus to surface scattering caused by roughness at the ice-water interface (Section 3.2.2). **Table 3.8** provides a summary of the main scattering types, the different mechanisms within lake ice mediums, the frequencies used to observe these mechanisms, and sample key references that have either identified or explored these mechanisms.

Table 3.8 Summary of scattering mechanisms observed for lake ice.

Scattering Type	Mechanism	Observed Frequency	Sample References
Surface Scattering			
	Cracks/Deformations at the Ice Surface	C/X-band	Morris et al., 1995; Gunn et al., 2017
	Roughness at the Ice-Water Interface	Ku/X/C/L-band	Jirberg et al., 1974; Weeks et al., 1977; Atwood et al., 2015; Gunn et al., 2018
	Extrusion of Bubble Terminuses	Ku/X/C-band	Weeks et al., 1978; Atwood et al., 2015; Gunn et al., 2018

	Methane Ebullition Bubbles	L-band	Engram et al. 2012; Engram et al., 2013
	Reflection from Wet Snow	X/C/L-band	Rott & Mätzler, 1987; Jeffries et al., 1994
Volume Scattering			
	Surface Ice Type – Spherical Bubbles (snow ice/grey ice)	Ku/X/C-band	Hall et al., 1994; Gunn et al., 2017; Gunn et al., 2018
	Snow Structure	Ku/X-band	Gunn et al., 2015a
Double Bounce			
	Tubular Bubbles	X/C/L-band	Weeks et al., 1978; Weeks et al., 1981; Jeffries et al., 1994; Morris et al., 1995

3.3.2.1 Early Support for Double-Bounce Scattering Within Lake Ice

Initial research on the response of microwave signals to lake ice using X-band SLAR suggested that scattering was a result of a double bounce mechanism due to the presence of long tubular shaped bubbles within the ice column (Weeks et al., 1978, 1981). These tubular bubbles form as the lake becomes supersaturated with gases that are rejected during lake ice growth (Bari & Hallett, 1974). Weeks et al. (1981) observed differences in radar response from lakes on the North Slope of Alaska using X-band SLAR and stated that observed bubbles oriented in the direction of ice growth acted as forward scatterers and scattered microwave signals downward. The scattered signal then returned from the ice-water interface due to the high dielectric contrast (Weeks et al., 1981). The formation of these bubbles is limited to lakes with a depth shallower than 4 m (Mellor, 1982). Observations of lakes on the North Slope of Alaska by satellite ERS-1 C-band data revealed increasing backscatter that coincided with thickening ice cover and the development of tubular bubbles within the ice column, further supporting this theory (Jeffries et al., 1994). Additionally, due to lower backscatter from grounded ice cover it was less likely that tubular bubbles were contributing to volume scattering (Jeffries et al., 1994). Radar images (C-band) and field studies of shallow lakes in Alaska and Churchill, Manitoba further supported the

role of tubular bubbles and double bounce scattering within lake ice (Morris et al., 1995; Duguay et al., 2002).

However, early research using airborne active microwave sensors also suggested opposing theories to the double bounce mechanism (e.g. Weeks, Sellmann, & Campbell, 1977). Radar imaging campaigns using X-band frequency suggested that roughness of the ice-water interface could be one of the reasons for observed backscatter from lakes in the Arctic and the Great Lakes (Jirberg et al., 1974; Weeks et al., 1977). Ground truth data suggested that the presence of bubbles extending from the bottom of the ice could create a rough surface responsible for scattering in X and L-band SLAR (Weeks et al., 1978). Furthermore, much of the early research on radar return from lakes supports that the presence of the ice-water interface is responsible for high return due to the strong dielectric contrast (Weeks et al., 1977, 1978). Visual observations made using ERS-1 satellite imagery of lakes in Montana supplemented with field measurements suggested that backscatter was likely a result of scattering within the upper snow ice layer and at the ice-water interface due to the minimal amount of bubbles observed in the ice column (Hall et al., 1994). Additionally, backscatter responses from large lakes at Sub-Arctic latitudes were 4 dB lower compared to shallow lakes (Morris et al., 1995). However, this difference was attributed to the lack of a double bounce mechanism as tubular bubbles have been found to not form when lakes are deeper than 4 m (Mellor, 1982; Morris et al., 1995).

3.3.2.2 Recent Support for Single Bounce Scattering Within Lake Ice

Several recent advancements have been made in understanding the scattering mechanisms within lake ice due to the availability of polarimetric SAR data. Polarimetric SAR data allows us to understand and characterize the contributions of the different scattering mechanisms, surface, volume, and double bounce, from lake ice cover (Atwood et al., 2015). For shallow lakes in Alaska, experiments found that the L-band return from floating ice covers was due to the roughness components of polarimetric decomposition (Engram et al., 2012, 2013). Engram et al. (2013) found that following the grounding of ice cover there was a reduction in the roughness component of the decomposition. This means that roughness at the ice-water interface where there is a high dielectric contrast must be driving this mechanism as this contrast is absent when the ice cover freezes to the lake bed (Engram et al., 2013). The dominance of surface scattering was a response to the presence of methane ebullition bubbles in these lakes. Lakes with a higher percentage of

bubble area (based on the lake surface) and high methane flux in the spring and fall were found to have a higher contribution from surface scattering (Engram et al., 2012). These bubbles are thought to cause this increase in surface scattering for two reasons: 1) bubbles suspended under the ice create a rough gas-water-ice interface; and 2) slower ice growth rates occur directly below bubbles trapped in the ice, resulting in the formation of domes which create a rough ice-water interface (**Figure 3.7**) (Engram et al., 2012, 2013). Atwood et al. (2015) demonstrated using polarimetric decomposition, numerical modelling, and the co-pol phase difference that for X, C, and L-band single bounce scattering at the ice-water interface is the dominant mechanism even without methane ebullition bubbles present. Numerical modelling demonstrated that at C-band and an incidence angle of 30°, bubbles were not able to generate an amount of backscatter measurable in the experiment. However, when a small amount of roughness at the ice-water interface was introduced (root mean square (RMS) roughness 5 mm and correlation length of 5 cm), the backscatter was at least 20 dB higher than the numerical noise floor and was similar between ice columns with and without tubular bubbles (Atwood et al., 2015). Investigation in this study of co-pol phase difference data from floating ice in Alaska using TerraSAR-X, ALOS PALSAR, and RADARSAT-2 images further supported that surface scattering from a rough ice-water interface is the dominant mechanism from ice cover (Atwood et al., 2015). Forward modelling and scatterometer experiments also demonstrated that a lack of snow cover decreases the return at Ku-band for shallow Subarctic lakes, with decreases of HH and VV backscatter by 1.6-6.2 dB, likely due to the loss of volume scattering (Rott et al., 2010; Gunn, Brogioni, et al., 2015). These same experiments demonstrated little impact on X-band signals (Gunn, Brogioni, et al., 2015). Further experiments were conducted using a Yamaguchi four-component decomposition and RADARSAT-2 images for shallow Sub-Arctic lakes near Churchill, Manitoba (Gunn et al., 2018). The temporal evolution of scattering mechanisms (single/surface bounce, double bounce, and volume scattering) provided evidence that surface scattering from the ice-water interface was the largest contributor to backscatter throughout the ice season, with volume scattering in the surface ice layer and double bounce from tubular bubbles providing a smaller contribution (**Figure 3.7**) (Gunn et al., 2018). Currently it is suggested that variations in roughness at the ice-water interface are due to the extrusion of bubbles terminuses below the bottom of the ice, due to differing snow depths across the ice surface resulting in variations in ice thickness, or due to the presence of methane ebullition bubbles (**Figure 3.7**) (Engram et al., 2012; Gunn et al., 2018). However, further

work is needed to better understand the causes of roughness at the ice-water interface. Additionally, limited research has been conducted on the scattering mechanisms for deeper lakes where the formation and emergence of tubular bubbles is less likely (Hall et al., 1994; Morris et al., 1995). Deeper lakes also show increasing backscatter throughout the ice season and research is needed to understand if this is also a result of ice-water interface roughness or if it is caused by additional factors.

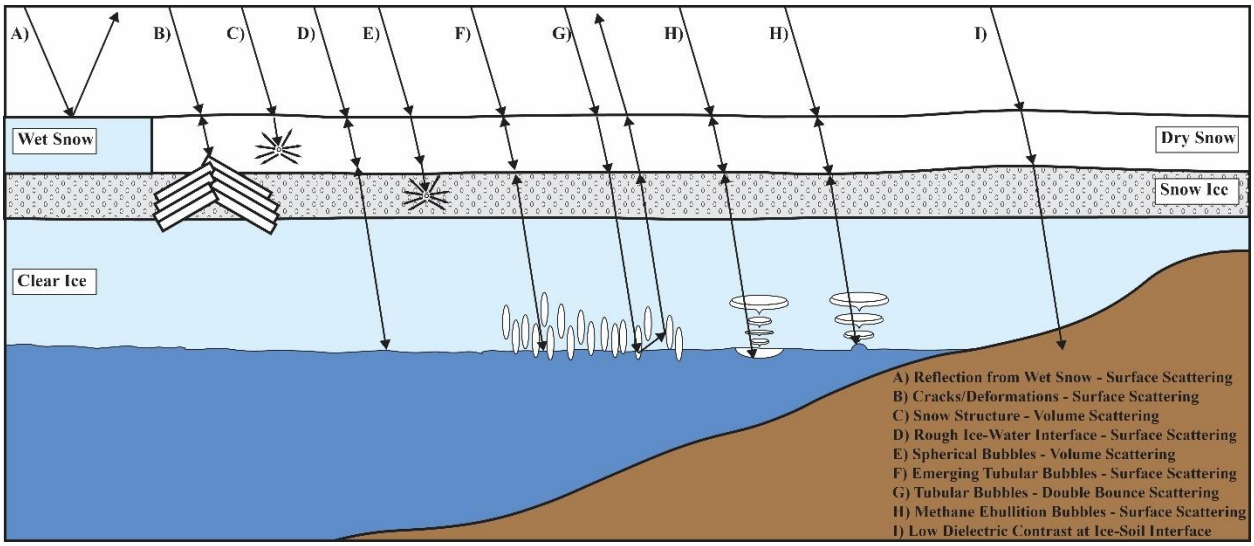

Figure 3.7 Updated scattering mechanisms (Ku to L-band frequencies) that show the influence of tubular bubbles and methane ebullition bubbles (Engram et al., 2013; Gunn et al., 2018). The influence of wet and dry snow is also illustrated with wet snow acting as a reflector since penetration depth can be on the order of one wavelength. The shallower penetration depth is a result of the high dielectric losses of liquid water (Rott & Mätzler, 1987; Jeffries et al., 1994) **compared to dry snow which is transparent to microwave signals at X to L-band frequencies** (Rott & Mätzler, 1987)**. However, volume scattering in the snowpack does occur at Ku-band as demonstrated in scatterometer experiments (Gunn, Brogioni, et al., 2015). Other scattering mechanisms are also included on this figure, B) shows surface scattering caused by deformation or cracks in the ice surface reported at X and C-band** (Morris et al., 1995; Gunn et al., 2017)**, D) shows surface scattering caused by a rough-ice water interface without the presence of bubbles as modelled using C-band by Atwood et al. (2015), E) demonstrates volume scattering as a result of spherical bubbles present in surface ice layers (grey or white ice) at Ku to C-band (Gunn et al., 2018), and I) shows the low return as a result of grounded ice cover at X to L-band (Weeks et al., 1978, 1981).**

3.3.3 Lake Ice Cover Monitoring Methods

The next sections highlight threshold-based and classification methods of identifying lake ice phenology dates (e.g., freeze onset, melt onset, water clear of ice) and cover extent for floating ice.

3.3.3.1 Threshold-based Methods of Monitoring Ice Phenology and Cover

Section 3.3.1 highlighted the general evolution in backscatter observed from SAR and Scatterometer systems. This backscatter evolution pattern has been used as a common method of extracting ice phenology dates. Howell et al. (2009), used Ku-band QuikSCAT data to determine ice phenology events (melt onset, water clear of ice and freeze onset dates) for Great Bear and Great Slave Lake, Northwest Territories, Canada between 2000 and 2006. The stable pattern of backscatter observed during the winter months allowed for the development of thresholds to estimate the timing of freeze onset, melt onset, and water clear of ice (Howell et al., 2009). This threshold method was also used to determine ice phenology for lakes on the North Slope of Alaska with a combination of ASAR and RADARSAT-2 data between 2005 and 2011 (Surdu et al., 2015). Research conducted on small/medium sized lakes in Central Ontario using RADARSAT-2 imagery applied a similar methodology but developed thresholds using the fluctuations in backscatter between different ice phenology stages (i.e. freeze-up to full ice cover and full ice cover to break-up) (Murfitt et al., 2018b). These threshold-based methods show accuracies that range between 0 and 37 days for freeze-up dates and from 0 to 43 days for water clear of ice dates when compared to optical satellite observations (MODIS) and visual interpretation of images by ice analysts at the Canadian Ice Service (CIS). However, these threshold methods are limited as the changes in backscatter are site specific and/or determined by user-analysis of the backscatter evolution, therefore the methods cannot be broadly applied (Murfitt & Duguay, 2020). Recent work attempted to address these issues, and focused on using the last and largest decrease in backscatter to identify ice cover phenology for Lake Hazen, Nunavut, Canada from Sentinel-1 imagery for 2015-2018, this eliminated the need for user-defined thresholds (**Figure 3.8**) (Murfitt & Duguay, 2020). The results were similar to previous analysis with errors ranging from 0 to 15 days when compared to visual analysis of SAR imagery. Additionally, this method was applied on a pixel-by-pixel basis allowing for the extraction of ice cover percentages, which were comparable to estimates made by the CIS (Murfitt & Duguay, 2020).

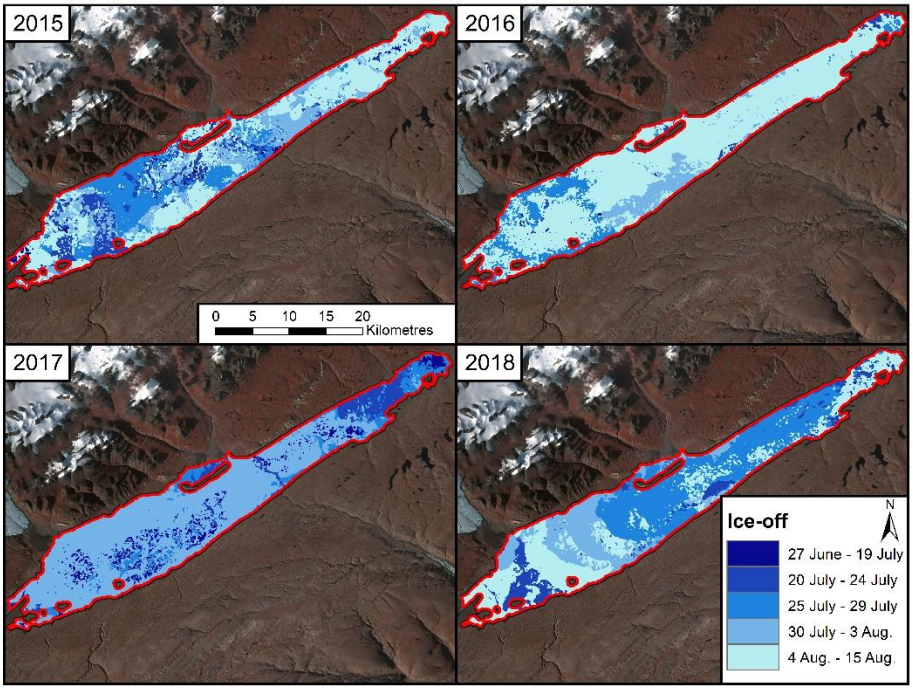

Figure 3.8 Lake ice-off dates between 2015-2018 for Lake Hazen identified using the last and largest decrease in backscatter. Landsat-8 Level-1 image courtesy of the U.S. Geological Survey (Digital Object Identifier (DOI) number: /10.5066/F71835S6). Source: Murfitt and Duguay, 2020.

Threshold-based classification methods can be used to extract ice cover percentages and infer the occurrence of phenology dates (ice formation and water clear of ice). Kouraev et al. (2003, 2007) demonstrated the utility of simultaneous radar altimetry data (Ku-band) and radiometer measurements from varying satellites for ice-water classification. These data were combined with ice-water classification results from SSM/I brightness temperature ratios. Classification thresholds for ice and water were developed from histograms and converted to a linear equation applicable to each satellite dataset (Kouraev et al., 2007). These equations were used to classify a 5-day mean of data. The method has shown to be successful for multiple European lakes (Kouraev et al., 2008) and showed good agreement with both satellite observations and historical records of ice phenology. During ice formation errors ranged from 2-17 days and during ice decay from 1-8 days (Kouraev et al., 2007). Other threshold classification methods have focused specifically on the use of polarimetric parameters to identify lake ice during freeze-up and break-up. Geldsetzer et al. (2010) used mean RADARSAT-2 (minimum mean HH and maximum mean HV) backscatter and standard deviations to define thresholds for the classification of decaying ice cover. The application of this method to small lakes in the Old Crow Flats, Yukon Territory, Canada, showed

overall accuracies of 66 to 97% for ice and open water classes using a pixel-based approach. Thresholds developed from relations between polarimetric parameters generated using RADARSAT-2 quad-pol imagery and incidence angle were used to identify ice during freeze-up for the same location (Geldsetzer & van der Sanden, 2013). This method showed high accuracies ranging from 76 to 99% when classifying ice and open water (Geldsetzer & van der Sanden, 2013). **Table 3.9** provides a summary of threshold methods for monitoring ice phenology and cover.

Table 3.9 Summary of Threshold Methods for Ice Phenology and Cover

Reference	Threshold	Radar Frequency	Radar Polarization	Error/Accuracy
Howell et al., 2009 *Great Bear Lake/Great Slave Lake*	FO: 6 dB MO: 4 dB WCI: 10 dB	Ku-band Scatterometer	HH	FO: 4-37 days WCI: 8-43 days
Surdu et al., 2015 *Alaska*	**ASAR** FO: 5.5 dB MO: 4 dB WCI: 7.5 dB **RADARSAT-2** FO: 6.5 dB MO: 5 dB WCI: 8.5 dB	C-band SAR	HH	FO: 0-15 days MO: 1-20 days WCI: 0-9 days
Murfitt et al., 2018b *Central Ontario*	Freeze: 2.4 dB Melt: -1.9 dB	C-band SAR	HH	FO: 3-10 days WCI: 2-8 days

Murfitt and Duguay, 2020 *Lake Hazen*	N/A	C-band SAR	HH	CFO: 3-15 days WCI: 0-12 days
Kouraev et al., 2003; 2007; 2008 *Eurasia*	Dependent on Lake	Simultaneous Ku-band Altimetry and Radiometry / SSM/I Radiometer	N/A	FO: 2-17 days WCI: 1-8 days
Geldsetzer et al., 2010 *Old Crow Flats*	HH: -21.35 dB HV: -24.35 dB	C-band SAR	HH+HV	Overall Accuracy: 66 to 97%
Geldsetzer and van der Sanden, 2013 *Old Crow Flats*	Incident Angle Dependent	C-band SAR	Quad-pol	Overall Accuracy: 76 to 99%

3.3.3.2 Classification Methods for Ice Cover

Unsupervised classification and segmentation methods allow for the automated identification of lake ice cover. TerraSAR-X and RADARSAT-2 images acquired for the Lena Delta were used to assess the pixel-based *k*-means algorithm for ice classification (Sobiech & Dierking, 2013). The *k*-means approach separates data into clusters and minimizes the distance between values and cluster means (Sobiech & Dierking, 2013). For the Lena Delta, the algorithm was set to identify 2 classes (ice and open water) with 5 iterations, the best results (mean error of 10.48%) were found when a closing filter was applied to the lake ice classification results (Sobiech & Dierking, 2013). The *k*-means approach was also used to identify ice cover and phenology dates for 11 lakes located in the Canadian Arctic Archipelago (CAA) and applied to 1600 C-band SAR

images, which spanned a period of 15 years (Surdu et al., 2016). Segmentation methods have recently seen increased popularity for ice cover classification. The Iterative Region Growing and Semantics (IRGS) algorithm was originally used for the identification of sea ice within the Map-Guided Ice Classification System (MAGIC) (Clausi et al., 2010), but is seeing increased usage for lake ice identification. IRGS repeatedly analyzes a randomly labelled segmented image and merges segments with the same label and minimum negative energy differences until the maximum number of iterations is reached (Yu & Clausi, 2008). For lake ice, the 'glocal' IRGS method has been used. This method creates smaller autopolygon regions that are first over-segmented and merged on the local scale before being combined across the entire scene (Leigh et al., 2013). Recently, 'glocal' IRGS was used for the identification of ice cover types on Lake Erie in RADARSAT-2 imagery, where accuracies of ice classification compared to analysis from the CIS reached 90% (**Figure 3.9C**) (J. Wang et al., 2018). The method was also used for Great Bear Lake and manual labelling accuracies of ice had an overall accuracy of 94% (**Figure 3.9B**) (M. Hoekstra et al., 2020). Recently, a segmentation method that has seen limited application for lake ice, the Otsu method (Otsu, 1979), was used to classify ice and water for Lake Hazen using Sentinel-1 imagery (Murfitt & Duguay, 2020). This method maximizes the inter-class variance in order to segment an image into foreground and background, the results for Lake Hazen were used to estimate ice phenology with errors of between 2 and 17 days (Murfitt & Duguay, 2020).

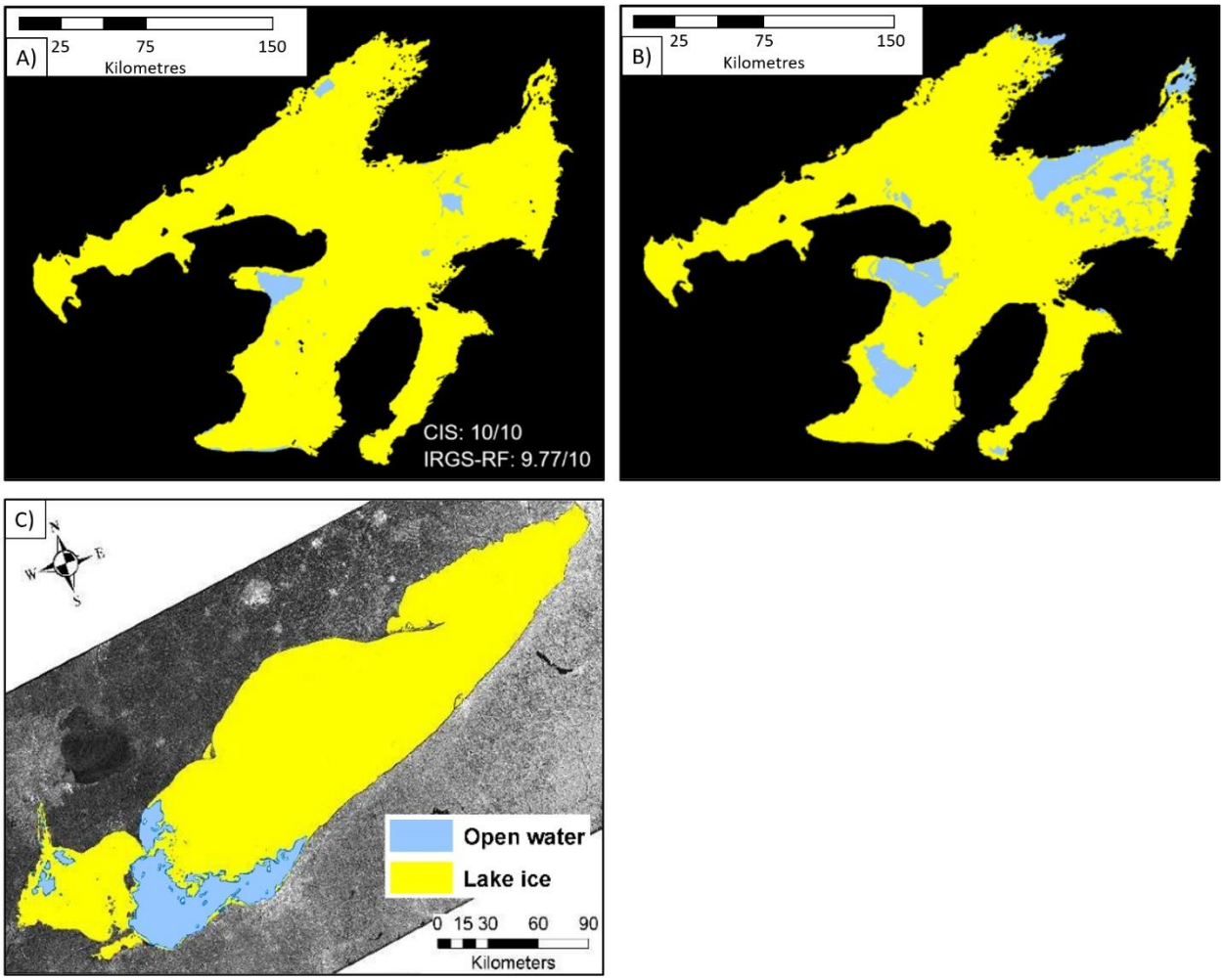

Figure 3.9 A) IRGS 'glocal' classification using Random Forest labelling of ice (yellow) and water (blue) for Great Bear Lake on May 18, 2016 (accuracy of 95.5%). B) IRGS 'glocal' classification using manual labelling of ice (yellow) and water (blue) for Great Bear Lake on November 27, 2014 (accuracy of 86%). C) IRGS 'glocal' classification of ice (yellow) and water (blue) for Lake Erie on February 21, 2014 (accuracy of 91.7%). RADARSAT-2 Data and Products © MacDonald, Dettwiler and Associates Ltd. (2014, 2016)—All Rights Reserved. Source: J. Wang et al. (2018) and Hoekstra et al. (2020).

3.3.3.3 Limitations of Mapping/Monitoring Methods

The various approaches described above experience common limitations in identifying ice phenology events and discriminating ice and water. The most common limitation reported is the presence of waves on the lake surface caused by wind action, resulting in increased backscatter due to the occurrence of Bragg scattering. Threshold methods are particularly impacted by this as

the fluctuation in backscatter due to wind can cause confusion and misidentification of ice cover/phenology events (Geldsetzer et al., 2010; Murfitt et al., 2018b). During the break-up process, the overlying snow or ice surface becomes brighter due to the surface becoming rougher and wetter as a result of the melt process. This rough/wet surface has similar backscatter values to a rough water surface causing confusion between the two features (Murfitt & Duguay, 2020). Additionally, the formation of melt ponds, snow melt, and pooling rainfall on the ice surface causes darker tones comparable to the backscatter that is observed for open, calm water (J. Wang et al., 2018). Ice formation results in lower backscatter values that can be easily confused with open water if there is little to no wind action (Murfitt & Duguay, 2020). Ice deformations (i.e. cracks and ridges) that are common during freeze-up have a higher backscatter compared to the rest of the ice surface (Morris et al., 1995) and can also be confused with the higher backscatter caused by waves (Murfitt & Duguay, 2020).

3.3.3.4 Advancements in Machine Learning

One area of increasing interest in remote sensing has been the use of deep learning and machine learning methodologies. Recent broad meta-analysis of remote sensing literature shows a dramatic increase in the number of papers (peer-reviewed and conference papers) that use deep learning techniques, reaching just under 400 publications in 2018 compared to less than 50 in 2015 (Ma et al., 2019). Machine learning algorithms are a popular choice for sea ice classification using synthetic aperture radar, and pixel-based neural networks are popular for classifying both sea ice type and sea ice concentration (e.g. Ressel, Frost, & Lehner, 2015; Wang, Scott, Xu, & Clausi, 2016). The application of these methods is limited for lake ice research and have focused on usage with optical remote sensing/shoreline camera imagery. Lake ice in Switzerland was classified using shoreline cameras and a convolutional neural network (CNN), with reported accuracies >95% on a pixel-by-pixel basis (Xiao et al., 2018). Multiple machine learning techniques (i.e. multinomial logistic regression, support vector machine, random forest, and gradient boosting trees) were recently tested using a pixel-based approach across the Northern Hemisphere for classification of MODIS data to identify ice, cloud, and water with reported accuracies exceeding 94% (Wu et al., 2021). Results of this analysis also identified random forest as having the greatest potential for lake ice mapping using optical data (Wu et al., 2021). Only recently have deep learning techniques been applied to SAR data. Deeplab v3+, a deep convolutional neural network

for semantic segmentation, was applied to Sentinel-1 imagery to conduct a pixel-based classification of ice and water in Switzerland, reported accuracies were > 84% (Tom et al., 2020). Additionally, recent literature shows the utility of combining automated segmentation and machine learning techniques using the IRGS algorithm in combination with a Random Forest labeller (M. Hoekstra et al., 2020). The combination of these algorithms resulted in ice-water classification with accuracies > 85% over Great Bear Lake for 36 RADARSAT-2 images between 2013 and 2016 (**Figure 3.9A**) (M. Hoekstra et al., 2020). Recent retrieval of ice and water from RADARSAT-2 images for Lake Erie and Lake Ontario used a CNN to determine the probability of a pixel being ice (K. A. Scott et al., 2020). When using dual-polarized images and probability thresholds < 0.1 this method was able to correctly classify 97-99% of ice pixels and 92-99% of water pixels as compared to image analysis charts of ice cover (K. A. Scott et al., 2020). The increasing prevalence of machine learning algorithms for lake ice mapping in the literature indicates that this is likely the direction the field will take in the coming decade, however, further investigation of these methods is needed. The high reported accuracies show that these algorithms are promising means of achieving the goals outlined in the GCOS requirements of lake ice cover with an uncertainty of 10% or less. Considerations for future research using these methodologies will be discussed in **Section 4** of this paper.

3.3.4 Other Applications of Radar Data

Active microwave data can also be used to monitor other characteristics of ice cover, including thickness and the presence of grounded ice. Section 3.3.4.1 will highlight the use of radar data for estimating ice thickness of floating and grounded ice regimes and Section 3.3.4.2 will highlight the use of radar data for classifying and monitoring grounded ice cover.

3.3.4.1 Retrieval of Ice Thickness

Ice thickness is a difficult parameter to extract using SAR data. In **Section 3.3.2** it was discussed that increasing backscatter observed from lakes is most likely caused by changes in roughness at the ice-water interface. Recent research evaluated the relation between ice thickness and backscatter for a small lake located in Central Ontario, but found that when using a linear model, predictions were inaccurate above 40 cm (Murfitt et al., 2018a). This could be due to a steeper increase in roughness associated with early ice growth as demonstrated in other analysis of polarimetric decomposition experiments for Churchill, Manitoba (Gunn et al., 2018).

SAR data has been used to determine the thickness of ice cover in areas with grounded ice regimes. Jeffries et al. (1996) combined ERS-1 SAR data and numerical ice modelling to identify the relative depths of lakes near Barrow Alaska. Areas of these lakes that did not experience the decrease in backscatter were determined to be deeper than the maximum ice thickness obtained from a numerical model (Jeffries et al., 1996). This was further explored in both Subarctic (Churchill, Manitoba (Duguay & Lafleur, 2003)) and Arctic (Northwest Territories (Hirose et al., 2008)) Canada. Areas of bedfast ice were determined using SAR data and connected to a source of ground truth data to estimate ice thickness. Examples of ground truth data include lake depths determined from optical imagery (Duguay & Lafleur, 2003) and bathymetric sounding data (Hirose et al., 2008). However, there are limitations associated with these data. Lake depths determined from optical images are influenced by the limnology of the lakes (i.e. dissolved organic carbon and water colour) (Duguay & Lafleur, 2003) and the accuracy of bathymetric data can be impacted by the water level at the time of measurement (Hirose et al., 2008).

Other active microwave data has shown success in estimating ice thickness. The most promising method on local scales is the application of Frequency Modulated Continuous Wave (FMCW) radars. Originally applied using airborne platforms for monitoring river ice (Venier & Cross, 1975; Yankielun et al., 1993), FMCW was tested on laboratory freshwater ice with a maximum thickness of 24 cm at C-band wavelengths (Leconte et al., 2009). The experiment found a strong linear relationship using the difference between the frequencies of interface reflections (ice-water and ice-air) and ice thickness ($R^2 = 0.99$) (Leconte et al., 2009). This method was further explored using an X and Ku-band FMCW radar under field conditions for Malcolm Ramsey Lake near Churchill, Manitoba (Gunn et al., 2015b). This research showed that the transmission angle of the signal through ice and the slant range distance from the ice-surface to ice-bottom interface for X and Ku-band frequencies can be used to estimate thickness with R^2 values of 0.95 and 0.96, respectively (Gunn et al., 2015b). Alternatively, the use of satellite radar altimetry has proven useful in estimating Arctic sea ice thickness (Laxon et al., 2003; Tilling et al., 2018), however, it has seen limited application for lake ice thickness retrieval. Recently, drawing from the work of Gunn et al. (2015b) on the exploitation of waveforms obtained with ground-based FMCW radar, CryoSat-2 (Ku-band) waveforms were used to estimate ice thickness on Great Bear and Great Slave Lake in northern Canada between 2010 and 2014 (Beckers et al., 2017). Correlation coefficients for ice thickness were >0.65 with root mean square error (RMSE) values of 0.12 to

0.41 m (Beckers et al., 2017). These errors are also influenced by Great Slave Lake in-situ data being interpolated for validation of Great Bear Lake estimations. These methods require further improvement for accurate and consistent monitoring of lake ice thickness to meet the goals put forth by GCOS (1-2 cm).

3.3.4.2 Bedfast Ice Identification

Section 3.3.1 discussed the special case of grounded ice covers regarding the decrease in backscatter noted for these lakes when maximum ice thickness is reached. Methods to determine the timing of these events/the amount of grounded ice cover has been an area of ongoing research in lake ice SAR remote sensing. Development of methods using SAR to actively determine bedfast ice regimes is critical for understanding water availability in northern communities during winter months (Jeffries et al., 1996; White et al., 2008). It can also help reduce the impact of water extraction from shallow lakes on northern fish ecology and has helped to identify important overwinter habitat for fish in Alaskan river systems (Hirose et al., 2008; R. S. Brown et al., 2010). Furthermore, the continued development and improvement of algorithms for identifying grounded ice cover is important as long term time series have shown that there is a decrease occurring in the fraction of grounded ice on the North Slope of Alaska with warming climates (Arp et al., 2012; Surdu et al., 2014). This decrease in grounded ice cover has important implications for permafrost thaw and the formation of taliks beneath these lakes (Ling & Zhang, 2003).

Methods for the classification and identification of lakes with grounded ice cover typically fall into two groups, The first, thresholding methods, has provided consistent classification results between grounded and floating ice covers. Kozlenko and Jeffries (2000) used the difference in backscatter between floating ice, grounded ice, and frozen tundra to identify a threshold capable of differentiating between the two types of ice cover. French et al. (2004) applied a similar method, however, used a binary threshold classification and uncalibrated pixel values to determine if lakes were frozen to bed (all pixel values for the lake <= 78) or not (at least one pixel value for the lake > 78). These methods were further developed in a study that analyzed changes in the area of floating and bedfast ice in Alaska over 25-years (Engram et al., 2018). Rather than use a single threshold, a variable threshold for each SAR scene in the time series was used, reporting a 93% accuracy in identifying grounded ice. This method avoided problems caused by differences in ice structure, issues with sensor degradation, and allowed for comparison between

SAR products (Engram et al., 2018). Recently, Tsui et al. (2019) developed a threshold method using dynamic time warping (DTW), a measure of similarity between time series, to compare time series of backscatter from lake ice pixels to reference time series for grounded lake ice pixels. Pixels were classified as being grounded ice if the normalized similarity was under 0.69; overall classification results for floating and grounded pixels was 89% (Tsui et al., 2019).

Regression-based thresholds have also been developed taking the dependence of backscatter on incidence angle into account for identification of grounded ice regimes. Bartsch et al. (2017) used this relation to develop a threshold function that was applied to lakes within the Arctic Circle and identified the total area of grounded ice cover during April 2008 (assumed maximum ice thickness). Pointner et al. (2019) proposed a flood-fill step when using the incidence angle thresholding method. This step 'fills' all connected background (non-grounded ice) and grounded ice pixels allowing for unconnected lake pixels to be reclassed as floating ice and a less patchy classification result (Pointner et al., 2019). Additionally, automated techniques (i.e. the previously mentioned IRGS method and watershed segmentation) have also been used to classify bedfast and floating ice cover (Surdu et al., 2014; Pointner et al., 2019). However, a recent study demonstrated that a threshold method, obtaining an accuracy of 92.6%, can provide slight improvement over IRGS and further improvement over an unsupervised k-means method for identifying grounded versus floating ice regimes when applied to lakes in Alaska, Canada, and Russia (Duguay & Wang, 2019).

3.4 Prospects for Active Microwave Remote Sensing of Lake Ice

3.4.1 Understanding Active Microwave and Lake Ice Interactions

This review previously discussed changes in our understanding of interactions between active microwave signals and lake ice properties. However, gaps remain in this understanding, primarily how ice characteristics such as ice-water interface roughness change throughout the ice season and how the interaction of microwave signals with this roughness is affected by other characteristics such as snow ice amounts and the presence of bubbles within the ice. Forward modelling experiments, using both radiative transfer models such as the dense medium radiative transfer (DMRT) model (Gunn, Brogioni, et al., 2015) and numerical models (Wakabayashi et al., 1994; Matsuoka et al., 1999), have been used to study lake ice and active microwave response. However, these studies have tended to focus on the response of microwave signals to bubbles in

the ice. Recent studies (Atwood et al., 2015; Tian et al., 2015), are now focusing on ice-water interface roughness within the models but current exploration has been limited. Additionally, a consistent model has not been used for lake ice research. In addition to forward modelling, polarimetric decompositions are important for understanding the scattering mechanisms from lake ice but have only focused on certain areas (e.g. Alaska (Engram et al., 2012, 2013) and Churchill, Manitoba (Gunn et al., 2018)).

Considerations for further studies of active microwave and lake ice interactions include:

1) *Broader Polarimetric Decomposition Analysis:* Although the current results of polarimetric decomposition experiments have been consistent, further application of the method is needed at additional study sites. Expanding the application of this methodology to larger lakes and lakes at different latitudes would improve our understanding of the interaction of microwave signals to different types of ice cover. Polarimetric decomposition can help to understand the impact that the absence of tubular bubble formation for lakes deeper than 4 m (Mellor, 1982) has on scattering mechanisms. Additionally, the study of lake ice at mid-latitudes in the Northern Hemisphere using SAR data has been limited. These locations are noted to experience increased snow ice and slush formation (Ariano & Brown, 2019), which may result in higher amounts of volume scattering.
2) *Forward Modelling Experiments:* Radiative transfer models, such as the recently published Snow Microwave Radiative Transfer (SMRT) model (Picard et al., 2018), are a useful tool in understanding how changing ice properties affect backscatter from lake ice. Experiments conducted using radiative transfer models should focus on roughness at the ice-water interface due to its importance highlighted in recent research (Engram et al., 2013; Atwood et al., 2015; Gunn et al., 2018). Forward modelling research conducted on river ice (Gherboudj et al., 2010) can serve as a guideline for determining appropriate values of ice-water interface roughness. The task of representing this characteristic will be particularly difficult as there are no established methodologies to retrieve these data (i.e., root mean square (RMS) roughness and correlation length) for lake ice cover. The development of this methodology is essential in continuing work on lake ice and active microwave interaction.

3) *Interactions within a Changing Climate:* Climate change is affecting lake ice cover phenology, structure, and processes. Analysis of successive 30-year near-surface air temperature trends for the Arctic reveal recent, post-1995, annual increases greater than 1.5°C/30-years (Johannessen et al., 2016). Additionally, modelling of lake ice in the late-21st century shows an estimated decrease in the length of ice cover duration by up to 30 days in North America (L. C. Brown & Duguay, 2011b). The combination of warming temperatures and shorter ice cover duration lead to the possibility of increased slushing events. These slushing events will likely affect backscatter due to changes in interface characteristics and changing contrasts in dielectric constants (e.g. Leconte & Klassen, 1991). Therefore, the overall effect of increased slushing events on backscatter, both for single events and throughout the ice season, will need to be evaluated through both forward modelling experiments and field investigations in the coming decade.

3.4.2 Classification of Ice Cover

The previously discussed methods of classifying ice cover/retrieving ice phenology work towards achieving the goals outlined in GCOS (10% accuracy), however, the most successful methods for binary classification of ice and water have been automated segmentation (90% accuracy) (J. Wang et al., 2018), combination segmentation and machine learning methods for labelling (>85% accuracy) (M. Hoekstra et al., 2020) and pixel-based classification using a CNN (>92% correct) (K. A. Scott et al., 2020). These automated methods are more suited for operational identification of ice cover compared to other previously developed methods (i.e., backscatter evolution thresholds). Additionally, these methods can be applied to high resolution data (10-50 m) allowing for lakes of all sizes to be characterized. While machine learning has shown promise for SAR lake ice mapping, further comprehensive investigations that compare methods using the same lakes and datasets are needed. Additionally, as we move forward with these new methods, we must ensure to acknowledge the physical basis for the interaction between SAR data and lake ice when selecting data and training parameters. Machine learning algorithms for lake ice classification should be investigated with consideration given to the following ideas:

1) *Expansion of Test Locations:* Currently the application of these algorithms has been limited to lakes in Switzerland, Lake Erie, Lake Ontario, and Great Bear Lake (J. Wang et al., 2018; K. A. Scott et al., 2020; M. Hoekstra et al., 2020; Tom et al., 2020). SAR data

for areas of dense lake coverage such as the North Slope of Alaska and near Churchill, Manitoba should also be explored to understand how the methods respond to different landscapes. These locations would also prove as good test regions for applying the machine learning algorithms for classification of floating and grounded ice covers. Furthermore, testing is needed to understand how these methods respond to differing ice types. Application to lakes in mid-latitude locations (i.e., Central Ontario), would provide a good case study for small/medium-sized lakes as well as the response of these algorithms to mid-winter melt events.

2) *Application to Dense Time Series:* Current application of these algorithms has been limited to one or two years of data, this also limits the amount of data available for training and testing purposes. The legacy of C-band SAR imagery now expands from the early 1990s to present with satellites such as ERS-1/2, RADARSAT-1/2, and Sentinel-1. The recent launch of the RADARSAT Constellation satellite system also means that there will be more frequent collection of imagery over areas such as northern Canada (Arkett et al., 2015). The application of these accurate algorithms would allow for the development of an extended lake ice record for a larger number of lakes and better understanding of how climate change has affected ice phenology/cover over the past 30 years. Additionally, these dense time series allow for access to large amounts of training data that are necessary to adequately train and parameterize these models.
3) *Exploration of SAR Parameters:* The exploration of these algorithms has been limited to dual-polarizations (i.e. VV+VH or HH+HV), however, quad-polarization options (HH+HV+VV+VH) from C and L-band satellites, ALOS-PALSAR-2 and RADARSAT-2, allow for the derivation of polarimetric parameters that have demonstrated high classification accuracies during freeze-up (Geldsetzer & van der Sanden, 2013). Additionally, RCM introduces circular polarization data which could help further refine these algorithms. Initial investigation of simulated RCM data led to the development of a CP-based classifier using multiple compact polarimetry parameters (RR, RR/RL, RH, RV/RH, and conformity) and an incidence angle-driven threshold procedure for pixel-based classification of ice and water during break-up, resulting in accuracies of 61 to 99% (van der Sanden & Geldsetzer, 2015). However, RCM has only been available for access since December 2019 and further exploration of the new circular polarimetric parameters

is needed. Exploration of these parameters through both RCM simulation using RADARSAT-2 data (e.g. Charbonneau et al., 2010) and analysis of available RCM data will help to better parametrize machine learning algorithms and further improve the classification of lake ice.

3.4.3 Ice Thickness Retrievals

Ice thickness estimates using active microwave data must be improved if it is to serve as a reliable source under the GCOS requirements. Recent estimates from satellite data highlighted in this review have shown errors ranging from 12-41 cm (Beckers et al., 2017). Passive microwave data may serve as the optimal data source for ice thickness retrieval from satellite data as estimates from these data sources show errors less than 20 cm (Kang et al., 2014). However, methods of ice thickness retrieval from active microwave require further exploration and should consider the following:

1) *Exploration of InSAR:* SAR interferometry has been explored for lake ice monitoring, both for the purpose of extracting lake ice cover and lake ice thickness (van der Sanden et al., 2013, 2018). Research on the application of InSAR for ice monitoring in the Mackenzie River Delta in 2013 found that short repeat pass satellites (i.e. COSMO-Skymed, <=4-day time interval) show the most promising results for further exploration of lake ice thickness mapping, and could be further explored using the recently launched RCM (van der Sanden et al., 2013). Additionally, this research highlights some of the limitations associated with the method, particularly how a mixture of snow and frazil ice types could cause larger estimation errors (van der Sanden et al., 2013). This means that the method could act as an adequate retrieval technique for Arctic regions but may experience difficulty at southern locations where there is an increased presence of snow ice cover. This is particularly true with the changes in climate that have been previously highlighted in this review. Both TanDEM-X bistatic and pursuit monostatic mode were investigated for possible use in lake ice discrimination, these modes allow for acquisition of closer image pairs compared to previous InSAR data with offsets ranging from 0 ms to 10 s, depending on latitude (Wendleder et al., 2013; van der Sanden et al., 2018). Pursuit monostatic coherence showed an advantage over bistatic as ice and water could be discriminated under windy conditions (van der Sanden et al., 2018). However, InSAR still requires further exploration for

applications to ice thickness retrieval, particularly because it can be applied to images with a finer spatial resolution compared to those acquired via passive microwave systems such as AMSR-2, helping to meet the horizontal resolution goals outlined in GCOS. Exploration of InSAR data for lake ice thickness retrievals may increase in the future with the launch of planned missions, such as TanDEM-L (Huber et al., 2018) and Radar Observing System for Europe (ROSE) L (Pierdicca et al., 2019).

2) *Exploration of Radar Altimetry:* This review has highlighted the recent work conducted with radar altimetry; however, this area still requires further exploration. There is a wide availability of data from various altimetry missions including Cryosat-2, Sentinel-3, ERS-1/2, ENVISAT, and the Jason series that has seen limited exploration in terms of ice thickness retrievals and could help to develop long term series of records. Altimetry waveforms have been used to retrieve lake ice thickness with current methods relying on the difference between identified intermediate and main peaks of these waveforms (Beckers et al., 2017). However, recent research on retrieval of river ice thickness suggests that the cumulative relative decrease in backscatter could be used to develop an empirical relation to ice thickness (Zakharova et al., 2020). While initial RMSE for river ice thickness compared to in situ observations has ranged from 0.07 to 0.18 m, exploration of this method for lake ice thickness is needed. The application of this methodology to additional lakes will help to better understand the use cases. The spatial resolution is a limiting factor for these data; however, it may serve as a good tool for larger lakes. The development of new satellites such as the Copernicus Polar Ice and Snow Topography Altimeter (CRISTAL) (Kern et al., 2020) and recently launched Sentinel-6 (Scharroo et al., 2016), which will provide continuation of the Jason series, could further help to expand the application of this methodology.

3) *Exploration of Emerging Technology:* In addition to these satellite methods, other technologies are currently being explored for active monitoring of ice thickness measurements. Global Navigation Satellite System Reflectometry (GNSS-R) is an active-passive remote sensing method explored for multiple environmental monitoring applications including snow depth monitoring (Larson & Small, 2016) and soil moisture observations (Camps et al., 2016). Recently the theoretical application of these data for lake ice thickness retrieval was explored using the Cyclone Global Navigation Satellite

System (CYGNSS) (Mayers & Ruf, 2018). However, the method was limited to lakes less than 40° N/S and has not seen practical application. Recently, TechDemoSat-1 was used to determine Arctic sea ice thickness (Yan & Huang, 2020). Upcoming and proposed GNSS-R missions (G-TERN, planned 2025, (Cardellach et al., 2018), 'Cookie' (Martin-Neira et al., 2016), and GEROS-ISS (Wickert et al., 2016)) could make spaceborne GNSS-R a viable source for lake ice thickness monitoring. However, to further validate this technology for the retrieval of ice thickness ground-based stations are presently the optimal choice for obtaining data. Recent experiments conducted using GNSS-IR methods for data from the Northwest Territories showed promising results for the retrieval of ice thickness with mean errors of 5 cm (Ghiasi et al., 2020)

3.4.4 Other Considerations

The above considerations represent some of the larger directions that active microwave could take in the coming decade. However, there are other items to consider in the field of active microwave research over lake ice:

1) *Data Accessibility:* In **Section 3.2.3** we discussed how the number of active microwave lake ice studies has increased in recent years in part due to the increasing availability of data through important hubs such as the Alaskan Satellite Facility, Copernicus Scihub, and Canada's EODMS. These sources allow for greater access to data from satellites such as RADARSAT-1, RADARSAT Constellation, Sentinel-1, and Sentinel-3. While research programs and government collaboration allow for increased access to satellites, RADARSAT-2, ALOS-2, and TerraSAR-X, that provide an extended range of radar frequencies (X to L-band), improved spatial resolution, and fully polarimetric data (RADARSAT-2 and ALOS-2), access remains limited for the scientific community at large. Increased open access to these data would make it easier to expand studies to a more diverse collection of lakes and make the field increasingly accessible. With the current trend in open remote sensing data, we hope to see increasing access to these satellites in the coming decade.
2) *Analysis of Archived Data:* With the launch of ERS-1 in 1991, there is now almost 30-years of C-band SAR data available covering the Northern Hemisphere. Long-term time series from this data (20-25 years) have been used to investigate bedfast ice conditions in

Alaska (Surdu et al., 2014; Engram et al., 2018), however, have not seen broad application. Additionally, other satellites such as TerraSAR-X (launched 2007) and ALOS (launched 2006) provide additional archives of X and L-band data that can be added to the C-band record. These frequencies have proven to be effective for monitoring lake ice in past research and could be helpful for establishing a climate data record (CDR), a time series that has the necessary length, consistency, and continuity to represent variability and change (National Research Council, 2004). This 30-year data record would be an effective method of observing trends in lake ice phenology for a broader number of lakes. This could also be helpful in better understanding the affect that differences in morphometry and location (latitude and longitude) as noted by Warne et al. (2020).

3) *Availability of Denser SAR Time Series:* Previous research has demonstrated that without consistent SAR image acquisition, algorithms can easily miss the occurrence of key ice phenology dates (Murfitt et al., 2018b). The utility of having these dense time series has been demonstrated for both scatterometer and SAR data in research conducted on two large Arctic lakes, Great Bear Lake (Scatterometer – daily passes) (Howell et al., 2009) and Lake Hazen (SAR – average image gap of 1.2 days) (Murfitt & Duguay, 2020). While varying imaging conditions may be different (see **Section 3.2.3.1** for a short discussion), dense time series allow for more accurate monitoring of ice events and also provide a better understanding of the spatial shifts in ice cover during break up and freeze up due to the consistent coverage (Murfitt & Duguay, 2020). This is important in the context of GCOS as the goal for lake ice cover monitoring is daily intervals. Whereas development of these time series was previously difficult at lower latitudes due to less frequent revisits, the recent RCM launch/coverage in combination with the current coverage provided by Sentinel-1 should allow for the creation of these time series for a broader number of lakes. Future SAR missions should consider the characteristics of currently available data (i.e., frequency, polarization, spatial resolution) so that the opportunity to construct intensive time series is not lost. The development of these time series is essential for machine learning/deep learning algorithms as it allows for increased collection of samples during diverse conditions.

4) *Snow Cover on Lake Ice:* The study of snow on lake ice has been quite limited in context of active microwave remote sensing (Gunn, Brogioni, et al., 2015). When snow is dry,

interaction over lake ice is limited as it is generally reported as transparent at lower frequencies. However, considerable changes in Ku-band backscatter (decreases of 1.6-6.2 dB) have been noted when snow cover is removed indicating greater interaction at higher frequencies (Gunn, Brogioni, et al., 2015). Terrestrial studies of snow water equivalent (SWE) retrieval algorithms have shown the utility of Ku and X-band backscatter from airborne missions (Zhu et al., 2018). Exploratory missions such as COREH$_2$O (Rott et al., 2012) act as a method of further developing these algorithms for broader application, however no tests have been conducted over lake ice. Additionally, Ka-band interferometry has shown in small scale explorations to be a promising source for snow depth/SWE retrieval (Moller et al., 2017) and may be ideal with the planned 2021 launch of the Surface Water and Ocean Topography Mission (SWOT) (Fu et al., 2012). Understanding snow mass on top of lake ice is important as the changing climate will likely lead to an increase in the formation of slush/snow ice which will affect the backscatter of frozen lakes. Improved retrieval of snow properties overlying ice covers are also important inputs for lake ice models such as CLIMo (Canadian Lake Ice Model (Duguay et al., 2003)), which can help predict changes in lake ice phenology and properties under future climate scenarios (e.g. Brown and Duguay, 2011; Dibike et al., 2011). Snow properties (i.e., depth and density) are also important for the accurate parameterization of radiative transfer models, such as SMRT, to effectively model backscatter.

3.5 Summary

This review discusses the status of the literature on lake ice remote sensing using active microwave data. A broad literature review found that in recent years there has been an increasing number of publications (conference papers, peer-reviewed articles, technical reports, and theses) on the use of active microwave remote sensing of lake ice. C-band SAR data has become the most common type of data due to the increasing number of satellites and availability of these data. There has also been a broadening of study areas, with an increasing number of study sites for small and medium sized lakes at Subarctic and temperate latitudes.

Recently there was a clear shift in the understanding of how active microwave signals interact with lake ice. Polarimetric decomposition experiments and forward modelling show that

roughness of the ice-water interface is a key parameter (Engram et al., 2013; Atwood et al., 2015) whereas previous research focused on the presence of tubular bubbles within the ice cover (e.g. Jeffries et al., 1994; Wakabayashi et al., 1994). However, further research is needed to better understand the processes that result in this roughness and the extent to which it impacts backscatter. Extensive research has been conducted on the classification of ice and water with methods working toward attaining the goals outlined within the GCOS requirements. Popular techniques include, threshold-based change algorithms (Howell et al., 2009), decision trees (Geldsetzer & van der Sanden, 2013), unsupervised classification methods (Sobiech & Dierking, 2013), and automated segmentation algorithms (J. Wang et al., 2018). Further research is needed on both the use of machine learning/deep learning algorithms and lake ice thickness retrieval using active microwave data as these areas have seen limited exploration.

This review makes several recommendations in four key areas of study: 1) understanding lake ice and active microwave interactions; 2) classification of lake ice; 3) retrieval of lake ice thickness; and 4) data availability/structures and snow properties. These recommendations focus on the use of modern modelling techniques, machine and deep learning algorithms, and exploration of new satellite data to lake ice applications. Exploration of lake ice in these areas will improve our overall understanding of ice cover and continue to develop records of lake ice as an important environmental variable in the current changing climate.

Chapter 4
Investigating the Effect of Lake Ice Properties on Multifrequency Backscatter Using the Snow Microwave Radiative Transfer (SMRT) Model

4.1 Introduction

Freshwater waterbodies across the Northern Hemisphere experience substantial ice cover throughout the winter season, with peak area coverage reaching 1.71×10^6 km^2 (Brooks et al., 2013). Although river ice makes up a portion of this coverage, 1.59×10^6 km^2 is lake ice (Brooks et al., 2013). The amount of ice coverage on a lake can influence the effect that lakes have on local meteorology. As an example, weather forecasting models revealed that temperature fluctuations in southern Finland during January/February 2012 were correctly determined when ice conditions of Lake Ladoga were best represented (Eerola et al., 2014). Additionally, low amounts of ice cover can result in the creation of severe lake-effect snow events in the Laurentian Great Lakes region (Baijnath-Rodino et al., 2018). Lake ice also plays an important role in freshwater ecosystems and there is increasing interest in the role that ice growth has on under-ice biology (Hampton et al., 2017). Social and economic systems are impacted by the presence and absence of lake ice as the formation of ice creates crucial ice road networks that allow for the transportation of goods to northern communities as well as travel between local communities (Mullan et al., 2017; Knoll et al., 2019). Recreation and tourism at mid-latitudes also rely on the formation of lake ice as it allows for the extension of snowmobile trails in provinces such as Ontario and northern United States. Establishment of these snowmobile trails contributes largely to the tourist economies in these locations (Cummings et al., 2019).

However, increasing temperatures have resulted in an increased probability that lakes will remain ice-free during winter months (Sharma et al., 2019; Filazzola et al., 2020). Additionally, the number of manual ice phenology records in northern countries has declined in recent years with an average of 198 observations across the Northern Hemisphere listed in the "Global Lake and River Ice Phenology" database for each year between 2004 and 2020 compared to an average of 970 between 1970 and 1990 (Benson et al., 2013). Due to the lack of reliable ground observations there has been a shift towards the use of remote sensing technologies for lake ice

observation (Duguay et al., 2015). While passive microwave and optical remote sensing data have been used to monitor both ice thickness (Kang et al., 2014) and ice phenology (Du et al., 2017; Cai et al., 2019), active microwave remote sensing has been the most common choice for monitoring and studying lake ice structure (Murfitt & Duguay, 2021). Active microwave data is preferred over passive microwave due to the higher spatial resolution which allows lakes to be resolved at a scale of metres compared to kilometre grids (Gunn et al., 2018). Additionally the longer wavelengths of radar systems allow penetration through cloud cover and continuous monitoring regardless of time of day compared to optical remote sensing that relies on the Sun's energy reflected from Earth (Duguay et al., 2015). Threshold and machine learning techniques have successfully used C-band synthetic aperture radar (SAR) to monitor both ice phenology dates and cover extent for high latitude lakes (M. Hoekstra et al., 2020; Murfitt & Duguay, 2020), while ground-based Frequency Modulated Continuous Wave (FM-CW) radar was used to estimate ice thickness for small Subarctic lakes near Churchill, Manitoba using Ku- and X-band radar (Gunn, Duguay, et al., 2015).

Early research on the interaction between lake ice and X-band Side Looking Airborne Radar (SLAR) attributed higher backscatter from lake ice to a double bounce mechanism caused by the presence of tubular bubbles in the lower layers of the ice column (Weeks et al., 1981). C-band satellite SAR observations of lake ice on the North Slope of Alaska combined with field observations appeared to support the theory that the thickening of ice cover and the development of these bubbles caused this increase in backscatter (Jeffries et al., 1994). However, the recent use of polarimetric decomposition techniques has demonstrated that increasing backscatter is likely due to changes in roughness at the ice-water interface. Decomposition of L-band images demonstrated that roughness of the ice-water interface was the largest contributor to backscatter for small lakes with floating ice cover in Alaska (Engram et al., 2012, 2013). For these lakes, roughness is a result of methane ebullition bubbles within the ice column. These bubbles can result in the formation of gas pockets beneath the ice or slow ice growth creating domes at the ice-water interface leading to increased roughness (Engram et al., 2012, 2013). Decomposition of C-band images was used to investigate the scattering mechanisms for Malcolm Ramsay Lake, near Churchill, Manitoba, Canada (Gunn et al., 2018). These results support the observations in Alaska, showing that the largest contributor to backscatter is ice-water interface roughness (Gunn et al.,

2018). However, dissimilar to lakes in Alaska, roughness at the ice-water interface is likely due to the extrusion of tubular bubbles from the bottom of the ice (Gunn et al., 2018).

In addition to decomposition methods, forward modelling has aided in understanding the impact of roughness on backscatter at the ice-water interface. Initial forward modelling of lake ice columns focused primarily on the inclusion of bubbles within the ice column and roughness at different interfaces (Wakabayashi et al., 1994, 1999; Matsuoka et al., 1999). However, recent research has shifted to focus on the impact of ice-water interface roughness. Numerical models noted that when roughness was parameterized at the ice-water interface with a root mean square (RMS) height of 5 mm and a correlation length of 50 mm, backscatter was generated above the noise floor and was similar between the same ice column with and without tubular bubble additions (Atwood et al., 2015). This demonstrates that tubular bubbles are a minor contributor to the response observed from lake ice (Atwood et al., 2015). Radiative transfer modelling (RTM) has also seen increased use for active microwave modelling of lake ice. C-band satellite VV-polarized backscatter was modelled using a dense discrete medium scattering model (Ewe et al., 1998) and the advanced integral equation model (AIEM) (Chen et al., 2003), to represent interface roughness, for lakes on the Qinghai-Tibet Plateau (Tian et al., 2015). These RTM experiments note that backscatter is most sensitive to changes in the roughness parameterization of the ice-water interface and bubble size (Tian et al., 2015). Additionally, (Gunn, Brogioni, et al., 2015) compared X- and Ku-band ground-based scatterometer measurements of lake ice for Malcolm Ramsay Lake to backscatter modelled using the dense medium radiative transfer (DMRT) model with quasi-crystalline approximations (QCA) (Tsang et al., 2007). Modelling results were within 5 dB of the observed backscatter for both frequencies.

While these past experiments demonstrate the applicability of forward modelling for improving understanding of the interaction between active microwave signals and lake ice, further investigation is needed. Research that has experimented with changes in freshwater ice properties focuses on small ranges of values or specific cases with little exploration of large ranges or extremes. Additionally, current research on ice-water interface roughness has focused on shallow lakes that form dense layers of tubular bubbles with little attention given to deeper lakes where tubular bubbles are absent. Further analysis also needs to be conducted on the impact of various ice properties on backscatter at different frequencies, polarizations, and incidence angles. Finally, previous modelling investigations have various noted limitations including, treating lake ice as a

single layer, ignoring the presence of snow/surface ice, and not incorporating roughness at different interfaces; no consistent model for lake ice forward modelling has been presented. This study works to address these limitations and provide a framework for further evaluation of lake ice using the recently published Snow Microwave Radiative Transfer (SMRT) model (Picard et al., 2018). SMRT helps to do this by providing a framework that can model multilayer snow and lake ice columns. This study investigates lakes that form and do not form tubular bubbles and uses a shallow and deep subarctic lake as a template to perform the described experiments. Using the Canadian Lake Ice Model (CLIMo; (Duguay et al., 2003)), an average of 20-years of modelled lake ice properties provides input for SMRT to explore the impacts that changing ice properties have on SAR backscatter from lake ice. CLIMo brings the microwave simulations more in line with reality as compared to past experiments that rely on synthetic input values. Ranges of properties from past studies help develop larger ranges for the testing of extreme values for ice properties. The objective of this study is to quantify the amount of impact changes in these properties have on backscatter and identify which properties have the largest impact. Additionally, this study looks to further evaluate the hypothesis that the dominant scattering mechanism for lake ice is roughness of the ice-water interface. These results provide a basis for future work on the retrieval of ice properties using the SMRT framework.

4.2 Methods

4.2.1 Snow Microwave Radiative Transfer Model

The SMRT model is designed for users to produce both active and passive microwave outputs (backscatter and brightness temperature) for multilayer snowpacks, with a full description of the model found in (Picard et al., 2018). SMRT is an open-source model and is available from https://github.com/smrt-model/smrt. The precise version used in this work is 10.5281/zenodo.5830262. The model permits the inclusion of saline and freshwater ice layers, which can be combined with user-defined snowpacks. Freshwater ice in SMRT is represented as an ice background (permittivity is calculated using (Mätzler et al., 2006) and is temperature dependent) with air inclusions (permittivity = 1). The model requires the temperature, thickness/depth, density, and microstructure parameters be set for each layer in the simulated medium. The model is run within a python environment and there is flexibility in selecting electromagnetic and microstructure models (Picard et al., 2018). The selected electromagnetic

model and microstructure parameters are used to solve the electromagnetic quantities (scattering coefficient, absorption coefficient, and phase matrix) for each layer. Reflectivity and transmittivity coefficients are determined through the interface and substrate components, with interlayer and substrate roughness being defined using the IEM theory (Fung et al., 1992), Geometrical Optics (Tsang & Kong, 2001), or Fresnel coefficients for flat interfaces (Picard et al., 2018). Once all layers and interfaces are defined, the radiative transfer equations are solved using the discrete ordinance and eigenvalue (DORT) method considering the active or passive sensors customized by the user by specifying frequency, incidence angle, and polarization or chosen from a list of pre-defined sensors. The result returned to the user is the emerging intensity in all or specific directions from the snowpack/ice column (Picard et al., 2018).

For the experiments conducted below, the sticky hard spheres (SHS) microstructure model and dense media radiative transfer (DMRT) theory with Quasi-Crystalline Approximation-Coherent Potential (QCACP) short range (Tsang et al., 1985; Picard et al., 2013) were used to configure the model for lake ice forward modelling in active mode. DMRT QCACP was selected to handle the smaller grain sizes present in clear/columnar lake ice and due to the use of DMRT in past lake ice modelling research (Gunn, Brogioni, et al., 2015). However, DMRT QCACP as implemented in SMRT is valid when the k_0a (k_0 is the wavenumber and a is the radius) is less than 0.6. Resulting backscatters for k_0a in this range are equivalent to other electromagnetic models (Picard, Löwe, & Mätzler, 2022). For the larger bubble radii tested, DMRT is not valid and the Improved Born approximation (IBA, (Mätzler, 1998; Picard et al., 2018)) is substituted for these experiments. IBA is valid when k_0a is less than 1.5 (Picard, Löwe, & Mätzler, 2022). In both cases, the SHS microstructure model represents grains in the snow and ice medium as sticky spheres. Sticky spheres form clumps and allow for the representation of large void spaces in the medium (Löwe & Picard, 2015). The parameter for SHS is stickiness (τ) that modulates the tendency of spheres in the medium to stick to each other, with lower values relating to increased stickiness (Picard et al., 2018). For parameterizing roughness of the ice-water interface, IEM with exponential autocorrelation function was selected as it is suitable for smaller scale roughness and has been used in past freshwater ice studies (Gherboudj et al., 2010). Roughness in IEM is represented through the use of two variables; root mean square height (referred to as *s* hereafter) and correlation length (referred to as *L* hereafter), where *s* refers to the vertical variation of surface roughness and *L* refers to the horizontal variation in roughness or displacement between two points

on the surface (Ulaby & Long, 2014). The validity range for IEM in SMRT is provided in **Table 4.1** below, where k is the wavenumber, epsr is the ratio between the dielectric constants of the upper the lower medium, $R_{V,H}(\theta_i)$ is the Fresnel coefficients for the incidence angle, and $R_{V,H}(\theta_{spec})$ is the Fresnel coefficients for a specular angle. Correlation Length in IEM is usually restricted where k2sL < √epsr, however, the range for L is expanded following (Brogioni et al., 2010), where Fresnel coefficients are determined using either the incidence angle or specular angle. This extension was introduced for Advanced IEM (AIEM) but can be used for IEM; however, caution should be used as the precise validity range of this extension on the original IEM remains to be determined.

Table 4.1 Validity range for IEM.

IEM Parameter	Validity Range	Reference
RMS Height	$ks < 2$	(Fung & Chen, 2010)
Correlation Length	if $k^2sL < \sqrt{eps_r}$: $R_{V,H}(\theta_i)$ if $k^2sL > \sqrt{eps_r}$: $R_{V,H}(\theta_{spec})$	(Brogioni et al., 2010)

4.2.2 Study Sites

To increase the realism of the SMRT experiments, two lakes were selected as templates for this study. Lake ice columns can be distinguished by those where tubular bubbles form and those without tubular bubbles. Tubular bubbles are elongated bubbles that form as the lake becomes super saturated with gases that are rejected as lake ice grows (Bari & Hallett, 1974). These bubbles have been reported to only form in shallow lakes or shallow areas that are <4 m deep (Mellor, 1982). To represent both ice columns in the sensitivity experiments, the two study sites selected represent a deeper lake with no tubular bubble formation and a shallow lake with dense tubular bubble layers. For the deeper lake, Noell Lake (68.53°, -133.56°, **Figure 4.1**), located north of Inuvik in the Northwest Territories, Canada, was selected. Ice cores and under-ice footage from this lake during the winter of 2019 showed no development of tubular bubbles in the central basin. Field measurements taken during the 2019 ice season also indicate the development of snow ice at Noell Lake and the presence of spherical bubbles in this surface ice layer. Noell Lake has an average depth of 6 m and a maximum depth of 18 m (Ogbebo et al., 2009;

Paquette-Struger et al., 2018). Typically, the ice season starts in late October and extends until mid or late June, 1981-2010 climate normals during the ice season show monthly average temperatures range from -26.9 to 11.6 °C (Environment and Climate Change Canada, 2021c). Snowfall can reach up to maximums of 0.99 m (Environment and Climate Change Canada, 2021c). Ice thickness data from Noell Lake is limited but a field campaign in March 2019 showed maximum thickness of 1.19 m. For the shallower lake, Malcolm Ramsay Lake (58.72°, -93.79°, **Figure 4.1**), located east of Churchill Manitoba, Canada, was selected. Field observations of this lake during the 2009-2010 and 2010-2011 ice seasons show formation of dense tubular bubbles at the bottom of the ice column (Gunn, Brogioni, et al., 2015; Gunn et al., 2018). Similar to Noell Lake, there is the development of surface grey/snow ice with small spherical bubbles. The mean depth of the lake is 2.4 m and the maximum depth is 3.2 m (Duguay & Lafleur, 2003). Typically, the ice season starts in early October and extends until late June, 1981-2010 climate normals during the ice season show average monthly temperatures ranging from -26 to 7 °C (Environment and Climate Change Canada, 2021a). Average monthly snow depth for the ice season ranges from 0.02 to 0.34 m, with reported ice thickness reaching up to 1.47 m (Duguay et al., 2002, 2003).

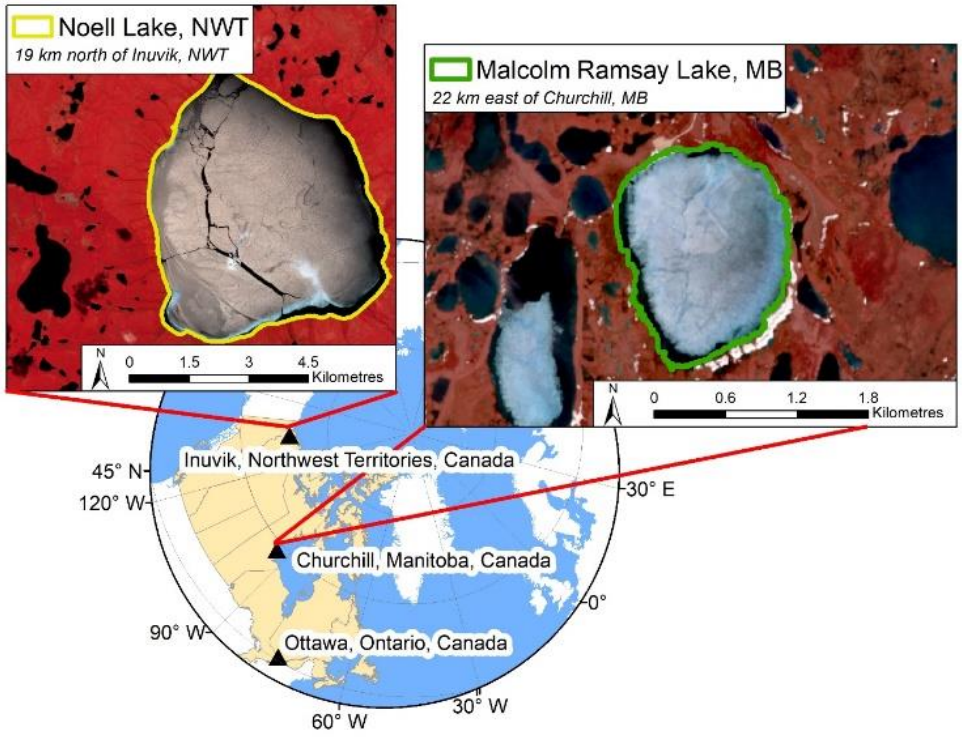

Figure 4.1 Locations of selected study sites to represent different lake ice conditions. This figure contains Copernicus Sentinel-2 data [2019, 2020], processed by the ESA.

4.2.3 Canadian Lake Ice Model

Ground observations can provide occasional input for snow depth and ice thickness; however, consistent daily measurements of ice/snow properties are more difficult to obtain. Therefore, to parametrize these aspects of SMRT, the Canadian Lake Ice Model (CLIMo) is used. CLIMo (see (Duguay et al., 2003)) is a one-dimensional model that is forced using local meteorological data to model ice layer properties and thickness and has been used in areas throughout Canada and Alaska. The model is based on a one-dimensional thermodynamic sea-ice model (see (Flato & Brown, 1996)), which makes use of the one-dimensional unsteady heat conduction equation (Maykut & Untersteiner, 1971) (1), where ρ (kg m^{-3}) is the density, C_p (J kg^{-1} K^{-1}) is the specific heat capacity, T (K) is the temperature of ice or snow, t (s) is the time, k (W m^{-1} K^{-1}) is the thermal conductivity, z (m) is the distance from the surface (positive if in the downward direction), F_{sw} (W m^{-2}) is the downwelling short wave radiative energy flux, I_o (W m^{-2}) is the fraction of short wave radiation flux that penetrates the surface layer, α is the surface albedo, and K is the bulk extinction coefficient for shortwave radiation (Duguay et al., 2003),

$$\rho C_p \frac{\partial T}{\partial t} = \frac{\partial}{\partial z} k \frac{\partial T}{\partial z} + F_{sw} I_o (1 - \alpha) K e^{-kz} \quad \textbf{(4.1)}$$

Following this, the surface energy budget can be solved from (2), where F_o (W m^{-2}) is the net downward heat flux absorbed at the surface, ε is the emissivity, σ is the Stefan-Boltzmann constant, F_{lw} is the downwelling long wave radiative flux, F_{lat} is the downward latent heat flux, and F_{sens} is the downward sensible heat flux,

$$F_o = F_{lw} - \varepsilon \sigma T_s^4(0, t) + (1 - \alpha)(1 - I_o) F_{sw} + F_{lat} + F_{sens} \quad \textbf{(4.2)}$$

Surface type (ice, snow, or open water), surface temperature, and ice thickness are used to determine how albedo is parameterized (Duguay et al., 2003). For CLIMo to produce a yearly ice-on and off cycle a fixed-depth mixed layer is included (Duguay et al., 2003). If there is ice cover on the lake, the temperature of the mixed layer is set to the freezing point (0 °C), however, if the

lake is ice free the temperature is set from the surface energy budget; thereby serving as a measure of heat storage within the lake (Duguay et al., 2003). CLIMo outputs used in this study include ice thickness, snow depth on the ice, and temperatures of snow and ice layers.

CLIMo was run for both Noell Lake and Malcolm Ramsay Lake using 2-m air temperature, 10-m wind speed, relative humidity, cloud cover, and snowfall from ERA5 data (Hersbach et al., 2018, 2020). ERA5 data were acquired as a 30 x 30 km^2 grid with one cell representing Noell Lake and two cells representing Malcolm Ramsay Lake. ERA5 data was used for all CLIMo inputs to maintain consistency in the input dataset and as discussed below showed strong correlation with available ground observations. Hourly ERA5 data were averaged to generate daily values for input into CLIMo. Air temperature and snow depth are the primary control factors for CLIMo model runs and the ERA5 data was validated using available data from the nearest Environment and Climate Change Canada (ECCC) meteorological station. For Noell Lake this was the Inuvik Climate station (-133.52°, 68.32°; 23.2 km south of Noell Lake) and the Churchill Climate station for Malcolm Ramsay Lake (-94.07°, 58.73°; 16 km west of Malcolm Ramsay Lake). Comparison between the respective stations and the ERA5 data show root mean square errors (RMSE) were <2.24 °C and <0.11 m for 2 m air temperature and snow depth, respectively. Kendall's Tau-b was used to calculate a rank coefficient due to ties in the data, values were $\geq$ 0.78 indicating a strong correlation between the observed and reanalysis data.

Mixing depth and snow density values for CLIMo were selected using observations or values applied to the lakes in previous research, these values and the references are listed in **Table 4.2**. The percentage scenario in CLIMo refers to the percentage of snow accumulation used to account for the difference between on-land and on-ice snow depth. Past comparisons show that on-ice snow depths are less than on-land snow depths by a ratio of 9 to 82% (Zhang & Jeffries, 2000; L. C. Brown & Duguay, 2011b, 2011a; Gunn, Duguay, et al., 2015), therefore, CLIMo was tested at varying on-ice snow depths for both lakes. Modelled snow depth and ice thickness for Churchill were compared to field measurements acquired during the 2009-2010 winter season and results for Noell Lake were compared to ice and snow measurements taken in March 2019 to identify the optimal snow cover percentage scenario. For Churchill, the best results were found when CLIMo was run with a 50% on-ice snow depth scenario with RMSE values of 0.05 m for ice thickness and 0.04 m for snow depth (**Table 4.3**). Field data were only available for Noell Lake between March 20 and 23, 2019; therefore, comparisons were made using this small subset of data.

CLIMo runs using a 35% on-ice snow depth produced the best results with an RMSE of 0.12 m for ice thickness and 0.05 m for snow depth (**Table 4.3**). **Figure 4.2** further supports the selection for Malcolm Ramsay Lake, showing good agreement between modelled ice thickness/snow depth and ground observations.

Table 4.2 Parameterization of CLIMo for Noell lake and Malcolm Ramsay Lake.

		Value	Reference			Value	Reference
Noell Lake	Mixing Depth	6 m	(Ogbebo et al., 2009)	**Malcolm Ramsay Lake**	Mixing Depth	2 m	(Gunn, Duguay, et al., 2015)
	Snow Density	283 kg m^{-3}	Field Campaign March 2019		Snow Density	276 kg m^{-3}	(L. C. Brown & Duguay, 2011a)
	On-ice Snow Depth	35%			On-ice Snow Depth	50%	

Table 4.3 Validation of CLIMo snow depth and ice thickness for Malcolm Ramsay and Noell lake.

Malcolm Ramsay Lake			**Noell Lake**		
Snow Cover Scenarios	**Average Snow Depth**	**Average Ice Thickness**	**Snow Cover Scenarios**	**Average Snow Depth**	**Average Ice Thickness**
*MAE**			*MAE**		
25%	0.08 m	0.11 m	35%	0.05 m	0.12 m
50%	0.04 m	0.04 m	50%	0.06 m	0.14 m
70%	0.06 m	0.10 m	70%	0.07 m	0.17 m
100%	0.07 m	0.11 m	100%	0.08 m	0.22 m

RMSE			*RMSE*		
25%	0.09 m	0.13 m	35%	0.05 m	0.12 m
50%	0.04 m	0.05 m	50%	0.06 m	0.14 m
70%	0.07 m	0.11 m	70%	0.07 m	0.17 m
100%	0.08 m	0.12 m	100%	0.08 m	0.22 m

*Mean Absolute Error

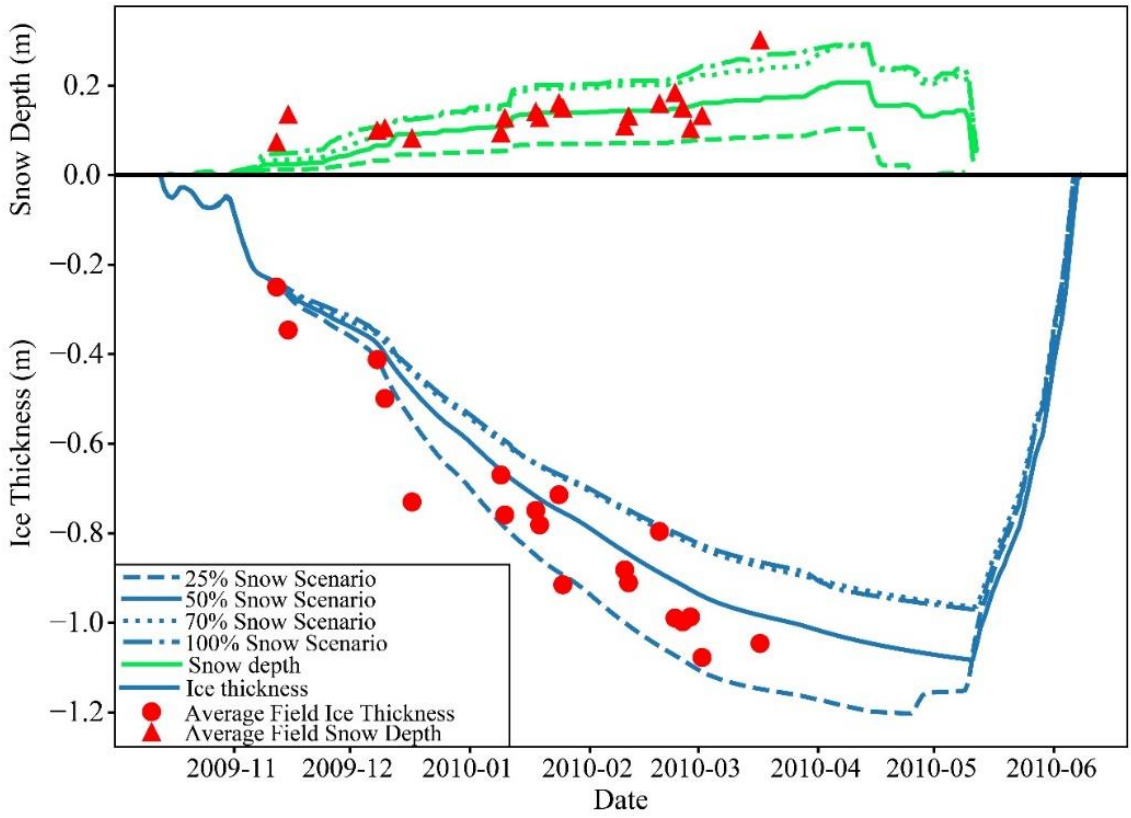

Figure 4.2 CLIMo simulations at 25, 50, 70, and 100% on-ice snow depth scenarios for Malcolm Ramsay Lake compared with measurements of snow depth and ice thickness from the 2009-2010 winter season.

4.2.4 Sensitivity Experiment Configuration

Following selection of the optimal snow depth scenario for CLIMo, the model outputs were translated for use with SMRT. CLIMo was run using a 5-layer configuration over 20 years (2000-2020). These data were averaged for each day of the year (1-365) over the 20 years to create a mean representation of an ice season for both shallow and deep lake. Interface temperatures from the lake ice model were averaged to determine layer temperatures. Snow ice thickness was assumed to be a consistent percentage of the total ice column, for the experiments presented in this paper 10% was used. The remainder of the ice column was split into 3 layers of equal thickness. If a scenario was run with no snow ice, the ice column was split into 4 layers of equal thickness. **Figure 4.3** shows a conceptualization of the conversion of CLIMo interface temperatures to SMRT layer temperatures for an ice column.

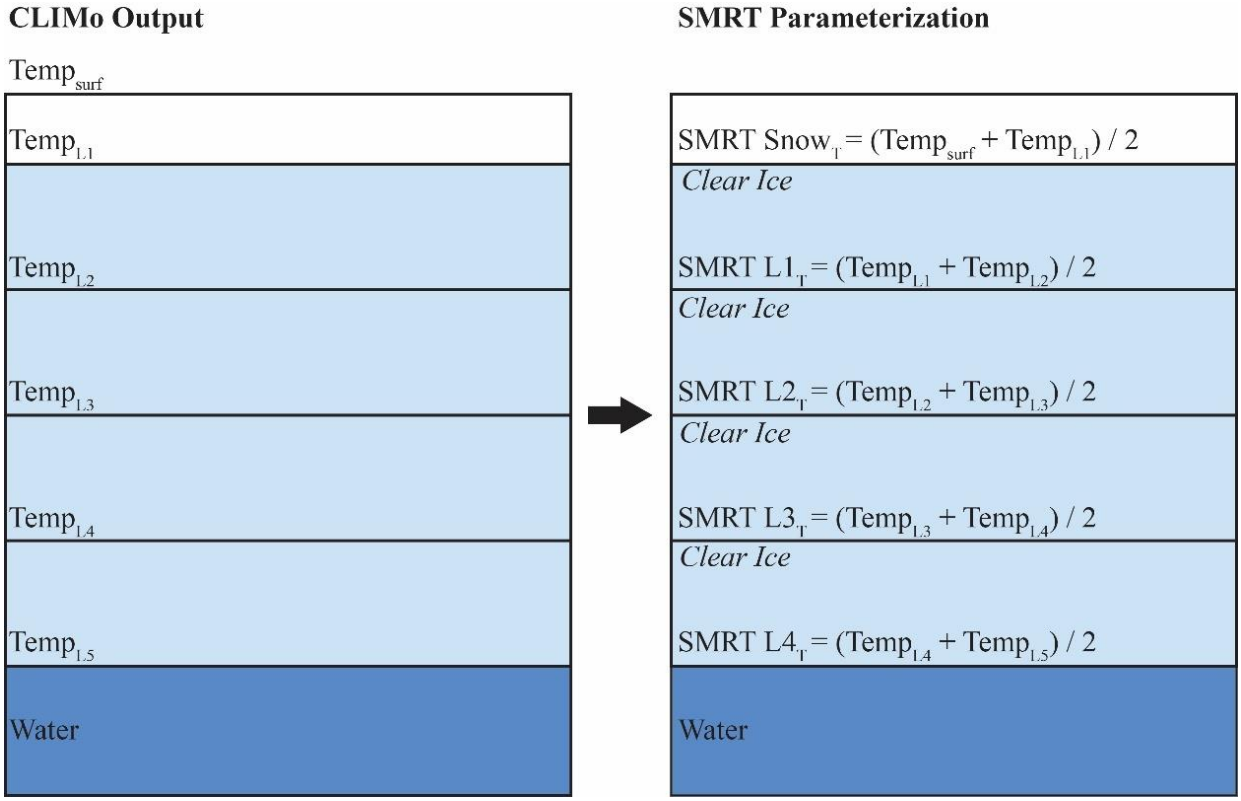

Figure 4.3 Conversion of CLIMo output data to SMRT input. For CLIMo, $Temp_{surf}$ is the temperature at the top of the snowpack and $Temp_{Lx}$ is the temperature at each layer interface.

SMRT LX_T are the average layer temperatures that were used as an input for SMRT. The top layer of clear ice in the SMRT ice column was replaced with a snow ice layer equal to 10% of the total ice thickness for some scenarios.

Optical radius (R_o) for snow grains, required for the parameterization of SHS, can be calculated as (4.3)

$$R_o = \frac{3}{\rho_{ice} * SSA} \quad \textbf{(4.3)}$$

where ρ_{ice} is the density of ice (916.7 kg m^{-3}) and *SSA* is the specific surface area (m^2 kg^{-1}). Due to an absence of direct measurements, a recent relation identified by (Vargel et al., 2020), between *SSA* and snow density (kg m^{-3}) developed using measurements from across the Canadian Arctic and Subarctic (including Trail Valley Creek, NWT, 24 km north of Noell Lake) was used to determine SSA for experiments in this study. The relation is given as (4.4)

$$SSA = -17.65 \ln(\rho) + 118.07 \quad \textbf{(4.4)}$$

where ρ was the dry snow density used to parameterize CLIMo (283 kg m^{-3} for Noell Lake and 276 kg m^{-3} for Malcolm Ramsay Lake). The resulting SSA was used to calculate R_o, 0.178 mm for Noell Lake and 0.173 mm for Malcolm Ramsay Lake. The limitation associated with using this approach is these values and relation are developed from terrestrial snow, not snow on lake ice. Therefore, it may not reflect the differences between these two systems. While snow conditions may change during the ice season, cold dry snow used in the modelling experiments will have a limited impact on microwave signals (Rott & Mätzler, 1987; Gunn, Brogioni, et al., 2015), and the use of constant snow density/SSA is acceptable under these conditions.

Table 4.4 provides a summary of the other parameters used for the experiments. The baseline conditions for ice properties were determined from ground observations and tested values in previous literature. Porosity was selected based on observations made for the Saint- François

River, Quebec and Athabasca River, Alberta, that ranged from 4 to 26% (Gherboudj, Bernier, Hicks, et al., 2007). These observations also provided some guidance for snow ice bubble radius, as observed bubble diameters ranged from 0.01 to 12 mm (Gherboudj, Bernier, Hicks, et al., 2007). For the shallow lake scenario, a bubble radius of 0.5 mm was selected due to the observation of 'microbubbles' in the snow/grey ice layers of Malcolm Ramsay Lake by (Gunn et al., 2018). For the deep lake scenario, a larger radius of 1 mm was used to provide contrast for the shallow lake experiment. DMRT as implemented in SMRT does not allow for the inclusion of tubular bubbles in freshwater ice columns. To represent the presence of tubular bubbles in the lower portions of the ice column spherical bubbles were added to the bottom layer of the shallow lake example. This bubbled ice is split into two layers, one with a small bubble radius (0.25 mm) and another with larger bubbles (1 mm). This was done to reflect observations at Malcolm Ramsay Lake by (Gunn et al., 2018) that stated tubular bubbles at the ice-water interface had a diameter ranging from 1 to 5 mm that narrowed to a diameter of approximately 0.5 mm as the bubbles extended into the ice. The bottom layer of larger bubbles was 5% of the total thickness for the bottom layer of the ice column. While the absence of cylinders may introduce modelling error, past research has indicated that it is unlikely cylindrical bubbles in the lower layers of the ice column significantly impact the radar signal (Atwood et al., 2015). Past numerical modelling has demonstrated that there is little difference in simulations when ice columns are represented with and without cylindrical bubbles (Atwood et al., 2015). Therefore, the substitution in this case is believed to have little impact on the overall results.

The impact of roughness on reflectivity of the snow-ice interface is assumed to be insignificant under the dry conditions used for these experiments due to the low dielectric contrast that exists between these two mediums. However, to properly represent the conditions of the ice column, a constant roughness was added at the snow-ice interface, this was parametrized with an s of 1 mm and L of 40 mm. These values are equivalent to those measured on floating ice cover on the North Slope of Alaska in April 1997 under frozen conditions (Wakabayashi et al., 1999). While larger deformations (cracks and ridges) can be present in ice covers, SMRT is currently unable to represent these larger 3D features and for the purposes of these experiments the ice cover

is assumed to be relatively smooth. Due to the expectation that tubular bubbles increase the *s* at the ice-water interface (Gunn et al., 2018), a larger value of 3 mm was selected for the baseline parameters for the shallow lake scenarios compared to 1 mm for the deeper lake. Stickiness (τ) was parameterized for each layer, for snow cover a value of 0.1 was used based on the optimal scaling factors in (Vargel et al., 2020) for Arctic and Subarctic snow. For ice, clear ice was assigned a τ of 1 due to the limited amount/absence of spheres, while for snow ice/tubular bubble layers a value of 0.4 was assigned due to the increased presence of bubbles and the tendency for bubbles to stick together. Since low values of stickiness are near the limit of the validity region of the SHS model (Löwe & Picard, 2015) an error may be encountered in SMRT. If such an error occurred when using the baseline τ value, τ was increased by small increments to limit discrepancies. The value for τ was incremented by 0.00001 for snow ice and 0.0001 for snow cover and clear ice. Stickiness (τ) values for snow ice reached a maximum of 0.40004 and for snow cover and clear ice a maximum of 0.1004 and 1.0004 respectively. Values for τ were reset to the baseline value of 0.4 and 0.1 for each model run.

Table 4.4 Baseline parameters for SMRT model runs.

Shallow Lake (based on Malcolm Ramsay Lake)			**Deep Lake (based on Noell Lake)**		
Snow		Ref.	**Snow**		Ref.
Depth	0.14	CLIMo	*Depth*	0.18 m	CLIMo
Density	276 kg m^{-3}	(L. C. Brown & Duguay, 2011a)	*Density*	283 kg m^{-3}	Field Campaign 2019
Optical Radius	0.173 mm	(Vargel et al., 2020)	*Optical Radius*	0.178 mm	(Vargel et al., 2020)
Stickiness	0.1	(Vargel et al., 2020)	*Stickiness*	0.1	(Vargel et al., 2020)
Snow Ice		Ref.	**Snow Ice**		Ref.
Thickness	0.1 m	CLIMo	*Thickness*	0.1 m	CLIMo

Bubble Radius	0.5 mm	(Gunn et al., 2018)	*Bubble Radius*	1 mm	(Gherboudj, Bernier, Hicks, et al., 2007)
Porosity	10%	(Gherboudj, Bernier, Hicks, et al., 2007)	*Porosity*	10%	(Gherboudj, Bernier, Hicks, et al., 2007)
Stickiness	0.4		*Stickiness*	0.4	
Clear Ice			**Clear Ice**		
Thickness	0.6 m	CLIMo	*Thickness*	0.9 m	CLIMo
Bubble Radius	0.0 mm		*Bubble Radius*	0.0 mm	
Porosity	1%		*Porosity*	1%	
Stickiness	1		*Stickiness*	1	
Bubble Ice					
Small Radius Thickness	0.285 m	CLIMo			
Interface Thickness	0.015 m	CLIMo			
Small Bubble Radius	0.25 m	(Gunn et al., 2018)			
Interface Bubble Radius	1 mm	(Gunn et al., 2018)			
Porosity	10%				
Stickiness	0.4				
Snow-Ice Interface			**Snow-Ice Interface**		
RMS Height (s)	1 mm	(Wakabayashi et al., 1999)	*RMS Height (s)*	1 mm	(Wakabayashi et al., 1999)

Correlation Length (L)	40 mm		*Correlation Length (L)*	40 mm	
Ice-Water Interface			**Ice-Water Interface**		
RMS Height (s)	3 mm	(Gherboudj et al., 2010)	*RMS Height (s)*	1 mm	(Gherboudj et al., 2010)
Correlation Length (L)	50 mm		*Correlation Length (L)*	50 mm	

Ice thickness, snow ice porosity, snow ice bubble radius, interface bubble radius, interface ice porosity, *s*, and *L* were tested to observe how these properties impact co-polarized backscatter. SMRT was run using L-band (1.27 GHz), C-band (5.405 GHz), and X-band (9.6 GHz) as these are the common frequencies used to study lake ice from SAR. Simulations were performed at 20°, 30°, and 40° incidence angles to represent the range of common imaging incidence angles of SAR products. Cross-polarized data was not investigated as it is currently underestimated by IEM as used in SMRT; this is an area of continued improvement. The ranges for these various properties can be found in **Table 4.5**. Ice thickness was tested using thickness and snow depth values produced by CLIMo up to end-of-winter maximum ice thickness. For the shallow lake experiments ice thickness ranged from 0.07 to 1.26 m and snow depth ranged from 0.01 to 0.21 m. For the deep lake experiments ice thickness range from 0.1 to 1.38 m and snow depth from 0.01 to 0.28 m. When one property was varied, all others were held constant at the baseline values from **Table 4.6** and ice thickness was held constant at the closest value to 1 m (deep lake snow depth of 0.18 m and shallow lake snow depth of 0.14 m). The range for other properties was determined from previous field observations (Gherboudj, Bernier, & Leconte, 2007; Gherboudj et al., 2010; Gunn et al., 2018). The range for *s* of the ice-water interface (0.5 to 7.5 mm) was determined from roughness observations of river ice (Gherboudj et al., 2010). It was assumed that smooth columnar river ice is most likely equivalent to what would be expected for ice-water interface roughness of a lake ice column. These values range from 0.1 – 10 mm (Gherboudj et al., 2010) and are consistent with those used in lake ice modelling experiments, with recent values of 1.48 to 1.66 mm for lakes

on the Qinghai-Tibet Plateau (Tian et al., 2015). This range is also consistent with numerical modelling experiments that used a value of 5 mm for *s* (Atwood et al., 2015). However, larger roughness values of 15 or 20 mm used in previous freshwater ice studies (Han & Lee, 2013; Gunn, Brogioni, et al., 2015) were not tested to respect the validity range of IEM. Similarly, *L* was not tested below 5 mm to respect the validity range of IEM. For the shallow and deep lake experiments a total of eight scenarios were conducted with an ice column of only clear ice and an ice column with a surface snow ice layer. In addition, these ice columns were both with and without snow cover. The full suite of scenarios is outlined in **Figure 4.4**.

Table 4.5 Ranges used for different ice properties. Values given in brackets are the increments used to increase the various properties.

Ice Property	Shallow Lake Ranges (Intervals)	Deep Lake Ranges (Intervals)
Snow Ice Bubble Radius	0.1 – 4 mm (0.05 mm)	0.1 – 4 mm (0.05 mm)
Interface Bubble Radius	0.5 – 2.5 mm (0.05 mm)	
Snow Ice Porosity	1 – 26% (1%)	1 – 26% (1%)
Bubbled Ice Porosity	1 – 40% (1%)	
RMS Height (*s*)	0.5 – 7.5 mm (0.1 mm)	
Correlation Length (*L*)	5 – 300 mm (1 mm)	

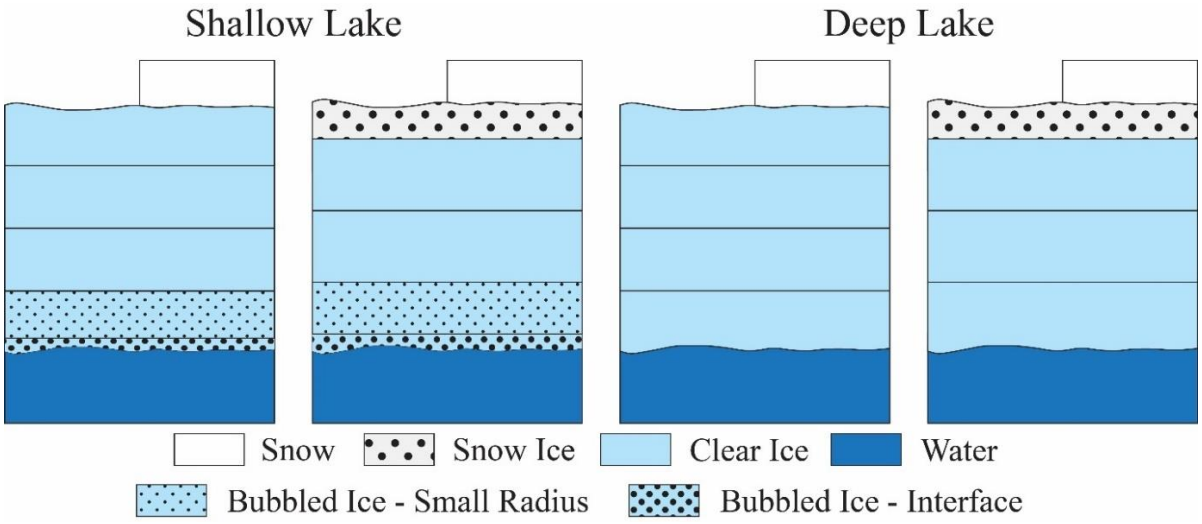

Figure 4.4 SMRT scenarios run for shallow and deep lakes.

To determine which properties had the largest impact on backscatter we calculated the percentage change between the backscatter determined using the minimum from the ranges given in **Table 4.5** and each iterative step. Percentage change was normalized by the percent change in ice property to compare values between properties. The normalized percentage change values will be referred to as NPC hereafter and are calculated using (4.5) and (4.6) given below,

$$Percent\ Change = \frac{\sigma^{\circ}_{0+i} - \sigma^{\circ}_{0}}{\sigma^{\circ}_{0}} * 100 \quad \textbf{(4.5)}$$

$$NPC = \frac{Percent\ Change}{\frac{Property_{0+i} - Property_{0}}{Property_{0}} * 100} \quad \textbf{(4.6)}$$

σ°_{0+i} is the linear backscatter iterated at a certain step (i) and σ°_{0} is the linear backscatter at the minimum range. $Property_{0+i}$ is the values of the ice property at the iterated step and $Property_{0}$ is the minimum ice property value. If the NPC value is 0.5, this indicates that a 1% change in the corresponding ice property will result in a 0.5% increase in linear backscatter. Quartile thresholds,

calculated from all obtained absolute NPC values, were used to classify the degree of effect that the different variables have on backscatter (**Table 4.6**).

Table 4.6 NPC categories determined by quartile divisions.

Classification	Threshold
No/Low	0 – 0.01
Medium	0.02 – 1.05
High	1.06 – 3.17
Very High	>3.17

4.3 Results

Sections 4.3.1 and **Section 4.3.2** focus on highlighting the NPC values observed for different scenarios and all properties tested. This portion of the results focuses on highlighting the properties that result in the largest changes in backscatter. **Section 4.3.3** is a closer examination of the changes in backscatter observed when *s*, *L*, and bubble radius are varied as these properties were observed to result in the largest changes in backscatter. To provide context to graphed backscatter in **Section 4.3.3**, comparisons were made to typical observed ranges in backscatter. These ranges are stated in (Murfitt & Duguay, 2021) and reference studies that include backscatter from floating ice cover for both shallow and deep lakes (e.g., Jeffries et al., 1994; Morris et al., 1995; Duguay et al., 2002; Engram et al., 2013; Antonova et al., 2016). Due to the limited observations of L and X-band backscatter from deeper lakes, one range is used for both shallow and deep experiments presented below. **Section 4.3.4** focuses on the patterns in co-pol ratios (VV/HH) and frequency ratios (C/L-band, X/L-band, and X/C-band) at VV-pol.

4.3.1 Normalized Percentage Change – Shallow Lake

Table 4.7 shows the response of backscatter to different ice properties for the shallow lake snow ice with snow cover scenario. The focus of the results is the snow ice experiments as it

is similar to those obtained for the clear ice scenario. Backscatter has no/low response (NPC of 0 to 0.01) to ice thickness, porosity at the ice surface and ice-water interface, and bubble radius at the ice surface and ice-water interface. There is a high response to *L* for L-band but a lower medium response (maximum 0.26) for C and X-band. Backscatter is most responsive to increases in *s*, with VV experiments having the highest NPC values across all three frequencies. L-band shows decreasing NPC (0.09-0.13) with incidence angle for HH-pol results. This decrease is also present for both X-band polarizations between 20° and 40° incidence angles. On the other hand, L-band VV-pol and both C-band polarizations show an increase in NPC with increasing incidence angle. The addition of snow to both the clear ice and snow ice scenarios results in a change in the magnitude of NPC values but does not impact the pattern in NPC values with changes in incidence angles. L-band VV-pol experiments where *s* was varied are an exception. With no snow present there is little change in the NPC value with incidence angle and with snow there is an increase in NPC with increasing incidence angle. Also, X-band *s* NPC values show slight variations between incidence angles depending on conditions. Clear ice with snow and snow ice without snow show increasing NPC values between 20 and 30° but a drop at 40°. Clear ice without snow shows a similar drop from 20 and 30° but not a drop at 40°. Snow ice with snow decreases from 30 to 40°.

Table 4.7 Absolute average NPC for the shallow lake snow ice with snow cover scenario.

	HH-pol								
Ice Property	**L-band 20°**	**L-band 30°**	**L-band 40°**	**C-band 20°**	**C-band 30°**	**C-band 40°**	**X-band 20°**	**X-band 30°**	**X-band 40°**
Ice Thickness	0.00	0.00	0.00	0.00	0.00	0.00	0.00	0.00	0.00
RMS Height (*s*)	6.50	6.41	6.28	2.80	3.45	3.52	1.32	1.24	0.91
Correlation Length (*L*)	1.63	0.85	0.54	0.19	0.08	0.05	0.26	0.12	0.07

Bubble Radius – Ice-Water Interface	0.00	0.00	0.00	0.00	0.00	0.00	0.01	0.00	0.01
Porosity – Ice-Water Interface	0.01	0.01	0.01	0.00	0.00	0.00	0.00	0.00	0.00
Bubble Radius – Surface	0.00	0.00	0.00	0.00	0.00	0.01	0.01	0.00	0.02
Porosity – Surface	0.00	0.00	0.00	0.00	0.00	0.00	0.00	0.00	0.00

VV-pol

Ice Thickness	0.00	0.00	0.00	0.00	0.00	0.00	0.00	0.00	0.00
RMS Height (*s*)	6.65	6.75	6.87	2.83	3.57	3.93	1.31	1.31	1.15
Correlation Length (*L*)	1.64	0.86	0.55	0.18	0.07	0.05	0.22	0.09	0.05
Bubble Radius – Ice-Water Interface	0.00	0.00	0.00	0.00	0.00	0.00	0.01	0.00	0.00
Porosity – Ice-Water Interface	0.00	0.00	0.00	0.00	0.00	0.00	0.00	0.00	0.00

Bubble Radius – Surface	0.00	0.00	0.00	0.00	0.00	0.00	0.01	0.00	0.01
Porosity – Surface	0.00	0.00	0.00	0.00	0.00	0.00	0.00	0.00	0.00

NPC Classification: No/Low; Medium; High; Very High

4.3.2 Normalized Percentage Change – Deep Lake

Table 4.8 shows the results of the deep lake clear ice with snow cover scenario. Backscatter has no/low response (0.00) to ice thickness. L-band at 20° incidence shows the highest response to *L* similar to the shallow lake scenario. Both C and X-band simulations show a lower response to *L* with a maximum NPC of 0.1. The largest NPC values for backscatter occur in response to increases in *s*, L-band has the highest with NPC >6 for all incidence angles and polarizations. Across incidence angles, there is an increase in *s* NPC values for 20° to 40°, with the largest change (1.40) occurring at C-band VV-pol. The exception to this is L-band HH, which shows a decrease in NPC from 20° to 40° of 0.21. Correlation length shows a decrease in NPC values for 20° to 40° that is most notable at L-band, dropping by >0.3 for both HH and VV-pol.

Table 4.8 Absolute average NPC for the deep lake clear ice with snow cover scenario.

	HH-pol								
Ice Property	**L-band 20°**	**L-band 30°**	**L-band 40°**	**C-band 20°**	**C-band 30°**	**C-band 40°**	**X-band 20°**	**X-band 30°**	**X-band 40°**
Ice Thickness	0.00	0.00	0.00	0.00	0.00	0.00	0.00	0.00	0.00
RMS Height (*s*)	6.24	6.15	6.03	2.61	3.48	3.98	1.38	1.69	1.68
Correlation Length (*L*)	0.65	0.41	0.30	0.10	0.05	0.04	0.04	0.04	0.04

	VV-pol								
Ice Thickness	0.00	0.00	0.00	0.00	0.00	0.00	0.00	0.00	0.00
RMS Height (*s*)	6.39	6.48	6.59	2.64	3.49	4.04	1.32	1.56	1.57
Correlation Length (*L*)	0.68	0.45	0.34	0.10	0.05	0.04	0.04	0.04	0.04

NPC Classification: No/Low; Medium; High; Very High

Table 4.9 details the results of the deep lake snow ice with snow cover scenario. Both HH and VV backscatter have a no/low or medium response to ice thickness, *L*, porosity, and bubble radius. The highest response to bubble radius occurs at X-band for HH-pol at a 40° incidence angle. Additionally, X-band NPC values for surface bubble radius are higher for HH-pol experiments compared to VV-pol. Similar to other scenarios, L-band is more responsive to *L*. C and L-band backscatter show the highest response to increases in *s*. C-band has a higher response for VV-pol backscatter compared to HH-pol and shows an increasing trend from 20° to 40° incidence angle. On the other hand, L-band backscatter displays an increase for VV but a decrease across incidence angles for HH. L-band shows the same higher response for VV-pol compared to HH-pol as C-band. For NPC values in X-band experiments the highest response to *s* was for the 20° incidence angle experiment. There are differences between snow and clear ice experiments. For example, most frequencies/polarizations show an increase in NPC values of *s* with increasing incidence angle for the clear ice scenario. However, for snow ice, C-band HH-pol and X-band HH-pol and VV-pol NPC values of *s* decrease with increasing incidence angle. Similar to the shallow lake scenario, when snow is added patterns in the NPC values for *s* are different for L-band VV-pol experiments. When no snow is present NPC values decrease with incidence angle, however, when snow is present NPC values increase with incidence angle.

Table 4.9 Absolute average NPC for the deep lake snow ice with snow cover scenario.

HH-pol									
Ice Property	**L-band 20°**	**L-band 30°**	**L-band 40°**	**C-band 20°**	**C-band 30°**	**C-band 40°**	**X-band 20°**	**X-band 30°**	**X-band 40°**
Ice Thickness	0.00	0.00	0.00	0.00	0.00	0.00	0.00	0.00	0.00
RMS Height (*s*)	6.46	6.39	6.27	2.49	2.74	2.41	1.28	0.86	0.49
Correlation Length (*L*)	0.75	0.45	0.32	0.10	0.05	0.04	0.04	0.03	0.03
Bubble Radius – Surface	0.00	0.00	0.00	0.01	0.04	0.10	0.03	0.13	0.31
Porosity – Surface	0.00	0.00	0.00	0.00	0.01	0.02	0.01	0.03	0.07
VV-pol									
Ice Thickness	0.00	0.00	0.00	0.00	0.00	0.00	0.00	0.00	0.00
RMS Height (*s*)	6.60	6.70	6.82	2.55	2.99	3.04	1.32	1.03	0.77
Correlation Length (*L*)	0.79	0.50	0.37	0.10	0.05	0.04	0.04	0.03	0.04
Bubble Radius – Surface	0.00	0.00	0.00	0.01	0.03	0.05	0.02	0.09	0.17
Porosity – Surface	0.00	0.00	0.00	0.00	0.00	0.01	0.01	0.02	0.04

NPC Classification: No/Low; Medium; High; Very High

4.3.3 Roughness and Surface Bubble Radius

From the NPC analysis *s* consistently resulted in the largest backscatter response. For L-band correlation length was also shown to be important, while for C and X-band bubble radius for the deeper lake scenario showed increased response. Therefore, it is important to further explore how backscatter changes as these properties increase. **Figure 4.5** shows the change in backscatter with increasing *s* for snow ice with snow cover scenarios from deep and shallow lakes. The clear ice scenario is not shown here due to its similarity with the shallow lake snow ice scenario. For both the shallow and deep lake scenarios there is an increase in backscatter with increasing *s* at L and C-band frequencies. For L-band the increase is consistent, however, C-band backscatter starts to decrease at higher *s*. X-band follows a similar pattern; however, it starts to decrease earlier compared to the other frequencies. Additionally, for the deep lake scenario the evolution of backscatter occurs at a slower rate compared to the shallow lake scenario. The increases across L and C-band frequency demonstrate the impact that a small amount of *s* can have on backscatter from freshwater ice. The change in *s* from 0.5 to 1 mm results in an average increase in linear L-band backscatter across all incidence angles of 255% and 253% for the deep lake and shallow lake scenarios respectively. For C-band, the increase is 180% and 209% respectively. **Figure 4.5** also shows that the modelled backscatter values correspond to typical observed ranges in backscatter from maximum ice thickness at different frequencies (Murfitt & Duguay, 2021). Modelled backscatter values tend to fall into the expected range when s > 1 mm, depending on the incidence angle. For example, modelled X-band backscatter falls outside the expected range with higher *s* and at larger incidence angles, this is due to the bell-shaped pattern of the backscatter. The discontinuity observed in the X-band, and to a lesser extent the C-band curves are due to abrupt changes caused by the extension of IEM (Brogioni et al., 2010) as noted in **Section 4.2.1**.

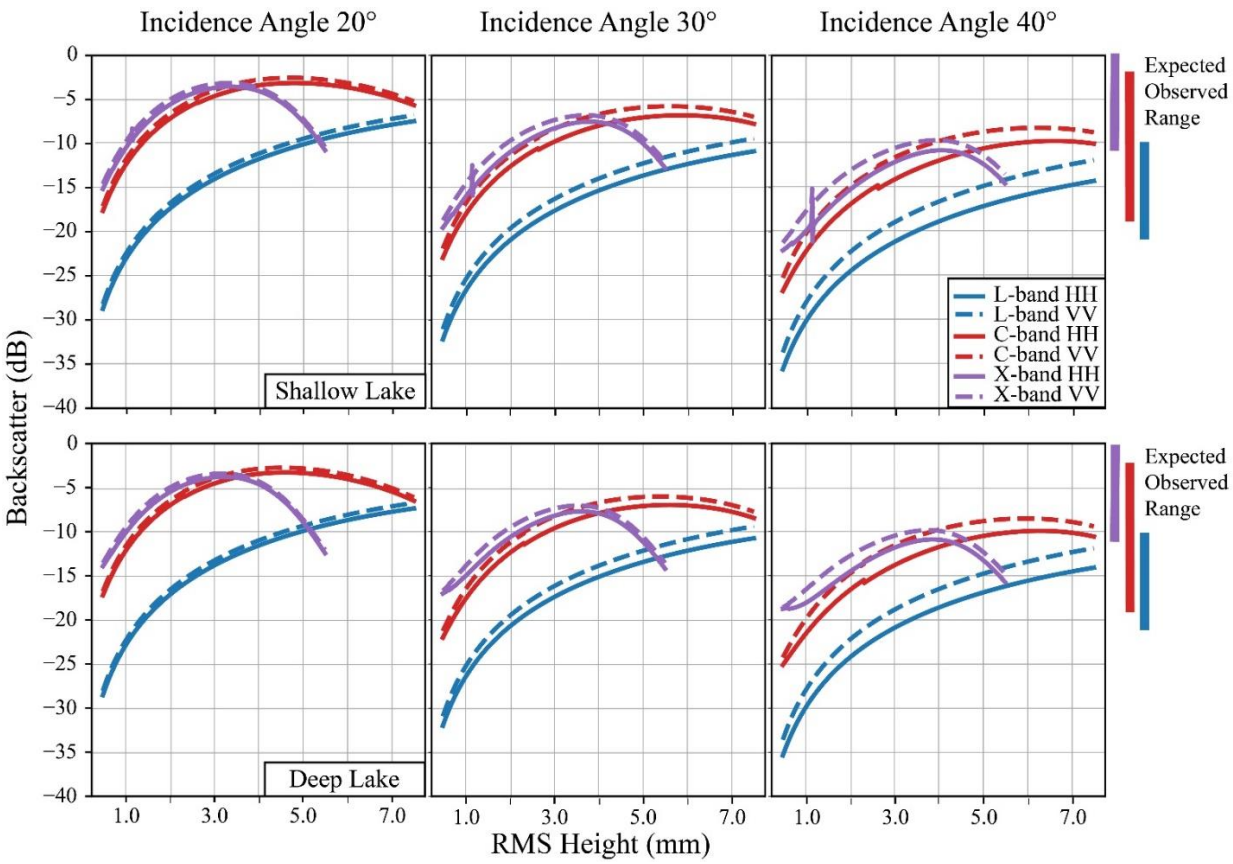

Figure 4.5 Change in backscatter with increasing RMS height (*s*) for snow ice with snow cover scenario for shallow and deep lake experiments. Ranges on the right-hand side of the plot showcase typical observed ranges in backscatter from maximum ice thickness at different frequencies (Murfitt & Duguay, 2022).

Correlation length is the other component of roughness within IEM. The NPC analysis showed lower response to *L* at C and X-band frequencies, this is reflected in **Figure 4.6**. For these two frequencies there is an initial increase in backscatter that then decreases as *L* increases. L-band shows a larger initial increase compared to the other two frequencies. After the initial increase backscatter decreases but does not drop below the initial modelled backscatter as C and X-band experiments do. Additionally, the low change in backscatter at higher values of *L* highlights the greater impact that *s* has on backscatter from lake ice. While modelled backscatter for the correlation length experiments from the shallow lake simulations fall within the expected range of

backscatter, this is likely due to the higher constant *s* used for these simulations (*s* = 3 mm). For the deep lake experiments (*s* = 1 mm), modelled backscatter falls outside the typical ranges except at low *L* values and incidence angles. This further supports that *s* has a greater impact on backscatter compared to *L*.

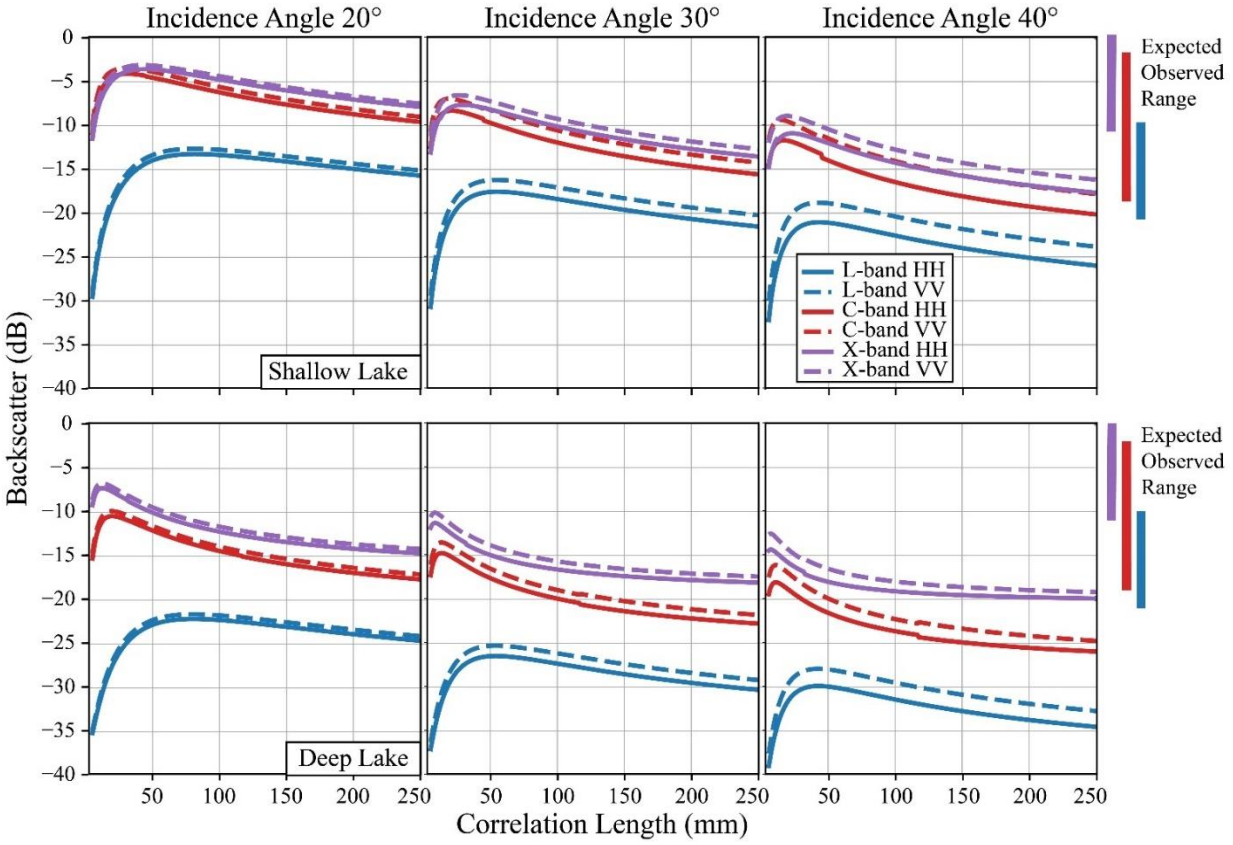

Figure 4.6 Change in backscatter with increasing correlation length (*L*) for snow ice with snow cover scenario for shallow and deep lake experiments. Ranges on the right-hand side of the plot showcase typical observed ranges in backscatter from maximum ice thickness at different frequencies (Murfitt & Duguay, 2022).

There are differing responses to increases in surface bubble radius between shallow and deep lake scenarios (**Figure 4.7**). For the shallow lake scenario, there is limited response of all frequencies to increasing bubble radius. X-band shows a slight increase; however, this only occurs when the bubble radius is larger than 3.3 mm. The response of C and X-band backscatter does

increase with higher incidence angles but only for higher bubble radii; at lower radii backscatter continues to show reduced or no response. For the deeper lake scenario, all three incidence angles show an increase in backscatter with increasing bubble radius. While backscatter increases with larger radii, at smaller radii it is less responsive. For C-band the maximum increase in linear backscatter between 0.1 mm and 1.5 mm radius is 63%. This occurs for the HH-pol experiment at an incidence angle of 40°. For other incidence angles the percentage increase in linear backscatter is less than 27% for the same range. However, at a higher range of bubble radii (1.5 to 3 mm) this percentage increase in linear backscatter rises to a minimum of 38% (VV-pol incidence angle 20°) and a maximum of 258% (HH-pol incidence angle 40°). Larger increases are observed for X-band, with maximum increases in linear backscatter of 281% for a range of smaller bubble radii (0.1 to 1.5 mm). This connects back to the increased NPC values that were observed for the X-band experiments.

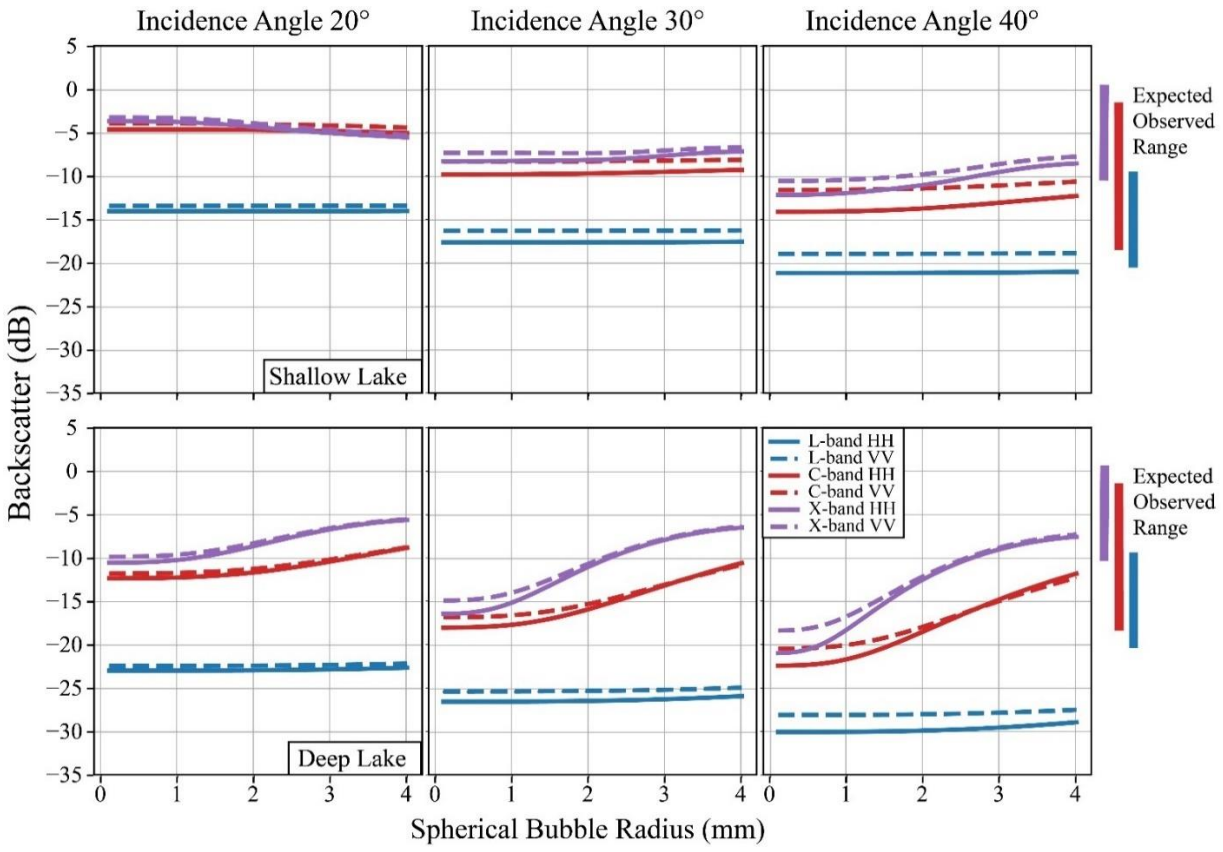

Figure 4.7 Change in backscatter with increasing surface bubble radius for snow ice with and without snow cover scenario for the deep lake experiment. Ranges on the right-hand side of the plot showcase typical observed ranges in backscatter from maximum ice thickness at different frequencies (Murfitt & Duguay, 2022).

Additional experiments were conducted to observe how backscatter responds to simultaneous changes in bubble radius and *s*, porosity and bubble radius, as well as *s* and *L*. Bubble radius was iterated between 0.25 and 4 mm at an interval of 0.25 mm, at each interval *s* was tested between 0.5 and 7.5 mm at an interval of 0.2 mm. Porosity was iterated between 1 and 26% at an interval of 1% and bubble radius was iterated between 0.25 and 4 mm at an interval of 0.25 mm. For *s*/*L*, *L* was tested between 2.5 and 100 mm at an interval of 2.5 mm, at each interval *s* was tested between 0.5 and 5 mm at an interval of 0.2 mm. This experiment also focused on the deep lake scenario due to the limited response of bubble radius in the shallow lake experiments. For these experiments *L* was restricted to ensure the ranges of IEM were respected. The results of the bubble radius/*s* experiment are shown in **Figure 4.8**. L-band shows little response to increases in bubble radius as was seen in **Figure 4.7**, the pattern in backscatter change reflects the results observed in **Figure 4.5**. C-band results show a similar pattern to increasing backscatter observed in **Figure 4.5** at lower bubble radii (<2 mm)**.** However, as bubble radius increases, the influence of *s* is reduced when <2 mm. This same result is observed at X-band but there is further evidence that this frequency is more responsive to increases in bubble radius. The patterns in backscatter are similar to those observed in **Figure 4.7**, with backscatter being more responsive to *s* at the steeper incidence angle and low bubble radii.

Figure 4.9 shows the response of backscatter to increase in both porosity and bubble radius. As expected for L-band there is little response to either change in property supporting the results in **Table 4.9**. For C- and X-band, the response of backscatter to bubble radius increases with rising porosity. However, this also shows that the response saturates around porosity values of 10 to 15%. This supports bubble radius as the key controlling property in relation to the impact of snow ice layers on backscatter. This figure also indicates the porosity and bubble radius play a larger role at higher incidence angles (i.e., 40º verse 20º).

Figure 4.10 shows the response of backscatter to increases in *s* and *L*. The response of *L* to backscatter is similar to the patterns observed in **Figure 4.6**, C and X-band show initial increases followed by a decrease and relatively stable patterns, while L-band only shows an initial increase. This experiment highlights the impact that lower *L* has on the range of modelled backscatter, particularly for L-band simulations. For smaller *L* (<10 mm), backscatter does not exceed -23.3 dB for L-band simulations as *s* above 4.2 mm are outside the validity range of IEM. However, as *L* increases, higher *s* can be used and the response in backscatter reflects what was observed in **Figure 4.5**.

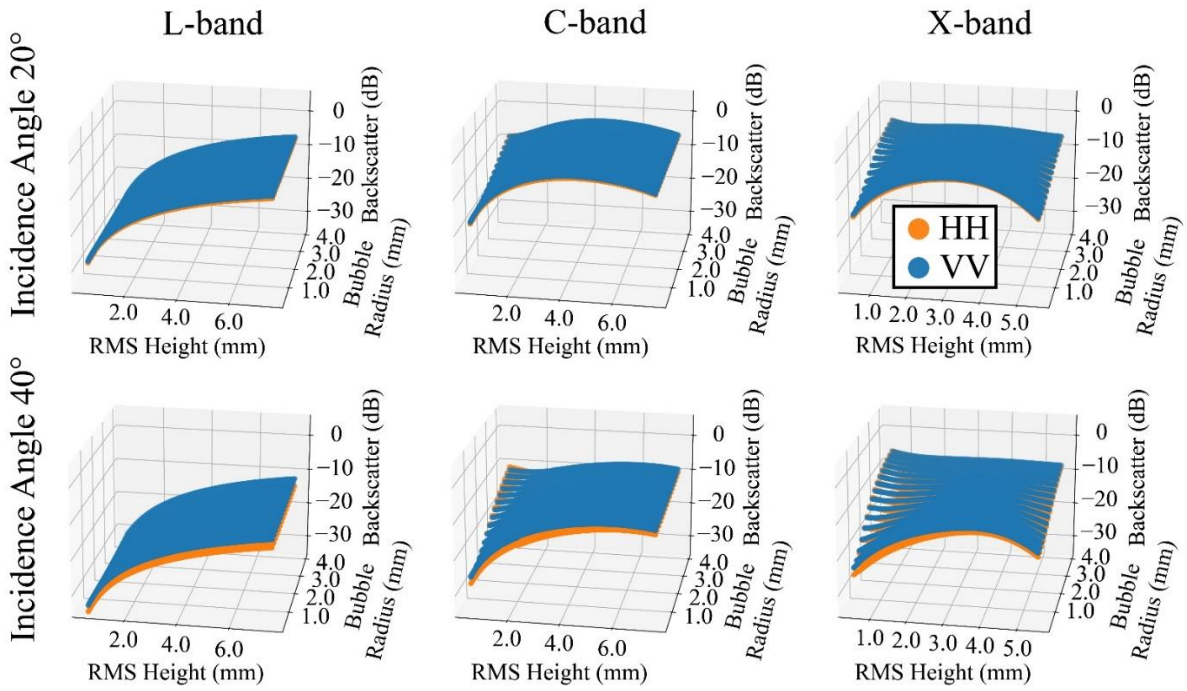

Figure 4.8 Change in backscatter with increasing both RMS height (*s*) and surface layer bubble radius size for the deep lake scenario with snow ice and snow cover.

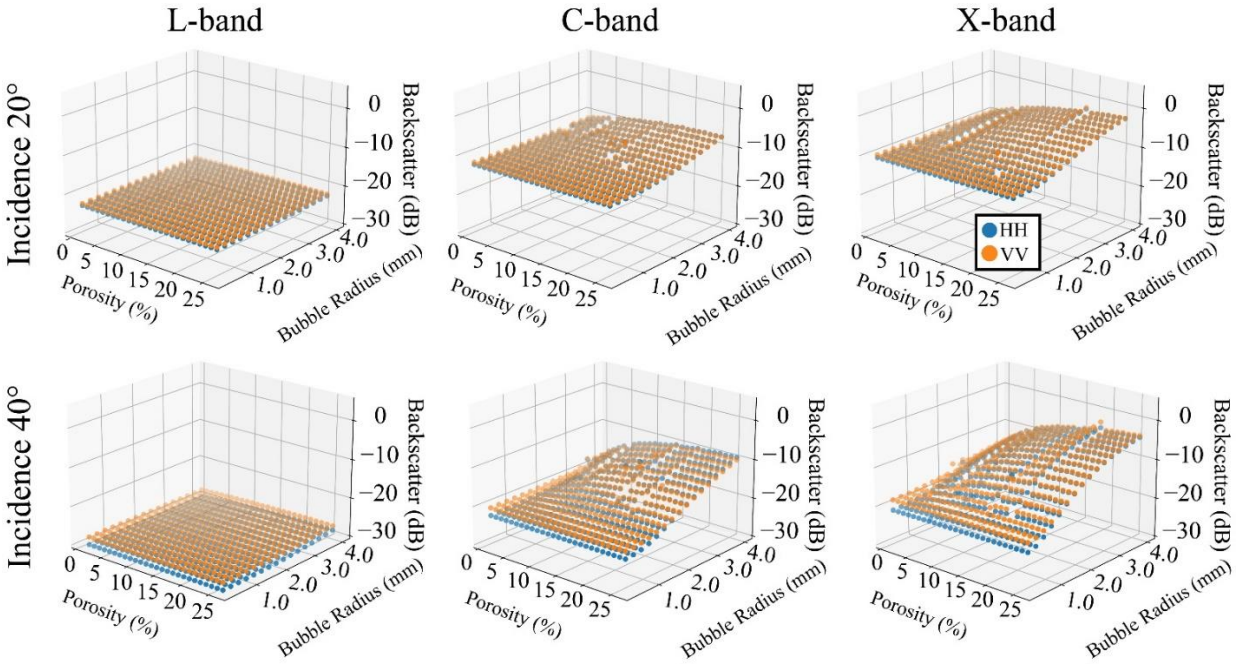

Figure 4.9 Change in backscatter with increasing both Porosity and surface layer bubble radius size for the deep lake scenario with snow ice and snow cover.

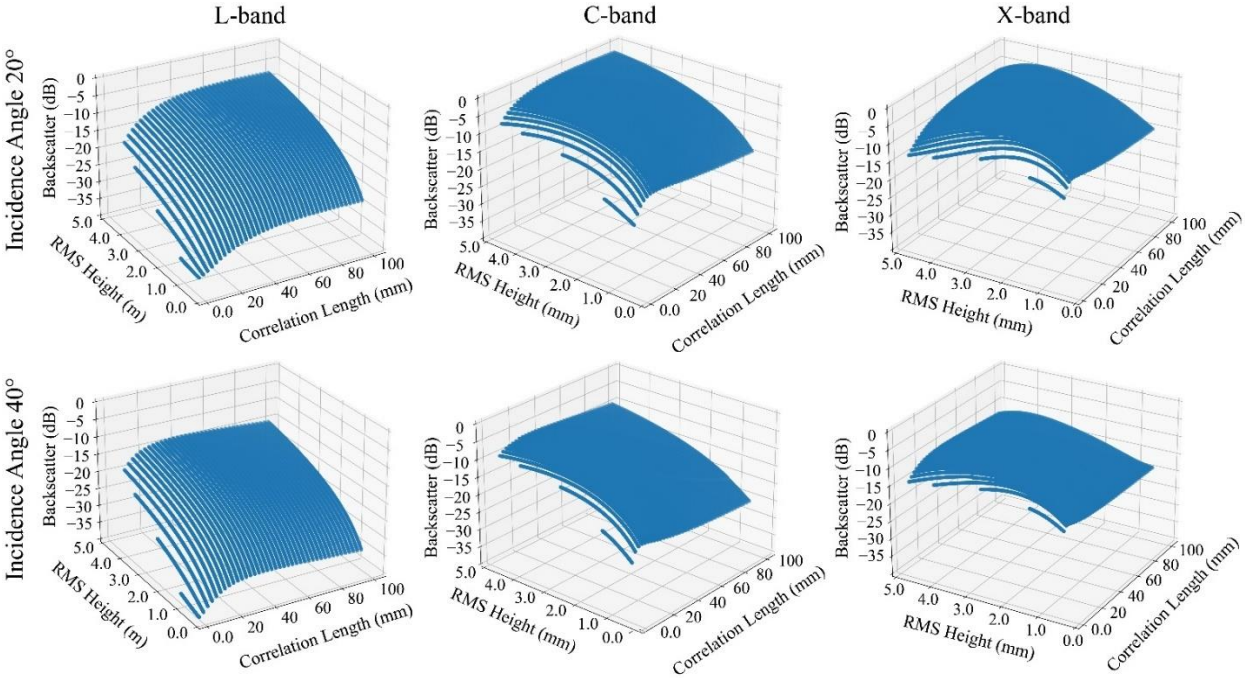

Figure 4.10 Change in backscatter with increasing both RMS height and correlation length for the deep lake scenario with snow ice and snow cover. Only VV-pol is shown to improve the interpretation of the backscatter response.

4.3.4 Backscatter Ratios and Lake Ice Properties

Co-pol ratios (VV/HH) and ratios between frequencies (C/L-band; X/L-band; X/C-band) are useful for discriminating between types of ice and between ice and water (Leconte et al., 2009; Antonova et al., 2016)A. Increasing porosity showed to have little impact on these ratios except for a slight increase in the co-pol ratio for X-band at an incidence angle of 40°. Therefore, these results focus on patterns for ice thickness, *s*, *L*, and bubble radius. Simulations were run using the same parameters outlined in **Section 4.2.4**, and ratios were calculated from the results shown in **Section 4.3.1** and **Section 4.3.2**. Frequency ratios at VV-pol and HH-pol were found to be similar, therefore, only VV-pol is focused on.

Increasing ice thickness results in a slight increase in the co-pol ratio for both C-band and X-band at the 40° incidence angle for both clear ice and snow ice scenarios. Increases in co-pol ratio also occur for shallow lake experiments at 20° when snow ice is present (**Figure 4.11**). However, while these patterns are observed, the magnitude of the changes for all experiments is small. Patterns in frequency ratios are more consistent with most experiments showing an increase with increasing ice thickness. For the deep lake experiments with snow ice there is a decrease in the ratio between X-band and C, L-band (**Figure 4.11**).

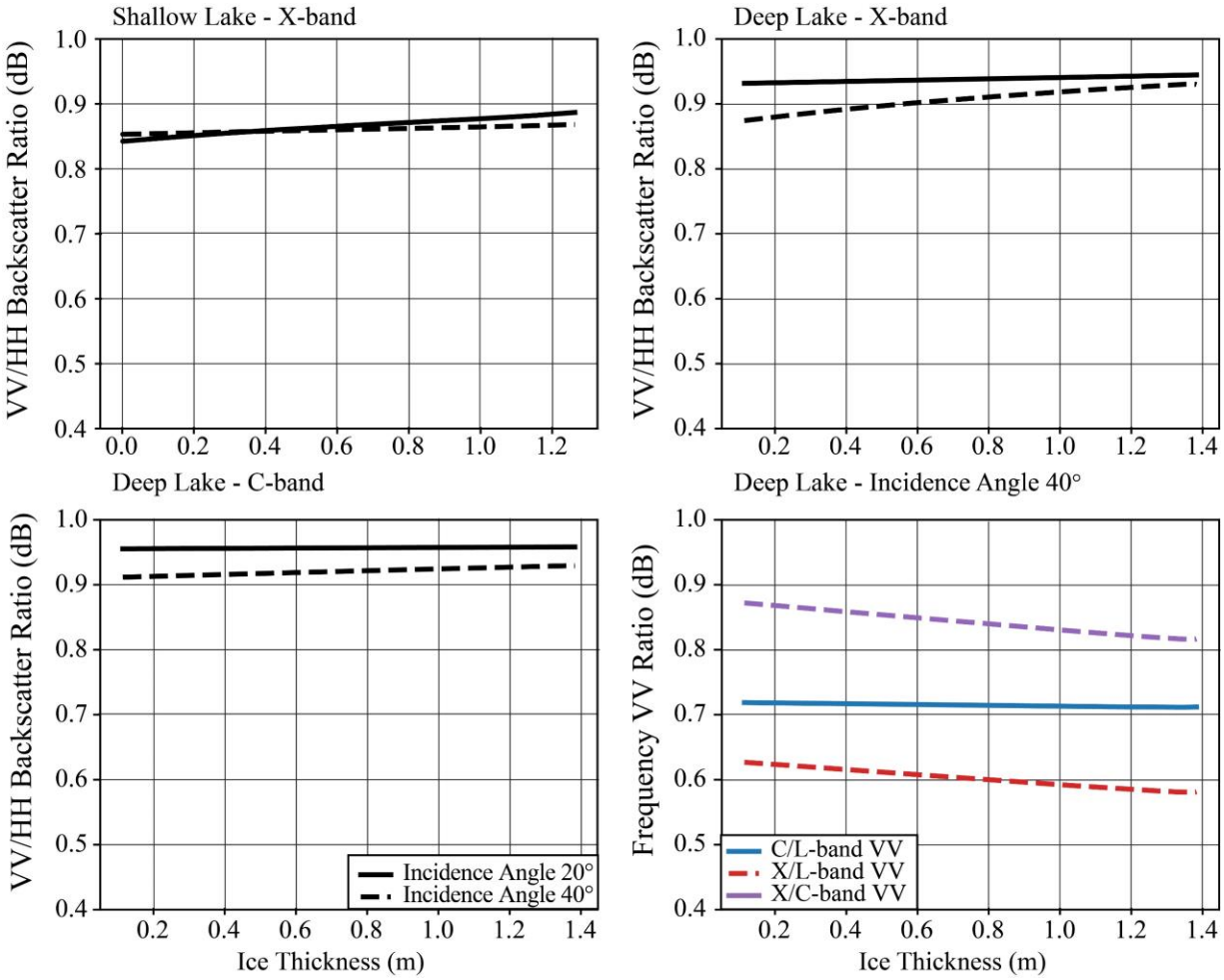

Figure 4.11 Co-pol and frequency ratios with increasing ice thickness for snow ice experiments. Examples highlight the key patterns observed in the results.

For *s*, co-pol ratios show different patterns depending on the frequency. However, the patterns observed are consistent for both shallow and deep scenarios. L-band shows a decrease in the co-pol ratio with increasing s, however, C- and X-band show a decrease followed by an increase at higher values of *s*. These patterns are consistent between incidence angles, yet co-pol ratios at an incidence angle of 20° are higher (**Figure 4.12**). Frequency ratios are similar between both deep and shallow lake experiments with ratios for 20° also being larger. All frequency ratios follow a similar pattern of initial decrease and then large increase as s increases. The key difference

is that the ratios between X/C-band and X/L-band increase at a faster rate and reach a higher maximum (**Figure 4.12**).

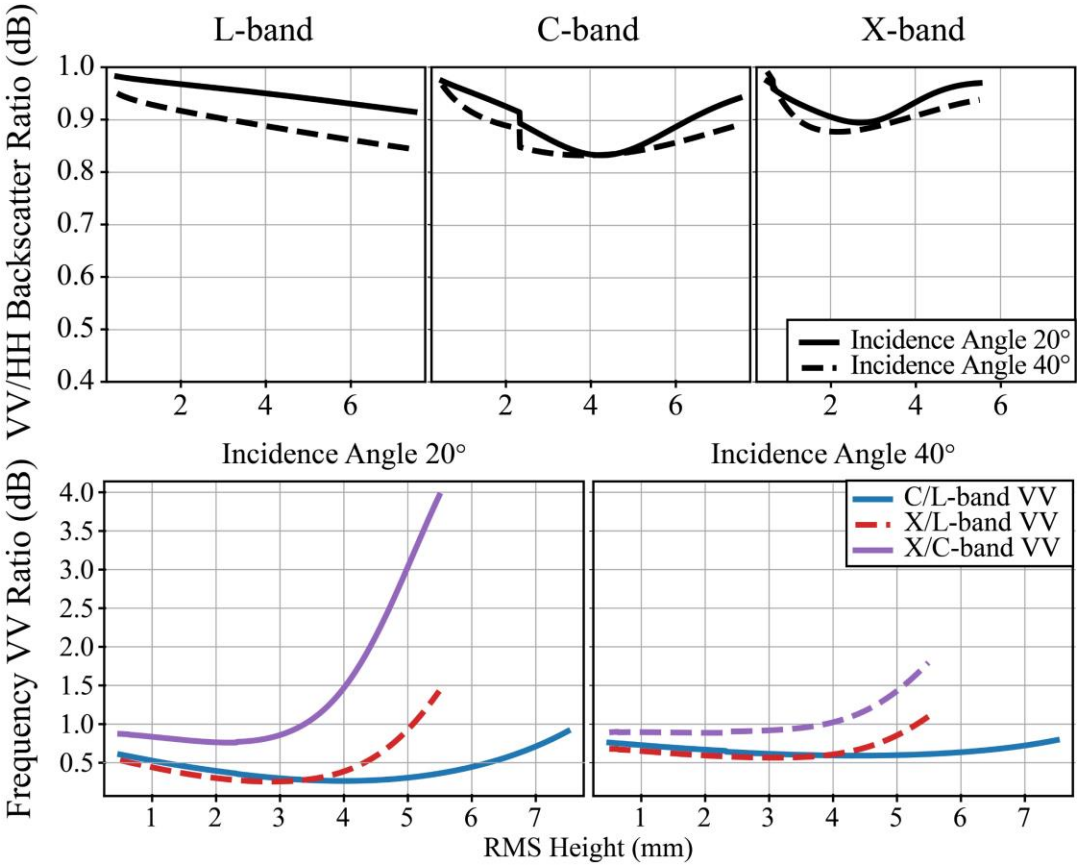

Figure 4.12 Co-pol and frequency ratios with increasing RMS height (*s*). Due to the similarity between shallow and deep lake experiments as well as snow and clear ice scenarios, only results from the deep lake snow ice scenarios are shown.

Co-pol ratios for *L* show similar patterns for shallow and deep lake experiments. There is an initial decrease that is followed by an increase that eventually saturates at a value of between 0.95 and 0.98 depending on the frequency (**Figure 4.13**). The key difference between the shallow and deep lake scenarios is that the increases and decreases for the shallow lake scenario are of a larger magnitude compared to the deep lake scenarios. Patterns for the 20° and 40° incidence angles are similar. Similar to ice thickness the magnitude of the changes for the co-pol ratios is

small. X/L and C/L frequency ratios show similar patterns between experiments. However, X/C ratios are slightly different with ratios for shallow lakes showing a small initial increase with increasing *L* followed by a plateau of the values. Deep lakes show a more gradual increase followed by a plateau of values at a larger magnitude compared to shallow lake experiments (**Figure 4.13**).

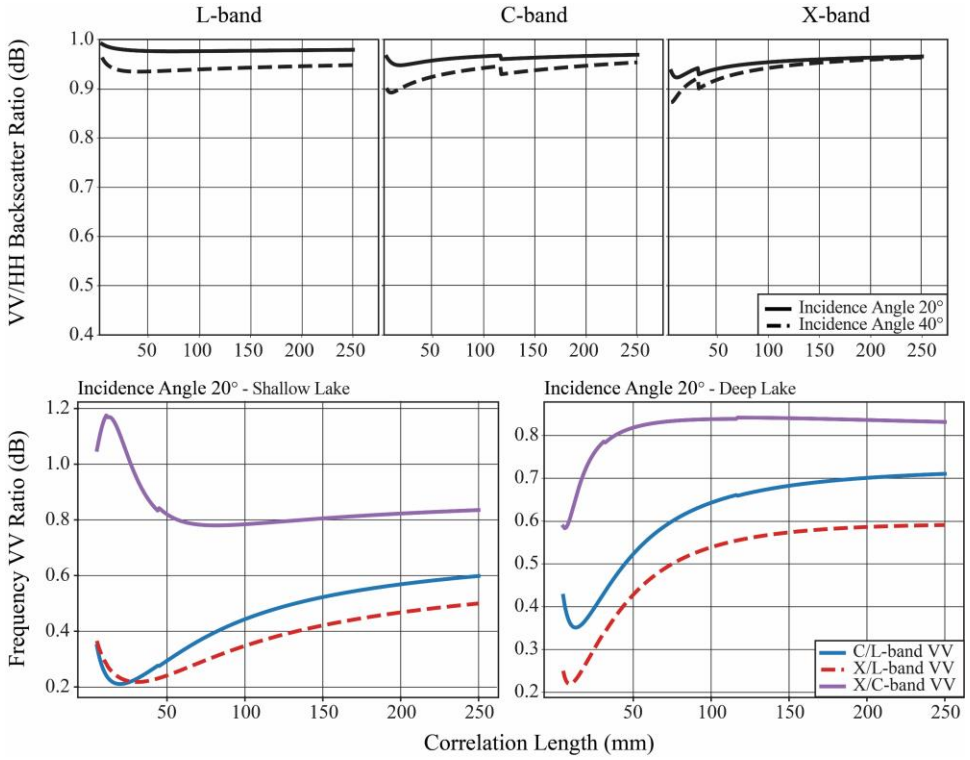

Figure 4.13 Co-pol and frequency ratios with increasing correlation length (*L*). Due to the similarity between shallow and deep lake experiments for co-pol ratios, only the results from deep lake experiments with snow ice are shown.

For bubble radius, co-pol ratios for L-band do show a limited increase with increasing bubble radius, except for the deep lake scenario at an incidence angle of 40° where the increase is more pronounced (**Figure 4.14**). Larger increases are observed for C and X-band, with the magnitude of values being higher for the deep lake experiments compared to shallow lake. One exception is X-band at 40° incidence angles which shows a decrease at very high bubble radii (>3

mm) (**Figure 4.14**). Most frequency ratio patterns show a decrease with increasing bubble radius. The highest magnitude of decrease occurs for the deep lake scenario at an incidence angle of 40°. However, the shallow lake experiment at an incidence angle of 20° shows a different pattern, with the frequency ratio increasing with increasing bubble radii (**Figure 4.15**).

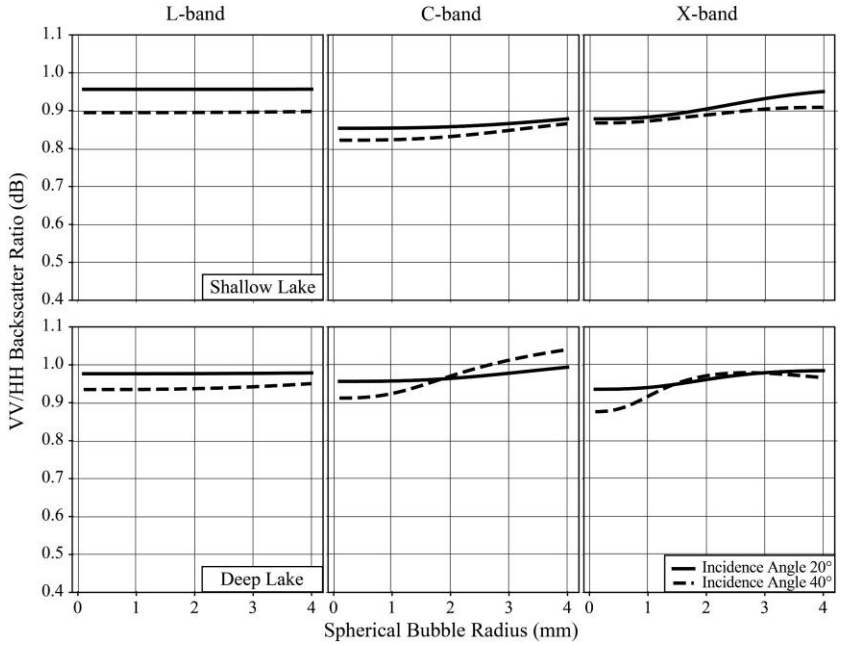

Figure 4.14 Co-pol ratios with increasing spherical bubble radius.

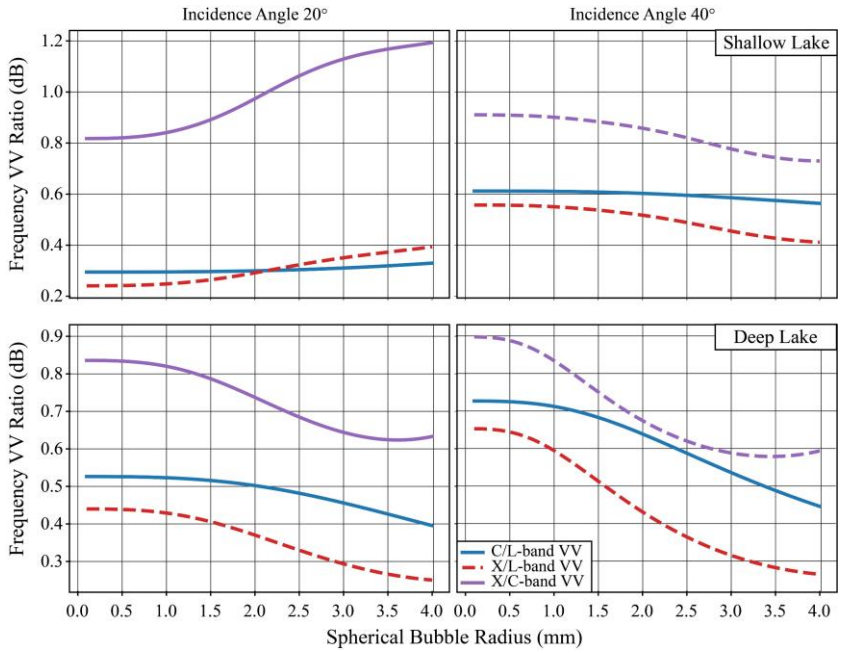

Figure 4.15 Frequency ratios with increasing spherical bubble radius.

4.4 Discussion

Section 4.4.1 and **Section 4.4.2** discusses the results presented above with a focus on the key properties identified, surface bubble radius and *s*. **Section 4.4.1** focuses on the role of surface bubble radius and **Section 4.4.2** focuses on the role of *s*. Correlation length is not discussed as the results showed that *s* is the more crucial component of ice-water interface roughness.

4.4.1 The Role of Surface Bubble Radius

Modelled backscatter from shallow and deep lakes showed differences in the response to the presence of surface bubbles and increasing radius. Shallow lakes showed limited response except for higher incidence angle X-band simulations with large bubble radii. This contrasts to the deep lake simulations that demonstrate an increased response across incidence angles and at lower bubble radii. The difference is likely explained by the *s* used for the two lakes. The shallow lake experiments used a higher *s* (3 mm) as the baseline to simulate the presence of tubular bubbles extruding at the ice-water interface as observed by (Gunn et al., 2018). For deep lakes experiments

a baseline *s* of 1 mm was used to reflect the absence of tubular bubbles. The higher *s* for shallow lake experiments shows itself as the dominant property that is reflected in the no/low NPC values for all other ice properties. The limited response for shallow lakes also explains the patterns observed in the co-pol and frequency ratios for thickness and bubble radius, where shallow lake experiments showed smaller magnitude responses to these changes in properties. On the other hand, for the deep lake scenario X-band shows a medium response to both *s* and bubble radius for HH-pol at an incidence angle of 40°. This is also shown in **Figure 4.14** and **Figure 4.15** where the deep lake experiments show a larger change in backscatter ratios with increasing bubble radius. The higher response in X-band experiments is likely due to scattering of the shorter wavelength by the surface bubbles (Leconte et al., 2009; Gunn et al., 2018). The increased response at a higher incidence angle is likely due to the increased travel distance compared to shallower incidence angles causing increased scattering. This is observed in previous modelling experiments that showed ice with small spherical air inclusions have a higher backscatter compared to clear ice (Gherboudj et al., 2010). The difference between these types of ice increases with shallower incidence angles and at higher frequencies (Gherboudj et al., 2010). Additionally, these conclusions are supported by past radiative transfer modelling experiments for the Tibetan Plateau that also identified bubble radius as one of two key factors for backscatter from lake ice (Tian et al., 2015). However, these results also indicate that bubble radius is only an important factor if snow ice is present and roughness is low. Otherwise, *s* remains the dominant factor. **Figure 4.5** and **Figure 4.7** indicate that X-band backscatter is likely a result of both bubbles in the ice and *s* of the ice-water interface, as larger bubble sizes cannot produce values in the upper range of typical observed backscatter.

Recent research has proposed models for estimating ice thickness from co-pol backscatter (Shokr & Dabboor, 2020), however, the NPC analysis suggests that a direct relation between increasing backscatter and ice thickness is unlikely. **Figure 4.16** shows the pattern in backscatter with increasing ice thickness for the deep lake clear ice and snow ice scenario. For the clear ice scenario backscatter decreases with increasing ice thickness. This decrease is expected due to results in past radiative transfer experiments which have attributed the decreasing backscatter to

an increase in the optical thickness of the ice (Gherboudj et al., 2010). Other past studies have demonstrated minimal change in backscatter with increasing ice thickness as well as an increase (decrease) in the extinction (transmission) coefficient of the medium as the ice thickens (Tian et al., 2015). However, if a layer of snow ice is added, backscatter at C and X-band frequencies appears to be increasing with thickening ice. Due to the pattern observed for clear ice, the increasing backscatter can be attributed to the presence of a thickening snow ice or increasing presence of bubbles within the ice, not directly to the thickening of the ice layer itself. However, it also demonstrates that while the addition of this layer results in an increase in backscatter, the response is minor at lower incidence angles. This experiment also does not consider changes in other surface properties (e.g., *s*). The increased response of X-band frequencies shown in multiple experiments (**Table 4.9**, **Figure 4.7**, and **Figure 4.8**) demonstrate that X-band is a valuable source for identifying surface ice types and understanding bubble characteristics within ice columns. This is supported by past research that has utilized this frequency for use in classifying surface ice types in the Northwest Territories (Gunn et al., 2017). Furthermore, co-pol ratios for X-band do show an increase with increasing thickness both with and without snow ice. While this could offer an alternative to estimating ice thickness, the overall magnitude of these changes is small. Therefore, further investigation of these patterns is needed using observations from X-band systems and is outside the scope of the current study.

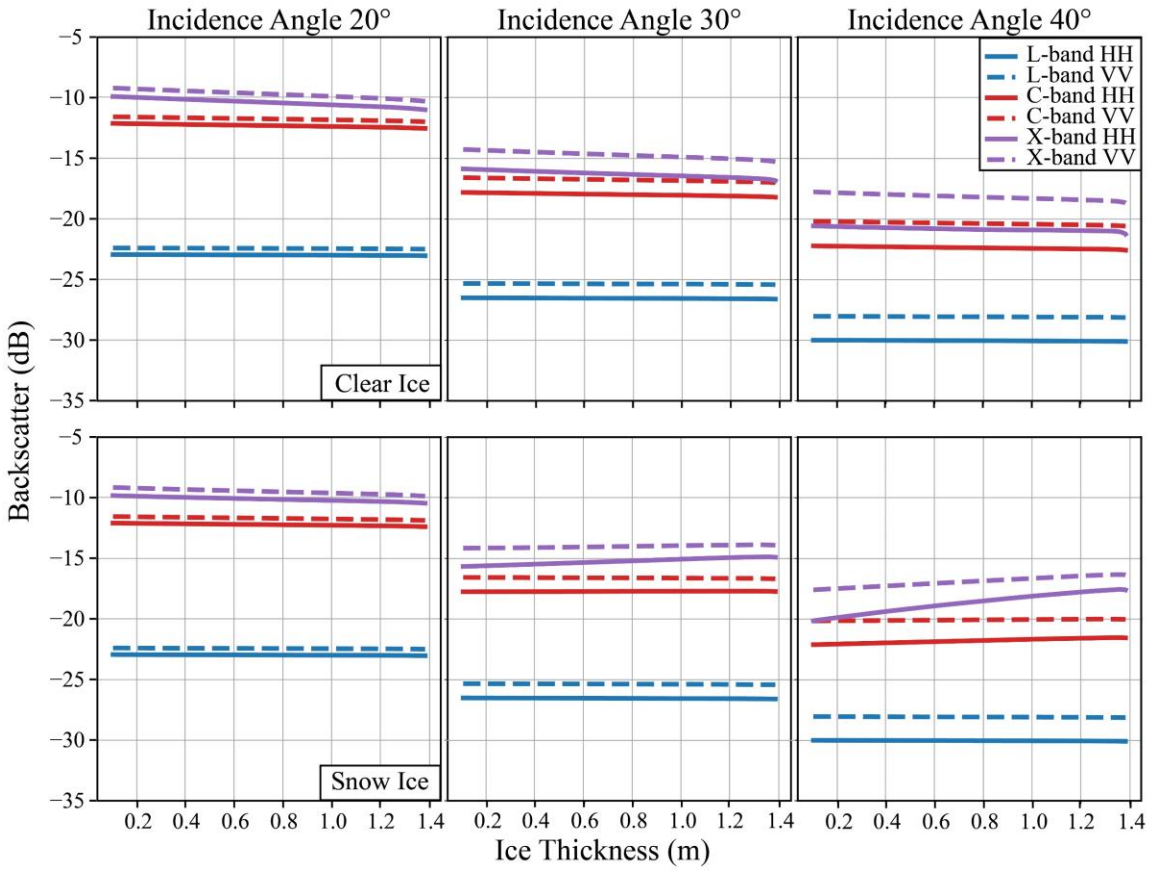

Figure 4.16 Change in backscatter with increasing ice thickness for clear ice and snow ice scenarios in the deep lake experiment.

4.4.2 The Role of RMS Height

The results of these experiments indicate that *s* of the ice-water interface is the key factor in backscatter response from lake ice for both shallow and deep lakes and for both tested ice columns backscatter increases with increasing RMS height. The behaviour of IEM results in a bell-shaped pattern as s increases, resulting in the observed decrease at C and X-band frequencies. At all frequencies, if IEM restrictions were ignored, increasing *s* results in an ensuing peak and decrease in backscatter. The value of *s* for when the peak occurs increases with larger incidence angles as seen for the X-band curves in **Figure 4.5**. At high s values, backscatter values for different incidence angles approach identical values (Fung & Chen, 2010). For L-band, HH NPC

values decrease with increasing incidence angle whereas VV NPC values increase. The decrease in HH NPC values is due to roughness having less of an impact on the HH backscatter at higher incidence angles compared to VV (Fung & Chen, 2010). Inconsistencies in NPC values between HH and VV-pol for L-band are caused by the snow having a small impact on the magnitude of change for the different scenarios. For C-band, both HH and VV NPC values decrease, this is due to the behaviour of IEM discussed above. This causes the backscatter for the smaller incidence angles to begin saturating and decreasing earlier, which lowers the average NPC value. X-band for both deep and shallow lake scenarios and C-band HH-pol for the deep lake scenario show a decrease in NPC values for s when snow ice is present. This is likely due to an increased sensitivity to the presence of spherical bubbles as mentioned in **Section 4.4.1**. This also helps explain the pattern in co-pol ratios observed in **Figure 4.12**. The high NPC values for modelled backscatter compared to other properties further support recent research that identified surface scattering at the ice-water interface as being the dominant scattering mechanism (Engram et al., 2012; Gunn et al., 2018) and aligns with other experiments that identified it as being a key lake ice parameter for modelling backscatter (Tian et al., 2015). This is also demonstrated through the comparison between the typical observed range in backscatter and modelling results shown in **Figure 4.5-7**. These comparisons show that *s* produces backscatter commonly in this range whereas *L* and bubble radius values typically lie on the lower end of the typical range or below.

Several criteria determined relative to the wavelength (λ) can be used to investigate the effectiveness of the roughness at a particular interface (van der Sanden & Drouin, 2011). One criterion is the Fraunhoffer criterion ($\sigma < \lambda/(32cos(\theta_i)$). When microwave signals pass through the ice medium the wavelength shortens due to increased permittivity, and the new wavelength can be found as (4.7),

$$\lambda = \frac{1}{\sqrt{\varepsilon'}} * \frac{c}{f} \quad \textbf{(4.7)}$$

where ε' is the real part of the complex relative permittivity of the respective medium (ε' for ice = 3.17), c is the speed of light in a vacuum (m s^{-1}), and f is the frequency of the signal (Hz). For L, C, and X-band the new wavelengths are 0.13 m, 0.03 m, and 0.02 m, respectively. Using these wavelengths, it is possible to determine criteria for a rough surface at different incidence angles based on the Fraunhoffer criterion (shown in **Table 4.10**). These thresholds show that the addition of a small amount of roughness (~1 mm) can result in increased backscatter at C and X-band. According to the Fraunhoffer criterion, L-band requires a larger s for a pronounced response (>4 mm), however, the presented results show that the addition of small amounts of roughness can result in substantial increases in backscatter when using the IEM model for the ice-water interface.

Table 4.10 RMS height thresholds for classifying a surface as rough according to the Fraunhoffer criteria.

	Incidence Angle 20°	**Incidence Angle 30°**	**Incidence Angle 40°**
L-band	4.4 mm	4.8 mm	5.4 mm
C-band	1.0 mm	1.1 mm	1.3 mm
X-band	0.6 mm	0.6 mm	0.7 mm

Past research has highlighted the evolution of backscatter throughout the ice season, with increasing backscatter earlier in the ice season and a plateau in backscatter as ice reaches maximum thickness (Jeffries et al., 1994; Duguay et al., 2002; Antonova et al., 2016). While bubble radius can partially explain this evolution pattern if snow ice is present (see **Section 4.4.1**), the results of the experiments in this study indicate that increasing s at the ice-water interface is the dominant mechanism as previously mentioned. This is reflected in the change in backscatter seen in **Figure 4.5**. From past observations of backscatter evolution throughout the ice season and the results observed in this study, it is likely that s changes more rapidly at the start of the ice season when rapid ice growth occurs and then plateaus once the rate of ice growth slows. As an example, for C-band where backscatter may increase by >10 dB throughout the ice season s could be expected to

increase by a magnitude of >1.5 mm. However, while other properties have less of an impact on backscatter there are still contributions that must be considered, and this could in turn impact the amount of change in *s*. This may also depend on the presence or absence of tubular bubbles and incidence angle of the imagery. The results of this analysis indicate that to properly evaluate the roughness of lake ice, C and L-band frequencies are the most appropriate. L-band is of key importance as it shows less sensitivity to other properties such as bubble radius. However, C-band is also valuable due to its availability on numerous satellite platforms (i.e., Sentinel-1, RADARSAT-2, RCM). These results demonstrate the importance of developing methods of retrieving ice-water interface roughness. While values exist for river ice, it is important to note that river ice-water interface roughness is typically assumed to decrease throughout the ice season due to the erosion action on the bottom of the ice surface or is assumed constant for forward modelling purposes (Michel, 1971; Gherboudj et al., 2010; Lindenschmidt & Li, 2018). For lake ice bottom interfaces, a decrease in roughness is unlikely unless there is a maintained inflow into the lake throughout the winter season.

4.5 Conclusion

These are the first published experiments using the snow microwave radiative transfer (SMRT) model to investigate imaging radar backscatter from lake ice and the first to integrate a radiative transfer model and thermodynamic lake model. Using the Canadian Lake Ice Model (CLIMo), a 20-year average ice season was produced for a shallow lake (tubular bubbles present) and a deep lake (no tubular bubbles present). The resulting ice thickness and temperature values were used to parameterize SMRT, with other previously observed values, to investigate how changes in ice thickness, bubble radius, RMS height, correlation length, and porosity would impact backscatter. SMRT simulations were conducted using simulated L, C, and X-band sensors at 20°, 30°, and 40° incidence angles.

The results showed that backscatter had limited response to ice thickness and layer porosity. The experiments demonstrate that backscatter is most responsive to increases in *s* and highest for L and C-band frequencies with VV-polarization. This supports recent observations that

indicate that lake ice is dominated by a single/surface bounce scattering mechanism at the ice-water interface (Engram et al., 2013; Gunn et al., 2018). Additionally, while L-band shows a high response to increasing *L*, it is limited for other frequencies. The response to *s* at the ice-water interface varies with incidence angle and is influenced by the selected roughness model (IEM) and properties of surface ice (i.e., bubble radius) for higher frequencies (X-band). X-band responds to increases in *s*, but this response decreases at higher incidence angles and the frequency becomes more responsive to increases in surface bubble radius or other scatterers such as snow. This demonstrates that X-band is useful for identifying surface ice types as noted in past research (Gunn et al., 2017). Additionally, results show that increases in backscatter are likely not a result of increasing ice thickness but are due to changes that occur in ice properties (i.e., bubble radius and *s*) throughout the ice season. This indicates that it may not be possible to retrieve ice thickness using only SAR total backscatter due to the limited response. Co-pol ratios do show some evidence of response to changes in ice thickness, however, due to the small magnitude of change further investigation is needed to confirm this interaction.

These results provide us with an initial understanding of how to utilize SMRT for modelling backscatter from lake ice and a better understanding of the importance of determining methods of effectively measuring ice-water interface roughness changes throughout the ice season. These sensitivity experiments and comparisons to typical ranges in backscatter also serve as a helpful baseline for exploring the inversion of SMRT for retrieving ice properties such as bubble radius, *L*, and *s*. Future research should investigate cross-polarization with future iterations of SMRT. Additionally, exploration of the contribution of individual scattering components in SMRT would further understanding about the contribution of different layers in the ice-column and the role of different interfaces. The next steps in this research are to use field data to parameterize SMRT and perform forward modelling of backscatter throughout an ice season and compare with backscatter measurements from spaceborne imaging SAR (e.g., RADARSAT-2, TerraSAR-X, ALOS-PALSAR).

Chapter 5
Forward Modelling of Synthetic Aperture Radar Backscatter from Lake Ice over Canadian Subarctic Lakes

5.1 Introduction

Lakes form a critical component of the Arctic and Subarctic landscape, ranging in areal coverage from 15 to 40% depending on location (Duguay et al., 2003). Lakes in these landscapes can form annual or perennial ice coverage that in turn impacts the surrounding energy balance and climate (Rouse et al., 2008; L. C. Brown & Duguay, 2010). The presence of lake ice is also important for social and economic activities across the Northern Hemisphere. Eighty-five percent of the Tibbitt to Contwoyto Winter Road is built over ice; more than 3800 tonnes of material were hauled across this road during the winter of 2020 and the road construction relies on the presence of thick and stable ice cover (Mullan et al., 2017; Tibbitt to Contwoyto Winter Road Joint Venture, 2020). Additionally, lake ice serves as a key travel route both to and between northern communities, allowing for the transport of goods during winter months (Knoll et al., 2019). However, since the 1980s there has been a decline in ground observations of both lake and river ice within the Northern Hemisphere, falling from the peak of observations occurring on 1046 lakes to an average of 165 per year between 2010 and 2020 (Benson et al., 2013; Murfitt & Duguay, 2021).

With the loss of extensive ground records there has been a shift to the use of remote sensing for studying and monitoring lake ice (Duguay et al., 2015). Optical remote sensing is primarily used to monitor ice phenology with recent literature showing high accuracy through the use of machine learning algorithms (Wu et al., 2021). However, these data are dependent on reflected sunlight from the Earth's surface and can be restricted by cloud cover and polar darkness (Wu et al., 2021). Passive microwave data are used to monitor both ice phenology (Du et al., 2017; Cai et al., 2022) and lake ice thickness (Kang et al., 2014), however, the coarse spatial resolution on the scale of kilometers per pixel limits the use of these data to larger lakes. Active microwave

remote sensing has been a key technology over the past 50 years for the study of lake ice, with synthetic aperture radar (SAR) being heavily relied on for both monitoring the presence of lake ice and investigating lake ice properties, as reviewed by (Murfitt & Duguay, 2021). Imaging SAR data have been used in combination with machine learning algorithms to monitor the presence of lake ice cover (K. A. Scott et al., 2019; M. Hoekstra et al., 2020) and the timing and distribution of ice frozen to the lake bed (grounded ice) (Surdu et al., 2014; Antonova et al., 2016; Engram et al., 2018). SAR sensors provide images independent of cloud conditions, at any time of day, and can provide resolutions ranging from 3-100 m allowing for the delineation of small and medium-sized lakes.

Pioneering research observing ice-covered lakes using a combination of X-band (frequency) side looking airborne RADAR (SLAR) and field data suggested that the RADAR response from lake ice was driven by the presence of tubular bubble inclusions in the lower layers of the ice which resulted in a double bounce scattering mechanism whereby forward scatter occurred off the tubular bubble, and subsequently reflecting off the high dielectric contrast ice-water interface (Weeks et al., 1981). This work was further supported by a combination of C-band (frequency) SAR satellite imagery and field measurements from lakes on the Alaskan Coastal Plain (Jeffries et al., 1994). However, current literature has found that the SAR response to lake ice is more dominated by a scattering mechanism due to roughness at the ice-water interface (Engram et al., 2012; Atwood et al., 2015; Gunn et al., 2018). This mechanism has been identified for multiple frequencies (L-band, X-band, and C-band) and demonstrated through co-pol phase difference analysis (Atwood et al., 2015), polarimetric decomposition (Engram et al., 2012, 2013; Atwood et al., 2015; Gunn et al., 2018), and numerical modelling (Atwood et al., 2015). The presence of bubbles at the ice-water interface is one cause of roughness. For many shallow lakes in Alaska methane ebullition bubbles at the bottom of the ice create pockets or areas where the ice grows at a slower rate, resulting in enhanced roughness (Engram et al., 2012, 2013). Roughness of the ice-water interface for ice cover of shallow lakes in Manitoba, Canada, is attributed to the extrusion of tubular shaped bubbles at the ice-water interface, resulting in local variations in roughness (Gunn et al., 2018). It has also been suggested that large scale variations in roughness

could be caused by differences in snow depth that in turn impact the rate of ice growth (Gunn et al., 2018).

Numerical radiative transfer (RT) models have been used to explore various aspects of lake ice and active microwave interactions. Numerical models were used to explore the differences in response between floating and grounded ice covers during the ice season and spring melt (Wakabayashi et al., 1994, 1999). Numerical RT models, including the integral equation model (IEM) (Fung et al., 1992), multilayer dense media-radiative transfer (DMRT-ML) under the quasi crystalline approximation (QCA), and a dense discrete medium scattering model (Ewe et al., 1998), were used to explore the impact of different ice properties (i.e., bubble radius, ice thickness, snow cover, and ice-water interface roughness) on SAR backscatter and scatterometer data (Matsuoka et al., 1999; Atwood et al., 2015; Tian et al., 2015). The results of recent modelling studies support other results using polarimetric decomposition and indicating that the impact of tubular bubbles at the ice-water interface on double-bounce interactions have a limited, if not negligible, impact on backscatter from lake ice (Atwood et al., 2015; Tian et al., 2015). Instead, these recent studies highlight the importance of ice-water interface roughness.

While backscatter models have been used as a tool to explore the interaction between lake ice and various ice properties, limited experiments focus on modelling backscatter evolution / time-series throughout an ice season (e.g. Gunn et al., 2015; Tian et al., 2015). Past research used approaches with limited descriptions of the medium or of the number of scattering mechanisms considered (e.g., limited inclusion of snow, shape of air inclusions, and ignoring interface roughness), however, more detailed modelling is now feasible. Furthermore, modelling of imaging SAR backscatter throughout an ice season has typically focused on a single polarization or frequency (Wakabayashi et al., 1994; Tian et al., 2015). The increased importance of ice-water interface roughness and the evidence of increasing ice-water interface roughness throughout the ice season also need to be accounted for within these models (Gunn et al., 2018). Lastly, past research has highlighted differences in backscatter between shallow and deep lakes (Morris et al., 1995), however, deep lakes have been largely ignored in the exploration of ice-water interface

roughness and within radiative transfer modelling. Due to the depth of these lakes, tubular bubble formation is limited (Mellor, 1982) and different considerations must be made from a modelling perspective. This study works to address these areas using the Snow Microwave Radiative Transfer (SMRT) model to simulate backscatter from two Subarctic lakes located in Canada. Noell Lake in the Northwest Territories will focus on modelling C-band data for the 2018-2019 ice season and Malcolm Ramsay Lake in Manitoba will focus on modelling multi-frequency data (L, C, and X-band) for the 2009-2010 ice season. There are two objectives to this study: 1) determine optimal ice-water interface roughness values throughout the ice season for both lakes within the SMRT framework; 2) identify limitations in modelling backscatter from lake ice throughout an ice season within the SMRT framework; and 3) provide recommendations for considerations with further modelling of backscatter from lake ice within the SMRT framework.

5.2 Methods

5.2.1 Snow Microwave Radiative Transfer Model

The snow microwave radiative transfer (SMRT) model is used to conduct forward modelling simulations in this study. A full description of this open-source model can be found in Picard et al. (2018). SMRT is a radiative transfer model that simulates both active microwave and passive microwave signals from snowpacks. The model also allows for the inclusion of subnivean freshwater and saline ice layers (Murfitt et al., 2022; Soriot et al., 2022). SMRT is run within a Python environment and includes a number of electromagnetic (e.g. improved Born approximation (IBA) and DMRT) and microstructure models (e.g. autocorrelation, exponential, sticky hard spheres) for user flexibility (Picard et al., 2018; Picard, Löwe, Domine, et al., 2022). The model determines the necessary electromagnetic quantities (scattering coefficient, absorption coefficient, and phase matrix) for each layer from user defined settings that include the selection of an electromagnetic model, microstructure model, and layer parameters (temperature, thickness, density/porosity, liquid-water content, grain size) (Picard et al., 2018). Roughness of interfaces and substrate components within the model are set using the Fresnel equations (Picard et al., 2018), the integral equation model (IEM) (Fung et al., 1992), or Geometrical Optics (Tsang & Kong,

2001) that determine the reflectivity and transmittivity coefficients. The user can define a customized passive or active sensor with specific frequency, incidence angle, and polarization or choose from a list of pre-built sensors. For this study, only co-polarizations are evaluated as cross-polarized data are underestimated with the current implementation of IEM in SMRT. When the necessary parameters are defined, the discrete ordinate and eigenvalue (DORT) method is used to solve the radiative transfer equation providing the user with the emerging intensity in all or specific directions from the specified snowpack/ice column (Picard et al., 2018).

For the purposes of this study, the dense media radiative transfer (DMRT) theory with Quasi-Crystalline Approximation-Coherent Potential (QCACP) short range (Tsang et al., 1985; Picard et al., 2013) is used for the electromagnetic model. One limitation of this model in SMRT is that bubbles can only be represented as spheres. Additionally, for DMRT QCACP as implemented in SMRT, the k_0a (k_0 is the wavenumber and a is the radius) must be less than 0.6. When k_0a is in this range, the resultant backscatter from SMRT is equivalent to other electromagnetic models (Picard, Löwe, & Mätzler, 2022). Sticky Hard Spheres (SHS) is used as the microstructure model. Stickiness (τ) is a required parameter for SHS and controls how spheres within the medium stick to each other; lower values result in stickier spheres (Picard et al., 2018). For roughness of both the snow-ice and ice-water interface, IEM with an exponential autocorrelation function was selected because it is suited to smaller roughness values and has been used for previous freshwater ice modelling (Wakabayashi et al., 1999; Gherboudj et al., 2010). IEM is parameterized using two properties; root mean square height (will be referred to as RMSH for the remainder of the study) and correlation length. RMSH is the approximation of the vertical variation of surface roughness and correlation length is the horizonal variation in roughness or displacement between two points on the surface (Ulaby & Long, 2014). IEM is valid when $k*RMSH < 2$ and $k^2 * RMSH * Correlation\ Length < \sqrt{eps_r}$, where k is the wavenumber and eps_r is the ratio between the permittivity of the mediums at the interface (Fung et al., 1992; Fung & Chen, 2010). SMRT allows for an extension of this final limitation using the formulas stated in Brogioni et al. (2010), where the Fresnel coefficients are determined using either the incidence

angle ($k^2 * RMSH * Correlation\ Length < \sqrt{eps_r}$) or an angle of 0° ($k^2 * RMSH * Correlation\ Length > \sqrt{eps_r}$). While this extension was first introduced for Advanced IEM (AIEM), it can be used for IEM. Caution should be used when applying this extension as the precise validity on the original IEM is supposed according to physical principle but unverified quantitatively.

5.2.2 Study Sites

To evaluate SMRT for forward modelling of SAR imaging backscatter from lake ice two Subarctic lakes were selected, Malcolm Ramsay Lake and Noell lake. These two lakes represent ice conditions with and without tubular bubbles. Noell Lake (68.53°, -133.56°, **Figure 5.1**) is located north of Inuvik in the Northwest Territories, Canada. Climate normals (1981-2010) from the closest Environment and Climate Change Canada weather station located at the Inuvik Airport (68.3°, -133.49°) show daily temperatures reach a maximum average of 14.1 °C in July and an average minimum of -26.9 °C in January (ECCC, 2021a). Most precipitation is received as snow between September and May with climate normals showing a total of 158.6 cm of snowfall (ECCC, 2021a). Noell Lake is located in a Tundra ecological zone with little to no tree cover and primarily dominated by short shrubs and willows (Ogbebo et al., 2009). The average depth of the lake is 6 m and is characterized by three larger depressions in the southwest and northeast; the deepest of these depressions is in the southwest and can reach a maximum of 18 m (Paquette-Struger et al., 2018). The depths of Noell Lake result in the absence of tubular bubble formation due to the water column not becoming saturated with gases in the main basin of the lake, this is confirmed by footage taken under the ice and ice cores extracted in March 2019. During the 2019 ice season surface snow ice containing small spherical bubbles was observed across the lake.

Malcolm Ramsay Lake (58.72°, -93.79°, **Figure 5.1**) is located east of Churchill Manitoba, Canada. Climate normals from the Churchill Airport weather station (58.74°, -94.07°) indicate the maximum average temperature occurs in July (12.7 °C) and the minimum average temperature occurs in January (-26 °C) (ECCC, 2021b). Snowfall occurs between September and June, with the maximum average snowfall in November at 39.2 cm (ECCC, 2021b). Churchill and

the surrounding area are located at the interaction of three ecoregions, boreal forest, tundra-boreal transition, and tundra (P. A. Scott et al., 1987). The mean depth of Malcolm Ramsay Lake is 2.4 m; the shallower depth of this lake results in the formation of a dense tubular bubble layer as shown in ice cores extracted from the lake during the 2009-2010 ice season (Duguay & Lafleur, 2003; Gunn et al., 2018). During the 2009-2010 ice season surface grey and snow ice with small spherical bubbles was also noted (Gunn et al., 2018).

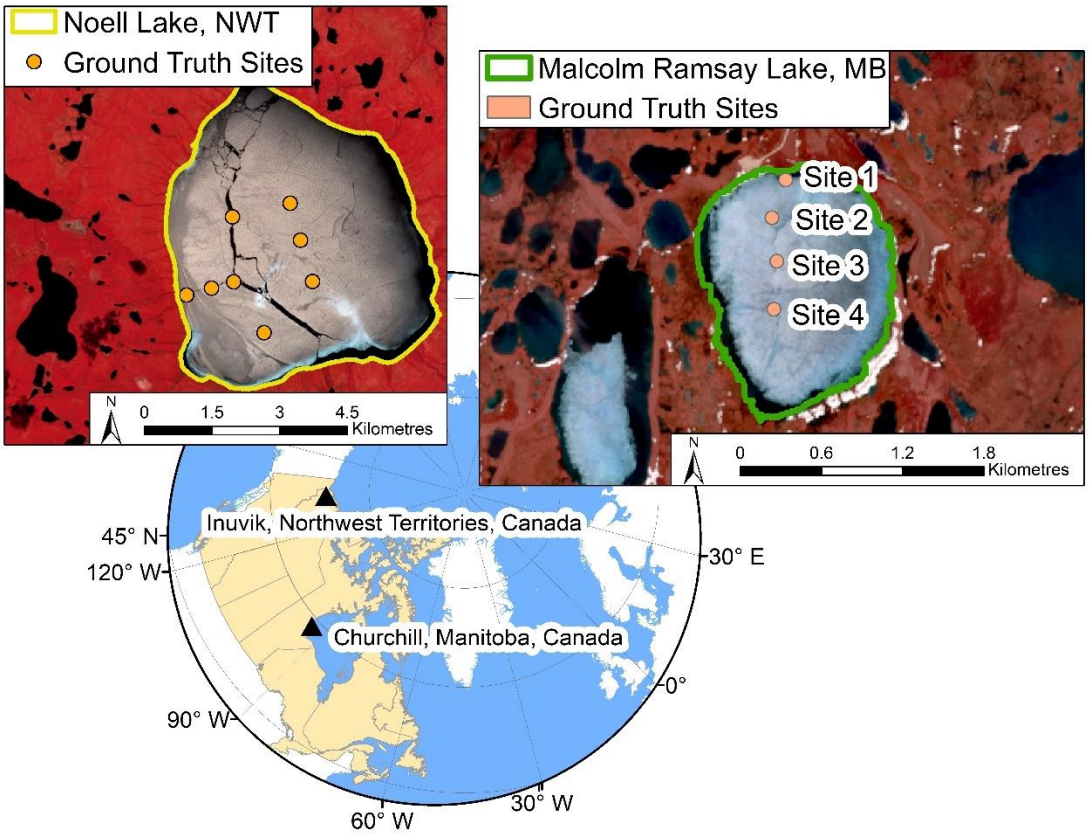

Figure 5.1 Location of the selected test lakes. The orange circles on both maps show the locations of field measurements taken during the respective field campaigns. This figure contains Copernicus Sentinel-2 data [2019, 2020], processed by the ESA.

5.2.3 SAR Imagery

5.2.3.1 Noell Lake Acquisitions

SAR imagery was acquired for both lakes to serve as validation of the results of the SMRT forward modelling. Two sets of SAR imagery were acquired for Noell Lake. First, 24 Wide Fine Quad-pol RADARSAT-2 images were obtained between October 17, 2018, and June 01, 2019. Images were obtained at three different swath positions: FQ2, FQ6, and FQ19 with mean projected incidence angles of 39°, 21°, and 27° respectively (**Table 5.1**). These images were preprocessed using the Sentinel Application Platform (SNAP, European Space Agency, 2020), with images being σ° calibrated and speckle filtered with the Refined Lee filter (Lee, 1981). Terrain correction was performed on the images using the 2 m resolution ArcticDEM (Porter et al., 2018) and images were resampled to a pixel spacing of 13 m.

Table 5.1 RADARSAT-2 Image Acquisitions for Noell Lake

Acquisition Data/Time	Swath Position/Mean Incidence Angle	Acquisition Data/Time	Swath Position/Mean Incidence Angle
2018-10-17 02:22:12 UTC	FQ19W – 39°	2019-03-10 02:21:59 UTC	FQ19W – 39°
2018-10-24 15:55:54 UTC	FQ02W – 21°	2019-03-17 15:55:41 UTC	FQ02W – 21°
2018-11-10 02:22:10 UTC	FQ19W – 39°	2019-03-21 02:01:07 UTC	FQ06W – 27°
2018-11-17 15:55:52 UTC	FQ02W – 21°	2019-04-03 02:21:58 UTC	FQ19W – 39°
2018-12-04 02:22:08 UTC	FQ19W – 39°	2019-04-10 15:55:40 UTC	FQ02W – 21°
2018-12-11 15:55:51 UTC	FQ02W – 21°	2019-04-14 02:01:07 UTC	FQ06W – 27°
2018-12-28 02:22:04 UTC	FQ19W – 39°	2019-04-27 02:21:58 UTC	FQ19W – 39°
2019-01-04 15:55:48 UTC	FQ02W – 21°	2019-05-04 15:55:39 UTC	FQ02W – 21°

2019-01-21 02:22:03 UTC	FQ19W – 39°	2019-05-08 02:01:06 UTC	FQ06W – 27°
2019-01-28 15:55:46 UTC	FQ02W – 21°	2019-05-21 02:21:57 UTC	FQ19W – 39°
2019-02-14 02:22:00 UTC	FQ19W – 39°	2019-05-28 15:55:38 UTC	FQ02W – 21°
2019-02-21 15:55:42 UTC	FQ02W – 21°	2019-06-01 02:01:04 UTC	FQ06W – 27°

Secondly, to extend the record of SAR imagery for Noell Lake during the 2018-2019 ice season, 128 Sentinel-1 images (**Table 5.2**) were downloaded from the Alaska Satellite Facility (https://asf.alaska.edu/). To provide the most complete record possible, a combination of both Extra Wide (EW) and Interferometric Wide (IW) swath images were acquired, with the revisit time between acquisitions ranging from 0 to 10 days. SNAP was used to perform preprocessing steps that included thermal noise removal, σ° calibration, and Refined Lee speckle filtering. Terrain correction was also performed using the ArcticDEM 2 m product (Porter et al., 2018) and EW images were resampled to a pixel spacing of 40 m and IW images to a spacing of 10 m. These resolutions were set to preserve the original pixel spacing of the acquisitions. Sentinel-1 and RADARSAT-2 images were visually assessed to ensure alignment of the lake shoreline.

Table 5.2 Sentinel-1 Image Acquisition Totals, Date Ranges, and Average Gap Between Images for Noell Lake

Extra Wide Swath (HH+HV)			**Interferometric Wide Swath (VV+VH)**		
Incidence Angle (°)	**Date Range**	**Number of Images (Date Gap)**	**Incidence Angle (°)**	**Date Range**	**Number of Images (Date Gap)**
22	2018-10-09 to 2019-05-01	18 (12 days)	31	2018-10-18 to 2019-06-03	9 (29 days)
33	2018-10-29 to 2019-05-03	29 (7 days)	41	2018-10-28 to 2019-06-01	14 (17 days)

39	2018-10-18 to 2019-04-28	29 (7 days)	
43	2018-10-31 to 2019-05-05	29 (7 days)	

5.2.3.2 Malcolm Ramsay Lake Acquisitions

While imagery from Noell Lake focused on C-band, data from multiple sensors were acquired for Malcolm Ramsay Lake to support multifrequency analysis. Eleven fine beam quad-pol RADARSAT-2 images for Malcolm Ramsay Lake were acquired between November 20, 2009, to April 13, 2010 (**Table 5.3**). Images were acquired over a number of swath positions with a diversity of incidence angles, FQ01 (19°), FQ11 (31°), FQ18 (38°), and FQ21 (41°). Images were preprocessed using SNAP and were σ° calibrated, speckle filtered using the Refined Lee Filter, and terrain corrected using the Shuttle Radar Topography Mission 1-sec DEM (NASA JPL, 2013) to a pixel spacing of 14 m, because ArcticDEM does not extend below 60° latitude.

Table 5.3 RADARSAT-2 Image Acquisitions for Malcolm Ramsay Lake

Acquisition Time RADRSAT-2	**Swath Position/Mean Incidence Angle**
2009-11-20 23:49:21 UTC	FQ11 – 31°
2009-12-14 23:49:20 UTC	FQ11 – 31°
2009-12-18 00:01:50 UTC	FQ21 – 41°
2010-01-07 23:49:21 UTC	FQ11 – 31°
2010-01-28 23:36:50 UTC	FQ01 – 19°
2010-02-10 23:57:40 UTC	FQ18 – 38°

2010-02-21 23:36:51 UTC	FQ01 – 19°
2010-02-24 23:49:20 UTC	FQ11 – 31°
2010-03-20 23:49:21 UTC	FQ11 – 31°
2010-03-24 00:01:52 UTC	FQ21 – 41°
2010-04-13 23:49:22 UTC	FQ11 – 31°

Smaller sets of L and X-band imagery were available for Malcolm Ramsay Lake during the 2009-2010 ice season (**Table 5.4**). TerraSAR-X images were acquired between January 7, 2010, and February 24, 2010, at incidence angles of 33° and 43° to provide VV X-band data for Malcolm Ramsay Lake. These images were processed using SNAP and were σ° calibrated, speckle filtered using the Refined Lee Filter, and terrain corrected using the Shuttle Radar Topography Mission 1-sec DEM (NASA JPL, 2013) to a pixel spacing of 5 m. ALOS-PALSAR imagery was acquired between January 5, 2010, and April 7, 2010, at incidence angles of 37° and 39° to provide HH L-band data. To ensure accuracy of the PALSAR images, the Alaska Satellite Facility radiometrically terrain corrected (RTC) product was used (ASF DAAC, 2015). This is a preprocessed product that has been calibrated, multi-looked, co-registered, and terrain corrected to a pixel spacing of 12.5 m. Due to the high location accuracy of this product it is also used as reference imagery to ensure consistency between other images for Malcolm Ramsay Lake.

Table 5.4 TerraSAR-X and ALOS-PALSAR Image Acquisitions for Malcolm Ramsay Lake

Acquisition Time TerraSAR-X	**Mean Incidence Angle**	**Acquisition Time ALOS-PALSAR**	**Mean Incidence Angle**
2010-01-07 12:43:20 UTC	33°	2010-01-05 04:27:43 UTC	39°
2010-01-18 12:43:19 UTC	33°	2010-02-03 04:25:29 UTC	37°
2010-01-29 12:43:19 UTC	33°	2010-02-20 04:27:32 UTC	39°

2010-02-13 23:56:43 UTC	43°	2010-03-21 04:25:12 UTC	37°
2010-02-20 12:43:19 UTC	33°	2010-04-07 04:27:13 UTC	39°
2010-02-24 23:56:35 UTC	43°		

5.2.4 In Situ Data

5.2.4.1 Noell Lake

Between March 20 and 23, 2019, in situ data were collected on Noell Lake to develop an understanding of the ice and snow cover properties (**Figure 5.2A**). Thirty-four measurements of ice thickness were made across the lake, including eight ice core locations, with an average ice thickness of 87 cm. Ice cores were used to develop a better understanding of the ice structure at Noell Lake and help define ice stratigraphy for the lake. Ice structure properties showed an average snow ice thickness of 16 cm and clear ice thickness of 79 cm, snow ice thickness ranged from 10 to 24 cm and clear ice from 55 to 85 cm. Snow ice was observed at all measurement sites with bubble size ranging from <1 mm to over 10 mm (**Figure 5.2B**). Only two ice core locations taken at the southern end of the lake showed tubular bubble development; the thickness of these layers was 17 and 12 cm. To observe the ice-water interface conditions, a GoPro Hero7 camera was lowered into the ice core holes for a qualitative assessment of conditions and verify the patterns in ice structure observed in the ice cores (**Figure 5.2C**). For snow properties, 345 measurements of snow depth were recorded using a SnowHydro Magnaprobe (Sturm & Holmgren, 1999), with an average depth of 26.4 ±6.3 cm. Densities of snow layers obtained from 8 snow pits across the lake ranged from 240 to 400 kg m^{-3}, the average bulk density of snow was 283 kg m^{-3} (**Figure 5.1**).

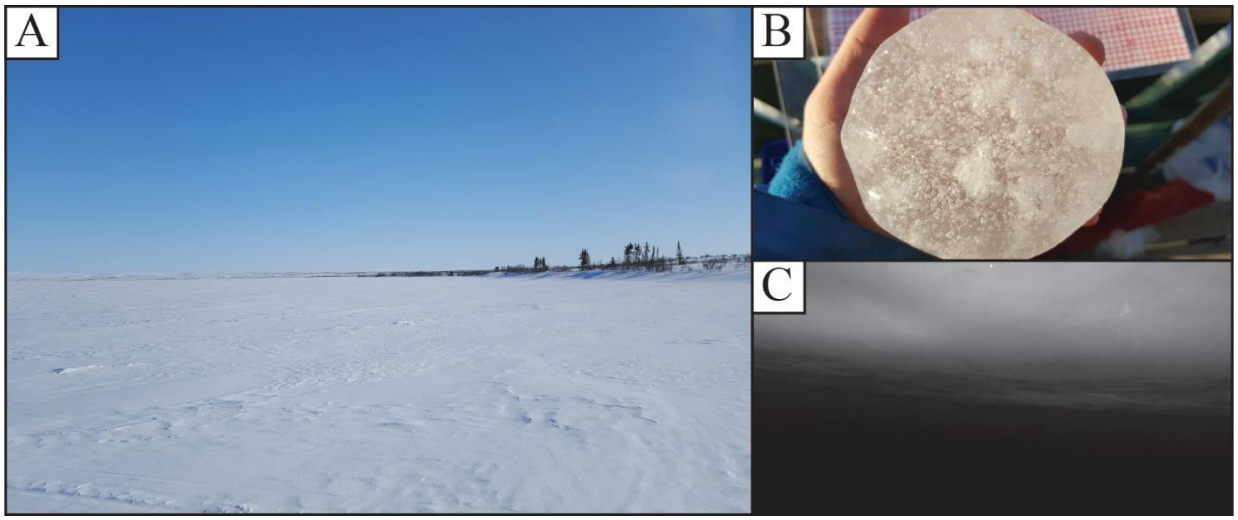

Figure 5.2 A) snow cover on Noell Lake during the field campaign between March 20-23, 2019, B) sample of snow ice from an ice core obtained on Noell Lake, C) black and white image of the bottom of the ice recorded using a GoPro Hero7 camera showing a smooth ice bottom with no extruding tubular bubbles.

5.2.4.2 Malcolm Ramsay Lake

Field measurements for Malcolm Ramsay Lake were recorded between November 15, 2009, and April 4, 2010. Full details about this dataset can be found in Gunn et al. (2018); data used in this study focused on the measurements recorded to provide context for RADARSAT-2 overpasses. Snow depth and ice thickness measurements were taken along a 100 m transect adjacent to the sites highlighted in **Figure 5.1**. Snow depth measurements were recorded every 0.5 m using a SnowHydro Magnaprobe (Sturm & Holmgren, 1999). Ice thickness measurements were recorded every 25 m. In addition to ice thickness, ice cores were extracted from the sites during intensive observations of the lake. These cores provide further information about the ice stratigraphy and are used to estimate the thickness of tubular bubble layers at the different sites (**Figure 5.3**). Additionally, two measurements of bulk snow density were recorded every 25 m using an ESC-30 snow core tube.

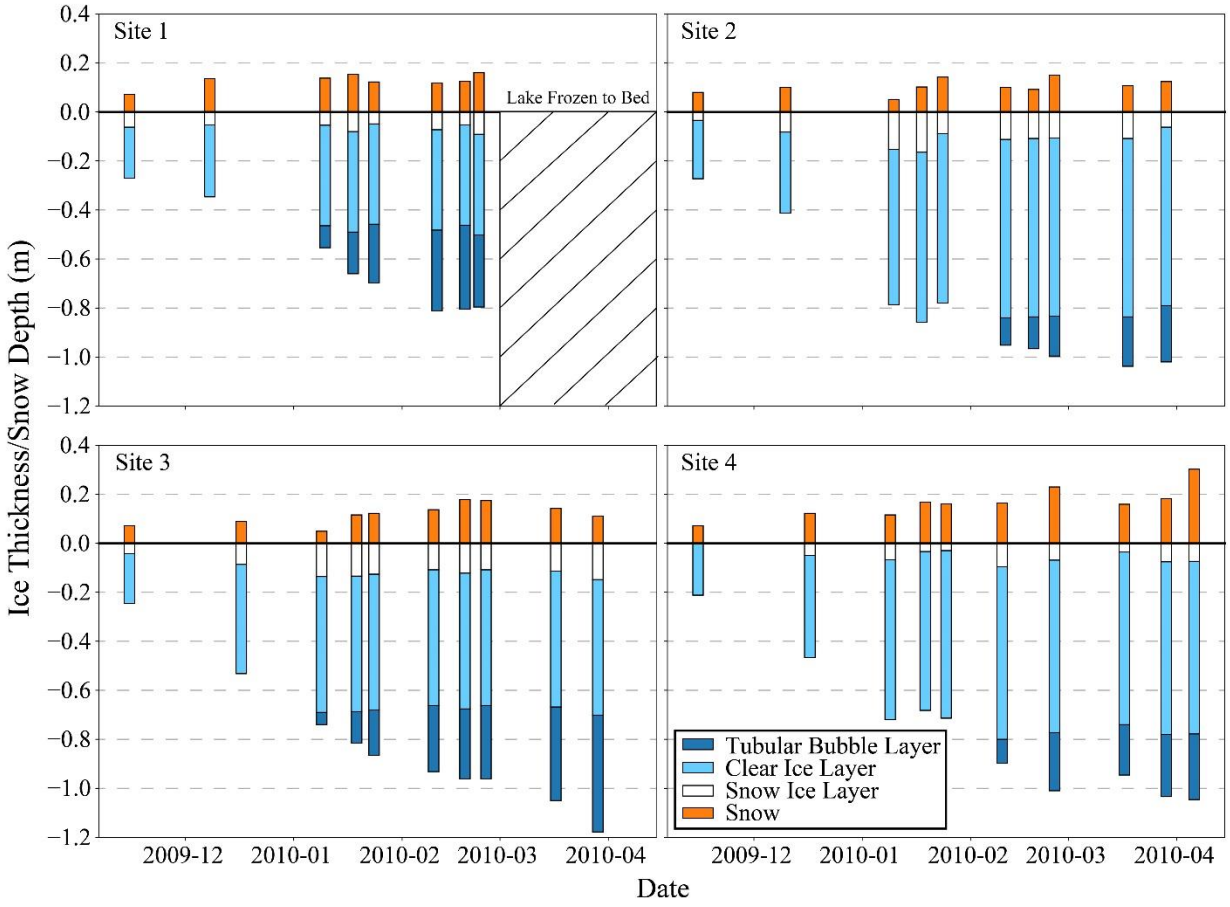

Figure 5.3 Field measurements for snow depth and lake ice stratigraphy recorded during the 2009-2010 ice season for Malcolm Ramsay Lake. Measurements are averaged along the 100 m transect where data were recorded.

Snow depth was similar for sites 1-3 ranging from 0.1 m to 0.13 m, site 4 showed a deeper snowpack reaching a maximum of 0.3 m on April 6, 2010. Snow density was found to be higher for sites 3 and 4 (368 kg m^{-3}) compared to sites 1 and 2 (296.6 kg m^{-3}). Lake ice structure differs between the field sites; maximum ice thickness was observed at site 3, 1.18 m (**Figure 5.3**). Ice at site 1 froze to the lakebed by March 2, 2010, reaching a maximum average thickness of 0.81 m. For all sites ice cores showed the development of a layer of tubular bubbles below clear ice. There was an increase in the presence of these inclusions near the ice-water interface, with the density of the inclusions dependent on the level of saturation of dissolved gas beneath the ice (Gunn et al.,

2018). Observations of the size of these bubbles noted that the diameter of the semicircle bubble origin at the ice-water interface ranged between ~1 to 5 mm (Gunn et al., 2018). This semicircle then reduced to a column or 'tube' and had a smaller diameter of ~0.5 mm (Gunn et al., 2018). The earliest formation of tubular bubbles, in early January, occurs for sites 1 and 3; therefore, these sites see the development of the thickest layers reaching a maximum of 0.47 m for site 3. These sites also have a greater bubble density and larger diameter at the ice-water interface compared to the other sites (Gunn et al., 2018). There was the development of surface ice (snow/grey ice) at all field sites with the presence of high-density spherical microbubbles; average thickness of this layer ranged from a minimum of 0.05 m (site 4) to a maximum of 0.11 m (site 3).

5.2.5 CLIMo Simulations

Field observations collected from both lakes provide data on ice thickness, snow depth, ice layers, and bubble characteristics. However, these measurements do not provide information on the layer temperature and do not offer data continuous in time. Therefore, to better parameterize SMRT, the Canadian Lake Ice Model (CLIMo) was used to address data gaps and realistically represent ice layer temperatures (Murfitt et al., 2022). CLIMo has been used in a number of studies in parallel or to support observations made from both spaceborne and ground-based systems (Kang et al., 2012; Pour et al., 2012; Gunn, Duguay, et al., 2015; Surdu et al., 2015) and to investigate long term changes in ice cover under different climate scenarios (L. C. Brown & Duguay, 2011b, 2012). A full description of CLIMo and the associated equations can be found in Duguay et al. (2003). CLIMo was forced using daily meteorological data (2 m air temperature, relative humidity, 10 m wind speed, cloud cover, and snow accumulation) from the ERA5 reanalysis dataset (Hersbach et al., 2020). To ensure that CLIMo inputs provide a good representation of local meteorological conditions, Environment and Climate Change Canada stations were used to validate ERA5 data. For Noell Lake the Inuvik Climate station (-133.52°, 68.32°; 23.2 km south of Noell Lake, ECCC, 2021c) was used and the Churchill Climate station was used for Malcolm Ramsay Lake (-94.07°, 58.73°; 16 km west of Malcolm Ramsay Lake, ECCC, 2021d). Consistent temperature and snow data are available for the Inuvik station from 2000 to 2020 and for Churchill

from 2005 to 2020, days with no data were excluded from validation. The ERA5 data were found to be a fair representation of the local station data with root mean square errors (RMSE) of <2.24 °C and <0.11 m for air temperature and snow depth respectively. Strong correlation values also exist between the two datasets with Kendall's Tau-b >=0.78 ($p<0.01$).

Both field data and past studies of CLIMo were used to parameterize the model, references for these values are listed in **Table 5.5**. These same settings were used in Murfitt et al. (2022). Regarding precipitation, the percentage scenario parameter in CLIMo helps characterize the difference between snow accumulation on-land and on-ice. Snow on-ice tends to be shallower compared to on-land due to snow redistribution (Duguay et al., 2003; Sturm & Liston, 2003). Various values of this percentage were tested for both lakes. Results for Churchill were compared to field measurements acquired during the 2009-2010 winter season and results for Noell Lake were compared to ice and snow measurements taken in March 2019. For Churchill, the best results are found when CLIMo is run with a 50% on-ice snow depth scenario with RMSE values of 0.05 m for ice thickness and 0.04 m for snow depth. For Noell Lake, CLIMo runs using a 35% on-ice snow depth are the best representation of conditions between March 20 – 23, resulting in an RMSE of 0.12 m for ice thickness and 0.05 m for snow depth. The key outputs from CLIMo for use in the SMRT simulations detailed in the next section are layer temperature (both snow and ice) as well as snow depth and ice thickness for Noell Lake where limited field measurements were available.

Table 5.5 Parameterization of CLIMo for Noell Lake and Malcolm Ramsay Lake (Murfitt et al., 2022).

		Value	Reference			Value	Reference
Noell Lake	Mixing Depth	6 m	Ogbebo et al., 2009	**Malcolm Ramsay Lake**	Mixing Depth	2 m	Gunn et al., 2015b
	Snow Density	283 kg m^{-3}	Field Campaign March 2019		Snow Density	276 kg m^{-3}	Brown and Duguay, 2011b
	On-ice Snow Depth	35%			On-ice Snow Depth	50%	

5.2.6 SMRT Parameterization

CLIMo was run using a 5-layer simulation (one layer of snow and four layers of ice) that was translated for input into SMRT. Due to the lack of field data throughout the ice season for Noell Lake, the output from CLIMo was used to parameterize snow depth, ice thickness, and layer temperature within SMRT for each date of image acquisition. For the snow ice layer on Noell Lake, when field data were collected the average amount of snow ice observed was 17%. This value was applied to all dates throughout the ice season. The amount of snow ice for each day was subtracted from the total ice thickness determined from CLIMo and the remaining ice was divided into three equal layers of clear ice for use in SMRT. **Figure 5.4** shows the configuration of CLIMo layer temperature output for SMRT input for Noell Lake. While some tubular bubbles are observed at Noell Lake, these bubbles are not present in the majority of the ice cover. Therefore, a tubular bubble layer is not included to best generalize the ice cover. For Malcolm Ramsay Lake, field data were used to parameterize layer thickness in SMRT and CLIMo was used for layer temperature.

Unlike Noell Lake, snow/grey ice, clear ice, and tubular bubble layers were observed for Malcolm Ramsay Lake. Therefore, CLIMo data were translated into both a two-layer (snow/grey ice and clear ice) and a three-layer (snow/grey ice, clear ice, and tubular bubble layer) set-up for SMRT. **Figure 5.5** shows the configuration of data for both scenarios.

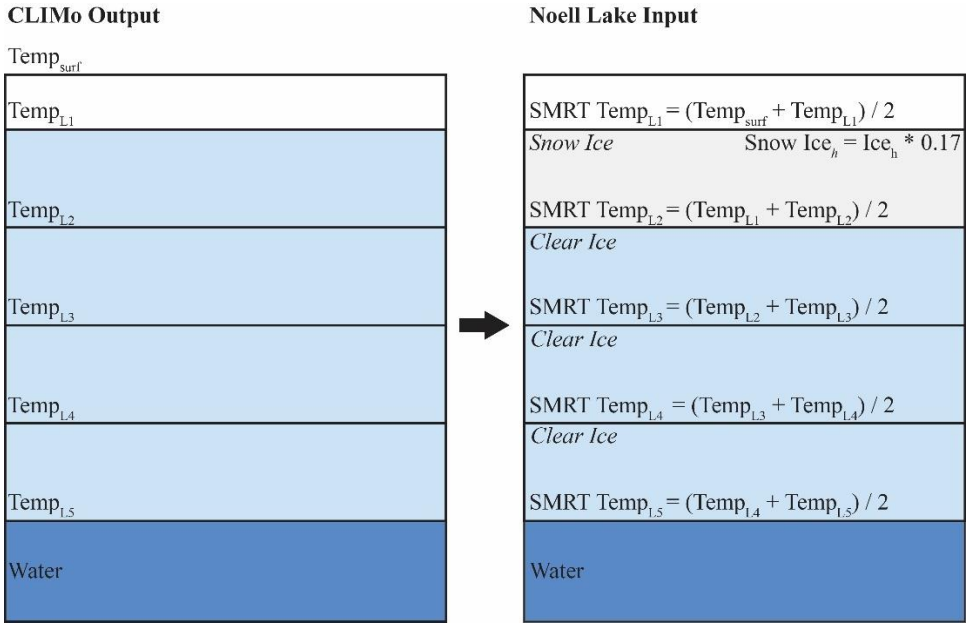

Figure 5.4 Configuration of CLIMo for 2018-2019 Noell Lake ice season. $Temp_{LX}$ indicates the corresponding interface temperature from CLIMo. Ice_h indicates the ice thickness output from CLIMo.

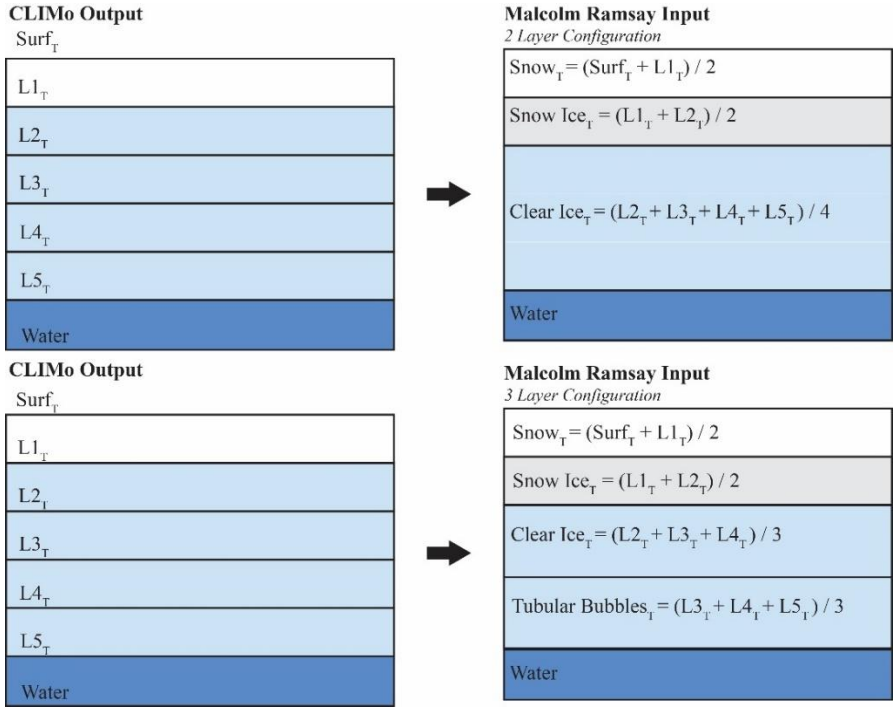

Figure 5.5 Configuration of CLIMo layer temperatures for the 2009-2010 Malcolm Ramsay Lake ice season. The top set of figures show the parameterization of SMRT for two ice layers and the bottom show the parameterization for three ice layers. Layer thicknesses were determined from field measurements. LX$_T$ indicates the temperature of the corresponding CLIMo interface, Surf$_T$ indicates the temperature of the top of the snowpack in CLIMo.

Bulk snow density values acquired in the field for the two lakes were used to parameterize optical radius (R_o) for snow grains that are needed for SHS in SMRT. Optical radius is calculated using (5.1),

$$R_o = \frac{3}{\rho_{ice} * SSA} \quad \textbf{(5.1)}$$

where ρ_{ice} is the density of ice (916.7 kg m^{-3}) and *SSA* is the specific surface area (m^2 kg^{-1}). *SSA* values were not collected in the field, therefore a recent relation identified by Vargel et al. (2020) between *SSA* and snow density (kg m^{-3}) was used. The relation was developed using data from the

Canadian Arctic and Subarctic (including Trail Valley Creek, NWT, 24 km north of Noell Lake). The relation is given as (5.2),

$$SSA = -17.65 \ln(p) + 118.07 \quad \textbf{(5.2)}$$

where p was the dry snow density. It should be noted that this approach does not take the differences between snow regimes on land and lake ice surfaces into account. Further research is needed on how to better represent on-ice snow microstructure. Snow density and R_o for Noell Lake were assumed constant throughout the ice season. These values were varied for Malcolm Ramsay Lake due to the availability of in situ bulk snow density data (**Table 5.6**).

Certain parameters were held constant for the model runs. Porosity of the bubbled ice layers (snow ice and tubular bubbles) and clear ice layers were held constant at 10% and 1%, respectively. Bubble radius of the clear ice layers was set at 0.0 mm. The implementation of DMRT in SMRT does not allow for the inclusion of tubular bubbles meaning that spherical bubbles were used as a substitute. Previous research has indicated that cylindrical bubbles in the lower ice layers have little impact on radar signals (Atwood et al., 2015). The results of previous numerical modelling show that resulting backscatter with and without tubular bubbles can be considered equivalent (Atwood et al., 2015). While it is possible this could introduce some error, recent sensitivity analysis conducted using SMRT indicated that bubbles in the lower ice layers have little to no impact on resulting co-pol backscatter, cross-pol has not been evaluated (Murfitt et al., 2022). The bottom layer of the ice column was used as the tubular bubble layer. The bottom 5% of the tubular bubble layer is assumed to contain larger bubbles observed in the field, the radius of these bubbles was set to 1 mm (Gunn et al., 2018). The radius of these bubbles decreases moving upwards through the ice column (Gunn et al., 2018) and therefore for the remainder of the tubular bubble layer the radius was set to 0.25 mm. While larger bubble sizes were observed in the field, previous sensitivity experiments demonstrated that increasing the radius of these bubbles had little impact on co-polarized backscatter (Murfitt et al., 2022).

Variations in the bubble radius of surface ice were experimented with to properly parameterize these layers. For Noell Lake bubble radii of 0.1 to 2 mm at 0.25 mm increments were tested to account for the larger bubbles observed in the surface ice layer. For Malcolm Ramsay Lake, bubble radii of 0.1, 0.25, 0.5, 0.75, and 1.0 mm were tested due to observations of microbubbles in the surface ice layers (Gunn et al., 2018). Stickiness (τ) values are also held constant for the different layers. Clear ice is assigned a stickiness of 1 while bubbled ice (both surface and tubular layers) is assigned a value of 0.4, meaning more sticky spheres. For snow a value of 0.1 is used consistent with previous SMRT experiments on Arctic and Subarctic snow (Vargel et al., 2020). Because low stickiness values may fall outside the validity range for SHS (Löwe & Picard, 2015), it may cause an error in SMRT. To address this issue the values were incremented by 0.00001 for ice and 0.0001 for snow. These values were reset to the baseline (0.4 and 0.1) for each model run. **Table 5.6** provides a summary of the constant values for each layer.

Table 5.6 SMRT Constant Parameters.

	Malcolm Ramsay Lake	Noell Lake
Snow		
Density	Varied	283 kg m^{-3}
Optical Radius	Varied	0.000178 m
Stickiness	0.1	0.1
Snow Ice		
Porosity	10%	10%
Stickiness	0.4	0.4
Clear Ice		
Bubble Radius	0.0	0.0
Porosity	1%	1%

Stickiness	1	1
Tubular Bubble Ice		
Small Bubble Radius	0.25 mm	n/a
Interface Bubble Radius	1.0 mm	n/a
Porosity	15%	n/a
Stickiness	0.4	n/a

RMSH and correlation length could not be estimated in the field. From previous studies, RMSH is the key parameter impacting backscatter from lake ice (Atwood et al., 2015; Tian et al., 2015; Murfitt et al., 2022), therefore we focus on selecting the optimal value for this parameter. For Noell Lake, the optimal value was only determined for RADARSAT-2 data as it provided concurrent HH and VV data. Sentinel-1 data for Noell Lake was reserved for validation of these results. For Malcolm Ramsay Lake, the optimal value was determined using L, C, and X-band SAR imagery and SMRT outputs. However, not every date had corresponding images from all frequencies. The most consistent record of imagery was RADARSAT-2 which provided both HH and VV imagery. The January 18, 2010, TerraSAR-X image is excluded from determining optimal RMSH as it is the only image available for corresponding field data collected January 18/19, 2010. To determine the optimal RMSH, SMRT was run using values between 0.5 mm and 7.5 mm at an interval of 0.05 mm for all days of available SAR data for both Noell Lake and Malcolm Ramsay Lake. The resulting backscatter was then compared to the appropriate SAR images (frequency and incidence angle) to determine the difference between modelled and observed data. For each date the mean absolute difference was obtained for each RMSH. To reduce the variation in mean absolute difference, the values were multiplied by the range of mean absolute difference values. The RMSH that corresponded to the minimum value of this modified mean absolute difference was selected as the optimal value for that date. In addition to testing the range of RMSH, differing values of correlation length and bubble radius were also explored. Correlation lengths of 5, 10, 30,

50, and 70 mm were tested, RMSH values for these tests were restricted to respect the validity of IEM.

Previous studies (Tian et al., 2015; Gunn et al., 2018) indicate it is likely that RMSH increases throughout the ice season. Therefore, RMSH values were assumed to always increase in the forward modelling. For example, if the optimal RMSH value was 1.0 mm at a given date, and the unconstrained optimal value would be 0.9 mm at the next available date, only the higher value of 1.0 mm was retained. Additionally, because past studies of backscatter evolution for lake ice have shown that backscatter increases throughout the ice season (Jeffries et al., 1994; Gunn et al., 2018; Murfitt & Duguay, 2020), a limit to RMSH was set to avoid issues with decreasing backscatter that occurs due to the bell-shaped behavior of IEM (Fung & Chen, 2010). The RMSH limit was set equal to highest RMSH observed at peak backscatter for C-band images because these images provided the best temporal coverage for both lakes, or to the maximum RMSH that allowed IEM to be valid for all frequencies at $k*RMSH < 2$. After all scenarios were run the optimal settings for bubble radius and correlation length were determined by comparing the root mean square error (RMSE) calculated using all available images.

Observed backscatter for Noell Lake was extracted as a lake-wide mean. For Churchill, mean backscatter was extracted using a 50 m buffer around each of the field sites. For Noell Lake, RMSE is calculated using all RADARSAT-2 incidence angles. For Malcolm Ramsay Lake, all frequencies were used at each site. The modelling results and selected optimal values were validated using the closest available image. Validation was done using correlation statistics (Spearman's ρ), and RMSE calculated in R via the hydroGOF package (Zambrano-Bigiarini, 2017). Images acquired after May 8 for Noell Lake and after April 16 for Malcolm Ramsay Lake were not included in validation due to changes in ice surface conditions due to melt onset after these dates; this is addressed in the discussion.

5.3 Results

5.3.1 RMS Height Optimization

Comparison of RMSE values for different bubble radii and correlation lengths shows that the optimal settings for Noell Lake were snow ice with a bubble radius of 2 mm and a correlation length of 30 mm (**Table 5.7**). These values resulted in an RMSE of 1.00 dB when using all RADARSAT-2 images at incidence angles of 21°, 27°, and 39°.

Table 5.7 Root Mean Square Error (dB) for all RADARSAT-2 incidence angles for Noell Lake.

	Correlation Length (m)				
Bubble Radius (mm)	**0.005**	**0.01**	**0.03**	**0.05**	**0.07**
0.1	4.331	1.223	1.727	1.982	2.090
0.25	2.196	1.223	1.727	1.982	2.090
0.5	2.197	1.220	1.712	1.953	2.063
0.75	2.201	1.216	1.646	1.904	2.061
1.00	2.187	1.210	1.623	1.890	2.015
1.25	2.177	1.186	1.506	1.803	1.898
1.50	2.172	1.192	1.385	1.595	1.753
1.75	2.173	1.225	1.200	1.428	1.534
2.00	2.181	1.274	***0.999***	1.183	1.298

For Malcolm Ramsay Lake, data were available for four sites. Therefore, the sites across the lake are parameterized using different optimal values to address variations that exist between locations. For site 3, the optimal correlation length was found to be 50 mm and the optimal bubble radius 1 mm (**Table 5.8**). For site 1, 2, and 4, the optimal correlation length was found to be 70

mm and the optimal bubble radius of 1 mm for site 1, 0.75 mm for site 2, and 0.1 mm for site 4 (**Table 5.8**).

Table 5.8 Root Mean Square Error (dB) for all frequencies for Malcolm Ramsay Lake.

		Correlation Length (m)				
	Bubble Radius (mm)	**0.005**	**0.01**	**0.03**	**0.05**	**0.07**
Site 1	0.1	4.514	3.492	2.195	2.929	1.468
	0.25	4.514	3.492	2.195	2.928	1.468
	0.5	4.514	3.514	2.197	2.919	1.465
	0.75	4.513	3.515	2.202	2.897	1.459
	1.00	4.513	3.491	2.214	2.892	***1.452***
Site 2	0.1	6.146	3.136	2.072	1.666	1.506
	0.25	6.145	3.136	2.073	1.666	1.506
	0.5	6.141	3.133	2.073	1.667	1.507
	0.75	6.130	3.126	2.075	1.670	***1.505***
	1.00	6.110	3.113	2.081	1.678	1.512
Site 3	0.1	7.092	3.827	1.373	1.290	1.418
	0.25	7.091	3.826	1.373	1.290	1.328
	0.5	7.084	3.821	1.372	1.288	1.324
	0.75	7.067	3.808	1.369	1.283	1.314
	1.00	7.033	3.766	1.363	***1.272***	1.296
Site 4	0.1	6.792	3.961	2.411	1.748	***1.501***

0.25	6.792	3.961	2.411	1.748	1.501
0.5	6.791	3.961	2.412	1.750	1.503
0.75	6.787	3.962	2.416	1.755	1.508
1.00	6.781	3.962	2.423	1.765	1.518

Figure 5.6 provides a visualization of the changes in optimal RMSH throughout the ice season when using these values for both lakes. **Figure 5.6** also shows the RMSH values that would be used if RMSH was not assumed to always increase. For Noell Lake, RMSH starts at 0.7 mm and increases to 0.85 mm by mid-November. It remains at this value until late February/early March where there is an increase to 1.05 mm. There are large increases in the optimal RMSH in early April, from 1.05 to 1.65 mm, and increases continue until May. The maximum RMSH value selected was 2.0 mm. For Malcolm Ramsay Lake, sites 2, 3, and 4 have similar patterns in RMSH, however, site 3 has the highest RMSH reaching a maximum of 5. 5 mm. Site 1 has a lower RMSH compared to the other three sites and reaches a maximum of 2.65 mm. The evolution for this site is shorter compared to the others as the ice cover froze to the lakebed in late February.

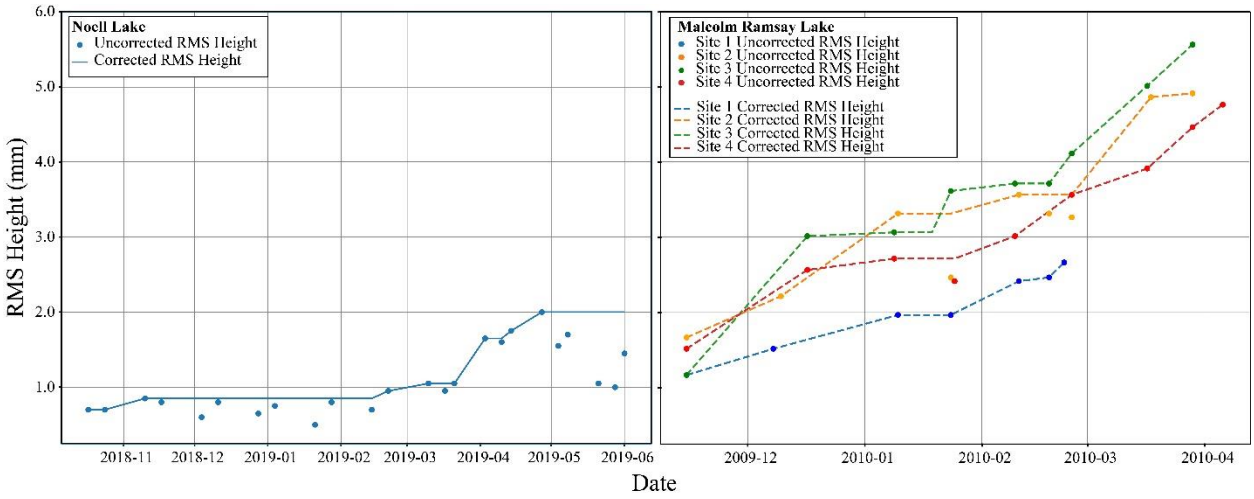

Figure 5.6 Optimal RMS height value selected for Noell Lake and Malcolm Ramsay Lake based on the minimum mean absolute difference. Circles show the uncorrected values and lines show the corrected values representing a constant increase in RMS height.

5.3.2 Noell Lake 2018 – 2019 Simulated Backscatter

There is good agreement between the modelled backscatter and observed backscatter from the RADARSAT-2 images after the optimization, with Spearman's ρ values >0.98 for all data at both polarizations ($p<0.01$) (**Table 5.9**, **Figure 5.7**). RMSE values range 0.38 to 1.45 dB, agreement is relatively consistent between incidence angle with modelled HH backscatter better representing the observed backscatter. VV-pol backscatter shows higher RMSE, and the modelled data are higher compared to the observed backscatter by a maximum of 2.06 dB on December 4. The largest differences are observed for all incidence angles after May 8, 2019; for these dates modelled backscatter is >1.86 dB higher compared to the observed data.

There remains good agreement between the Sentinel-1 imagery and SMRT backscatter when the RADARSAT-2 derived parameters are used with Spearman's ρ values >0.91 ($p<0.01$). The RMSE values are slightly higher for the different incidence angles ranging from 0.77 to 1.38 dB. The HH-pol data at incidence angles of 22° and 33° show the best results with RMSE values <1 dB. Between December 1 and March 31, the difference in backscatter between modelled and observed data were lowest, ranging from 0.01 to 2.00 dB. The largest difference for these data occurs after April 1, similar to the RADARSAT-2 results. Differences between observed and modelled after April 1 are more variable ranging from 0.10 to 7.67 dB. Additionally, at the start of the ice season there are larger differences with the modelled backscatter being up to 3 dB lower than the observed backscatter.

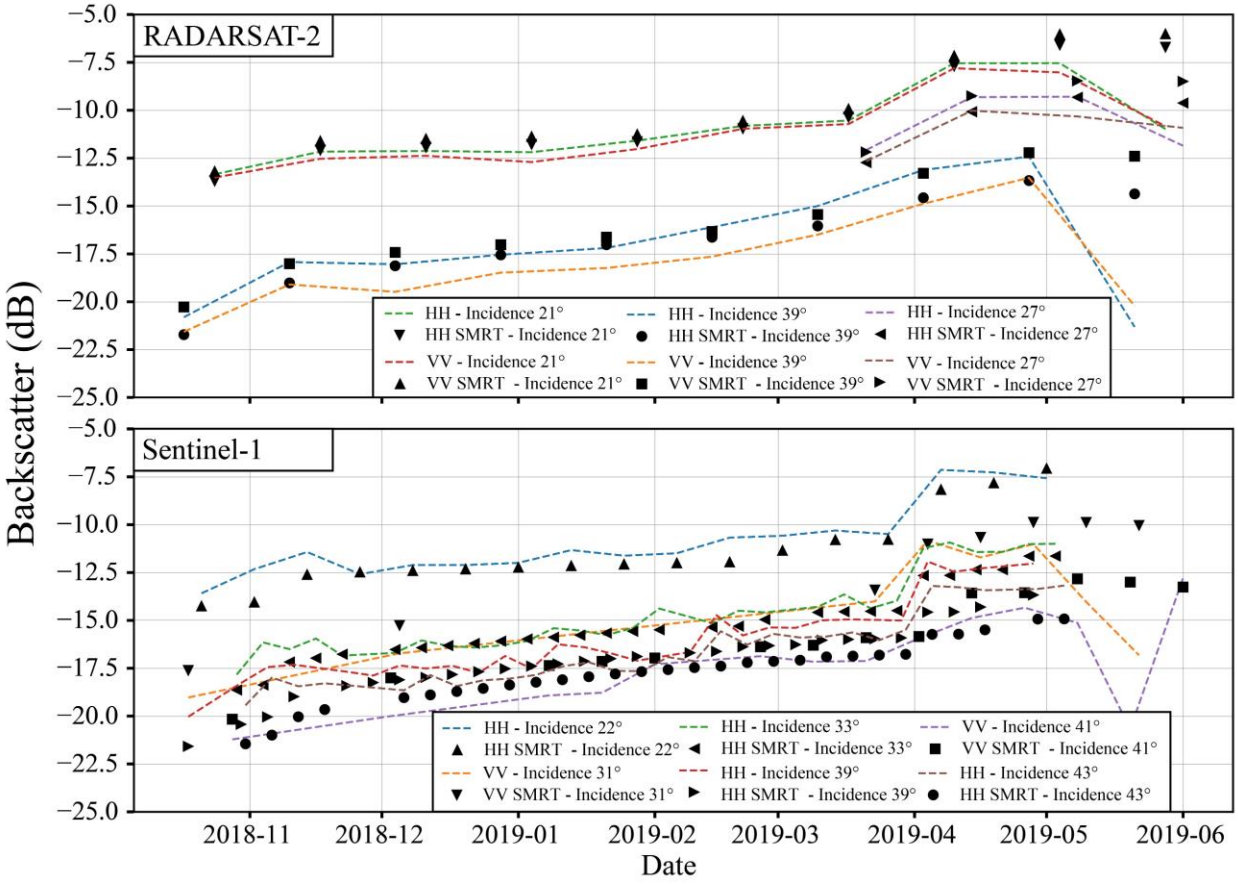

Figure 5.7 Comparison of modelled and observed backscatter for both RADARSAT-2 (top) and Sentinel-1 (bottom) imagery for Noell Lake for the 2018-2019 ice season.

Table 5.9 Validation of SMRT outputs for Noell Lake using optimal parameters.

		RMSE (dB)	Spearman's Rho (Sρ)
RADARSAT-2	Incidence 21° – HH n=9	0.380	
	Incidence 21° – VV n=9	1.021	
	Incidence 27° – HH	0.580	

	n=3 Incidence 27° – VV n=3	1.195	
	Incidence 39° – HH n=9	0.888	
	Incidence 39° – VV n=9	1.447	
	All Data – HH n=21	0.669	0.986*
	All Data – VV n=21	1.244	0.987*
Sentinel-1	Incidence 22° – HH n=17	0.774	0.917*
	Incidence 31° – VV n=9	1.073	
	Incidence 33° – HH n=29	0.798	0.949*
	Incidence 39° – HH n=29	1.287	0.928*
	Incidence 41° – VV n=14	1.304	0.958*

Incidence 43° – HH n=29	1.384	0.956*
All Data – HH n=104	1.128	0.960*
All Data – VV n=23	1.232	0.973*

**Indicate p-value <0.01*

5.3.3 Malcolm Ramsay Lake 2009 – 2010 Simulated Backscatter

There is good agreement between the modelled and observed backscatter for all Malcolm Ramsay field sites at all frequencies, RMSE ranges from 0.95 to 1.89 dB with Spearman's ρ values >0.86 ($p < 0.01$) (**Table 5.10**). For L-band, sites 2 and 3 have the best results with RMSE < 1.55 dB. There are larger differences for sites 1 and 4 with RMSE >2.21 dB and modelled backscatter is lower compared to the observed backscatter throughout the season (**Figure 5.8**). HH polarized C-band data are well modelled throughout the ice season for all sites with RMSE values <1.43 dB. The modelled values for C-band HH data follow closely to the observed backscatter, however, there are dates for sites 2 and 4 where the modelled backscatter is noticeably higher compared to the observed values. The modelled C-band VV backscatter is consistently higher compared to the observed data, RMSE values range from 1.31 to 1.81 dB. Additionally, the largest difference of >3.38 dB between the observed and modelled data occurs on April 13 in both polarizations for site 4 (**Figure 5.8**). SMRT performed the best for modelling the X-band backscatter with an RMSE <1.14 dB for all sites.

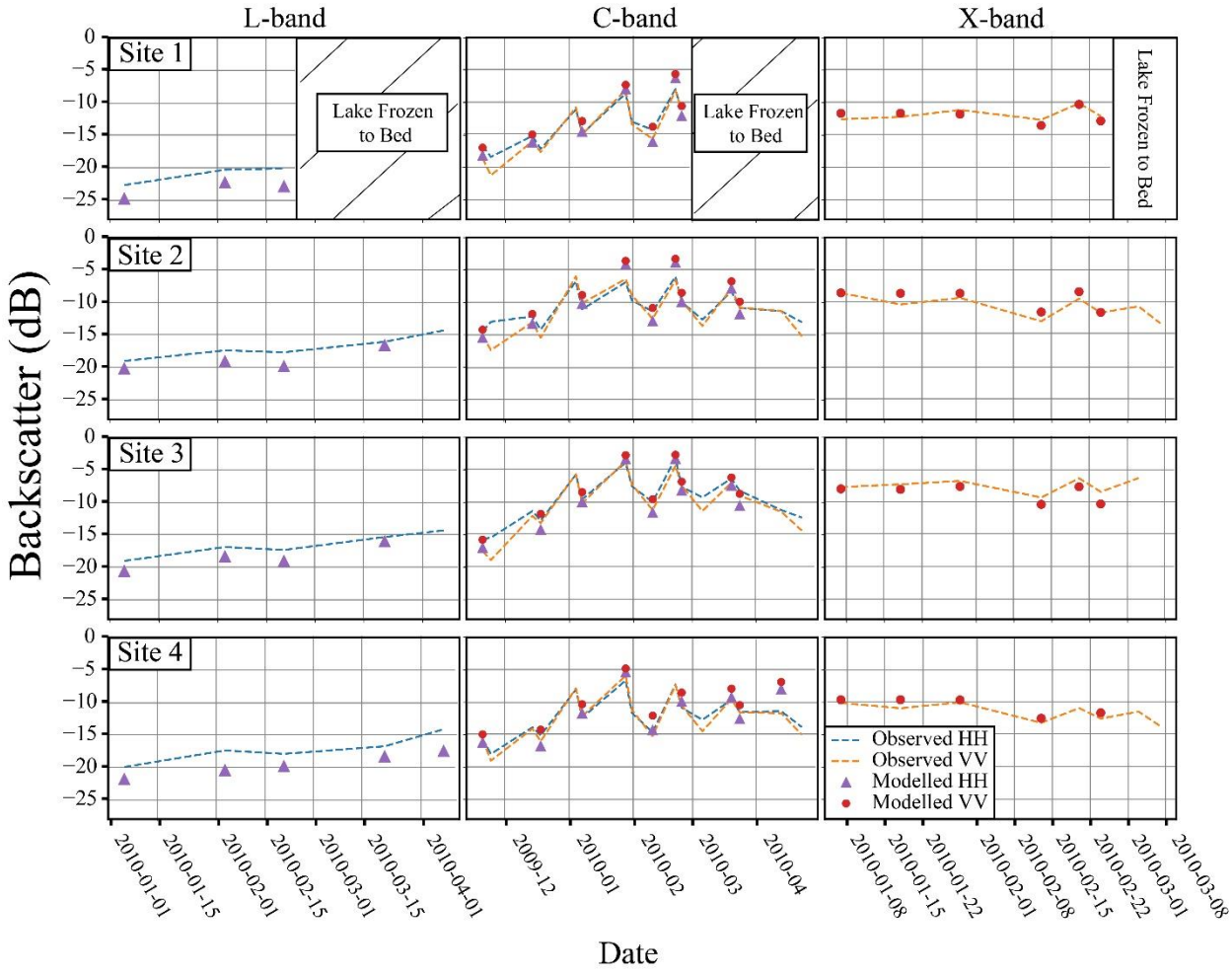

Figure 5.8 Comparison of modelled and observed backscatter for L-band (left), C-band (middle), and X-band (right) imagery for each field site over Malcolm Ramsay Lake for the 2009-2010 ice season.

Table 5.10 Validation of SMRT outputs for Malcolm Ramsay Lake using optimal parameters.

** indicates p-values < 0.01

		L-band HH	C-band HH	C-band VV	X-band VV	All Data
Site 1	RMSE (dB)	2.326	1.218	1.645	0.696	1.452
	Spearman's ρ					0.956**
Site 2	RMSE (dB)	1.548	1.434	1.784	1.053	1.505
	Spearman's ρ					0.964**
Site 3	RMSE (dB)	1.441	1.234	1.308	1.139	1.270
	Spearman's ρ					0.944**
Site 4	RMSE (dB)	2.205	0.956	1.810	0.818	1.501
	Spearman's ρ					0.950**
All Sites	RMSE (dB)	1.890	1.230	1.644	0.948	1.432
	Spearman's ρ	0.971**	0.970**	0.982**	0.860**	0.960**

5.4 Discussion

5.4.1 Ice-Water Interface Roughness Height

One of the main objectives of this study was to determine optimal roughness height values for the two lakes. RMSH values from Malcolm Ramsay Lake are higher compared to those of Noell Lake (**Figure 5.6**). This provides support for the hypothesis that the presence of tubular bubbles at the ice-water interface results in increased overall roughness (Atwood et al., 2015; Gunn et al., 2018). Optimal RMSH values for Noell Lake are <=2 mm, however, for Malcolm Ramsay Lake optimal RMSH values are ~3 mm by early January for most sites. Additionally, the optimal

RMSH values for Noell Lake were more consistent compared to Malcolm Ramsay Lake and did not increase above 0.85 mm until late in the ice season. This reflects the under-ice observations for Noell Lake that showed little development of tubular bubbles. On the other hand, the increasing RMSH and differences between sites at Malcolm Ramsay Lake is connected to the observed backscatter and ice stratigraphy. For example, site 3 has the highest RMSH and the highest backscatter across all frequencies as well as the thickest layer of tubular bubbles (**Figure 5.9**). This is followed by sites 2 and 4, with site 1 having the lowest backscatter and lowest RMSH. This is unexpected for site 1 as the earlier tubular bubble formation at this site indicates a higher concentration of bubbles (Gunn et al., 2018), and possibly higher RMSH values. However, the lower L-band backscatter observed for this site supports the selection of lower RMSH values and indicates a smoother ice-water interface (**Figure 5.9**).

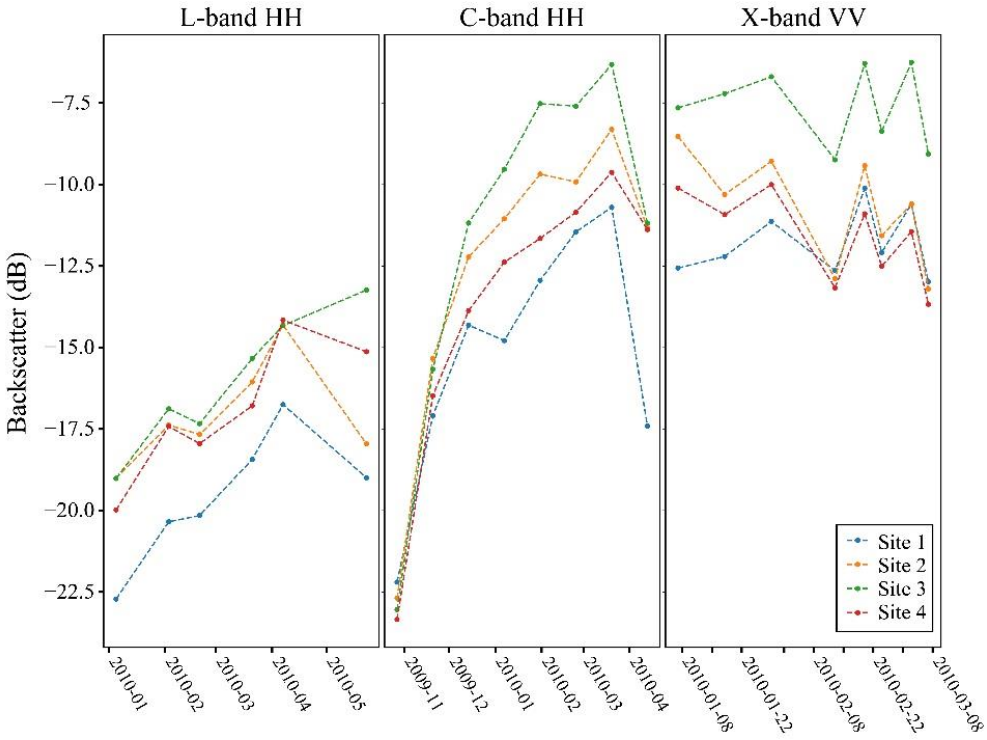

Figure 5.9 Multifrequency backscatter comparison for Malcolm Ramsay Lake field sites. C-band backscatter is only shown for 38° incidence angle as it had the highest number of images.

There has been limited research conducted on modelling backscatter throughout an ice season. Gunn et al. (2015a) modelled backscatter for Malcolm Ramsay Lake during the 2010-2011 ice season. Modelled X-band VV backscatter compared to ground-based scatterometer data showed underestimation by up to 5 dB, likely due to the use of a fixed roughness at the ice-water interface. On the other hand, Tian et al. (2015) modelled C-band VV backscatter from lake ice on the Qinghai-Tibet Plateau (QTP) for ice seasons between 2003 and 2010. Roughness height was estimated using an empirical model relating roughness height to ice thickness. Results of modelling for the QTP also show underestimation of backscatter. While the results of the modelling from the current paper are comparable to these past examples, the modelling presented differs by assuming roughness increased throughout the ice season and was independent of other properties (i.e., thickness). The advantage of this approach compared to the previous studies is that it allows for increasing RMSH throughout the ice season but only when an increased RMSH results in a better fit.

To support the use of increasing RMSH as a better way to parameterize RMSH compared to stationary values, modelling scenarios assuming constant RMSH were compared to the results of increasing RMSH presented in this paper. Bubble radius and correlation were assumed equal to the optimized values originally determined. For Noell Lake, constant RMS heights of 0.5, 1, 1.5, and 2 mm were tested, with 1 mm showing the best representation. This is not unexpected as the optimal RMSH for Noell Lake remained stationary at 0.85 mm from November to late January and only increased slightly later in the ice season. However, the optimal RMSH did show an improvement over a constant value; on average modelled HH backscatter using the optimal RMSH was 1 dB closer compared to a constant RMSH and modelled VV backscatter was 0.6 dB closer. The largest improvements were at the start of the ice season, likely when the ice-water interface is smoother, and a lower RMSH is more appropriate.

Using a variable RMSH was critical for the multifrequency analysis conducted for Malcolm Ramsay Lake. For Malcolm Ramsay Lake, constant RMS heights ranging from 1.5 to 5 mm at 0.5 mm intervals were tested. The problem encountered with using a constant RMSH was

that the best constant value differed with frequency. For example, at site 3, the best constant value for L-band HH was 4.5 mm and showed improvement over the varying optimal RMSH. However, when comparing the modelling results for this RMSH to those from the optimal RMSH modelling for C-band HH and VV, the modelled backscatter for optimal RMSH was an average of 1.4 dB closer to observed values. Across all sites, the optimal RMS heights result in backscatter that is closer to observed backscatter by an average ranging from 0.7 to 2.9 dB compared to the best constant RMS heights. Similar to Noell Lake, the largest differences were early in the ice season, likely when the ice-water interface is smooth. Examples from Noell Lake and Malcolm Ramsay Lake demonstrate that selection of an evolving RMSH is a more appropriate method of parameterizing ice-water interface values both for single and multifrequency analysis. The method used in this analysis for variable RMSH captures both the smooth ice-water interface at the start of the ice season and the period mid-season where RMS height appears to stabilize. The stabilization of RMSH is likely due to a slowing of the ice growth process supported by plateaus in backscatter evolution shown in this research and past investigations (Jeffries et al., 1994; Antonova et al., 2016; Gunn et al., 2018) as well as smaller changes noted in the thickness of ice layers for Malcolm Ramsay Lake.

5.4.2 Limitations in Parameterization

For Noell Lake, there were difficulties modelling backscatter at the start of the ice season. Modelled backscatter between October 30 and November 6 was up to 3 dB lower compared to observed values in Sentinel-1 images. HH backscatter for RADARSAT-2 was also underestimated during this time, however, at a lower magnitude up to 1.09 dB. This is likely due to the presence of linear features (deformations and cracks) in the ice surface resulting in increased backscatter. **Figure 5.10** illustrates that these cracks are present early in the ice season for Noell Lake, however, as the ice grows co-pol backscatter from the lake becomes more homogenous and results are more consistent between the modelled and observed backscatter. Co-polarized backscatter has been noted to be 10 dB higher for deformation features over Arctic lakes at C-band (Morris et al., 1995). For Noell Lake, an average HH backscatter of -8.6 dB was calculated for sample deformation

features, but -27.8 dB for other areas of the lake. SMRT does not represent the 3D surface created by these variations in roughness. Malcolm Ramsay Lake did not encounter this issue; however, it should be noted that there was a maximum gap of 8 days between acquired images and field measurements. Changes in field conditions during these gaps may explain some of the error observed for the modelling results.

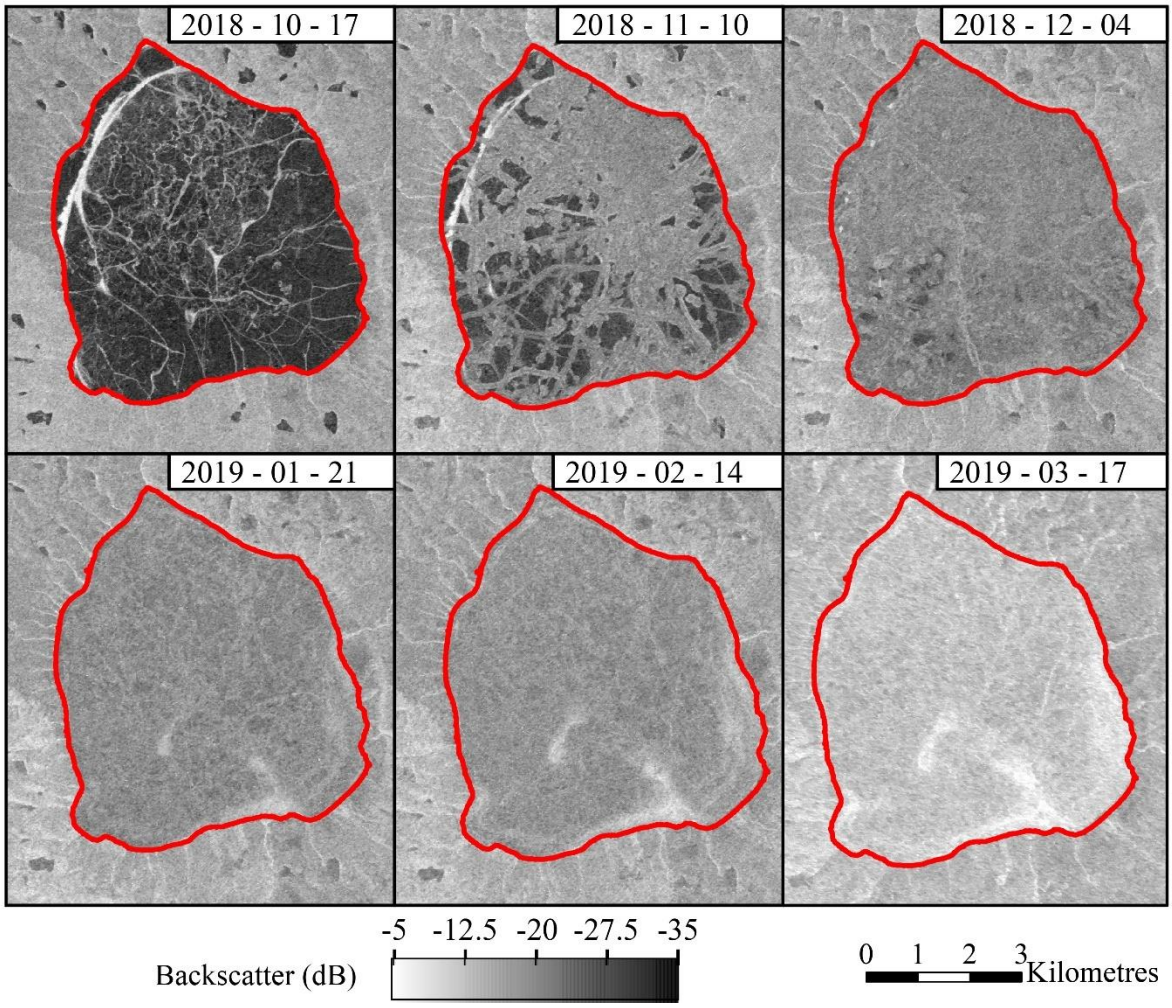

Figure 5.10 Disappearance of surface features for Noell Lake between October 17, 2018, and February 14, 2019, shown in HH-polarized images. RADARSAT-2 Data and Products © MacDonald, Dettwiler and Associates Ltd. (2019) – All Rights Reserved.

The main limitation faced in parameterizing SMRT throughout the ice season was addressing changes in the ice surface conditions. **Figure 5.11** shows that for Noell Lake after the end of March, observed Sentinel-1 HH backscatter is consistently higher than modelled backscatter up to 2.64 dB. Only three incidence angles were shown to emphasize the results. The average difference between modelled and observed RADARSAT-2 data also increases during this time to 0.90 dB compared to 0.14 dB earlier in the season. This impact on HH backscatter is most likely due to a change in either the snow cover or ice surface not captured in the modelling. Between March 23 and March 31 maximum daily temperatures at the Inuvik meteorological station ranged from 1 to 4.6 °C, likely causing surface melt. Temperatures returned to daily maximums of <-5 °C after April 1, causing a refreeze of any melt. This melt and refreeze may have resulted in an increased formation of snow ice and increased presence of spherical bubbles. Alternatively, it may have resulted in a change in the structure of the overlying snowpack, with the formation of ice layers or layers with increased water content. The Sentinel-1 images (**Figure 5.11 A**, **B**, and **C**) capture this change, showing little variation in backscatter tones between February 9 and March 29, but brighter tones present in the April 4 image.

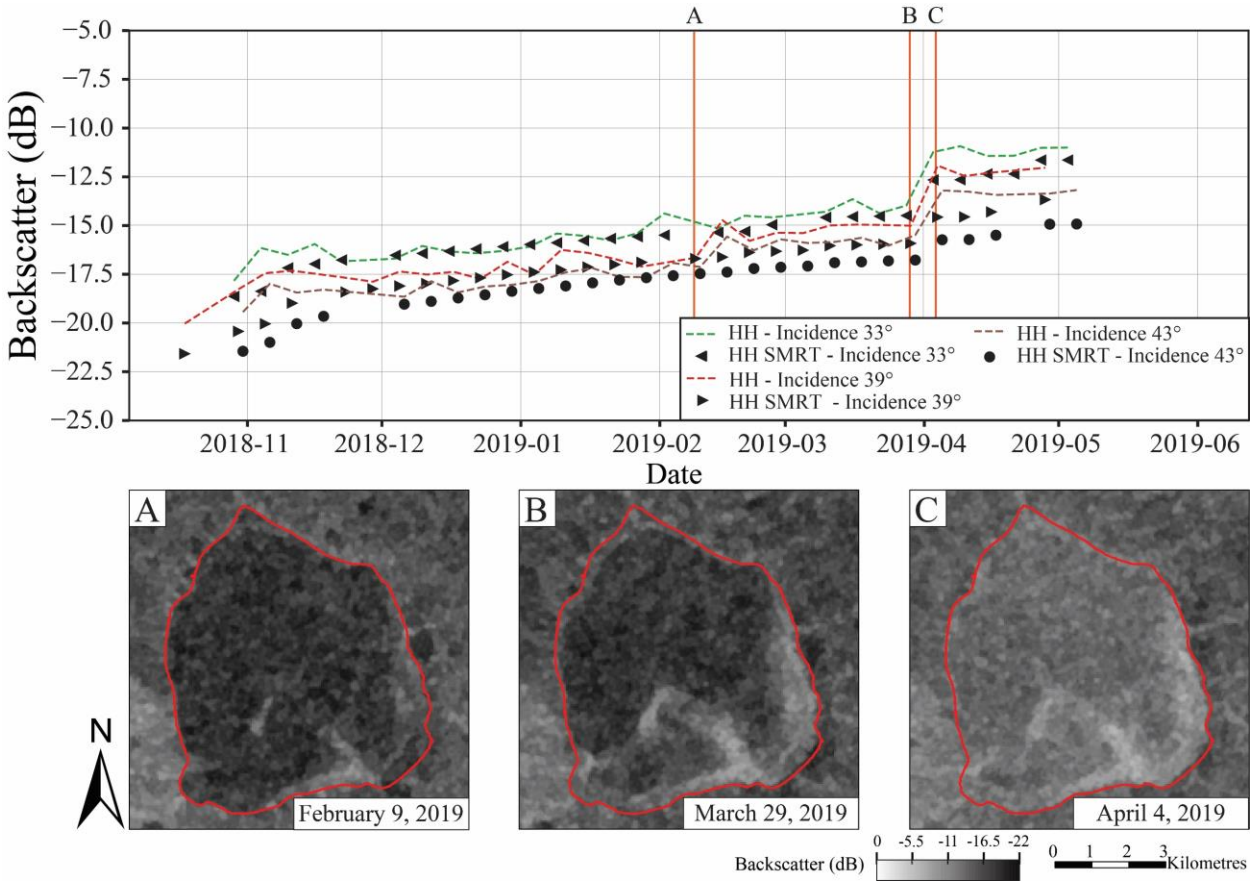

Figure 5.11 Modelled and observed backscatter for 33°, 39°, and 43° incidence angles highlight the increase in backscatter that occurs after the end of March. Sample images A, B, and C demonstrate the brighter tones observed for the lake between dates throughout the ice season. Data are from Copernicus Sentinel-1 (2019), processed by ESA.

Another explanation is that the fluctuating temperatures resulted in a change in ice surface roughness or change in snow surface roughness. This could explain the large increase in optimal ice-water interface RMSH observed on April 3 from 1.05 mm to 1.65 mm as an attempt to compensate for the increase in backscatter observations. Malcolm Ramsay Lake also shows an increase in ice-water interface RMSH following a period of warmer temperatures, maximum temperatures of 1.1 to 6.1 °C observed between March 12 and March 16, followed by a return to lower maximum temperatures reaching -19.1 °C the following week. This could cause similar

changes in the ice surface properties or snowpack properties for Malcolm Ramsay Lake. Ice-water interface RMSH for Malcolm Ramsay Lake increases by between 0.35 and 0.9 mm for dates between late February and March 17 (corresponding to images acquired on or after March 20). Similar to Noell Lake, C-band images for Malcolm Ramsay Lake show the appearance of brighter tones (**Figure 5.12**). Observations of ice surface RMSH during spring thaw have been noted an increase by 0.5 mm for floating ice covers (Wakabayashi et al., 1999). Past research has also noted that melt and refreeze can result in a rougher snow surface causing an increase in backscatter (Duguay et al., 2002; Antonova et al., 2016). Another possible explanation for the jump in RMSH is that warming water temperatures corresponding to increasing temperatures could create ripples or dunes on the underside of the ice sheet (Ashton, 1986); however, this cannot be verified for Noell Lake and Malcolm Ramsay Lake. The uncertainty around the impact of freeze-melt events and warming temperatures on key ice and snow properties (RMSH, increased water content, changes in ice and snow stratigraphy) indicate that further field data are needed to properly understand how to represent these changes in lake ice and snowpack properties within SMRT. The complexity of these processes indicate that more research is needed to properly model conditions and is beyond the scope of this study.

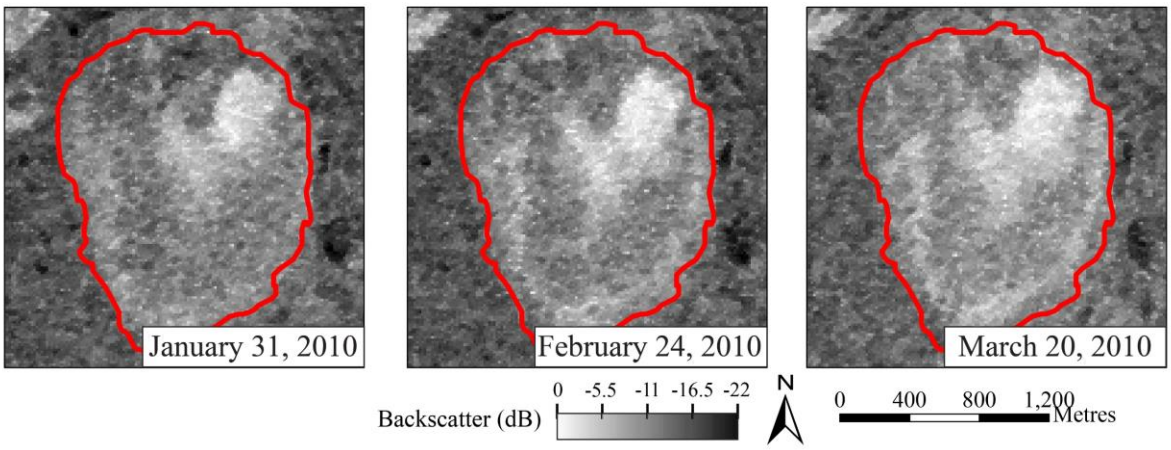

Figure 5.12 Change in image tones before the melt-refreeze event (January 31 and February 24) and after the event (March 20) for Malcolm Ramsay Lake. RADARSAT-2 Data and Products © MacDonald, Dettwiler and Associates Ltd. (2010) – All Rights Reserved.

Modelling backscatter during ice decay also posed challenges during this study. For both lakes, higher temperatures result in the start of the melt process with snowpack entering the pendular regime, and a decrease in backscatter due to increased water content in the snow layer, increasing the lossy imaginary component of the relative permittivity and thereby increasing signal absorption. RADARSAT-2 images for Noell Lake during late May and early June demonstrate the evolution of SAR backscatter during the melt period, with darker tones showing high snow water content and a switch to bright tones as the water drains from the ice cover (**Figure 5.13**). Due to these reasons, the images after May 8 were excluded from the validation of SMRT backscatter. For Malcolm Ramsay Lake, there is a large disagreement for C-band backscatter at site 4 on April 13, 2010, where modelled backscatter is higher than the observed by >3.3 dB. This image was also excluded from the validation of modelled backscatter. Future work should investigate the representation of snow and ice conditions during spring melt within the SMRT framework.

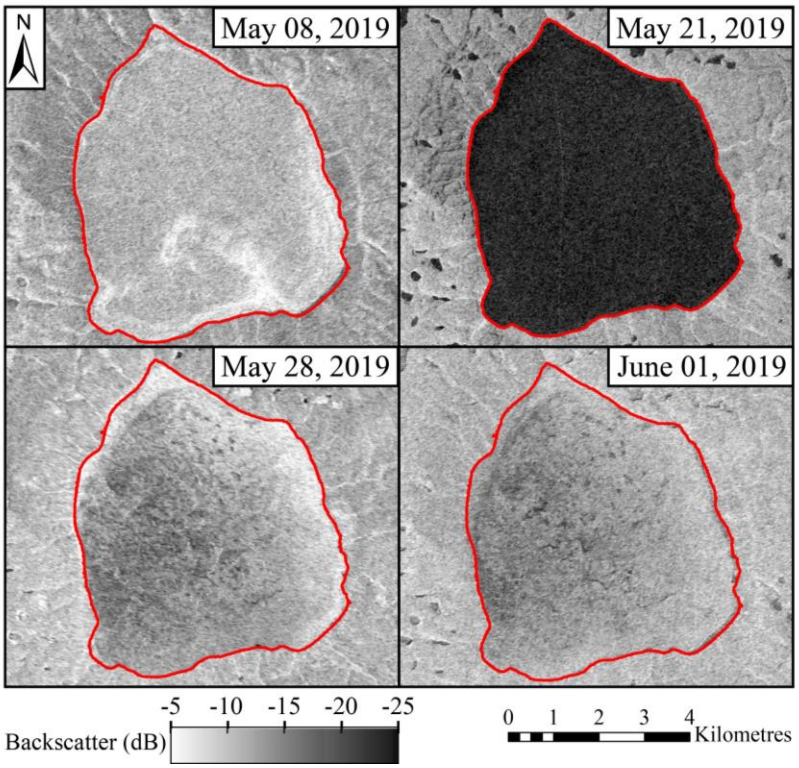

Figure 5.13 SAR co-pol backscatter evolution for Noell Lake during the melt period. RADARSAT-2 Data and Products © MacDonald, Dettwiler and Associates Ltd. (2019) – All Rights Reserved

5. Conclusions and Future Work

This research is the first application of the Snow Microwave Radiative Transfer (SMRT) model for utilization in forward modelling of active microwave backscatter from lake ice throughout an ice season. The application of SMRT was tested for two freshwater lakes with and without tubular bubble development near the ice-water interface, Noell Lake and Malcolm Ramsay Lake respectively. This was done for L, C, and X-band frequencies across a range of incidence angles for conditions prior to melt events in early May.

For Noell Lake modelling focused on C-band for the 2018-2019 season using RADARSAT-2 and Sentinel-1 data for validation. Optimized RMSH values were found to be <= 2 mm. RMSE between the observed and modelled backscatter ranged from 0.38 to 1.45 dB with Spearman's ρ greater than 0.91 ($p<0.01$) for all tested incidence angles. Diverse frequencies (L, C, and X-band) were available for Malcolm Ramsay Lake and backscatter was modelled well for these frequencies despite a limited number of optimized parameters. Optimal RMSH values were higher compared to Noell Lake, reaching 5.5 mm for one of the field sites. These higher values are expected due to the development of tubular bubbles at Malcolm Ramsay Lake. RMSE between the observed and modelled backscatter were slightly higher for Malcolm Ramsay Lake compared to Noell Lake, ranging from 0.70 to 2.33 dB. These results are similar to past studies (Gunn, Brogioni, et al., 2015; Tian et al., 2015), however, the results of this paper demonstrate the advantages of using an increasing RMS height at the ice-water interface not dependent on increases in other ice properties (i.e. ice thickness). This was found to be a better representation of RMSH evolution compared to constant RMSH at the ice-water interface as it captured increasing backscatter at the start of the ice season and the more stable RMSH during the middle of the season. Modelled backscatter using an increasing RMSH was closer to observed backscatter by 0.6 to 2.9 dB. However, this method of optimization may poorly compensate for other effects. For example, Mid-season melt events and generalized melt in May were found to be the largest limitation in

modelling for both lakes. Fluctuating temperatures likely resulted in changes of the ice and snow surface conditions (air-snow interface, ice-snow interface roughness and surface ice types). These surface changes resulted in large increases in RMSH for both lakes, likely as an overcompensation to account for increased backscatter.

These results reveal areas for further investigation with the framework of SMRT for modelling backscatter from freshwater ice. Future exploration of roughness at multiple interfaces will help to address the previously discussed issues and improve the representation of ice columns within the model. Research is needed on how melt-freeze events and generalized melt impact ice surface and overlying snowpack conditions so that these aspects can be properly incorporated into the model as well as how to properly represent interface roughness under these conditions. Also identified is the need to develop a technique of easily and accurately measuring in situ ice-water interface roughness, this has also been suggested as part of past studies (e.g. Gunn et al., 2018). While images of the ice-water interface provide some qualitative insight, quantitative data on this property will be key for future parameterization of backscatter models for lake ice. Good representation of backscatter from lake ice using SMRT under dry conditions shows that the modelling framework is a strong candidate for inversion modelling, allowing for the retrieval of lake ice properties such as ice-water interface roughness and surface ice conditions throughout the ice season.

Chapter 6 Forward Modelling of SAR Backscatter during Lake Ice Melt Conditions using the Snow Microwave Radiative Transfer (SMRT) Model

6.1 Introduction

There is increasing interest in the study of lake ice across different latitudes. Both lakes and lake ice act as important controls of local climate and energy balance, impacting local precipitation amounts and temperatures (Rouse et al., 2008; Eerola et al., 2014; Baijnath-Rodino et al., 2018). Beyond the impact on local conditions, lake ice provides crucial ecological services across the northern hemisphere. The formation of lake ice is crucial to the establishment of ice roads which aid in the transportation of goods and people during winter months. The majority of the Tibbitt to Contwoyto Winter Road in the Northwest Territories, Canada is constructed over ice and provides a supply line to mining operations; over 3800 tonnes of material was hauled on the road during the 2020 season (Tibbitt to Contwoyto Winter Road Joint Venture, 2020). The formation of lake ice at mid-latitudes is also important for recreational activities such as ice fishing and snowmobiling which are major contributors to local economies in winter months (Cummings et al., 2019). Furthermore, under the World Meteorological Organizations Global Climate Observation System (GCOS) both lake ice cover and lake ice thickness are named as thematic products of lakes as an essential climate variable (ECV), meaning that it is important to have accurate and consistent records of changes in these variables to act as indicators of climate change (World Meteorological Organization, 2022).

While long-term ice phenology records >500 years do exist for a small sample of lakes (Sharma et al., 2022), observations of lake and river ice phenology have been declining since the 1980s (Murfitt & Duguay, 2021). These observations remain critical as warming climate is resulting in later ice formation and earlier ice decay, leading to shorter ice seasons (Hewitt, 2019; Lopez et al., 2019). These patterns are expected to continue into the future under different climate modelling scenarios (L. C. Brown & Duguay, 2011b; Dibike et al., 2012). One possible issue for

the use of lake ice with increasing temperatures is that the occurrence of mid-winter melt events and slushing events, most common at mid-latitudes (Ariano & Brown, 2019), will increase. Increased occurrence of these events could pose serious safety risks to the use of lake ice for transportation and recreation.

Although ground observations of lake ice phenology have declined in recent decades, the use of remote sensing technologies has become more popular. Optical, passive microwave, and active microwave have shown to be capable of determining lake ice phenology dates and ice cover extents (Du et al., 2017; M. Hoekstra et al., 2020; Wu et al., 2021). Active microwave data, specifically synthetic aperture radar (SAR), is the most popular choice of the three due to several reasons. For example, unlike optical imagery, it does not require sunlight to image the ice surface and can do so under most weather conditions. Additionally, SAR imagery provides resolutions of <50 m for most image products allowing for the delineation of small and medium lakes (Murfitt & Duguay, 2021). In recent years there has been a shift in the understanding of how active microwave signals interact with lake ice. Initial investigations of lake ice in the 1980s using X and L-band side-looking airborne radar systems connected high radar returns to the presence of tubular bubbles in the ice, stating that bright signals in the imagery were due to a double-bounce scattering mechanism (Weeks et al., 1981). This double-bounce was created as the radar signal interacted with the vertical tubular bubbles and then with the ice-water interface where there is a high dielectric contrast between the ice and water. Further investigations using spaceborne C-band systems (ERS-1 and RADARSAT-1) continued to support this theory and quantified the backscatter observed from lake ice (Jeffries et al., 1994; Duguay et al., 2002). However, in more recent years with the advent of fully polarimetric SAR data, new research has analyzed the scattering contributions from lake ice and determined that the dominant mechanism is a single bounce or surface scattering mechanism (Engram et al., 2012; Atwood et al., 2015; Gunn et al., 2018). This is attributed to roughness at the ice-water interface. Explanations for the roughness at this interface include the presence of tubular bubbles in the lower layers of the ice, methane ebullition bubbles, and differing rates of ice growth (Engram et al., 2012, 2013; Gunn et al., 2018).

Modelling approaches provide a further valuable opportunity to explore the impact of changing ice properties (ice thickness, roughness, bubble size) on backscatter from lake ice. The results of recent modelling studies support the new polarimetric decomposition results, finding that the presence of elongated tubular bubbles at the ice-water interface has little impact on the backscatter from lake ice and that roughness of the ice-water interface is the key factor (Atwood et al., 2015; Tian et al., 2015). However, past modelling approaches have several limitations where applied models ignore different aspects of the lake ice column. For example, models have not factored in the presence of snow, ignored roughness of different interfaces, or considered the ice column to be a single homogenous layer. Recently the snow microwave radiative transfer (SMRT) model was used to conduct sensitivity analysis for lake ice under dry conditions (Murfitt et al., 2022). SMRT provides a framework where different electromagnetic, microstructure, and interface models can be used, allowing for more faithful modelling of true conditions. Results of the recent sensitivity analysis using SMRT were found to be consistent with the results of other lake ice modelling and satellite observations, supporting the crucial role of the ice-water interface (Murfitt et al., 2022).

While recent modelling has focused on the roughness of the ice-water interface, increased water content and the representation of melt conditions has been largely ignored. Wakabayashi et al. (1999) used the integral equation model (IEM) for surface scattering to investigate scattering mechanisms from floating and grounded ice cover on the North Slope of Alaska. Simulations indicated that for both ice conditions the inclusion of water on the ice surface, either in a limited area or across the entire ice cover, results in an increase in backscatter (Wakabayashi et al., 1999). More recently, Han and Lee (2013) investigated the role that ice phase transition plays on backscatter due to changes that occur in the dielectric constant and roughness conditions using a ground-based C-band scatterometer. Similar to Wakabayashi et al. (1999), IEM was also used for the experiments conducted on Chuncheon Lake in South Korea. Changes of phase were simulated by spreading a thin layer of water on the top of the ice cover and analysis showed that when the water was initially spread on the ice, scattering from the top of the ice surface was strong due to the high dielectric constant (Han & Lee, 2013). However, as the water froze, ice-bottom and

volume scattering increased due to more transmission of the signal through the ice column (Han & Lee, 2013). The experiments in Alaska and South Korea provide important insights into how changes in water content can impact the backscatter signal from lake ice. However, these experiments have certain limitations, for example representations of the snow cover. Further research is still needed to explore a range of ice cover conditions throughout the winter season. Additional sensitivity tests parameterized using collected field data can provide additional insights and confirmation of how radar backscatter over ice cover is impacted by wet conditions.

SMRT allows us to address these gaps and work toward modelling a complete picture of ice conditions during melt events. Previously mentioned lake ice studies using SMRT only evaluated changes in backscatter under dry conditions (Murfitt et al., 2022). Therefore, experiments during wet conditions are an important next step in the application of this model for lake ice cover. The objective of this paper is to use field data collected for Lake Oulujärvi in Finland to determine how changes in the water content of snow overlying ice cover and the appearance of slush layers impact backscatter. To meet this objective, sensitivity tests are conducted to understand how backscatter changes with increases in snow water content and interface roughness. These modelling results are compared to observed Sentinel-1 backscatter during different field conditions, providing support for the results of the sensitivity analysis and insight into the connection between ice conditions and backscatter during the 2020-2021 field season.

6.2 Methods

6.2.1 Snow Microwave Radiative Transfer (SMRT) Model

The Snow Microwave Radiative Transfer (SMRT) model is an active-passive model for conducting simulations of microwave intensities from snowpacks. A full description of the model can be found in Picard et al. (2018). The model also allows for the inclusion of freshwater and saline ice layers that can be combined with snowpacks to properly represent observed conditions (Murfitt et al. 2022; Soriot et al., 2022). The model is run within a python environment and allows

for user flexibility by allowing model runs to be set using different electromagnetic models (e.g., improved Born approximation, DMRT) and microstructure models (e.g., exponential, and sticky hard spheres). The user-selected electromagnetic model is parameterized using the selected microstructure model and user defined properties (medium temperature, thickness, density, volumetric liquid water content, etc.). The electromagnetic model is used to determine the necessary electromagnetic quantities, such as the scattering coefficient, absorption coefficient, and phase matrix (Picard et al., 2018). Roughness and associated reflectivity and transmissivity coefficients within the defined snow and ice columns are set using either Fresnel equations, the integral equation model (IEM), or Geometrical Optics (Fung et al., 1992; Tsang & Kong, 2001; Picard et al., 2018). Roughness can be set between different layers of a single medium, at the interface between two mediums (e.g., snow-ice interface), or between a medium and the underlying substrate (e.g., ice-water interface). SMRT uses the discrete ordinate and eigenvalue (DORT) method to solve the radiative transfer equation once the necessary parameters have been solved in the other components of the model. The user can create a custom sensor to parameterize the model (e.g., specific frequency, incidence angle, and polarization) or choose from a list of pre-defined sensors. Resulting intensity from SMRT can be obtained from all or specific directions from the defined snowpack or ice column (Picard et al., 2018). This study only evaluated modelled co-pol backscatter because cross-pol is under modelled with the current implementation of IEM in SMRT which is used for parameterization of interface roughness as discussed below. Additionally, experiments assume that there were no tubular bubbles present in the ice column because SMRT does not currently allow for the inclusion of vertically oriented bubbles and the impact of these bubbles has been demonstrated to be limited (Atwood et al., 2015; Murfitt et al., 2022).

This study uses the improved Born approximation for the electromagnetic model in SMRT. This model is utilized to allow for a broader exploration of volumetric water content (VWC) within SMRT. Under dry conditions, the real and imaginary components of permittivity for snow grains and ice mediums is determined using the formulations given in Mätzler et al. (2006). However, this cannot be used for wet snow mediums that mix air, ice, and water. SMRT was recently updated to include several models for addressing the mixing of these different

components in snow mediums (Picard, Leduc-Leballeur, et al., 2022). While the results of these models are different, there is agreement that increases in the VWC increase both the real and imaginary components of a medium's permittivity. This study uses the MEMLS v3 permittivity model for wet snow conditions (Mätzler & Wiesmann, 2007). Following Picard et al. (2022), this model was selected because it is based on real measurements and provides reliable performance at higher water content values. Both the sticky hard spheres (SHS) and exponential microstructure models were utilized in this study (Picard et al., 2018; Picard, Löwe, & Mätzler, 2022). SHS was used specifically for ice mediums due to its use in past RT modeling studies (Gunn et al., 2015; Murfitt et al., 2022). SHS is parameterized using the stickiness parameter (τ) which is a representation of the tendency of spheres within the medium to cluster. Increased values of τ indicate a lower tendency of spheres to stick together. The microstructure of snow mediums was parameterized using the exponential microstructure model. This model was used due to the availability of detailed snow pit measurements during the 2020-2021 ice season. Density and SSA measurements were used to calculate the effective correlation length (p_{ex}) and parameterize the microstructure model, this is discussed further in section 2.5.

Roughness of different interfaces within the ice and snow mediums for this study were represented using IEM with an exponential autocorrelation function. IEM was selected because it is better suited to small roughness values and has been used in previous freshwater ice and snow modelling studies (Gherboudj et al., 2010, Murfitt et al., 2022). As such this study will focus on variations in small scale roughness of interfaces within the snow and ice column. IEM is parameterized using root mean square height (RMSH) which is the approximation of vertical variation of surface roughness and interface correlation length which is the horizontal displacement between two points on the rough surface (Ulaby & Long, 2014). The validity of IEM is maintained when $k*RMSH < 2$ and $k^2 * RMSH * Correlation\ Length < \sqrt{eps_r}$, where k is the wavenumber and eps_r is the ratio between the permittivity of the mediums at the interface (Fung et al., 1992; Fung & Chen, 2010). The range of IEM is extended in SMRT using the method stated in Brogioni et al. (2010), where the Fresnel coefficients are determined using either the

incidence angle ($k^2 * RMSH * Correlation\ Length < \sqrt{eps_r}$) or an angle of 0° ($k^2 * RMSH * Correlation\ Length > \sqrt{eps_r}$). This extension was first developed for Advanced IEM (AIEM), as such caution should be used when applying this extension as the precise validity on the original IEM has not been verified.

6.2.2 Study Site

This study focuses on Lake Oulujärvi (27.25° E, 64.29° N), which is one of the largest lakes in Finland (**Figure 6.1**). Lake Oulujärvi is located 473 km north of Helsinki and the outflow of the lake is to the Oulujoki River which drains into the Gulf of Bothnia (Hyvaerinen, 2004). The lake has a surface area of 928 km^2 with a mean depth of 7.6 m that can range up to 36 m (Hyvaerinen, 2004). Historical data for the lake indicates that the average date of freeze-up ranges from November 10 to 20 and average date of break-up ranges from May 15th and 20th (Korhonen, 2005, 2006). The average thickness of the ice cover on the lake is between 60 and 70 cm (Korhonen, 2005, 2006). However, trends in the date of freeze-up and break-up over the last 150 years indicate that freeze-up is shifting later and break-up is shifting earlier (Korhonen, 2006). Climate normals (1981 – 2010) for the Kajaani meteorological station, 23 km east of the main basin of Lake Oulujärvi, show that maximum average temperatures of 20.8 °C occur in July and minimum average temperatures of -15.2 °C occur in January (Pirinen et al., 2012). Maximum snow depth is reported during March, reaching an average of 53 cm during the 1981 – 2010 normals period (Pirinen et al., 2012).

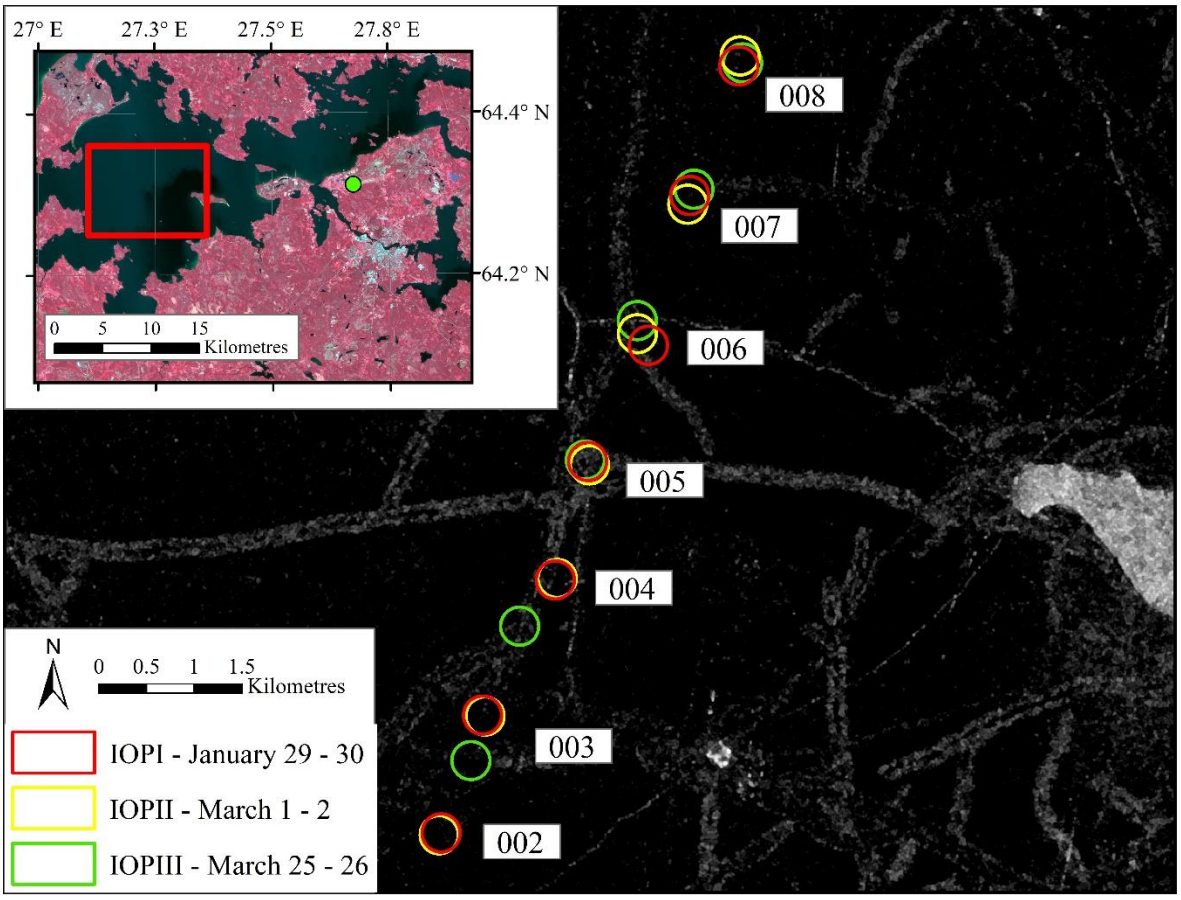

Figure 6.1 In Situ data collection locations on Lake Oulujärvi during the 2020-2021 ice season. This figure contains Copernicus Sentinel-1 data (2021), processed by ESA.

6.2.3 SAR Imagery

To provide a record of backscatter for the 2020 - 2021 ice season on Lake Oulujärvi and a point of comparison for the modelled results, 134 Sentinel-1 (C-band, 5.405 GHz) images were downloaded from the Alaska Satellite Facility (https://asf.alaska.edu/) between December 13, 2020, and May 7, 2021. Sentinel-1 Extra Wide (EW) images have a pixel spacing of 40 m and there was an average of 2 days between images. Interferometric Wide (IW) swath images, pixel spacing 10 m, were also acquired with a gap of 2.4 days (some days had two images available).

The combination of both image sets results in a temporal gap of 1.09 days for Lake Oulujärvi. The Sentinel-1 images were preprocessed using the Sentinel Application Platform (SNAP, European Space Agency, 2020), with images being σ° calibrated and speckle filtered with the Refined Lee filter (Lee, 1981). Terrain correction was performed using the ACE30 DEM and both IW and EW images were resampled to a pixel spacing of 40 m to ensure consistency between datasets.

Incidence angles for both datasets ranged from 24 to 43°, this difference in incidence angle resulted in fluctuations in the backscatter extracted from the lake ice sites. To address these fluctuations, linear regression was used to normalize the backscatter. This method has been applied for both Arctic sea ice, high Arctic lakes, and mid-latitude small/medium-sized lakes (Mahmud et al., 2016; Murfitt et al., 2018b; Murfitt & Duguay, 2020). Two hundred points were randomly generated across Lake Oulujärvi to serve as sample sites. These sample sites were at least 300 m from shore and not within 40 m of each other to prevent shoreline contamination and repetition of samples. The backscatter and projected incidence angle were extracted from these sites for each image in the acquired set, resulting in a total sample size of 26,800. Only images where there was full ice cover on the lake were used. The resulting samples were then split into a training and testing set of 70 and 30% respectively. The training set was then used to develop a linear regression representing the impact of incidence angle on backscatter for Lake Oulujärvi. The linear regression showed a slope of -0.34 dB/° ($R^2 = 0.26$, $p < 0.01$. RMSE = 3.33 dB), this slope is similar to past corrections for Sentinel-1 imagery acquired over Lake Hazen of -0.35 dB/° (Murfitt & Duguay, 2020). For the correction of IW and EW images, the median incidence angle of all samples was used, 36.31°. Around each of the sites shown in **Figure 6.1**, a 200 m buffer was generated to extract average, maximum, and minimum normalized linear intensity values which were converted to backscatter (dB).

6.2.4 In Situ Data: 2021 Field Campaign

During the 2020 – 2021 ice season a field campaign was conducted to collect in situ data on snow and ice cover for Lake Oulujärvi. The field campaign took place during three observation periods (IOPI, IOPII, and IOPIII). The first observation period, IOPI, occurred on January 29 and

January 30, the second observation period, IOPII, occurred on March 1 and 2, and the final observation period, IOPIII, occurred on March 25 and 26. For IOPI and IOPIII measurements of ice thickness and the thickness of layers (snow and clear ice) were taken approximately every 400 to 900 m. For IOPII, ice thickness measurements were made every 1200 to 1600 m. In addition to ice thickness measurements, snow depth and bulk density were also recorded at each of these locations. During IOPII, a SnowHydro Magnaprobe (Sturm & Holmgren, 1999) was used to collect snow depth measurements approximately every 5 m. For IOPIII, 10 snow depth measurements were recorded using a manual probe every 100 m along the study transect. For the purposes of this study only the points shown in **Figure 6.1** are used, this is due to the availability of matching snow pit data discussed below. Additionally, the points selected incorporated locations where both dry snow and wet snow conditions were observed throughout the ice season. A summary of the ice thickness and snow depth and bulk density data collected on each IOP is provided in **Table 6.1**.

Table 6.1 Summary of snow and ice data collected during the 2021 field campaign on Lake Oulujärvi. Density values show bulk density measurements made at the ice thickness measurement sites.

	Ice Thickness (m)	Snow Ice Thickness (m)	Snow Depth (m)	Snow Density (kg m^{-3})
IOPI				
January 29	0.31	0.03	0.26	183.63
January 30	0.30	0.03	0.29	185.45
Average	0.30	0.03	0.27	184.49
IOPII				
March 1	0.35	0.06	0.39	256.33
March 2	0.37	0.03	0.33	228.81

Average	0.35	0.05	0.36	245.07
IOPIII				
March 25	0.43	0.10	0.25	322.28
March 26	0.40	0.02	0.37	312.75
Average	0.42	0.07	0.31	319.27

In addition to these measurements, detailed snow pit data were collected for the sites identified in **Figure 6.1**. Data were collected for each layer of the snowpack through manual means and through the IceCube instrument (Gallet et al., 2009). This study relied on the layer properties such as specific surface area (SSA), layer temperature, water content, density, thickness, maximum and minimum grain size, and grain type. However, these data were inconsistent and missing for some sites due to conditions not allowing for the accurate collection of these properties. The collected data were used to investigate the relation between SSA, and density as discussed further in section 2.5. Additionally, these data provided key information about the temperature of the snowpacks. During IOPI, the average temperature was 270.22 ± 2.11 K. The average density was 214.09 ± 77.56 kg m^{-3} and average SSA was 34.34 ± 11.88 m^2 kg^{-1}. For IOPII, temperatures increased to an average of 272.09 ± 1.47 K, temperatures were higher on March 1 reaching 273.20 K. Density was higher for IOPII with an average of 296.89 ± 47.82 kg m^{-3}, with a higher average density of 305.53 kg m^{-3} on March 1. SSA decreased for IOPII to an average of 14.96 ± 11.88 m^2 kg^{-1}, average SSA was higher on March 1 at 17.37 m^2 kg^{-1}. Finally, on IOPIII, temperatures further increased to 272.51 ± 1.03 K, however, data were only available on March 25. Average density was highest for IOPIII with an average of 335.16 ± 61.48 kg m^{-3}. Average SSA was similar to IOPII at 14.46 ± 2.28 m^2 kg^{-1}, however, was only available for one site.

6.2.5 SMRT Experiments

To study how wet conditions impact the backscatter from lake ice, three distinct experiments were conducted. Each experiment reflects conditions that were observed during the field campaign in 2021. The field data described in section 2.4 were used to parameterize SMRT for the respective dates when each condition was observed. Additionally, snowpack observations across the lake were generalized to create a single snowpack for each of the different experiments. For each IOP the snow depth was determined by averaging the most detailed data available (i.e., manual or magnaprobe measurements). The temperature of the snowpack was determined by averaging the available measurements from the snow pit analysis. While water content was one of the measured parameters, the values were not successfully recorded and therefore qualitative observations were relied on for determining the state of the snow layers. The key inputs for SMRT are the layer thickness (i.e., snow depth and ice thickness), snow density, p_{ex}, layer temperature (i.e., snow and ice temperature), ice porosity, spherical bubble radius, VWC, roughness parameters, and ice layer stickiness. For ice layers, to properly parametrize the sticky hard spheres microstructure model, a value of stickiness (τ) had to be decided. Due to clear ice being considered as inclusion free, the layer was assigned a τ of 1, which corresponds to relatively random positions of the bubbles. Snow ice on the other hand can have an increased presence of spherical bubbles and therefore a value of 0.4 was used. Parameterization of the snow microstructure model will be discussed later in this section.

The majority of parameters were collected during the field campaign, except for ice temperature and p_{ex}. Ice temperature was determined using the Canadian Lake Ice Model (CLIMo, Duguay et al., 2003). CLIMo is a 1-D model that uses an unsteady heat conduction equation (Maykut & Untersteiner, 1971) and surface energy budget to determine layer boundary temperatures, ice thickness, and snow depth throughout an ice season. For the purposes of this study the main output used is the ice layer boundary temperatures. For Lake Oulujärvi, CLIMo is parameterized using both daily averaged ERA5 data (Hersbach et al., 2020) for temperature (C), humidity (%), cloud cover (0-1), and wind speed (m/s). The snow accumulation input for CLIMo

was determined using local meteorological data from the Kajaani weather station located 23 km southwest from the field sites. CLIMo was run using a mixing depth of 7 m and a snow density of 150 kg/m^3, which reflected values observed for dry snow cover during the 2021 field campaign. Validation data is limited to only dates where field data was collected and showed good comparison with ice thicknesses estimated by CLIMo, with an average difference of 0.03 m. Snow depth in CLIMo is underestimated compared to field measurements, likely due to the distance between the meteorological measurements and the location of the field measurements and a single value for snow density being used, the average difference was 0.12 m. While this difference is large, thermodynamic modelling is the best alternative for determining layer temperatures and was used as the input for ice temperature in SMRT. CLIMo was run to produce a five-layer ice column, however, only snow and clear ice measurements were taken from Lake Oulujärvi. Therefore, the temperatures for the boundary of layers 1 and 2 were averaged to determine a snow ice layer temperature and the temperatures for the boundaries between layers 2 - 5 were averaged to produce a temperature for the clear ice layer.

To properly parameterize the exponential microstructure model used in SMRT for the snow layers, p_{ex} is needed. Correlation length can be determined using relations determined between this parameter and grain size in Mätzler (2002). Following the SMRT simulations in Rutter et al. (2019), p_{ex} was calculated using **Equation 6.1**:

$$p_{ex} = 0.75 \left(\frac{4 * \left(1 - \frac{\rho}{\rho_{ice}}\right)}{SSA * \ \rho_{ice}}\right) \quad \textbf{(6.1)}$$

where ρ_{ice} is the density of the ice, assumed to be 916.7 kg m^{-3}, ρ is the density of the snow layer, and SSA is the specific surface area (m^2 kg^{-1}). The empirical coefficient 0.75 was confirmed as a possible value for fine grained snow by recent theoretical investigations (Picard, Löwe, & Mätzler, 2022). When SSA values were unavailable, snow density is used to estimate the SSA value through a logarithmic regression. In past SMRT experiments, regressions developed for terrestrial snow have been applied to lake ice snow covers (Murfitt et al., 2022). Concern has been raised that these

representations may not reflect the differences between these two systems (i.e., wind redistribution, and differences in snow structure). Therefore, for the SMRT experiments over Lake Oulujärvi, SSA values acquired during the 2021 field campaign were used to develop a similar regression as this will better represent the relation between snow properties over ice cover. In total 78 samples were used, and the resulting regression is shown in **Equation 6.2** ($R^2 = 0.41$):

$$SSA = -24.00 \ln(\rho) + 156.09 \quad \textbf{(6.2)}$$

Vargel et al. (2020) developed an equation using observations for terrestrial Canadian Subarctic and Arctic snow, shown by **Equation 6.3**:

$$SSA = -17.65 \ln(\rho) + 118.07 \quad \textbf{(6.3)}$$

The difference in coefficients between these two relations indicates that these snow systems may be dissimilar. Further collection of snow microstructure data over lake ice is an area of continued interest to better understand the distinction between snow cover on lake ice and terrestrial snow and represent this in modelling experiments. **Equation 6.2** was used to determine an SSA values for the generalized snowpack and **Equation 6.1** was used to calculate the p_{ex} for each of the experiments.

For use in SMRT the generalized snowpack was split into two layers. Two layers were used so that wet snow could be added at different depths in the snowpack (section 2.5.2). The following subsections detail the experiments performed during the different observation periods for the 2020-2021 ice season. **Figure 6.2** below provides a graphical representation of these different experiments indicating the location of wet snow layers and rough interfaces using Site 005 (see Figure 1) as an example. **Table 6.2** details the snow and ice layer parameters for the different IOPs and **Table 6.3** shows the ice thicknesses for each site across the IOPs.

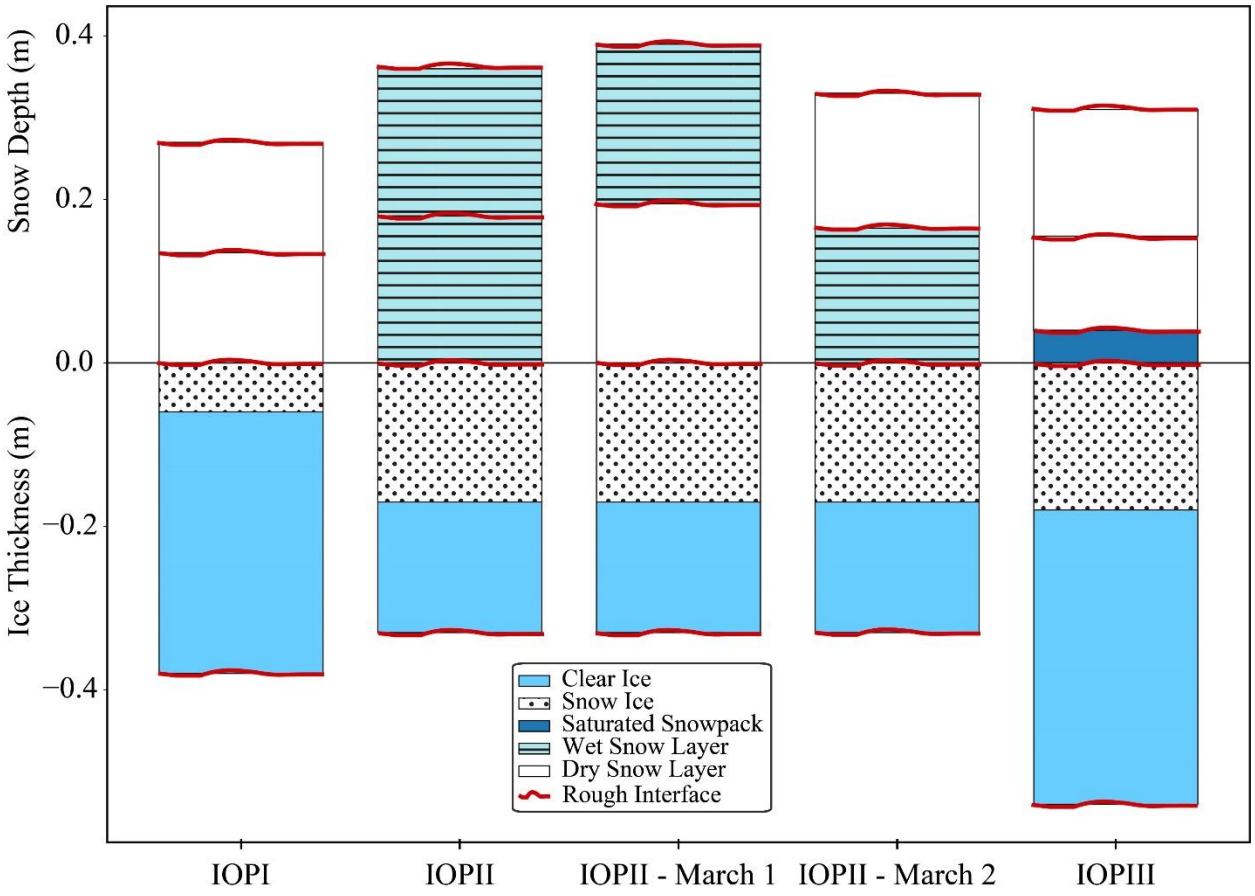

Figure 6.2 SMRT simulations for the different experimental conditions using observations from the 2021 field campaign. The ice columns displayed are representative of Site 005 (Figure 1). Red lines indicate where rough interfaces were added for each of the different scenarios.

Table 6.2 Constant snow and ice parameters for during IOPs conducted for the 2021 ice season.

Physical Property	**IOPI**	**IOPII**	**IOPIIa**	**IOPIIb**	**IOPIII**
Snow Depth (m)	0.274	0.362	0.388	0.332	0.311
Wet Snow Density (kg m^{-3})		296.89	320.95	218.17	354.81
Dry Snow Density (kg m^{-3})	184.5		269.56	295.97	317.48
Wet Snow SSA (m^2 kg^{-1})		14.96	18.19	10.16	15.86

Dry Snow SSA (m^2 kg^{-1})	30.47		15.47	13.95	18.34
Wet Snow Temperature (K)		273.15	273.15	273.15	271.94
Dry Snow Temperature (K)	270.22		272.99	271.02	273.15
Snow Ice Temperature (K)	272.85	272.76	272.77	272.76	272.82
Clear Ice Temperature (K)	272.88	272.91	272.91	272.91	272.95

Constant Snow RMSH (mm)	1.00
Constant Snow Correlation Length (mm)	10.00
Snow-Ice Correlation Length (mm)	50.00
Correlation Length Ice-Water Interface (mm)	70.00
Bubble Radius (mm)	1.00
Snow Ice Porosity (%)	10

Table 6.3 Snow and clear ice thickness observed during each IOP.

	IOPI		**IOPII**		**IOPIII**	
Ice Thickness (m)	**Snow Ice**	**Clear Ice**	**Snow Ice**	**Clear Ice**	**Snow Ice**	**Clear Ice**
Site 002	0.01	0.27	0.08	0.19	0.03	0.40
Site 003	0.05	0.28	0.01	0.32	0.02	0.39

Site 004	0.01	0.28	0.00	0.51	0.04	0.37
Site 005	0.06	0.32	0.17	0.16	0.18	0.36
Site 006	0.00	0.29	0.00	0.32	0.10	0.32
Site 007	0.00	0.32	0.01	0.35	0.02	0.36
Site 008	0.09	0.25	0.06	0.33	0.02	0.34

6.2.5.1 Dry Snow Conditions

The first experiment reflected dry snow conditions that were observed on Lake Oulujärvi on January 29 – 30 and is represented by IOPI in **Figure 6.2**. The constant values determined from the field data can be found in **Table 6.2**. Snow and clear ice thickness varied depending on the site SMRT was run for, the site-dependent values sites can be found in **Table 6.3**. Snow density values were determined by averaging the snow bulk density measurements. RMSH and correlation length of the air-snow interface were not varied for these conditions as the impact of this interface was assumed to be negligible due to the relatively small difference in permittivity between air and dry snow. The RMSH for the air-snow interface was set to 1 mm and the correlation length to 10 mm. The correlation length of the snow-ice interface was set to 50 mm.

While the above parameters were available for dry snow conditions, information on the RMSH and interface correlation length for both the snow-ice interface and ice-water interface, snow ice porosity, and snow ice bubble radius were unknown. Therefore, these properties were varied to determine the optimal values for the ice cover on Lake Oulujärvi. The ranges of these properties can be found in **Table 6.4**. These ranges were selected due to past observations of snow-ice RMSH (Wakabayashi et al., 1999) and past experiments conducted using SMRT that showed likely ranges for deeper lakes (Murfitt et al., 2022).

Table 6.4 Tested ranges for unknown properties under dry snow conditions.

Unknown Property	Property Range (Interval)
Snow-Ice RMSH (mm)	1.0, 2.0, 3.0
Ice-Water RMSH (mm)	0.5 – 2.5 (0.01)
Ice-Water Correlation Length (mm)	10, 30, 50, 70, 100
Snow Ice Bubble Radius (mm)	0.5, 1.0, 1.5, 2.0
Snow Ice Porosity (%)	1, 3, 5, 7, 10

The modelled backscatter was compared to observed Sentinel-1 backscatter to select values for the unknown properties. One value was selected for each parameter to determine generalized conditions across all sites. For each SMRT run with the varying parameters, the difference between the modelled and observed HH and VV backscatter (decibels) was calculated at each site. The difference was then multiplied by the range in difference values for all sites to reduce the impact of extreme values. These values were then averaged, and the optimal parameter was based on the minimum average out of all SMRT runs.

6.2.5.2 Wet Snow Conditions: Varying Depths

The second experiment reflects wet snow conditions that were observed on Lake Oulujärvi on March 1 and 2, and are represented by IOPII, IOPIIa, and IOPIIb in **Figure 6.2**. There were three different conditions tested in this experiment. The first assumed the entire snowpack had the same VWC (IOPII). The second assumed that only the top layer of the snowpack contained water (IOPIIa). The final condition assumed that the layer of snow directly on the ice cover contained water (IOPIIb). This reflects observations from the field which indicated that on March 1 the top of the snow was wet but by March 2 the water had percolated through the snowpack and was present in the lower layers. These observations are reflected in the changes in layer temperature recorded. For IOPII, snow pit density values were averaged across both days. SSA

values were also determined by averaging all observed values. For IOPIIa, density and SSA measurements were determined by averaging layers where observed snow temperatures were >=273.15. The temperature, density, and SSA for the bottom layer of the generalized snowpack were determined using layers where the temperature was <273.15 K. This was done to reflect observations of a wet top snow layer during IOPIIa and matches snow pit observations where the temperatures of the upper layers were consistently above melting. For IOPIIb, density and SSA of the lower layer were averaged for layers where observed snow temperature was >=273.15. The properties for the upper layer were determined by averaging temperatures, density, and SSA for layers with temperatures <273.15 K. This reflected observations on March 2 that indicated the lower layers of the snowpack were wetter and that the temperatures of lower layers were consistently at the melting point. In addition, simulations using different densities were assessed with a range of 225 to 450 kg m^{-3} at an interval of 5 kg m^{-3} to explore the impact of changing snow densities on backscatter under wet conditions. **Table 6.2** shows the constant snow and ice properties for these experiments. **Table 6.3** shows the ice thickness data for each of the sites. The optimal values for ice properties (interface correlation length, bubble radius, and porosity) from the dry snow experiment were continued forward.

Root mean square height values near the optimal RMSH were used to explore whether variations would impact backscatter when VWC of the snowpack changed. The ranges for the varied parameters are shown in **Table 6.5**. The same ranges were applied to all three conditions, however, the interface that was focused on differed. The selected values for the roughness parameters (RMSH and correlation length) of air-snow and snow layer boundaries are derived from previously published studies of snow roughness over both land and sea ice due to the limited observations of these parameters on lake ice (Baghdad et al., 2000; Petrich & Eicken, 2010; Komarov et al., 2017; Dinardo et al., 2018; Landy et al., 2019). For these experiments, Sentinel-1 observations are used to investigate the values of the parameters likely to result in the observed backscatter values.

Table 6.5 Tested ranges for different properties for IOPII, IOPIIa, and IOPIIb simulations.

Tested Property	Property Range (Interval)
All Snow Layers Wet (IOPII)	
RMSH Air-Snow Interface (mm)	0 – 5.0 (0.25)
Correlation Length Air-Snow Interface (mm)	10, 30, 50, 150
RMSH Snow-Ice Interface (mm)	0.5 – 4.0 (0.5)
RMSH Ice-Water Interface (mm)	1.0, 2.0
Volumetric Liquid Water Content (%)	0.02 – 1.00 (0.02) & 0 – 20.00 (1.00)
Single Snow Layer Wet (IOPIIa & IOPIIb)	
RMSH Wet Snow Layer Boundaries (mm)	0 – 5.0 (0.25)
Air-Snow for IOPIIa and Snow-Snow for IOPIIb	
Correlation Length Snow Layer Boundaries (mm)	10, 30, 50, 150
RMSH Snow-Ice Interface (mm)	0.5 – 4.0 (0.5)
RMSH Ice-Water Interface (mm)	1.0, 2.0
Volumetric Liquid Water Content (%)	0 – 1.00 (0.02) & 1.00 – 20.00 (1.00)

6.2.5.3 Wet Snow Conditions: Saturated Layer

The final experiment focuses on the observations made on March 25 – 26 which is represented as IOPIII in **Figure 6.2**. Observations on these dates indicate that there was a substantial amount of water present between the snow and the top of the ice. This experiment represents this condition by adding a thin 0.04 m saturated snow layer on top of the ice. The water fraction for the saturated layer is 63% and the remainder is ice, this could also be thought of as a slush layer that has been observed for lakes at mid-latitudes (Ariano & Brown, 2019). Only one

high value of water fraction was tested to focus on how changes in other properties impacted backscatter under these conditions. Due to capillarity, the dry snow layer above the saturated layer is also likely wet. Therefore, additional tests were conducted using varying VWC, 1%, 2.5%, 5%, for a 0.04 m snow layer above the saturated layer. Following a similar process to the conditions established for the variable wet snow layers (IOPIIa and IOPIIb), snow pit data for layers where the temperature was >=273.15 K were used to determine the density for wet layers of the generalized snowpack. Layers where the temperature was <273.15 K were used for dry snow layers in the generalized snowpack. Unlike the experiments for IOPII, SSA values were not available for IOPIII and therefore values are determined from **Equation 6.2,** and p_{ex} was deduced from **Equation 6.1**. The snow and ice conditions can be found in **Table 6.2** and ice thickness values for each site in **Table 6.3**. As with the second experiment, optimal properties determined under dry conditions were held constant.

Properties that were varied include the RMSH of the air-snow, snow-slush, slush-ice, and ice-water interface as well as the correlation length of the snow-slush interface. The ranges for these values are shown in **Table 6.6**. As with the second experiment, Sentinel-1 observations are used to investigate the most likely conditions.

Table 6.6 Tested ranges for different properties for IOPIII simulations.

Tested Property	Property Range (Interval)
RMSH Air-Snow Interface (mm)	0.0 – 5.0 (1.0)
RMSH Slush-Ice Interface (mm)	0.5 – 4.0 (0.5)
RMSH Ice-Water Interface (mm)	1.0 & 2.0
RMSH Snow-Slush Interface (mm)	0 – 5.0 (0.25)
Correlation Length Snow-Slush Interface (mm)	10, 50, 150

6.3 Results

6.3.1 Dry Snow Conditions

Under dry snow conditions the optimal values for the different parameters were found to be 1.26 mm for RMSH, an ice-water interface correlation length of 70 mm, a porosity of 10%, and a bubble radius of 1 mm. Differences between observed and modelled backscatter ranged from 0.25 to 2.36 dB (**Figure 6.3**), with an RMSE of 1.91 dB for HH-pol, 1.55 dB for VV-pol, and a combined RMSE of 1.74 dB. When using a bubble radius of 1.5 and 2 mm similar combined RMSE values were found, 1.84 dB and 1.64 dB respectively, however, the modelled backscatter for the minimum tested RMSH exceeded the minimum observed values from the field sites.

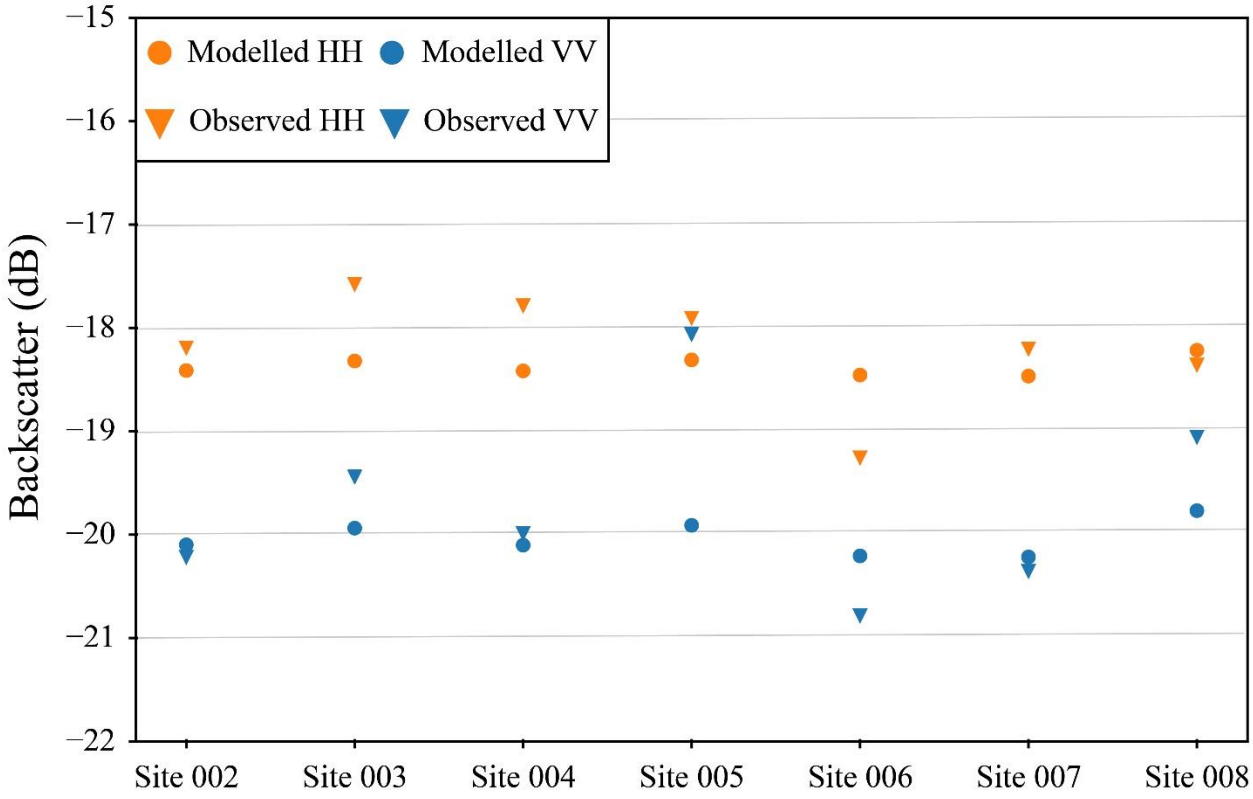

Figure 6.3 Comparison between modelled and observed Sentinel-1 backscatter for IOPI.

Figure 6.4 shows the change in modelled backscatter with increasing RMSH at the ice-water interface, for this example sites 006 and 008 are displayed to show a site from IOPI with and

without snow ice. The red and blue boxes in the figure show the range of backscatter values extracted at the different locations. As the RMSH increases to between 1 and 1.75 mm, the modelled backscatter falls within the ranges of observed backscatter for both HH and VV-pol. Additionally, **Figure 6.4** shows the impact of increasing snow-ice RMSH on backscatter under dry conditions. When an increased value of RMSH is used at the snow-ice interface, the difference between HH backscatter is a maximum of 3.3 dB for site 006 and 2.0 dB for site 008. Modelled HH backscatter is identical above RMSH values of 1.1 mm. The difference between modelled VV backscatter is larger, a maximum of 5.69 dB for site 006 and 4.39 dB for site 008. Similar to HH backscatter the difference between backscatter values decreases with increasing RMSH and values are identical when RMSH >1.9 mm.

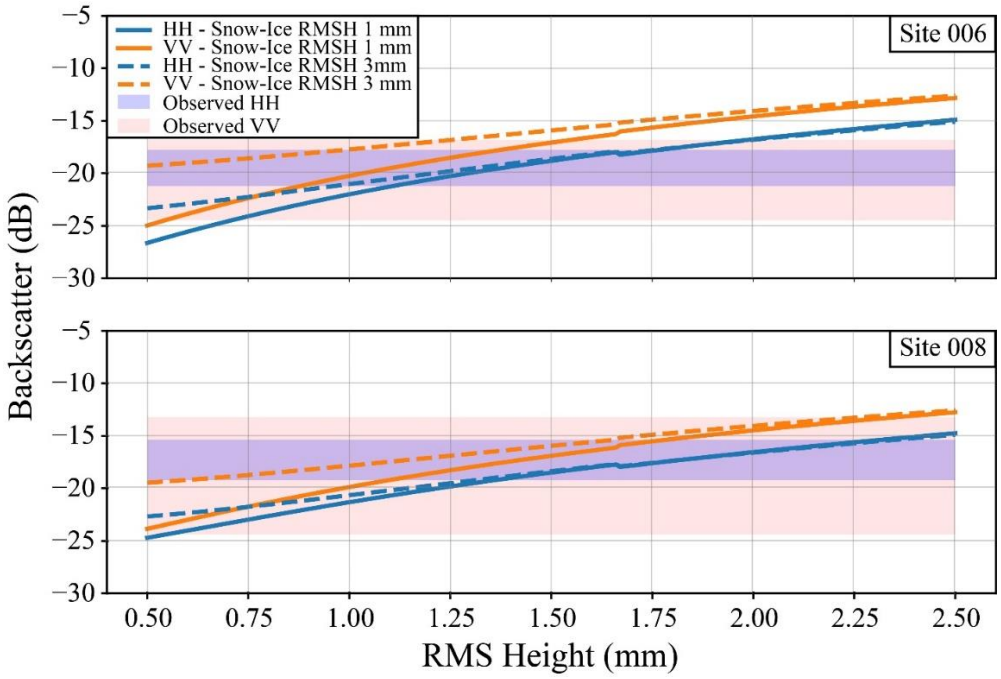

Figure 6.4 Modelled backscatter for dry snow conditions (IOPI). Site 006 shows results where no snow ice was found during the field campaign and site 008 shows results where snow ice was found.

6.3.2 Wet Snow Conditions: Varying Depths

Figure 6.5 shows the modelled backscatter for the simulation using data from IOPII where all layers of the snowpack have the same VWC. These results are for site 005, the values for other sites are not shown as the resulting backscatter is identical when snowpacks are wet. Increasing VWC by 1% with an interface correlation length of 10 mm results in an average decrease of 9.18 dB and an average decrease of -11.80 dB for an interface correlation length of 50 mm for all RMSH used (Figure 5). This decrease is largest, >-22 dB, when the surface of the snowpack (air-snow interface) is flat (i.e., has a RMSH of 0 mm). Backscatter is higher for simulations conducted using an interface correlation length of 10 mm compared to 50 mm. Simulated VV backscatter is comparable to observed backscatter for conditions with an interface correlation length of 10 mm, RMSH >3 mm, and when the VWC is above 7.5%. Simulated HH backscatter is lower compared to observed backscatter except when conditions are modelled with large RMSH and VWC values and when an interface correlation length of 10 mm is used. These experiments also show that for both polarizations the rate at which backscatter increases slows for VWC >15%. Changes in backscatter in Figure 5 are not consistent at a correlation length of 50 mm. This is likely due to IEM, but further investigation is needed.

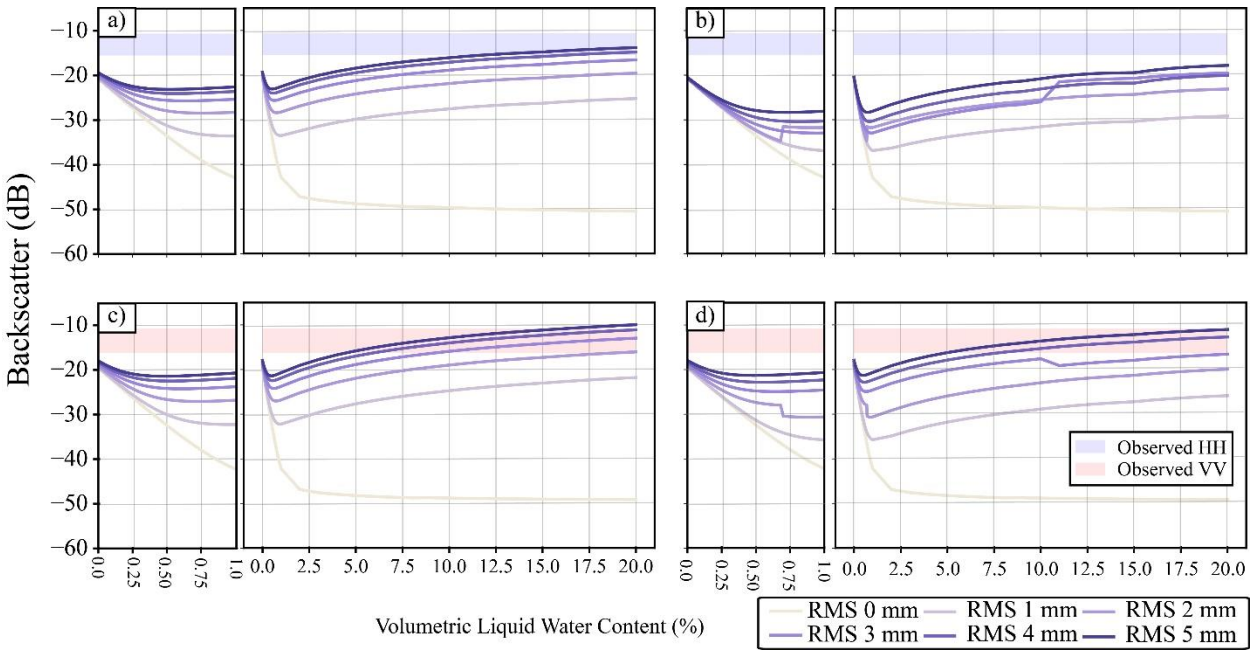

Figure 6.5 Modelled backscatter for site 005 where all layers of the snowpack have the same volumetric liquid water content. The different lines represent different values for the RMSH at the top of the snowpack (air-snow interface). a) and c) show results with a correlation length of 10 mm and b) and d) show results with a correlation length of 50 mm. The blue and red boxes show the observed backscatter from Sentinel-1.

Figure 6.6 evaluates the role that the RMSH of snow-ice and ice-water interfaces have when the entire snowpack has the same VWC. The RMSH of the air-snow interface was held constant at 5 mm for these simulations. Increasing either the snow-ice or ice-water interface RMSH has no impact on the backscatter when VWC >0%. There is a slight increase in backscatter at 0% VWC when a larger snow-ice interface values is used, however, it is small, <1.5 dB. At 0% VWC, backscatter increases by >3 dB when a larger ice-water RMSH of 2 mm is used. Similar to **Figure 6.5**, modelled backscatter is most comparable to observed VV-pol when the interface correlation length is 10 mm and the VWC is >7.5%.

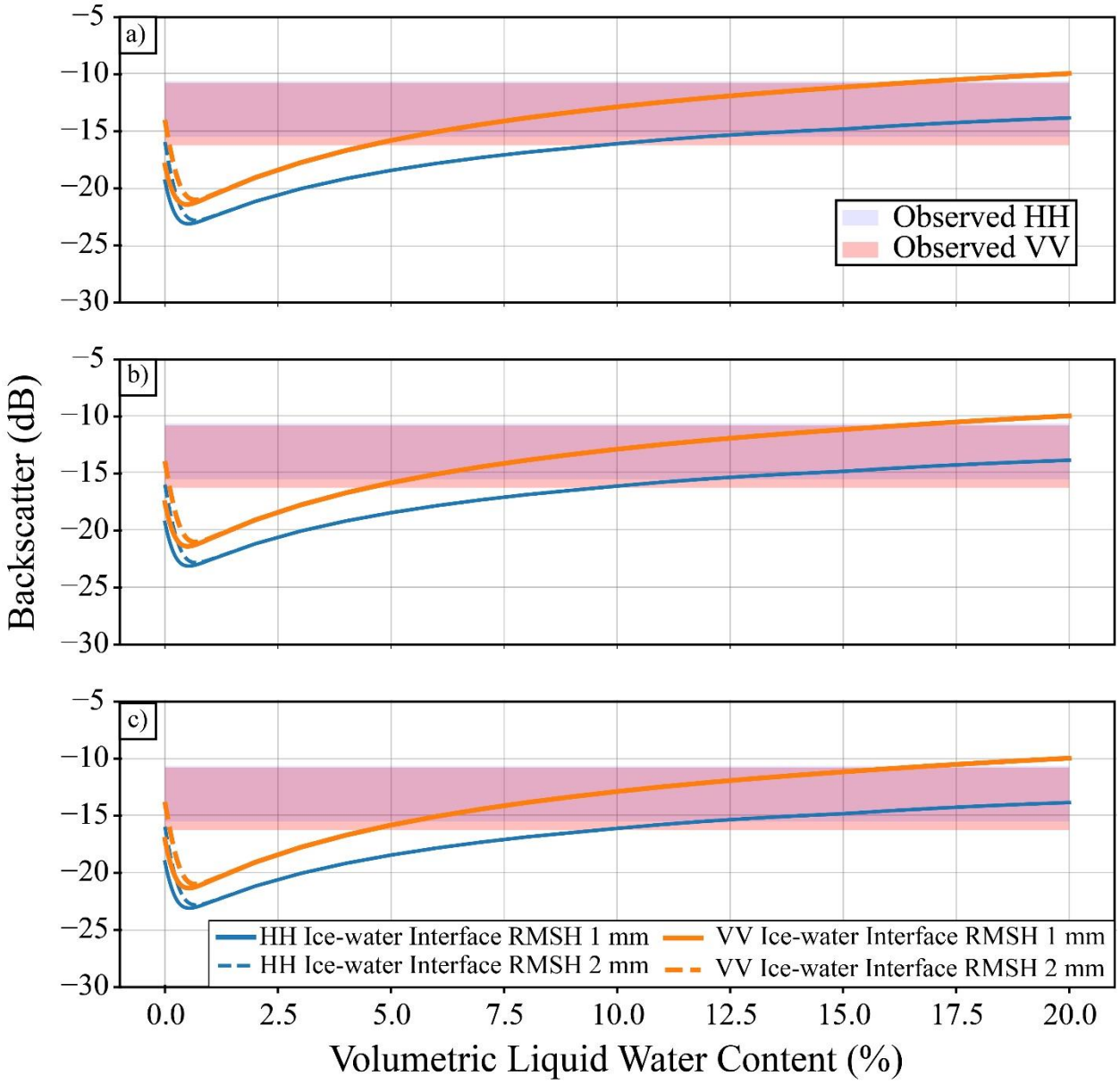

Figure 6.6 Modelled backscatter for site 005 where all layers of the snowpack have the same volumetric liquid water content and the air-snow boundary was held at a constant RMSH of 5 mm. a) shows results where the snow-ice interface is 1 mm, b) is where the snow-ice interface is 2 mm,

and c) is where the snow-ice interface is 3 mm. The blue and red boxes show the observed backscatter from Sentinel-1.

Figure 6.7 shows the impact of changing snow density on backscatter when the VWC of the snowpack is equal. For this experiment the ice-water interface RMSH was set as 1 mm and the snow-ice interface RMSH was 2 mm. Similar to **Figure 6.5**, backscatter increases with higher VWC. Increasing total snow density results in a rate of change of backscatter less than 0.01 dB/kg m^{-3}.

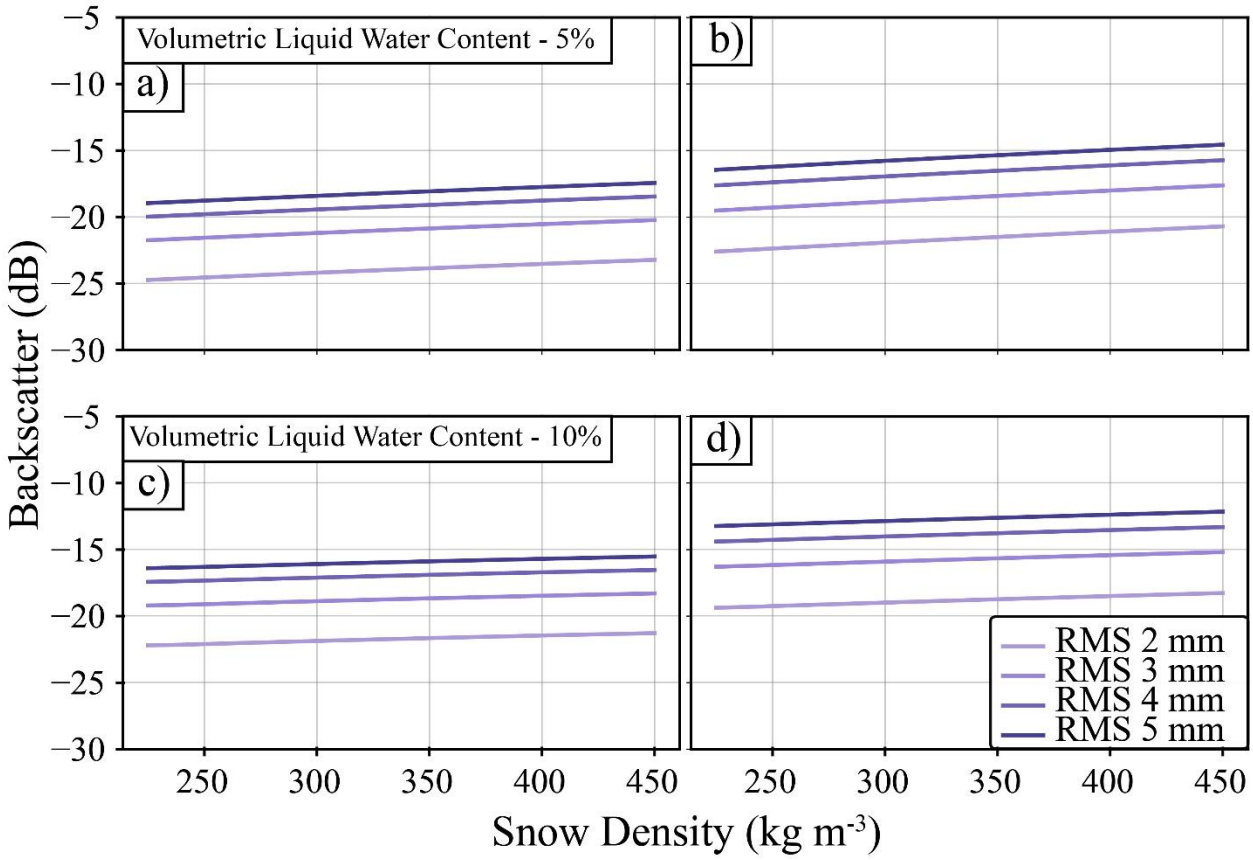

Figure 6.7 Modelled backscatter for site 005 where all layers of the snowpack have the same volumetric liquid water content, the RMSH of the ice-water interface is set to 1 mm and the RMSH of the snow-ice interface is set to 2 mm. The scenario was run for different volumetric liquid water

content values and a range of densities. a) and c) show modelled HH results and b) and d) show modelled VV results.

Figure 6.8 shows the difference in modelled backscatter when water was added to different layers of the snowpack. For March 1, when the top of the snowpack contained water, only VV backscatter from Sentinel-1 was available, therefore only VV modelled results are shown. Similar to previous experiments, modelled backscatter was closest to observations when VWC >7.5% and an interface correlation length of 10 mm was used. According to simulations, the RMSH of the air-snow interface would need to be >3 mm to produce backscatter comparable to the observed values. Overall results are similar to the patterns observed in **Figure 6.5**. For March 2, where the layer of snow directly on the ice contained water, only HH backscatter from Sentinel-1 was available and only modelled HH backscatter is shown. Modelled HH backscatter is lower compared to the range of observed HH backscatter. Compared to the change in VV backscatter, when RMSH >0 mm, there is a smaller decrease with increasing VWC. Similar to the initial experiments conducted when water was present throughout the snowpack, modelled backscatter for March 1 and March 2 saturates at high levels of VWC.

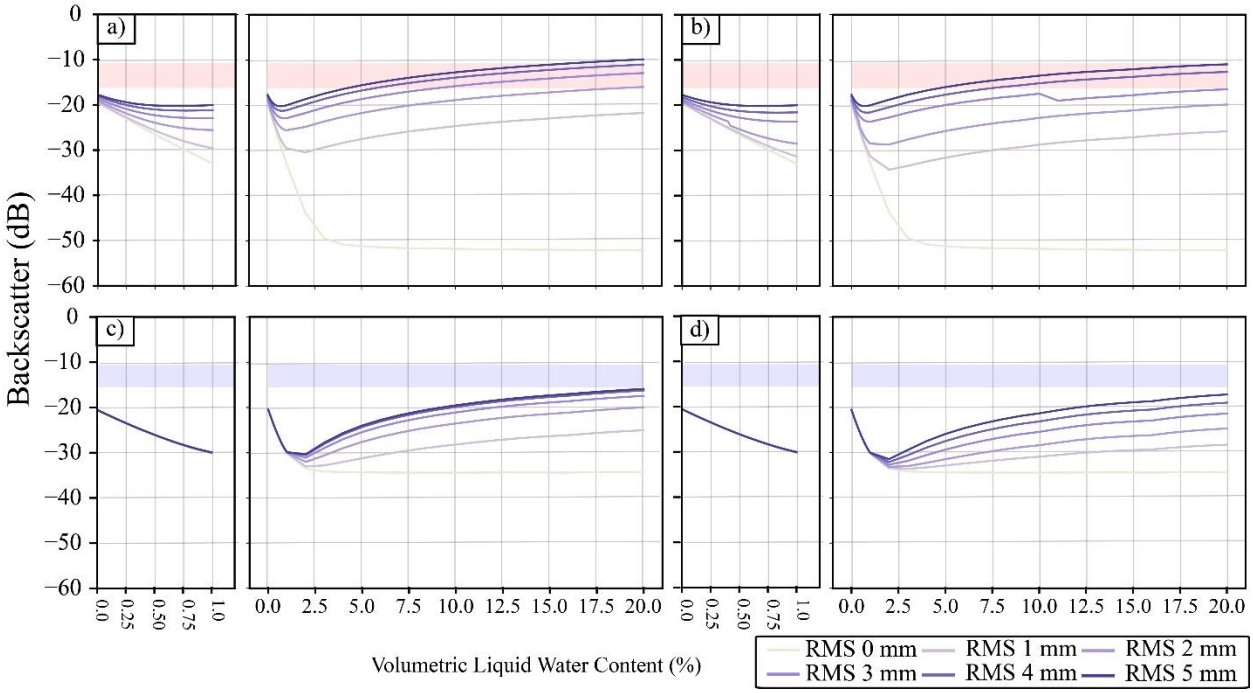

Figure 6.8 Modelled backscatter for site 005 representing IOPIIa, water in the top layer of the snowpack, and IOPIIb, water in the lower layer of the snowpack. The different lines represent different values for the RMSH at the top of the snowpack (air-snow interface). The blue and red boxes show the observed backscatter from Sentinel-1.

6.3.3 Wet Snow Conditions: Saturated Layer

The final experiment added a 0.04 m slush layer at the bottom of the snowpack with fractional water content of 63%. Previous experiments contained a mix of snow, ice, and water, however, for this experiment the saturated layer only contains ice and water resulting in a higher overall density of 954.81 kg m^{-3}. Additional tests with a wet snow layer over the saturated layers were also conducted. **Figure 6.9** shows how the modelled backscatter changes with increasing RMSH at the interface between the snow and slush layer for site 008 with snow layers of differing VWC overlying the slush layer. This site was selected as field observations noted that there was a large amount of water located between the snow and the ice surface. Similar to the experiments in section 3.2, modelled backscatter was identical for the different sites due to the high VWC. The range of observed backscatter is similar between IOPII and IOPIII, however, modelled backscatter can reproduce observed values at a lower RMSH (<3 mm) for IOPIII compared to IOPII. The range of modelled backscatter decreases as the VWC of the overlying wet snow layer increases. Modelled values when the overlying snow layer has a VWC of 2.5 and 5% fall outside the observed range of both HH and VV backscatter except at 5% when RMSH of the snow slush layer is >2.5 mm.

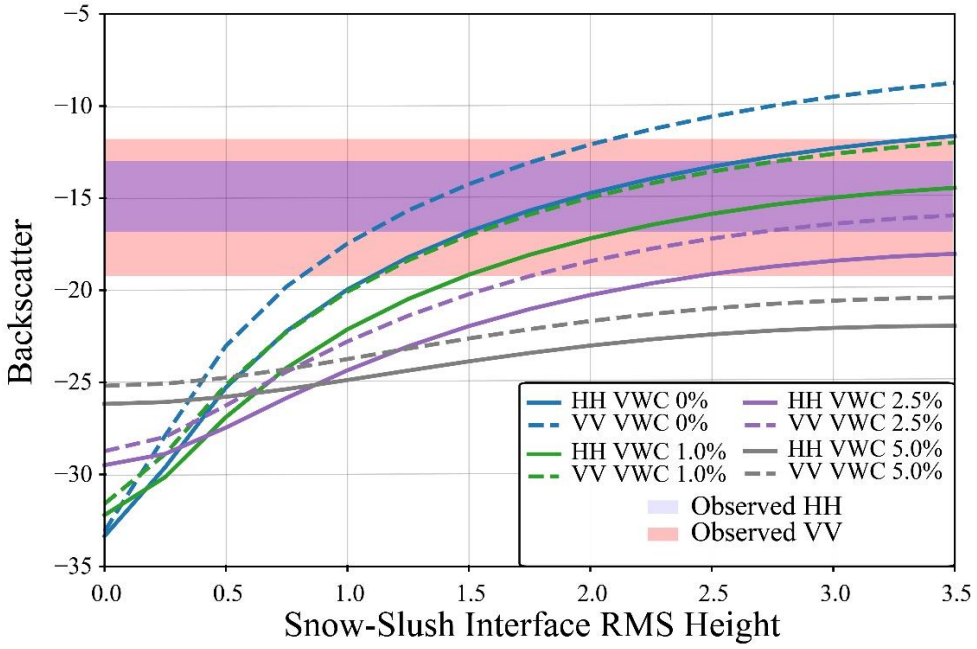

Figure 6.9 Modelled backscatter for site 008 where there is a 0.04 m layer of slush between the lowest snow bottom of the snowpack and the ice surface. All other properties are held constant except the RMSH of the interface between the lowest snow layer and the slush layer. The VWC of the lowest 0.04 m of snow was varied between 0 and 5% The blue and red boxes show the observed backscatter from Sentinel-1.

6.4 Discussion

Recent research has focused on the key role that roughness of the ice-water interface plays in backscatter from lake ice using both observed data and modelling (Engram et al., 2012; Atwood et al., 2015; Gunn et al., 2018). The results from IOPI further support that under dry snow conditions, roughness of the ice-water interface is the key interface for the surface scattering mechanism. However, it should be noted that the results in **Figure 6.4** also indicate that at lower values of RMSH for the ice-water interface, larger RMSH at the snow-ice interface causes an increase in backscatter. Yet, field observations indicate that under dry conditions RMSH values of 1 mm at the snow-ice interface are more likely (Wakabayashi et al., 1999; Han & Lee, 2013). Additionally, when RMSH values at the ice-water interface are higher modelled backscatter

becomes near identical when using different RMSH for the snow-ice interface. The difference between modelled backscatter values with different snow-ice RMSH values also reduces when smaller interface correlation lengths are used. For example, the difference at site 006 was 5.69 dB at an interface correlation length of 50 mm but drops to 2.84 dB when an interface correlation length of 10 mm is used. This highlights the importance of properly parameterizing all aspects of roughness for the difference interfaces, which is notoriously known as difficult. For lake ice, while recent studies have been able to extract roughness using ground penetrating radar (Gunn et al., 2021), no measurements have been acquired at cm or mm scale which would impact SAR backscatter. Obtaining accurate in situ data for these measurements is an area of continuing study. While lower RMSH values are more likely at the snow-ice interface, higher values are not impossible and can be created when there are deformations in the ice surface. For example, in **Figure 6.10**, backscatter for site 005 increases faster compared to the other two sites and is higher prior to IOPII. This is most likely due to the site being located near a crack in the ice surface identified from brighter tones in the Sentinel-1 imagery. Cracks and deformations have been noted to result in higher backscatter by up to 10 dB compared to areas where the ice surface is smoother (Morris et al., 1995). **Figure 6.10** also supports recent conclusions that suggest ice-water interface roughness increases rapidly at the start of the ice season but then become stable as ice growth slows (Chapter 5). Backscatter for sites 006 and 008 remains stable between IOPI and the end of February. With recent sensitivity analysis indicating that backscatter change is primarily driven by increasing RMSH (Murfitt et al., 2022), it is likely that RMSH of the ice-water interface varies little during this period for these sites.

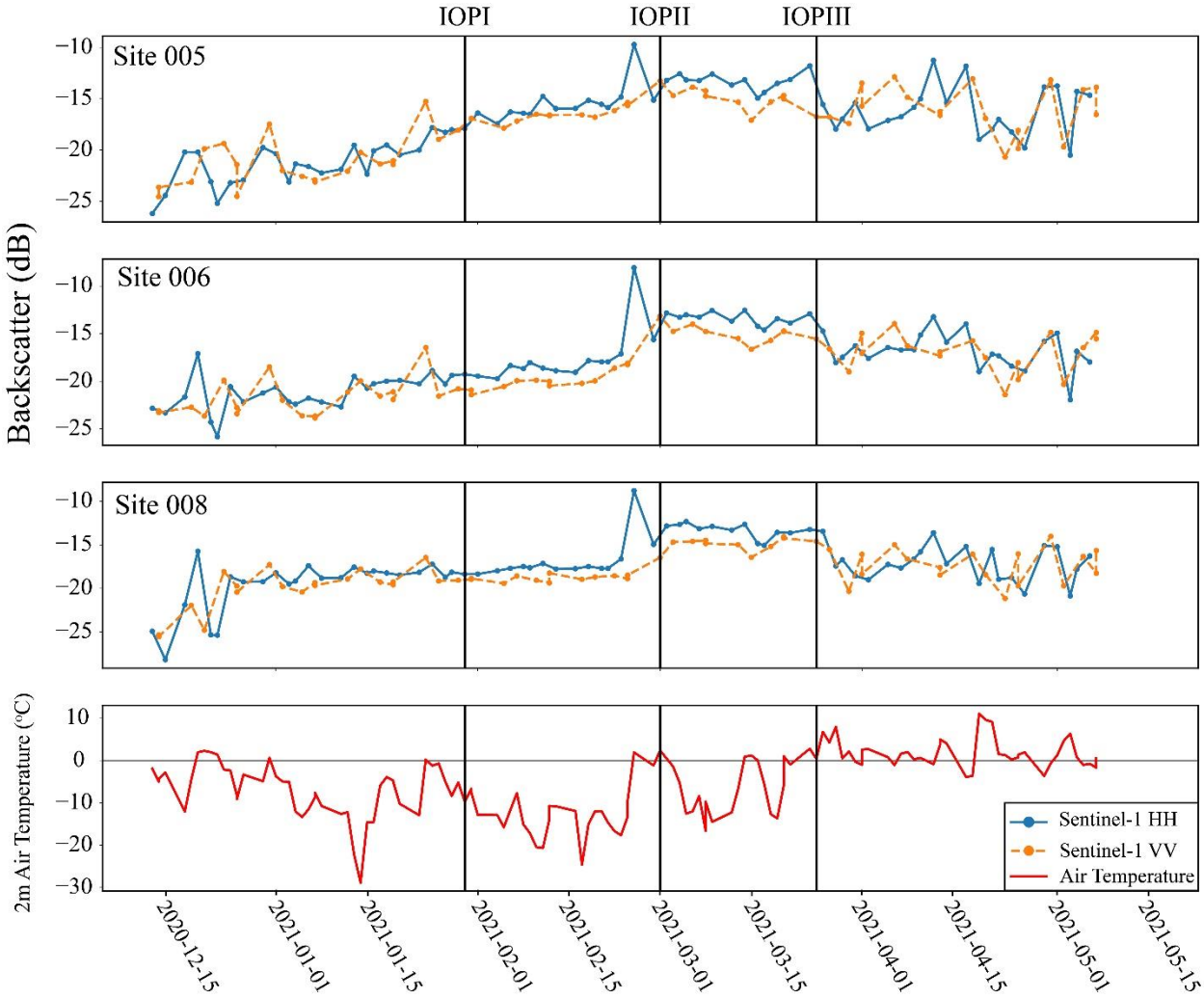

Figure 6.10 Backscatter evolution for selected sites on Oulujärvi and 2-m air temperature from ERA5 reanalysis data.

Under wet conditions, the ice-water interface is not the dominant interface for surface scattering as the key interface changes to the top of the snow layer with the highest VWC. This is demonstrated in **Figure 6.6** that shows no difference in modelled backscatter when RMSH of the snow-ice and/or ice-water interface is increased. This agrees with modelling work conducted in South Korea which demonstrated that when the ice surface was wet it was the primary scattering interface but the contribution decreased as the surface froze (Han & Lee, 2013). **Figure 6.5** and

Figure 6.8 both demonstrate that the addition of RMSH at the top of the wet snow layer causes a change in the response of backscatter to increasing VWC. When the interface is smooth, backscatter decreases with increasing VWC. This is commonly reported in lake ice literature, with backscatter decreasing during break-up as snow melts and the ice cover decays (Duguay et al., 2002; Antonova et al., 2016; Murfitt & Duguay, 2020). The explanation for the increasing backscatter with the increase in VWC and RMSH is due to the increasing contrast in permittivity at the surface (or between dry and wet layers). The value of the real permittivity component for dry snow is 1.41, similar to that of air meaning there is little reflection occurring at the interface between these two surfaces. However, when water is added to the snowpack, the permittivity increases to 2.34 when VWC is 5% and 5.46 when VWC is 20%. The increased permittivity results in an increase in the single backscattering component from IEM. This results in the modelled backscatter from the wet and rough surface increasing. While there has been limited investigation of these interactions for lake ice, these results are expected based on modelling conducted for terrestrial snow which shows increasing backscatter with increasing water content at increasing values of RMSH (Shi et al., 1992; Baghdad et al., 2000; Nagler & Rott, 2000). Furthermore, terrestrial snow experiments demonstrate that increasing water content leads to surface scattering being dominant at all incident angles, supporting the results observed in SMRT experiments (Shi et al., 1992).

Observations support the increase in backscattering because of melt under certain conditions. Between IOPI and IOPII there is an increase in observed backscatter (**Figure 6.10**). The results of the simulations indicate that this is due to a change in interface roughness combined with increasing water content. This change in interface roughness is likely a result of a melt-freeze event. The occurrence of this event is supported by the temperature profiles shown in **Figure 6.10**. Prior to data collection for IOPII between February 25 and 28, hourly air temperature fluctuated between 2.31 °C and -2.52 °C. Temperatures also fluctuated between March 1 and March 2 when IOPII data was collected, with maximums of 3.97 °C on March 1 and minimums of -2.64 °C on March 2. The fluctuations in temperature could result in the higher backscatter observed on IOPII and is supported by the results of simulations conducted in **Figure 6.5** and **Figure 6.8** which show

that the increased VWC and RMSH are both necessary to model the observed backscatter for these dates. However, these conditions may not be true at all sites as some sites did report lower backscatter on March 1. **Figure 6.11** shows the Sentinel-1 imagery for the images proceeding and including IOPII (February 25, 28, March 1, and 2, 2021). Sites 003, 007, and 008 are all located over areas of darker tones, resulting in average backscatter ranging from -14.3 to -16.5 dB compared to backscatter ranging from -12.4 to -13.1 dB for other sites. The darker tones observed for these sites could indicate that the change in RMSH was lower or that less water was present in the overlying snow layer at this site. Observations of backscatter from other lakes indicate that this increase is not uncommon for melt events (Antonova et al., 2016; Murfitt et al., 2018; Chapter 5).

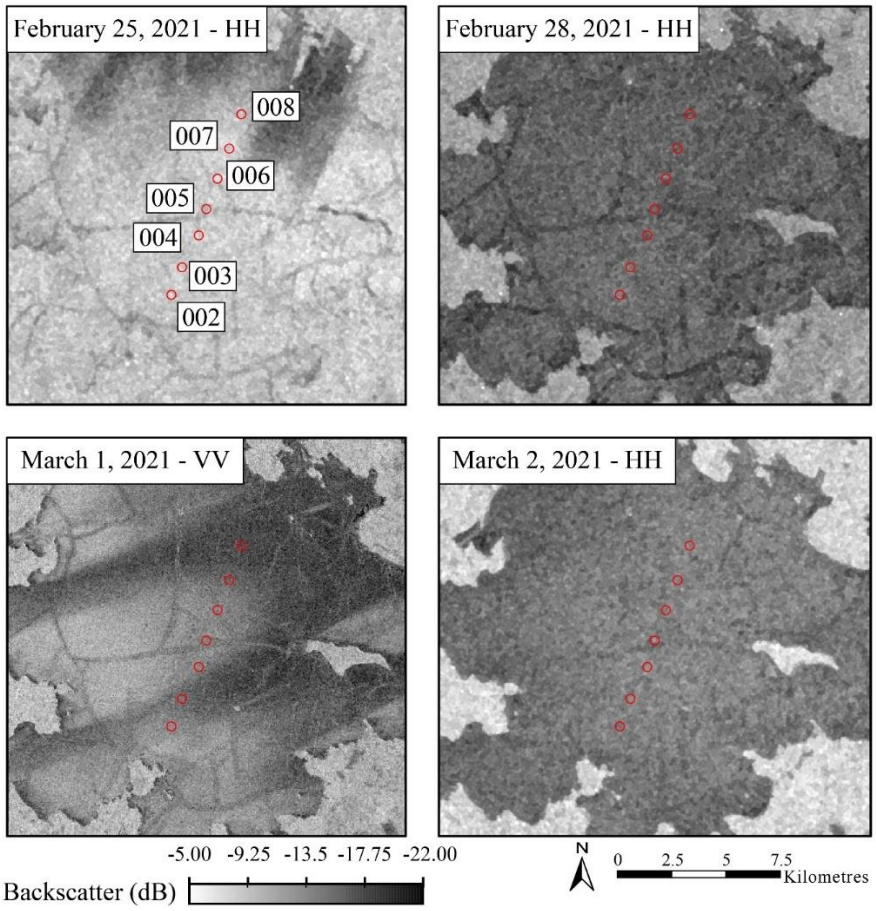

Figure 6.11 The change in SAR backscatter for available images between February 25 and March 2, 2021. Data are from Copernicus Sentinel-1 (2021), processed by ESA.

The above explanation supports the increase in backscatter between January/February and March. However, when temperatures become colder, a minimum of -26.60 °C between March 5 – 13 and a minimum of -14.16 °C between March 17 – 20, backscatter remains similar to the values observed during IOPII. This is unexpected as the return to colder temperatures indicates that conditions should become drier, and the ice-water interface would become the dominant control over backscatter. However, when backscatter values for two dates, March 14 and 19, are compared to Sentinel-1 observations during IOPI there is an average increase in backscatter of 5.16 dB for HH-pol and 3.69 dB for VV-pol. This suggests that mid-winter melt-freeze events have a lasting impact on the ice conditions and backscatter from lake ice. There are likely explanations for this increase, the first is that the melt-refreeze caused an increase in the snow ice thickness. The refreeze of water from the melt event prior to and during IOPII at the ice surface causes an increase in the thickness of the snow ice layer, this is supported by field measurements. Due to the presence of large spherical scatterers, the snow ice layer has a strong scattering behavior. If larger spherical bubbles were formed this would also contribute to a higher backscatter, however, the results of the dry experiment indicate that this results in a weak increase of <2 dB. Another possible explanation is that the melt-freeze event resulted in an increase in the RMSH at the snow-ice interface or at the ice-water interface through the formation of ripples or dunes on the underside of the ice sheet (Ashton, 1986). While this cannot be confirmed for Lake Oulujärvi, it seems likely given the dominant interface under dry conditions. As a conclusion, it is difficult to fully elucidate the cause of the sustained high backscatter during the refreezing after the March melt-event, but it reveals that internal changes in the snow and ice likely occurred during this period. Further research is required to explore how melt-freeze events impact the lake ice properties and the influence this has on backscatter.

The highest backscatter values were obtained when simulations were conducted using a saturated layer between the bottom of the snowpack and the ice column with either dry snow or a

layer of snow with a low VWC (<1%) overlying it. These larger values are related to the increased permittivity of the saturated layer, 22.47, compared to the previous observations noted for wet snow layers. According to the backscatter evolution in **Figure 6.10**, values for IOPIII are lower compared to IOPII. This is likely a result of both increased water content and lower RMSH between the slush layer and the bottom of the snowpack. The Sentinel-1 images in **Figure 6.12** support this with darker tones around the edge of the ice and throughout the ice cover being an indication of decay. **Figure 6.10** shows that beyond March 26 there is large fluctuations in backscatter patterns as temperatures are around 0 °C and result in melt-freeze cycles discussed above. The large backscatter values produced through the saturated layer experiments also provide the most likely explanation for the spike in backscatter that occurred on February 25, reaching a maximum of -7.58 dB (**Figure 6.10 and 6.11**). The experiments conducted for IOPII were not able to produce these values of backscatter, however, the saturated layer experiments were able to achieve similar values. Similar bright radar returns have been observed for areas of slush in past side-looking airborne radar images from Manitoba, Canada (Leconte & Klassen, 1991). Bright tones were connected to layers of slush under dry layers of ice and snow leading to an increased contrast in the permittivity of the layers and higher returns (Leconte & Klassen, 1991). This is a likely explanation for the spike observed on February 25 and is supported by the results of the modelling for IOPIII. However, it is important to note that the simulations also showed that when a layer of snow with a higher VWC (>2.5%) is overlying the slush layer, it becomes the dominant surface. Therefore, accurate information on the VWC throughout the snowpack is crucial and further work is needed on studying the complexity of slush events.

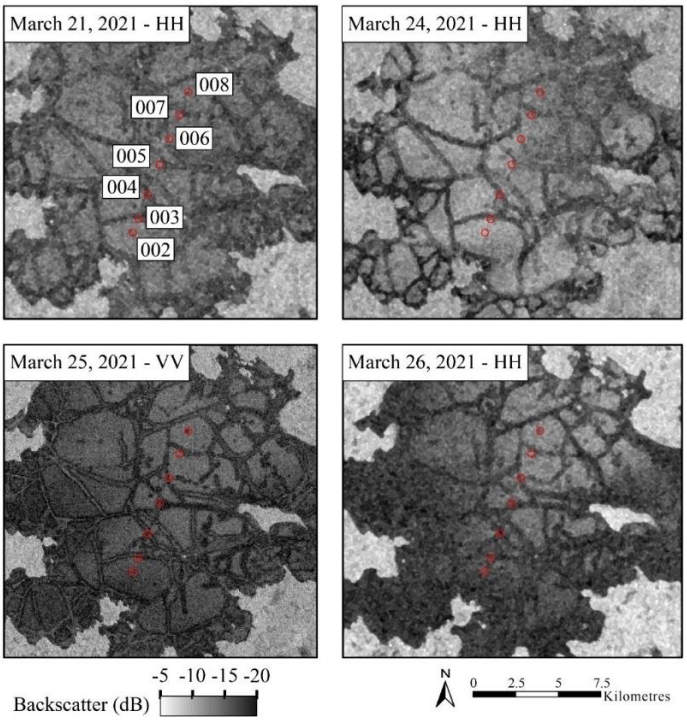

Figure 6.12 The change in SAR tones for available images between March 21 and March 26, 2021. This figure contains Copernicus Sentinel-1 data (2021), processed by ESA.

The main limitation of this study is the creation of a generalized snowpack, which may differ from reality. The generalized snowpack was used to simplify the modelling set up and address variations across the different sampling sites. However, using a 2-layer approach meant that differences in snow morphology (i.e., grain type) were largely ignored. Additionally, other features in the snowpack, such as highly scattering ice lenses and pipes, were not included. While this limitation could introduce error for the dry snow simulations, as demonstrated by the IOPII experiments, differences in density and volume scattering in general had little impact on the backscatter observed from the wet snowpack (**Figure 6.7**). Another issue encountered in the modelling was the underestimation of HH backscatter throughout the experiments. This was observed regardless of if modelling was conducted under dry or wet snow experiments. One possible explanation for this underestimation is that VV backscatter is more responsive to changes in the roughness of the surface when represented using IEM (Fung & Chen, 2010). This is

supported by the results of the experiments where varying different ice properties result in lower HH backscatter compared to VV. Other explanations could be that the snowpack is oversimplified as stated above, and this causes the difference between modelled and observed HH backscatter.

6.5 Conclusions

This is the first study to explore the impact of changing volumetric liquid water content on backscatter from lake ice using SMRT. Initial experiments conducted assuming dry snow conditions continue to support previous assertions that the ice-water interface is plays the key role in controlling the backscatter from lake ice. However, as indicated by the experiments, increasing the liquid water content in the overlying snow layers causes the dominant interface to shift from the ice-water to the surface, resulting in higher backscatter, and a major increase / emergence of the role of the surface roughness. The largest backscatter values were produced when slush layers were present overlying the ice column. The impact of these interfaces on the backscatter can be attributed to the increasing dielectric constant of the wetter snow layers combined with the increasing roughness. These patterns are supported by field observations and congruent Sentinel-1 overpasses. Furthermore, it provides support for past explanations of bright returns observed from lake ice surfaces (Leconte & Klassen, 1991).

Further work is needed to continue to improve understanding on how snow and ice properties change under these conditions. While the field observations used in this study provide valuable information, continued study of snow and ice properties such as SSA, RMSH, and interface correlation length both before and after mid-winter melt events will be useful in parameterizing radiative transfer models throughout the ice season. Also of interest is the impact of these events on the properties of snow ice layers, particularly with the bubble radius and porosity, which have been noted as factors impacting backscatter in past sensitivity analysis (Tian et al., 2015; Murfitt et al., 2022). Improving the parameterization of wet snow conditions over lake ice will be important for retrieval of properties such as RMSH. Accurate retrieval of RMSH is also crucial for developing algorithms for ice thickness retrieval. Additionally, effective modelling of backscatter under wet conditions is useful in training lake ice classification models to identify

areas of weaker ice types or slush that could pose hazardous to users of lake ice for transportation and recreation during winter months. However, further work is needed as the processes are complex and collection of additional field data and observations on conditions are needed to improve the representation of these events in modelling.

Chapter 7 General Conclusions

7.1 Summary

The overall objective of this thesis was to investigate how changes in lake ice properties impact microwave backscatter and explore the representation of lake ice using the snow microwave radiative transfer (SMRT) model under both dry and wet conditions. This work was needed because, as identified in Chapter 1, past modelling approaches have limitations associated with creating a faithful representation of lake ice. The flexibility provided by SMRT and the incorporation of multiple electromagnetic, microstructure, and interface models allow for the creation of more realistic ice columns from a modelling standpoint. The representation of lake ice within a well-designed modelling framework is crucial for developing accurate inversion models that can aid in the retrieval of important lake ice properties such as roughness (root mean square height and correlation length). Retrieval of these properties is critical in continuing to improve models capable of estimating other lake ice properties such as ice thickness from active microwave data.

Chapter 2 and 3 of this thesis provide critical background on the topic of active microwave remote sensing and lake ice. Chapter 2 provides a brief overview of the interaction between radar signals and lake ice and details the various components of SMRT. Within this breakdown of the various aspects support is provided for the selection of electromagnetic, microstructure, and interface models within the other components of the thesis. Chapter 3 provides a thorough overview of active microwave research on lake ice over the last 50 years. A comprehensive literature review details the variety of sensors and study areas within the existing literature. Furthermore, this chapter compares the traditional viewpoint of a double-bounce mechanism to more recent results which support a surface scattering mechanism at the ice-water interface. This chapter also identifies important avenues of future research in the field of active microwave and lake ice. Four key areas are listed in Chapter 3, understanding of microwave and lake ice interactions, classification of ice cover, ice thickness retrievals, and broader considerations

focusing on topics such as data availability, analysis of time series, and snow cover on lake ice. Recommendations made in these key areas encourage the use of modern modelling techniques, machine/deep learning, and new satellite technology to improve our understanding of lake ice, especially as climate continues to change.

Building on recommendations made in Chapter 3, Chapter 4 is the first use of the Snow Microwave Radiative Transfer (SMRT) model to conduct forward modelling experiments for the backscatter response to lake ice properties. The experiments conducted in this chapter expand on past forward modelling experiments by using SMRT to develop a more faithful representation of a lake ice column. Experiments compared a simulated shallow and deep lake, as deeper lakes have been largely ignored in past modelling experiments. Additionally, by integrating SMRT and the Canadian Lake Ice Model (CLIMo), ice and snow properties (temperature and thickness) were more realistic compared to past synthetic values. Simulations from both lake depths indicated that changes in ice porosity and ice thickness had little impact on backscatter under cold conditions. The addition of bubbled layers at the bottom of the ice column, representing tubular bubbles, also had little to no impact on backscatter. The response to bubble radius in a surface ice layer was limited. However, larger bubble radii, > 2 mm, did result in large increases in backscatter. The property that had the most impact on simulated backscatter was root mean square (RMS) height of the ice-water interface, which corresponds to findings in the most recent literature. L and C-band frequencies were found to be most responsive to RMS height, while X-band is likely more suited for the study of surface ice properties.

The findings of Chapter 4 were important in parameterizing the full season simulations conducted in Chapter 5. Chapter 5 is the first application of SMRT to model backscatter from ice cover throughout an entire ice season. Modelling experiments were conducted on a shallow lake, Malcolm Ramsay Lake in Manitoba, and a deeper lake, Noell Lake in the Northwest Territories, to represent conditions both with and without tubular bubbles. Field data collected from both lakes and CLIMo were used to parameterize SMRT throughout the ice season. Because ice-water

interface RMS height was identified as the property having the largest impact on backscatter, SMRT was iterated to identify the optimal value for RMS height resulting in the minimum error between modelled and observed backscatter. Optimal values for RMS height differed between shallow and deep lakes, with shallow lakes having higher RMS height values and deeper lakes having lower values. This is most likely due to the emergence of tubular bubbles at the ice-water interface in shallow lakes and is supported by both field observations and observed backscatter values. Comparisons between modelled and observed backscatter found that the RMSE for Noell Lake was <1.38 dB and <2.33 dB for Malcolm Ramsay Lake. The optimization of RMS height was also found to be an improvement over using fixed values of RMS height and indicates it is likely roughness of the ice-water interface increases rapidly at the start of the ice season but plateaus once the ice growth slows.

There has been limited exploration of the interaction between microwave signals and lake ice when the overlying snowpack is wet, or slush layers are present. Chapter 6 used SMRT to further explore the impact that changing ice and snow properties had on backscatter under these wet conditions. The focus of these experiments was Lake Oulujärvi in Finland, and extensive field data collected during the winter of 2021 was used to parameterize SMRT. Three distinct experiments were conducted, one assuming dry conditions, one with a wet layer of snow, and one with a saturated slush layer on top of the ice. These experiments reflected field observations. Experiments under dry conditions supported the results of previous chapters, highlighting the importance of roughness at the ice-water interface. However, when water was added to different layers, the dominant interface responsible for surface scattering corresponded to the top of the wet layer. Similar results were found when a saturated slush layer was added to the top of the ice column. The increased scattering due to these layers is due to the higher dielectric contrast that develops when the wet layers are present. Additionally, it was found that modelled results were most representative of observed backscatter when there was increased roughness of the dominant interface. This indicates that melt/freeze events, which corresponded to these observations, result

in a change in key ice properties. These results indicate that brighter returns from lake ice covers can reveal increased water content and possibly unsafe areas.

7.2 Limitations

The main limitation throughout the work conducted in this thesis is the lack of field measurements of roughness (RMS height and correlation length) at the ice-water interface. While this property has been noted as the dominant control on backscatter from lake ice cover both in this work and others (Engram et al., 2013; Atwood et al., 2015; Tian et al., 2015; Gunn et al., 2018), measurements of these values have not been reported. One possible reason for this is that there is currently no established methodology for obtaining these values. Measurements do exist for possible proxies of lake ice roughness at the ice-water interface, such as smooth river ice, however, it remains important that values specific to lake ice are obtained. One possible solution is the extraction of larger ice blocks that can then be used to measure roughness parameters, however, due to the COVID-19 pandemic field work conducted for this thesis was limited.

Limitations were also present with the use of SMRT. While SMRT does allow for the representation of a more faithful ice column, there are some aspects that currently cannot be fully modelled. For example, SMRT does not currently allow for the integration of vertically oriented tubular bubbles that are observed in ice cover for shallower lakes. While these bubbles likely have a limited impact on the backscatter from lake ice, it is still important to represent these features in the model. Furthermore, with the current implementation of IEM in SMRT, cross-pol backscatter is lower than anticipated and not properly modelled. This is an ongoing area of work within the framework but means that only co-pol can currently be evaluated when using IEM for surface scattering. Finally, SMRT does not allow for horizontal variations in modelled mediums. When modelling backscatter for Noell Lake, experiments were set up to assume that conditions were homogenous across the lake and there were no variations in roughness of the ice-water interface. However, results from Malcolm Ramsay Lake indicate that variations likely exist and that these differences should be represented within the model.

There are also limitations of using reanalysis data as an input for CLIMo and then using the output of CLIMo in the SMRT parameterization. ERA5 data used throughout this thesis will not be a perfect representation of observed conditions, however, it was compared to observations from weather stations to ensure accuracy. Using these data in CLIMo can cause any errors to propagate further, however, CLIMo output was also validated to ensure that errors were within reasonable ranges.

7.3 Future Directions

The modelling experiments conducted in this thesis further confirm recent findings that surface scattering at the ice-water interface is the dominant control of backscatter for lake ice covers. While it has been noted in past research (e.g., Gunn et al., 2018), there is a crucial need to collect field measurements of roughness at the ice-water interface. Expanding further on this point, to continue improvement of modelling from lake ice covers intensive field campaigns are needed. This thesis has identified bubble radius and roughness as two of the key properties for lake ice covers. Field work focused on collecting these data from both different lakes as well as different locations on lakes can help to better parameterize these properties within modelling frameworks. Collection of field data should also consider the role of depth and latitude in determining ice properties. As demonstrated in this thesis, roughness of the ice-water interface is important for both shallow and deep lakes but the mechanism for this roughness is likely different for these depths. Additionally, while this thesis did explore the addition of wet layers within the ice column, further investigations of this process at mid-latitudes, where water layers in the ice and slush layers are common, should be conducted this thesis focused on lakes located at high latitudes, and the stratigraphy of ice covers at mid-latitudes can differ with the inclusion of water layers and additional slush layers (Ariano & Brown, 2019). It is also critical that in situ data be collected both during cold conditions and wet conditions to understand how lake ice properties change with the occurrence of freeze-thaw events, as results from Chapter 6 indicate that these events have a lasting impact on the ice cover and microwave response.

From the modelling perspective, this thesis has demonstrated that SMRT is a suitable framework for modelling backscatter from lake ice. Additionally, this thesis coupled CLIMo with SMRT allowing for a more realistic representation of ice properties compared to previous modelling studies. The next step is to expand this modelling and develop inversion algorithms for key lake ice properties. Collection of roughness measurements through field campaigns would help to train inversion models to retrieve these key properties. Retrieval of accurate measurements of roughness would aid in the development of other inversion models. For example, if accurate roughness could be obtained through SMRT using SAR imagery, these values could then be used to train inversion models to retrieve ice thickness using other active remote sensing data such as altimetry. Additionally, future work should evaluate CLIMo-SMRT using other frequencies and radar data (e.g., altimetry). Frequencies such as Ku-band were not explored in this thesis and could prove valuable for obtaining key information about overlying snow cover on lake ice. Altimetry data can also be modelled using SMRT and recent research has demonstrated that accurate estimates of ice thickness can be obtained with these data (Mangilli et al., 2022). Forward modelling would help to provide additional knowledge about how ice properties impact altimetry signals.

References

Antonova, S., Duguay, C. R., Kääb, A., Heim, B., Langer, M., Westermann, S., & Boike, J. (2016). Monitoring Bedfast Ice and Ice Phenology in Lakes of the Lena River Delta Using TerraSAR-X Backscatter and Coherence Time Series. *Remote Sensing*, *8*(903). https://doi.org/10.3390/rs8110903

Ariano, S. S., & Brown, L. C. (2019). Ice Processes on Medium-Sized North-Temperate Lakes. *Hydrological Processes*, *33*(18), 2434–2448. https://doi.org/10.1002/hyp.13481

Arkett, M., Braithwaite, L., Pestieau, P., Carrieres, T., Pogson, L., Fabi, C., & Geldsetzer, T. (2015). Preparation by the Canadian Ice Service for the Operational Use of the RADARSAT Constellation Mission in Their Ice and Oil Spill Monitoring Programs. *Canadian Journal of Remote Sensing*, *41*(5), 380–389. https://doi.org/10.1080/07038992.2015.1104631

Arp, C. D., Jones, B. M., & Grosse, G. (2013). Recent Lake Ice-Out Phenology Within and Among Lake Districts of Alaska, U.S.A. *Limnology and Oceanography*, *58*(6), 2013–2028. https://doi.org/10.4319/lo.2013.58.6.2013

Arp, C. D., Jones, B. M., Lu, Z., & Whitman, M. (2012). Shifting Balance of Thermokarst Lake Ice Regimes Across the Arctic Coastal Plain of Northern Alaska. *Geophysical Research Letters*, *39*, 1–5. https://doi.org/10.1029/2012GL052518

ASF DAAC. (2015). *ALOS PALSAR_Radiometric_Terrain_Corrected_high_res; Includes Material © JAXA/METI 2007*. https://doi.org/10.5067/JBYK3J6HFSVF

Ashton, G. D. (1986). *River and Lake Ice Engineering.* Water Resources Publication.

Atwood, D. K., Gunn, G. E., Roussi, C., Wu, J., Duguay, C., & Sarabandi, K. (2015). Microwave Backscatter From Arctic Lake Ice and Polarimetric Implications. *IEEE Transactions on Geoscience and Remote Sensing*, *53*(11), 5972–5982. https://doi.org/10.1109/TGRS.2015.2429917

Baghdad, N., Gauthier, Y., Bernier, M., & Fortin, J.-P. (2000). Potential and Limitations of RADARSAT SAR Data for Wet Snow Monitoring. *IEEE Transactions on Geoscience and Remote Sensing*, *38*(1), 316–320. https://doi.org/10.1109/36.823925

Baijnath-Rodino, J. A., Duguay, C. R., & LeDrew, E. (2018). Climatological Trends of Snowfall Over the Laurentian Great Lakes Basin. *International Journal of Climatology*, *38*(10), 3942–3962.

https://doi.org/10.1002/joc.5546

Bari, S. A., & Hallett, J. (1974). Nucleation and Growth of Bubbles at an Ice-Water Interface. *Journal of Glaciology*, *13*(69), 489–520. https://doi.org/10.3189/S0022143000023248

Bartsch, A., Pointner, G., Leibman, M. O., Dvornikov, Y. A., Khomutov, A., & Trofaier, A. M. (2017). Circumpolar Mapping of Ground-Fast Lake Ice. *Frontiers in Earth Science*, *5*, 1–16. https://doi.org/10.3389/feart.2017.00012

Beckers, J. F., Casey, J. A., & Haas, C. (2017). Retrievals of Lake Ice Thickness From Great Slave Lake and Great Bear Lake Using CryoSat-2. *IEEE Transactions on Geoscience and Remote Sensing*, *55*(7), 3708–3720. https://doi.org/10.1109/TGRS.2017.2677583

Belward, A., Bourassa, M., Dowell, M., Briggs, S., Dolman, H., Holmlund, K., & Verstraete, M. (2016). The Global Observing System for Climate: Implementation Needs. *Reference Number GCOS-200*, 315. https://library.wmo.int/index.php?lvl=notice_display&id=19838#.XWP_nuhKgal

Benson, B. J., Magnuson, J. J., & Sharma, S. (2013). *Global Lake and Rive Ice Phenology Database, Version 1*. https://doi.org/10.7265/N5W66HP8

Brodzik, M. J., & Long, D. G. (2018). *NASA MEaSUREs Calibrated Passive Microwave Daily EASE - - - Grid 2.0 Brightness Temperature ESDR (CETB): Algorithm Theoretical Basis Document.*

Brogioni, M., Pettinato, S., Macelloni, G., Paloscia, S., Pampaloni, P., Pierdicca, N., & Ticconi, F. (2010). Sensitivity of Bistatic Scattering to Soil Moisture and Surface Roughness of Bare Soils. *International Journal of Remote Sensing*, *31*(15), 4227–4255. https://doi.org/10.1080/01431160903232808

Brooks, R. N., Prowse, T. D., & O'Connell, I. J. (2013). Quantifying Northern Hemisphere Freshwater Ice. *Geophysical Research Letters*, *40*(6), 1128–1131. https://doi.org/10.1002/grl.50238

Brown, L. C., & Duguay, C. R. (2010). The Response and Role of Ice Cover in Lake-Climate Interactions. *Progress in Physical Geography*, *34*(5), 671–704. https://doi.org/10.1177/0309133310375653

Brown, L. C., & Duguay, C. R. (2011a). A Comparison of Simulated and Measured Lake Ice Thickness using a Shallow Water Ice Profiler. *Hydrological Processes*, *25*(19), 2932–2941.

https://doi.org/10.1002/hyp.8087

Brown, L. C., & Duguay, C. R. (2011b). The Fate of Lake Ice in the North American Arctic. *The Cryosphere*, *5*(4), 869–892. https://doi.org/10.5194/tc-5-869-2011

Brown, L. C., & Duguay, C. R. (2012). Modelling Lake Ice Phenology With an Examination of Satellite-Detected Subgrid Cell Variability. *Advances in Meteorology*, *2012*, 1–19. https://doi.org/10.1155/2012/529064

Brown, R. S., Duguay, C. R., Mueller, R. P., Moulton, L. L., Doucette, P. J., & Tagestad, J. D. (2010). Use of Synthetic Aperture Radar (SAR) to Identify and Characterize Overwintering Areas of Fish in Ice-Covered Arctic Rivers: A Demonstration with Broad Whitefish and Their Habitats in the Sagavanirktok River, Alaska. *Transactions of the American Fisheries Society*, *139*(6), 1711–1722. https://doi.org/10.1577/t09-176.1

Cai, Y., Duguay, C. R., & Ke, C. (2022). A 41-year (1979-2019) Passive Microwave Derived Lake Ice Phenology Data Record of the Northern Hemisphere. *Earth System Science Data*, *14*(7), 3329–3347. https://doi.org/10.5194/essd-14-3329-2022

Cai, Y., Ke, C. Q., & Duan, Z. (2017). Monitoring Ice Variations in Qinghai Lake from 1979 to 2016 using Passive Microwave Remote Sensing Data. *Science of the Total Environment*, *607–608*, 120–131. https://doi.org/10.1016/j.scitotenv.2017.07.027

Cai, Y., Ke, C. Q., Li, X., Zhang, G., Duan, Z., & Lee, H. (2019). Variations of Lake Ice Phenology on the Tibetan Plateau From 2001 to 2017 Based on MODIS Data. *Journal of Geophysical Research : Atmospheres*, *124*, 1–19. https://doi.org/10.1029/2018JD028993

Camps, A., Park, H., Pablos, M., Foti, G., & Gommenginger, C. P. (2016). Sensitivity of GNSS-R Spaceborne Observations to Soil Moisture and Vegetation. *IEEE Journal of Selected Topics in Applied Earth Observations and Remote Sensing*, *9*(10), 4730–4742. https://doi.org/10.1109/JSTARS.2016.2588467

Cardellach, E., Wickert, J., Baggen, R., Benito, J., Camps, A., Catarino, N., Chapron, B., Dielacher, A., Fabra, F., Flato, G., Fragner, H., Gabarró, C., Gommenginger, C., Haas, C., Healy, S., Hernandez-Pajares, M., Høeg, P., Jäggi, A., Kainulainen, J., … Zuffada, C. (2018). GNSS Transpolar Earth Reflectometry ExploriNg System (G-TERN): Mission Concept. *IEEE Access*, *6*, 13980–14018.

https://doi.org/10.1109/ACCESS.2018.2814072

Charbonneau, F. J., Brisco, B., Raney, R. K., Mcnairn, H., Liu, C., Vachon, P. W., Shang, J., Deabreu, R., Champagne, C., Merzouki, A., & Geldsetzer, T. (2010). Compact Polarimetry Overview and Applications Assessment. *Canadian Journal of Remote Sensing*, *36*(2), 298–315. https://doi.org/10.5589/m10-062

Chen, K. S., Wu, T.-D., Tsang, L., Li, Q., Shi, J., & Fung, A. K. (2003). Emission of Rough Surfaces Calculated by the Integral Equation Method With Comparison to Three-Dimensional Moment Method Simulations. *IEEE Transactions on Geoscience and Remote Sensing*, *41*(1), 90–101. https://doi.org/10.1109/TGRS.2002.807587

Choudhury, B. J., Schmugge, T. J., Chang, A., & Newton, R. W. (1979). Effect of Surface Roughness on the Mircowave Emission From Soils. *Journal of Geophysical Research*, *84*(9), 5699–5706. https://doi.org/10.1029/JC084iC09p05699

Chuah, H., Tjuatja, S., Fung, A. K., & Bredow, J. W. (1996). A Phase Matrix for a Dense Discrete Random Medium: Evaluation of Volume Scattering Coefficient. *IEEE Transactions on Geoscience and Remote Sensing*, *34*(5), 1137–1143.

Clausi, D. A., Qin, A. K., Chowdhury, M. S., Yu, P., & Maillard, P. (2010). MAGIC: MAp-Guided Ice Classification System. *Canadian Journal of Remote Sensing*, *36*, S13–S25. https://doi.org/10.5589/m10-008

Crétaux, J.-F., Yésou, H., Merchant, C. J., Duguay, C. R., Simis, S., & Calmettes, B. (2020). *ESA Lakes Climate Change Initiative (Lakes CCI): Lake Products, Version 1.0*. https://doi.org/10.5285/3c324bb4ee394d0d876fe2e1db217378

Cummings, H., Cooper, C. Z., & Lokram, R. (2019). *The Economic Impact of Snowmobiling in Ontario*.

Dibike, Y., Prowse, T., Bonsal, B., Rham, L. D., & Saloranta, T. (2012). Simulation of North American Lake-Ice Cover Characteristics under Contemporary and Future Climate Conditions. *International Journal of Climatology*, *32*(5), 695–709. https://doi.org/10.1002/joc.2300

Dibike, Y., Prowse, T. D., Saloranta, T., & Ahmed, R. (2011). Response of Northern Hemisphere Lake-Ice Cover and Lake-Water Thermal Structure Patterns to a Changing Climate. *Hydrological Processes*, *25*(19), 2942–2953. https://doi.org/10.1002/hyp.8068

Dinardo, S., Fenoglio-marc, L., Buchhaupt, C., & Becker, M. (2018). Coastal SAR and PLRM altimetry in German Bight and West Baltic Sea. *Advances in Space Research*, *62*, 1371–1404. https://doi.org/10.1016/j.asr.2017.12.018

Du, J., Kimball, J. S., Duguay, C., Kim, Y., & Watts, J. D. (2017). Satellite Microwave Assessment of Northern Hemisphere Lake Ice Phenology From 2002 to 2015. *The Cryosphere*, *11*, 47–63. https://doi.org/10.5194/tc-11-47-2017

Duguay, C. R., Bernier, M., Gauthier, Y., & Kouraev, A. (2015). Remote Sensing of Lake and River Ice. In M. Tedesco (Ed.), *Remote Sensing of the Cryosphere* (1st ed., pp. 273–306). John Wiley & Sons, Ltd.

Duguay, C. R., Flato, G. M., Jeffries, M. O., Ménard, P., Morris, K., & Rouse, W. R. (2003). Ice-Cover Variability on Shallow Lakes at High Latitudes: Model Simulations and Observations. *Hydrological Processes*, *17*(17), 3465–3483. https://doi.org/10.1002/hyp.1394

Duguay, C. R., & Lafleur, P. M. (2003). Determining Depth and Ice Thickness of Shallow Sub-Arctic Lakes Using Space-Borne Optical and SAR Data. *International Journal of Remote Sensing*, *24*(3), 475–489. https://doi.org/10.1080/01431160304992

Duguay, C. R., Pultz, T. J., Lafleur, P. M., & Drai, D. (2002). RADARSAT Backscatter Characteristics of Ice Growing on Shallow Sub-Arctic Lakes, Churchill, Manitoba, Canada. *Hydrological Processes*, *16*(8), 1631–1644. https://doi.org/10.1002/hyp.1026

Duguay, C. R., & Wang, J. (2019). Advancement in Bedfast Lake Ice Mapping from Sentinel-1 SAR Data. *IGARSS 2019 - 2019 IEEE International Geoscience and Remote Sensing Symposium*, 6922–6925.

Eerola, K., Rontu, L., Kourzeneva, E., Pour, H. K., & Duguay, C. (2014). Impact of Partly Ice-Free Lake Ladoga on Temperature and Cloudiness in an Anticyclonic Winter Situation – a Case Study Using a Limited Area Model. *Tellus A: Dynamic Meteorology and Oceanography*, *66*(1), 23929. https://doi.org/10.3402/tellusa.v66.23929

Elachi, C., Bryan, M. L., & Weeks, W. F. (1976). Imaging Radar Observations of Frozen Arctic Lakes. *Remote Sensing of Environment*, *5*, 169–175. https://doi.org/10.1016/0034-4257(76)90047-X

Engram, M., Anthony, K. W., Meyer, F. J., & Grosse, G. (2012). Synthetic Aperture Radar (SAR)

Backscatter Response From Methane Ebullition Bubbles Trapped by Thermokarst Lake Ice. *Canadian Journal of Remote Sensing*, *38*(6), 667–682. https://doi.org/10.5589/m12-054

Engram, M., Anthony, K. W., Meyer, F. J., & Grosse, G. (2013). Characterization of L-Band Synthetic Aperture Radar (SAR) Backscatter From Floating and Grounded Thermokarst Lake Ice in Arctic Alaska. *Cryosphere*, *7*(6), 1741–1752. https://doi.org/10.5194/tc-7-1741-2013

Engram, M., Arp, C. D., Jones, B. M., Ajadi, O. A., & Meyer, F. J. (2018). Analyzing Floating and Bedfast Lake Ice Regimes Across Arctic Alaska Using 25 Years of Space-Borne SAR Imagery. *Remote Sensing of Environment*, *209*(March), 660–676. https://doi.org/10.1016/j.rse.2018.02.022

Environment and Climate Change Canada. (2021a). *Churchill Airport Climate Normals*. https://climate.weather.gc.ca/climate_normals/results_1981_2010_e.html?stnID=3871&autofwd=1

Environment and Climate Change Canada. (2021b). *Churchill Climate Historical Daily Weather Data*. https://climate.weather.gc.ca/historical_data/search_historic_data_e.html

Environment and Climate Change Canada. (2021c). *Inuvik Airport Climate Normals*. https://climate.weather.gc.ca/climate_normals/results_1981_2010_e.html?stnID=1669&autofwd=1#normals-data

Environment and Climate Change Canada. (2021d). *Inuvik Climate Historical Daily Weather Data*. https://climate.weather.gc.ca/historical_data/search_historic_data_e.html

European Space Agency. (2020). *SNAP - ESA Sentinel Application Platform* (v7.0.0). http://step.esa.int

Ewe, H. T., Chuah, H. T., & Fung, A. K. (1998). A Backscatter Model for a Dense Discrete Medium: Analysis and Numerical Results. *Remote Sensing of Environment*, *65*(2), 195–203. https://doi.org/10.1016/S0034-4257(98)00027-3

Filazzola, A., Blagrave, K., Imrit, M. A., & Sharma, S. (2020). Climate Change Drives Increases in Extreme Events for Lake Ice in the Northern Hemisphere. *Geophysical Research Letters*, *47*(18). https://doi.org/10.1029/2020GL089608

Flato, G. M., & Brown, R. D. (1996). Variability and Climate Sensitivity of Landfast Arctic Sea Ice. *Journal of Geophysical Research C: Oceans*, *101*(C11), 25767–25777. https://doi.org/10.1029/96JC02431

French, N., Savage, S., Shuchman, R., Edson, R., Payne, J., & Josberger, E. (2004). Remote Sensing of Frozen Lakes on the North Slope of Alaska. *IEEE International Geoscience and Remote Sensing Symposium*, *5*, 3008–3011. https://doi.org/10.1109/IGARSS.2004.1370330

Fu, L. L., Alsdorf, D., Morrow, R., Rodriguez, E., & Mognard, N. (2012). *SWOT: the Surface Water and Ocean Topography Mission: Wide-Swath Altimetric Elevation on Earth*. https://trs.jpl.nasa.gov/handle/2014/41996

Fung, A. K., & Chen, K. S. (2010). *Microwave Scattering and Emission Models for Users*. Artech House.

Fung, A. K., Li, Z., & Chen, K. S. (1992). Backscattering From a Randomly Rough Dielectric Surface. *IEEE Transactions on Geoscience and Remote Sensing*, *30*(2), 356–369. https://doi.org/10.1109/36.134085

Gallet, J.-C., Domine, F., Zender, C. S., & Picard, G. (2009). Measurement of the Specific Surface Area of Snow Using Infrared Reflectance in an Integrating Sphere at 1310 and 1550 nm. *The Cryosphere*, *3*, 167–182. https://doi.org/10.5194/tc-3-167-2009

Geldsetzer, T., & van der Sanden, J. J. (2013). Identification of Polarimetric and Nonpolarimetric C-Band SAR Parameters for Application in the Monitoring of Lake Ice Freeze-Up. *Canadian Journal of Remote Sensing*, *39*(3), 263–275. https://doi.org/10.5589/m13-033

Geldsetzer, T., van der Sanden, J. J., & Brisco, B. (2010). Monitoring Lake Ice During Spring Melt Using RADARSAT-2 SAR. *Canadian Journal of Remote Sensing*, *36*(2), 391–400. https://doi.org/10.5589/m11-001

Gherboudj, I., Bernier, M., Hicks, F., & Leconte, R. (2007). Physical Characterization of Air Inclusions in River Ice. *Cold Regions Science and Technology*, *49*(3), 179–194. https://doi.org/10.1016/j.coldregions.2007.02.008

Gherboudj, I., Bernier, M., & Leconte, R. (2007). Validation of a Backscatter Model of a River Ice Covers Using RADARSAT-1 Images. *International Geoscience and Remote Sensing Symposium (IGARSS)*, 1087–1090. https://doi.org/10.1109/IGARSS.2007.4422990

Gherboudj, I., Bernier, M., & Leconte, R. (2010). A Backscatter Modeling for River Ice: Analysis and Numerical Results. *IEEE Transactions on Geoscience and Remote Sensing*, *48*(4 PART 1), 1788–1798. https://doi.org/10.1109/TGRS.2009.2034256

Ghiasi, Y., Duguay, C. R., Murfitt, J., van der Sanden, J. J., Thompson, A., Drouin, H., & Prévost, C. (2020). Application of GNSS Interferometric Reflectometry for the Estimation of Lake Ice Thickness. *Remote Sensing*, *12*(17), 2721. https://doi.org/10.3390/rs12172721

Gunn, G. E., Brogioni, M., Duguay, C., Macelloni, G., Kasurak, A., & King, J. (2015). Observation and Modeling of X- and Ku-Band Backscatter of Snow-Covered Freshwater Lake Ice. *IEEE Journal of Selected Topics in Applied Earth Observations and Remote Sensing*, *8*(7), 3629–3642. https://doi.org/10.1109/JSTARS.2015.2420411

Gunn, G. E., Duguay, C., Derksen, C., Clausi, D., & Toose, P. (2017). Investigating the Influence of Variable Freshwater Ice Types on Passive and Active Microwave Observations. *Remote Sensing*, *9*(12), 1242. https://doi.org/10.3390/rs9121242

Gunn, G. E., Duguay, C. R., Atwood, D. K., King, J., & Toose, P. (2018). Observing Scattering Mechanisms of Bubbled Freshwater Lake Ice Using Polarimetric RADARSAT-2 (C-Band) and UW-Scat (X- and Ku-Bands). *IEEE Transactions on Geoscience and Remote Sensing*, *56*(5), 2887–2903. https://doi.org/10.1109/TGRS.2017.2786158

Gunn, G. E., Duguay, C. R., Brown, L. C., King, J., Atwood, D., & Kasurak, A. (2015). Freshwater Lake Ice Thickness Derived Using Surface-Based X- and Ku-Band FMCW Scatterometers. *Cold Regions Science and Technology*, *120*, 115–126. https://doi.org/10.1016/j.coldregions.2015.09.012

Gunn, G. E., Duguay, C. R., Derksen, C., Lemmetyinen, J., & Toose, P. (2011). Evaluation of the HUT Modified Snow Emission Model Over Lake Ice Using Airborne Passive Microwave Measurements. *Remote Sensing of Environment*, *115*(1), 233–244. https://doi.org/10.1016/j.rse.2010.09.001

Gunn, G. E., Tarabara, V., Rutty, M., Bessette, D. L., & Richardson, R. B. (2021). Roughness and Storage Capacity of Freshwater Ice in the Straits of Mackinac. *Cold Regions Science and Technology*, *186*, 1–9. https://doi.org/10.1016/j.coldregions.2021.103278

Hall, D. K., Fagre, D. B., Klasner, F., Linebaugh, G., & Liston, G. E. (1994). Analysis of ERS 1 Synthetic Aperture Radar Data of Frozen Lakes in Northern Montana and Implications for Climate Studies. *Journal of Geophysical Research*, *99*(C11), 22473–22482. http://www.agu.org/pubs/crossref/1994/94JC01391.shtml

Hallikainen, M., Ulaby, F., & Abdelrazik, M. (1986). Dielectric Properties of Snow in the 3 to 37 GHz.

IEEE Transactions on Antennas and Propagation, *34*(11), 1329–1340. https://doi.org/10.1109/TAP.1986.1143757

Hampton, S. E., Galloway, A. W. E., Powers, S. M., Ozersky, T., Woo, K. H., Batt, R. D., Labou, S. G., O'Reilly, C. M., Sharma, S., Lottig, N. R., Stanley, E. H., North, R. L., Stockwell, J. D., Adrian, R., Weyhenmeyer, G. A., Arvola, L., Baulch, H. M., Bertani, I., Bowman, L. L., … Xenopoulos, M. A. (2017). Ecology Under Lake Ice. *Ecology Letters*, *20*(1), 98–111. https://doi.org/10.1111/ele.12699

Han, H., & Lee, H. (2013). Radar Backscattering of Lake Ice During Freezing and Thawing Stages Estimated by Ground-Based Scatterometer Experiment and Inversion From Genetic Algorithm. *IEEE Transactions on Geoscience and Remote Sensing*, *51*(5), 3089–3096.

Harzing, A. W. (2020). *Publish or Perish*. https://harzing.com/resources/publish-or-perish

Heinilä, K., Metsämäki, S., & Mattila, O.-P. (2017). Lake Ice Extent - Algorithm Theoretical Basis Document. In *Copernicus Global Land Operations "Cryosphere and Water"* (p. 22). https://land.copernicus.eu/global/products/lie

Hersbach, H., Bell, B., Berrisford, P., Hirahara, S., Horányi, A., Nicolas, J., Peubey, C., Radu, R., Bonavita, M., Dee, D., Dragani, R., Flemming, J., Forbes, R., Geer, A., Hogan, R. J., Janisková, H. M., Keeley, S., Laloyaux, P., Cristina, P. L., & Thépaut, J. (2018). *ERA5 Hourly Data on Single Levels From 1979 to Present. Copernicus Climate Change Service (C3S) Climate Data Store (CDS)*. https://doi.org/10.24381/cds.adbb2d47

Hersbach, H., Bell, B., Berrisford, P., Hirahara, S., Horányi, A., Nicolas, J., Peubey, C., Radu, R., Bonavita, M., Dee, D., Dragani, R., Flemming, J., Forbes, R., Geer, A., Hogan, R. J., Janisková, H. M., Keeley, S., Laloyaux, P., Cristina, P. L., & Thépaut, J. (2020). The ERA5 Global Reanalysis. *Quarterly Journal of the Royal Meteorological Society*, *146*(730), 1999–2049. https://doi.org/10.1002/qj.3803

Hewitt, B. A. (2019). *Effects of Climate Change on Lake Ice Freeze Up Across the Northern Hemisphere: Historical Patterns and Future Predictions* [York University]. http://hdl.handle.net/10315/36314

Hirose, T., Kapfer, M., Bennett, J., Cott, P., Manson, G., & Solomon, S. (2008). Bottomfast Ice Mapping and the Measurement of Ice Thickness on Tundra Lakes Using C-Band Synthetic Aperture Radar Remote Sensing. *Journal of the American Water Resources Association*, *44*(2), 285–292.

https://doi.org/10.1111/j.1752-1688.2007.00161.x

Hoekstra, M., Jiang, M., Clausi, D. A., & Duguay, C. R. (2020). Lake Ice-Water Classification of RADARSAT-2 Images by Integrating IRGS Segmentation with Pixel-Based Random Forest Labeling. *Remote Sensing*, *12*(1425), 1–21. https://doi.org/10.3390/rs12091425

Hoekstra, P., & Delaney, A. (1974). Dielectric Properties of Soils at UHF and Microwave Frequencies. *Journal of Geophysical Research*, *79*(11), 1699–1708. https://doi.org/10.1029/JB079i011p01699

Howell, S. E. L., Brown, L. C., Kang, K.-K., & Duguay, C. R. (2009). Variability in Ice Phenology on Great Bear Lake and Great Slave Lake, Northwest Territories, Canada, from SeaWinds/QuikSCAT: 2000-2006. *Remote Sensing of Environment*, *113*(4), 816–834. https://doi.org/10.1016/j.rse.2008.12.007

Howell, S. E. L., Yackel, J. J., De Abreu, R., Geldsetzer, T., & Breneman, C. (2005). On the Utility of SeaWinds/QuikSCAT Data for the Estimation of the Thermodynamic State of First-Year Sea Ice. *IEEE Transactions on Geoscience and Remote Sensing*, *43*(6), 1338–1350. https://doi.org/10.1109/TGRS.2005.846153

Huber, S., De Almeida, F. Q., Villano, M., Younis, M., Krieger, G., & Moreira, A. (2018). Tandem-L: A Technical Perspective on Future Spaceborne SAR Sensors for Earth Observation. *IEEE Transactions on Geoscience and Remote Sensing*, *56*(8), 4792–4807. https://doi.org/10.1109/TGRS.2018.2837673

Hyvaerinen, P. (2004). *Determining the Optimal Release Window for Lake-Stocked Brown Trout : Interactions between Release Size , Prey Availability , Predation Risks and Fishing Mortality* [University of Helsinki]. http://ethesis.helsinki.fi/

Jeffries, M. O., Morris, K., & Duguay, C. R. (2012). State of the Earth's Cryosphere at the Beginning of the 21st Century: Glaciers, Global Snow Cover, Floating Ice, and Permafrost and Periglacial Environments - Floating Ice: Lake Ice and River Ice. In R. S. Williams & J. G. Ferrigno (Eds.), *Satellite Image Atlas of Glaciers of the World* (pp. A381–A424). https://doi.org/https://doi.org/10.3133/pp1386A

Jeffries, M. O., Morris, K., & Liston, G. E. (1996). A Method to Determine Lake Depth and Water Availability on the North Slope of Alaska With Spaceborne Imaging Radar and Numerical Ice

Growth Modelling. *Arctic*, *49*(4), 367–374. www.jstor.org/stable/40512022

Jeffries, M. O., Morris, K., Weeks, W. F., & Wakabayashi, H. (1994). Structural and Stratigraphic Features and ERS 1 Synthetic Aperture Radar Backscatter Characteristics of Ice Growing on Shallow Lakes in NW Alaska, Winter 1991-1992. *Journal of Geophysical Research*, *99*(C11), 22459–22471. https://doi.org/10.1029/94JC01479

Jirberg, R. J., Schertler, R. J., Gedney, R. T., & Mark, H. (1974). Application of SLAR for Monitoring Great Lakes Total Ice Cover. In H. S. Santeford & J. L. Smith (Eds.), *Advanced Concepts and Techniques in the Study of Snow and Ice Resources* (p. 789). National Academy of Sciences.

Johannessen, O. M., Kuzmina, S. I., Bobylev, L. P., & Miles, M. W. (2016). Surface Air Temperature Variability and Trends in the Arctic: New Amplification Assessment and Regionalisation. *Tellus, Series A: Dynamic Meteorology and Oceanography*, *68*(1), 1–12. https://doi.org/10.3402/tellusa.v68.28234

Kang, K.-K., Duguay, C. R., & Howell, S. E. L. (2012). Estimating Ice Phenology on Large Northern Lakes from AMSR-E: Algorithm Development and Application to Great Bear Lake and Great Slave Lake, Canada. *The Cryosphere*, *6*(2), 235–254. https://doi.org/10.5194/tc-6-235-2012

Kang, K.-K., Duguay, C. R., Lemmetyinen, J., & Gel, Y. (2014). Estimation of Ice Thickness on Large Northern Lakes from AMSR-E Brightness Temperature Measurements. *Remote Sensing of Environment*, *150*, 1–19. https://doi.org/10.1016/j.rse.2014.04.016

Ke, C.-Q., Tao, A.-Q., & Jin, X. (2013). Variability in the Ice Phenology of Nam Co Lake in Central Tibet From Scanning Multichannel Microwave Radiometer and Special Sensor Microwave/Imager: 1978 to 2013. *Journal of Applied Remote Sensing*, *7*(1), 073477. https://doi.org/10.1117/1.jrs.7.073477

Kern, M., Cullen, R., Berruti, B., Bouffard, J., Casal, T., Drinkwater, M. R., Gabriele, A., Lecuyot, A., Ludwig, M., Midthassel, R., Traver, I. N., Parrinello, T., Ressler, G., Andersson, E., Martin-Puig, C., Andersen, O., Farrell, S., Fleury, S., Gascoin, S., … Yackel, J. (2020). The Copernicus Polar Ice and Snow Topography Altimeter (CRISTAL): Expected Mission Contributions. *The Cryosphere Discussions*, *Preprint*, 1–27. https://doi.org/https://doi.org/10.5194/tc-2020-3

Knoll, L. B., Sharma, S., Denfeld, B. A., Flaim, G., Hori, Y., Magnuson, J. J., Straile, D., &

Weyhenmeyer, G. A. (2019). Consequences of Lake and River Ice Loss on Cultural Ecosystem Services. *Limnology and Oceanography Letters*, *4*(5), 119–131. https://doi.org/10.1002/lol2.10116

Komarov, A. S., Landy, J. C., Komarov, S. A., & Barber, D. G. (2017). *Evaluating Scattering Contributions to C-Band Radar Backscatter From Snow-Covered First-Year Sea Ice at the Winter – Spring Transition Through Measurement and Modeling*. *55*(10), 5702–5718.

Korhonen, J. (2005). Ice Conditions in Lakes and Rivers in Finland. *The Finnish Environment*, *751*, 1–145.

Korhonen, J. (2006). Long-Term Changes in Lake Ice Cover in Finland. *Nordic Hydrology*, *37*(4–5), 347. https://doi.org/10.2166/nh.2006.019

Kouraev, A. V., Papa, F., Buharizin, P. I., Cazenave, A., Cretaux, J. F., Dozortseva, J., & Rémy, F. (2003). Study and Monitoring of Sea Ice Cover in the Caspian and Aral Seas from TOPEX/POSEIDON Microwave Data. *Elsevier Oceanography Series*, *69*(C), 141–145. https://doi.org/10.1016/S0422-9894(03)80024-7

Kouraev, A. V., Shimaraev, M. N., Buharizin, P. I., Naumenko, M. A., Crétaux, J. F., Mognard, N., Legrésy, B., & Rémy, F. (2008). Ice and Snow Cover of Continental Water Bodies From Simultaneous Radar Altimetry and Radiometry Observations. *Surveys in Geophysics*, *29*(4–5), 271–295. https://doi.org/10.1007/s10712-008-9042-2

Kouraev, A. V, Semovski, S., Shimaraev, M., Mognard, N., Legresy, B., & Rémy, F. (2007). Observations of Lake Baikal Ice From Satellite Altimetry and Radiometry. *Remote Sensing of Environment*, *108*(3), 240–253. https://doi.org/10.1016/j.rse.2006.11.010

Kozlenko, N., & Jeffries, M. O. (2000). Bathymetric Mapping of Shallow Water in Thaw Lakes on the North Slope of Alaska with Spaceborne Imaging Radar. *Arctic*, *53*(3), 306–316.

Landy, J. C., Tsamados, M., & Scharien, R. K. (2019). *A Facet-Based Numerical Model for Simulating SAR Altimeter Echoes From Heterogeneous Sea Ice Surfaces*. *57*(7), 4164–4180.

Larrowe, B. T. (1971). *Fine-Resolution Radar Investigation of Great Lakes Ice Cover*.

Larson, K. M., & Small, E. E. (2016). Estimation of Snow Depth Using L1 GPS Signal-to-Noise Ratio Data. *IEEE Journal of Selected Topics in Applied Earth Observations and Remote Sensing*, *9*(10),

4802–4808.

Latifovic, R., & Pouliot, D. (2007). Analysis of Climate Change Impacts on Lake Ice Phenology in Canada using the Historical Satellite Data Record. *Remote Sensing of Environment*, *106*(4), 492–507. https://doi.org/10.1016/j.rse.2006.09.015

Laxon, S., Peacock, H., & Smith, D. (2003). High Interannual Variability of Sea Ice Thickness in the Arctic Region. *Nature*, *425*(6961), 947–950. https://doi.org/10.1038/nature02050

Leconte, R., Daly, S., Gauthier, Y., Yankielun, N., Bérubé, F., & Bernier, M. (2009). A Controlled Experiment to Retrieve Freshwater Ice Characteristics From an FM-CW Radar System. *Cold Regions Science and Technology*, *55*(2), 212–220. https://doi.org/10.1016/j.coldregions.2008.04.003

Leconte, R., & Klassen, P. D. (1991). Lake and River Ice Investigations in Northern Manitoba Using Airborne SAR Imagery. *Arctic*, *44*(1), 153–163.

Lee, J. (1981). Refined Filtering of Image Noise Using Local Statistics. *Computer Graphics and Image Processing*, *15*, 380–389.

Leigh, S., Wang, Z., & Clausi, D. A. (2013). Automated Ice-Water Classification Using Dual Polarization SAR Satellite Imagery. *IEEE Transactions on Geoscience and Remote Sensing*, *52*(9), 5529–5539. https://doi.org/10.1109/TGRS.2013.2290231

Lemmetyinen, J., Derksen, C., Pulliainen, J., Strapp, W., Toose, P., Walker, A., Tauriainen, S., Pihlflyckt, J., Kärnä, J. P., & Hallikainen, M. T. (2009). A Comparison of Airborne Microwave Brightness Temperatures and Snowpack Properties Across the Boreal Forests of Finland and Western Canada. *IEEE Transactions on Geoscience and Remote Sensing*, *47*(3), 965–978. https://doi.org/10.1109/TGRS.2008.2006358

Lemmetyinen, J., Kontu, A., Kärnä, J., Vehviläinen, J., Takala, M., & Pulliainen, J. (2011). Correcting for the Influence of Frozen Lakes in Satellite Microwave Radiometer Observations Through Application of a Microwave Emission Model. *Remote Sensing of Environment*, *115*, 3695–3706. https://doi.org/10.1016/j.rse.2011.09.008

Lemmetyinen, J., Pulliainen, J., Rees, A., Kontu, A., Qiu, Y., & Derksen, C. (2010). Multiple-Layer Adaptation of HUT Snow Emission Model: Comparison With Experimental Data. *IEEE Transactions on Geoscience and Remote Sensing*, *48*(7), 2781–2794.

https://doi.org/10.1109/TGRS.2010.2041357

Leshkevich, G. A. (1977). *Great Lakes Ice Cover, Winter 1975-76 (No. 104)*.

Lindenschmidt, K.-E., & Li, Z. (2018). Monitoring River Ice Cover Development Using the Freeman–Durden Decomposition of Quad-Pol RADARSAT-2 Images. *Journal of Applied Remote Sensing*, *12*(02), 1. https://doi.org/10.1117/1.jrs.12.026014

Ling, F., & Zhang, T. (2003). Numerical Simulation of Permafrost Thermal Regime and Talik Development Under Shallow Thaw Lakes on the Alaskan Arctic Coastal Plain. *Journal of Geophysical Research: Atmospheres*, *108*(16), 1–11. https://doi.org/10.1029/2002jd003014

Lopez, L. S., Hewitt, B. A., & Sharma, S. (2019). Reaching a Breaking Point : How is Climate Change Influencing the Timing of Ice Breakup in Lakes Across the Northern Hemisphere? *Limnology and Oceanography*, *64*, 2621–2631. https://doi.org/10.1002/lno.11239

Löwe, H., & Picard, G. (2015). Microwave Scattering Coefficient of Snow in MEMLS and DMRT-ML Revisited: The Relevance of Sticky Hard Spheres and Tomography-based Estimates of Stickiness. *Cryosphere*, *9*, 2101–2117. https://doi.org/10.5194/tc-9-2101-2015

Ma, L., Liu, Y., Zhang, X., Ye, Y., Yin, G., & Johnson, B. A. (2019). Deep Learning in Remote Sensing Applications: A Meta-Analysis and Review. *ISPRS Journal of Photogrammetry and Remote Sensing*, *152*(March), 166–177. https://doi.org/10.1016/j.isprsjprs.2019.04.015

Magnuson, J. J., Robertson, D. M., Benson, B. J., Wynne, R. H., Livingstone, D. M., Arai, T., Assel, R. A., Barry, R. G., Card, V., Kuusisto, E., Granin, N. G., Prowse, T. D., Stewart, K. M., & Vuglinski, V. S. (2000). Historical Trends in Lake and River Ice Cover in the Northern Hemisphere. *Science*, *289*(5485), 1743–1746. c:%5CPublications%5Cmagnuson-FreezeUpDatesLater.pdf

Mahmud, M. S., Howell, S. E. L., Geldsetzer, T., & Yackel, J. (2016). Detection of Melt Onset Over the Northern Canadian Arctic Archipelago Sea Ice from RADARSAT, 1997 – 2014. *Remote Sensing of Environment*, *178*, 59–69. https://doi.org/10.1016/j.rse.2016.03.003

Mangilli, A., Thibaut, P., Duguay, C. R., & Murfitt, J. (2022). A New Approach for the Estimation of Lake Ice Thickness From Conventional Radar Altimetry. *IEEE Transactions on Geoscience and Remote Sensing*, *60*. https://doi.org/10.1109/TGRS.2022.3186253

Martin-Neira, M., Li, W., Andres-Beivide, A., & Ballesteros-Sels, X. (2016). “Cookie”: A Satellite Concept for GNSS Remote Sensing Constellations. *IEEE Journal of Selected Topics in Applied Earth Observations and Remote Sensing*, *9*(10), 4593–4610. https://doi.org/10.1109/JSTARS.2016.2585620

Matsuoka, T., Uratsuka, S., Takahashi, A., Kobayashi, T., Satake, M., Nadai, A., Umehara, T., Wakabayashi, H., & Nishio, F. (1999). A Backscattering Model for Bubbles in Lake Ice and Comparisons With Satellite and Airborne SAR Data. *IEEE 1999 International Geoscience and Remote Sensing Symposium*, 107–109. https://doi.org/10.1109/igarss.1999.773416

Mätzler, C. (1998). Improved Born Approximation for Scattering of Radiation in a Granular Medium. *Journal of Applied Physics*, *83*(11), 6111–6117. https://doi.org/10.1063/1.367496

Mätzler, C. (2002). Relation Between Grain-Size and Correlation Length of Snow. *Journal of Gl*, *48*(16), 461–466. https://doi.org/10.3189/172756502781831287

Mätzler, C., Rosenkranz, P. W., Battaglia, A., & Wigneron, J. P. (2006). *Thermal Microwave Radiation: Applications for Remote Sensing*. Institution of Engineering and Technology.

Mätzler, C., & Wegmüller, U. (1987). Dielectric Properties of Freshwater Ice at Microwave Frequencies. *Journal of Physics D: Applied Physics*, *20*(12), 1623–1630. https://doi.org/10.1088/0022-3727/20/12/013

Mätzler, C., & Wiesmann, A. (2007). *Documentation for MEMLS, Version 3*.

Mayers, D., & Ruf, C. (2018). Measuring Ice Thickness With CYGNSS Altimetry. *International Geoscience and Remote Sensing Symposium (IGARSS)*, 8535–8538. https://doi.org/10.1109/IGARSS.2018.8519310

Maykut, G. A., & Untersteiner, N. (1971). Some Results from a Time-Dependent Thermodynamic Model of Sea Ice. *Journal of Geophysical Research*, *76*(6), 1550–1575. https://doi.org/10.1029/JC076i006p01550

Mellor, J. C. (1982). *Bathymetry of Alaskan Arctic Lakes : A Key to Resource Inventory With Remote-Sensing Methods* [University of Alaska Fairbanks]. https://scholarworks.alaska.edu/handle/11122/5106

Michel, B. (1971). Winter Regime of Rivers and Lakes. In *Cold Regions Science and Engineering Monograph lll-B1a*.

Moller, D., Andreadis, K. M., Bormann, K. J., Hensley, S., & Painter, T. H. (2017). Mapping Snow Depth from Ka-Band Interferometry: Proof of Concept and Comparison with Scanning Lidar Retrievals. *IEEE Geoscience and Remote Sensing Letters*, *14*(6), 886–890. https://doi.org/10.1109/LGRS.2017.2686398

Morris, K., Jeffries, M. O., & Weeks, W. F. (1995). Ice Processes and Growth History on Arctic and Sub-Arctic Lakes Using ERS-1 SAR Data. *Polar Record*, *31*(177), 115–128. https://doi.org/10.1017/S0032247400013619

Mullan, D., Swindles, G., Patterson, T., Galloway, J., Macumber, A., Falck, H., Crossley, L., Chen, J., & Pisaric, M. (2017). Climate Change and the Long-Term Viability of the World's Busiest Heavy Haul Ice Road. *Theoretical and Applied Climatology*, *129*(3–4), 1089–1108. https://doi.org/10.1007/s00704-016-1830-x

Murfitt, J., & Brown, L. C. (2017). Lake Ice and Temperature Trends for Ontario and Manitoba: 2001 to 2014. *Hydrological Processes*, *31*(21), 3596–3609. https://doi.org/10.1002/hyp.11295

Murfitt, J., Brown, L. C., & Howell, S. E. L. (2018a). Estimating Lake Ice Thickness in Central Ontario. *PLoS ONE*, *13*(12), 1–20. https://doi.org/10.1371/journal.pone.0208519

Murfitt, J., Brown, L. C., & Howell, S. E. L. (2018b). Evaluating RADARSAT-2 for the Monitoring of Lake Ice Phenology Events in Mid-Latitudes. *Remote Sensing*, *10*(10), 1641. https://doi.org/https://doi.org/10.3390/rs10101641

Murfitt, J., & Duguay, C. R. (2020). Assessing the Performance of Methods for Monitoring Ice Phenology of the World's Largest High Arctic Lake Using High-Density Time Series Analysis of Sentinel-1 Data. *Remote Sensing*, *12*(382), 1–26. https://doi.org/10.3390/rs12030382

Murfitt, J., & Duguay, C. R. (2021). 50 Years of Lake Ice Research From Active Microwave Remote Sensing: Progress and Prospects. *Remote Sensing of Environment*, *264*, 1–21. https://doi.org/10.1016/j.rse.2021.112616

Murfitt, J., Duguay, C. R., Picard, G., & Gunn, G. E. (2022). Investigating the Effect of Lake Ice Properties on Multifrequency Backscatter Using the Snow Microwave Radiative Transfer (SMRT)

Model. *IEEE Transactions on Geoscience and Remote Sensing*, *60*, 1–26. https://doi.org/10.1109/TGRS.2022.3197109

Nagler, T., & Rott, H. (2000). Retrieval of Wet Snow by Means of Multitemporal SAR Data. *IEEE Transactions on Geoscience and Remote Sensing*, *38*(2), 754–765.

NASA JPL. (2013). *NASA Shuttle Radar Topography Mission Global 1 arc second [Data set]. NASA EOSDIS Land Processes DAAC*. https://doi.org/10.5067/MEaSUREs/SRTM/SRTMGL1.003

National Research Council. (2004). *Climate Data Records from Environmental Satellites: Interim Report*. https://doi.org/10.17226/10944

National Weather Service. (2014). *Lake Effect Summary - November 17-19, 2014*. https://www.weather.gov/buf/lake1415_stormb.html

Notaro, M., Bennington, V., & Vavrus, S. (2015). Dynamically Downscaled Projections of Lake-Effect Snow in the Great Lakes Basin. *Journal of Climate*, *28*(4), 1661–1684. https://doi.org/10.1175/JCLI-D-14-00467.1

Ogbebo, F. E., Evans, M. S., Waiser, M. J., Tumber, V. P., & Keating, J. J. (2009). Nutrient Limitation of Phytoplankton Growth in Arctic Lakes of the Lower Mackenzie River Basin, Northern Canada. *Canadian Journal of Fisheries and Aquatic Sciences*, *66*(2), 247–260. https://doi.org/10.1139/F08-202

Oh, Y., Sarabandi, K., & Ulaby, F. T. (2002). Semi-Empirical Model of the Ensemble-Averaged Differential Mueller Matrix for Microwave Backscattering From Bare Soil Surfaces. *IEEE Transactions on Geoscience and Remote Sensing*, *40*(6), 1348–1355. https://doi.org/10.1109/TGRS.2002.800232

Otsu, N. (1979). A Threshold Selection Method From Gray-Level Histograms. *IEEE Transactions on Systems, Man, and Cybernetics*, *9*(1), 62–66.

Paquette-Struger, B., Wrona, F. J., Atkinson, D., & Di Cenzo, P. (2018). Seasonal Variations in the Limnology of Noell Lake in the Western Canadian Arctic Tracked by In Situ Observation Systems. *Arctic*, *71*(2), 149–166. https://doi.org/10.14430/arctic4716

Petrich, C., & Eicken, H. (2010). Growth, Structure and Properties of Sea Ice. In *Sea Ice* (pp. 23–78).

Blackwell.

Picard, G., Brucker, L., Roy, A., Dupont, F., Fily, M., Royer, A., & Harlow, C. (2013). Simulation of the Microwave Emission of Multi-Layered Snowpacks Using the Dense Media Radiative Transfer Theory: the DMRT-ML Model. *Geoscientific Model Development*, *6*(4), 1061–1078. https://doi.org/10.5194/gmd-6-1061-2013

Picard, G., Leduc-Leballeur, M., Banwell, A. F., Brucker, L., & Macelloni, G. (2022). The Sensitivity of Satellite Microwave Observations to Liquid Water in the Antarctic Snowpack. *The Cryosphere Discussions*, 1–34. https://doi.org/10.5194/tc-2022-85

Picard, G., Löwe, H., Domine, F., Arnaud, L., Larue, F., Favier, V., & Meur, E. Le. (2022). The Microwave Snow Grain Size : A New Concept to Predict Satellite Observations Over Snow-Covered Regions. *AGU Advances*, *3*. https://doi.org/10.1029/2021AV000630

Picard, G., Löwe, H., & Mätzler, C. (2022). Brief Communication : A Continuous Formulation of Microwave Scattering from Fresh Snow to Bubbly Ice from First Principles. *Cryosphere Discussions*, *March*, 1–9. https://doi.org/https://doi.org/10.5194/tc-2022-63

Picard, G., Sandells, M., & Löwe, H. (2018). SMRT: An Active-passive Microwave Radiative Transfer Model for Snow With Multiple Microstructure and Scattering Formulations (v1.0). *Geoscientific Model Development*, *11*(7), 2763–2788. https://doi.org/10.5194/gmd-11-2763-2018

Pierdicca, N., Davidson, M., Chini, M., Dierking, W., Djavidnia, S., Haarpaintner, J., Hajduch, G., Laurin, G. V., Lavalle, M., López-Martínez, C., Nagler, T., & Su, B. (2019). The Copernicus L-band SAR mission ROSE-L (Radar Observing System for Europe) (Conference Presentation). *Active and Passive Microwave Remote Sensing for Environmental Monitoring III*. https://doi.org/10.1117/12.2534743

Pirinen, P., Simola, H., Aalto, J., Kaukoranta, J.-P., Karlsson, P., & Ruuhela, R. (2012). *Tilastoja Suomen Ilmastosta 1981-2010*. http://hdl.handle.net/10138/35880

Pointner, G., Bartsch, A., Dvornikov, Y. A., & Kouraev, A. V. (2021). Mapping Potential Signs of Gas Emissions in Ice of Lake Neyto, Yamal, Russia, Using Synthetic Aperture Radar and Multispectral Remote Sensing Data. *The Cryosphere*, *15*(4), 1907–1929. https://doi.org/10.5194/tc-15-1907-2021

Pointner, G., Bartsch, A., Forbes, B. C., & Kumpula, T. (2019). The Role of Lake Size and Local

Phenomena for Monitoring Ground-Fast Lake Ice. *International Journal of Remote Sensing*, *40*(3), 832–858. https://doi.org/10.1080/01431161.2018.1519281

Porter, C., Morin, P., Howat, I., Noh, M.-J., Bates, B., Peterman, K., Keesey, S., Schlenk, M., Gardiner, J., Tomko, K., Willis, M., Kelleher, C., Cloutier, M., Husby, E., Foga, S., Nakamura, H., Platson, M., Wethington, Michael, J., Williamson, C., … Bojesen, M. (2018). *ArcticDEM, V3*. Harvard Dataverse. https://dataverse.harvard.edu/dataset.xhtml?persistentId=doi:10.7910/DVN/OHHUKH

Pour, H. K., Duguay, C. R., Martynov, A., & Brown, L. C. (2012). Simulation of Surface Temperature and Ice Cover of Large Northern Lakes with 1-D Models: a Comparison with MODIS Satellite Data and In Situ Measurements. *Tellus A*, *64*(0), 1–19. https://doi.org/10.3402/tellusa.v64i0.17614

Pulliainen, J. T., Grandell, J., & Hallikainen, M. T. (1999). HUT Snow Emission Model and Its Applicability to Snow Water Equivalent Retrieval. *IEEE Transactions on Geoscience and Remote Sensing*, *37*(3), 1378–1390. https://doi.org/10.1109/36.763302

Qiu, Y., Xie, P., Leppäranta, M., Wang, X., Lemmetyinen, J., Lin, H., & Shi, L. (2019). MODIS-based Daily Lake Ice Extent and Coverage dataset for Tibetan Plateau. *Big Earth Data*, *3*(2), 170–185. https://doi.org/10.1080/20964471.2019.1631729

Raney, R. K. (2019). Hybrid Dual-Polarization Synthetic Aperture Radar. *Remote Sensing*, *11*(1521), 1–18. https://doi.org/10.3390/rs11131521

Reed, B., Budde, M., Spencer, P., & Miller, A. E. (2009). Integration of MODIS-Derived Metrics to Assess Interannual Variability in Snowpack, Lake Ice, and NDVI in Southwest Alaska. *Remote Sensing of Environment*, *113*(7), 1443–1452. https://doi.org/10.1016/j.rse.2008.07.020

Ressel, R., Frost, A., & Lehner, S. (2015). A Neural Network-Based Classification for Sea Ice Types on X-Band SAR Images. *IEEE Journal of Selected Topics in Applied Earth Observations and Remote Sensing*, *8*(7), 3672–3680. https://doi.org/10.1109/JSTARS.2015.2436993

Richards, J. A. (2009). *Remote Sensing with Imaging Radar*. Springer.

Riggs, G. A., Hall, D. K., & Román, M. O. (2019). *MODIS Snow Products User Guide to Collection 6.1*. http://scholar.google.com/scholar?hl=en&btnG=Search&q=intitle:MODIS+Snow+Products+User+Guide+to+Collection+5#0

Rott, H., Cline, D. W., Duguay, C., Essery, R., Etchevers, P., Hajnsek, I., Kern, M., Macelloni, G., Malnes, E., Pulliainen, J., & Yueh, S. H. (2012). COREH2O, A Dual Frequency Radar Mission for Snow and Ice Observations. *2012 IEEE International Geoscience and Remote Sensing Symposium*, 5550–5553. https://doi.org/10.1109/IGARSS.2012.6352348

Rott, H., & Mätzler, C. (1987). Possibilities and Limits of Synthetic Aperture Radar for Snow and Glacier Surveying. *Annals of Glaciology*, *9*(1), 195–199.

Rott, H., Yueh, S. H., Cline, D. W., Duguay, C., Essery, R., Haas, C., Heliere, F., Kern, M., MacElloni, G., Malnes, E., Nagler, T., Pulliainen, J., Rebhan, H., & Thompson, A. (2010). Cold regions hydrology high-resolution observatory for snow and cold land processes. *Proceedings of the IEEE*, *98*(5), 752–765. https://doi.org/10.1109/JPROC.2009.2038947

Rouse, W. R., Binyamin, J., Blanken, P. D., Bussières, N., Duguay, C. R., Oswald, C. J., Schertzer, W. M., & Spence, C. (2008). The Influence of Lakes on the Regional Energy and Water Balance of the Central Mackenzie. In M. Woo (Ed.), *Cold Region Atmospheric and Hydrologic Studies: The Mackenzie GEWEX Experience 1* (pp. 309–325). Springer Berlin Heidelberg.

Rutter, N., J. Sandells, M., Derksen, C., King, J., Toose, P., Wake, L., Watts, T., Essery, R., Roy, A., Royer, A., Marsh, P., Larsen, C., & Sturm, M. (2019). Effect of Snow Microstructure Variability on Ku-Band Radar Snow Water Equivalent Retrievals. *Cryosphere*, *13*(11), 3045–3059. https://doi.org/10.5194/tc-13-3045-2019

Scharroo, R., Bonekamp, H., Ponsard, C., Parisot, F., Engeln, A. Von, Tahtadjiev, M., de Vriendt, K., & Montagner, F. (2016). Jason Continuity of Services : Continuing the Jason Altimeter Data Records as Copernicus Sentinel-6. *Ocean Science*, *12*(2).

Schwarz, J., Frederking, R., Goodman, D. J., Gow, A., Kohnen, H., Reuter, H., Schwerdtfeger, B., & Sinha, K. N. (1986). Ice Physics. In G. D. Ashton (Ed.), *River and Lake Ice Engineering* (pp. 19–85). Water Resources Publications.

Scott, K. A., Xu, L., & Pour, H. K. (2019). Retrieval of Ice/Water Observations and Uncertainty Information in Lake Erie Using a Convolutional Neural Network. *American Geophysical Union Fall Meeting 2019*.

Scott, K. A., Xu, L., & Pour, H. K. (2020). Retrieval of Ice/Water Observations from Synthetic Aperture

Radar Imagery for Use in Lake Ice Data Assimilation. *Journal of Great Lakes Research*, *46*(6), 1521–1532. https://doi.org/10.1016/j.jglr.2020.08.018

Scott, P. A., Bentley, C. V, Fayle, D. C. F., & Hansell, R. I. C. (1987). Crown Forms and Shoot Elongation of White Spruce at the Treeline , Churchill , Manitoba , Canada. *Arctic and Alpine Research*, *19*(2), 175–186. https://doi.org/10.1080/00040851.1987.12002591

Sellmann, P. V., Weeks, W. F., & Campbell, W. J. (1975). Use of Side-Looking Airborne Radar To Determine Lake Depth on the Alaskan North Slope. *CRREL Special Report (US Army Cold Regions Research and Engineering Laboratory)*, *230*.

Sharma, S., Blagrave, K., Magnuson, J. J., Reilly, C. M. O., Oliver, S., Batt, R. D., Magee, M. R., Straile, D., Weyhenmeyer, G. A., Winslow, L., & Woolway, R. I. (2019). Widespread Loss of Lake Ice Around the Northern Hemisphere in a Warming World. *Nature Climate Change*, *9*, 227–231. https://doi.org/10.1038/s41558-018-0393-5

Sharma, S., Filazzola, A., Nguyen, T., Imrit, M. A., Bouffard, D., Daly, J., Feldman, H., Felsine, N., & Hendricks-Franssen, H.-J. (2022). Long-Term Ice Phenology Records Spanning up to 578 Years for 78 Lakes Around the Northern Hemisphere. *Scientific Data*, *9*(318), 1–15. https://doi.org/10.1038/s41597-022-01391-6

Shi, J., Dozier, J., & Barbara, S. (1992). Radar Backscattering Response to Wet Snow. *IGARSS 1992*, *2*. https://doi.org/10.1109/IGARSS.1992.578299

Shih, S.-E., Ding, K.-H., Kong, J. A., & Yang, Y. E. (1997). Modeling of Millimeter Wave Backscatter of Time-Varying Snowcover. *Progress in Electromagnetics Research*, *16*, 305–330.

Shokr, M., & Dabboor, M. (2020). Observations of SAR Polarimetric Parameters of Lake and Fast Sea Ice During the Early Growth Phase. *Remote Sensing of Environment*, *247*, 1–16. https://doi.org/10.1016/j.rse.2020.111910

Sihvola, A. H. (1999). *Electromagnetic Mixing Formulas and Applications*. The Institution of Electrical Engineers.

Šmejkalová, T., Edwards, M. E., & Dash, J. (2016). Arctic Lakes Show Strong Decadal Trend in Earlier Spring Ice-Out. *Scientific Reports*, *6*, 1–8. https://doi.org/10.1038/srep38449

Sobiech, J., & Dierking, W. (2013). Observing Lake and River-Ice Decay With SAR: Advantages and Limitations of the Unsupervised K-Means Classification Approach. *Annals of Glaciology*, *54*(62), 65–72. https://doi.org/10.3189/2013AoG62A037

Soriot, C., Picard, G., Prigent, C., & Domine, F. (2022). Year-Round Sea Ice and Snow Characterization from Combined Passive and Active Microwave Observations and Radiative Transfer Modeling. *Remote Sensing of Environment*, *278*. https://doi.org/10.1016/j.rse.2022.113061

Sturm, M., & Holmgren, J. (1999). *Self-Recording Snow Depth Probe* (Patent No. 5864059 A).

Sturm, M., & Liston, G. E. (2003). The Snow Cover on Lakes of the Arctic Coastal Plain of Alaska, U.S.A. *Journal of Glaciology*, *49*(166), 370–380. https://doi.org/10.3189/172756503781830539

Surdu, C. M., Duguay, C. R., Brown, L. C., & Prieto, D. F. (2014). Response of Ice Cover on Shallow Lakes of the North Slope of Alaska to Contemporary Climate Conditions (1950-2011): Radar Remote-Sensing and Numerical Modeling Data Analysis. *The Cryosphere*, *8*(1), 167–180. https://doi.org/10.5194/tc-8-167-2014

Surdu, C. M., Duguay, C. R., Pour, H. K., & Brown, L. C. (2015). Ice Freeze-Up and Break-Up Detection of Shallow Lakes in Northern Alaska With Spaceborne SAR. *Remote Sensing*, *7*(5), 6133–6159. https://doi.org/10.3390/rs70506133

Surdu, C. M., Duguay, C. R., & Prieto, D. F. (2016). Evidence of Recent Changes in the Ice Regime of Lakes in the Canadian High Arctic From Spaceborne Satellite Observations. *The Cryosphere*, *10*(3), 941–960. https://doi.org/10.5194/tc-10-941-2016

Tian, B., Li, Z., Engram, M. J., Niu, F., Tang, P., Zou, P., & Xu, J. (2015). Characterizing C-band Backscattering From Thermokarst Lake Ice on the Qinghai-Tibet Plateau. *ISPRS Journal of Photogrammetry and Remote Sensing*, *104*, 63–76. https://doi.org/10.1016/j.isprsjprs.2015.02.014

Tibbitt to Contwoyto Winter Road Joint Venture. (2020). *2020 Winter Road Poster*. https://jvtcwinterroad.ca/wp-content/uploads/2020/01/2020-Winter-Road-Poster-1.pdf

Tilling, R. L., Ridout, A., & Shepherd, A. (2018). Estimating Arctic Sea Ice Thickness and Volume Using CryoSat-2 Radar Altimeter Data. *Advances in Space Research*, *62*(6), 1203–1225. https://doi.org/10.1016/j.asr.2017.10.051

Tom, M., Aguilar, R., Imhof, P., Leinss, S., Baltsavias, E., & Schindler, K. (2020). Lake Ice Detection From Sentinel-1 SAR with Deep Learning. *ISPRS Annals of the Photogrammetry, Remote Sensing and Spatial Information Sciences*, 409–416. https://doi.org/10.5194/isprs-Annals-V-3-2020-409-2020

Tsang, L., & Kong, J. A. (2001). *Scattering of Electromagnetic Waves: Advanced Topics* (J. A. Kong (ed.)). John Wiley & Sons, Inc.

Tsang, L., Kong, J. A., & Shin, R. T. (1985). *Theory of Microwave Remote Sensing*. Wiley-Interscience.

Tsang, L., Pan, J., Liang, D., Li, Z., Cline, D. W., & Tan, Y. (2007). Modeling Active Microwave Remote Sensing of Snow Using Dense Media Radiative Transfer (DMRT) Theory With Multiple-Scattering Effects. *IEEE Transactions on Geoscience and Remote Sensing*, *45*(4), 990–1004. https://doi.org/10.1109/TGRS.2006.888854

Tsui, O. W., Chiang, M., & Dean, A. (2019). Mapping of Bottomfast Lake Ice in the Northwest Territories Via Data Mining of Synthetic Aperture Radar Image Time Series. *Canadian Journal of Remote Sensing*, *45*(5), 572–590. https://doi.org/10.1080/07038992.2019.1680278

Ulaby, F. T., & Long, D. (2014). *Microwave Radar and Radiometric Remote Sensing*. The University of Michigan Press.

van der Sanden, J. J., & Drouin, H. (2011). Satellite SAR Observations of River Ice Cover : A RADARSAT-2 (C-band) and ALOS PALSAR (L-band) Comparison. *16th Workshop of River Ice*, 179–197.

van der Sanden, J. J., Drouin, H., & Bian, Y. (2013). Repeat Pass InSAR Observations of River and Lake Ice Cover : A Preliminary Evaluation of Information Content. *CGU HS Committee on River Ice Processes and the Environment: 17th Workshop on River Ice*.

van der Sanden, J. J., & Geldsetzer, T. (2015). Compact Polarimetry in Support of Lake Ice Breakup Monitoring: Anticipating the RADARSAT Constellation Mission. *Canadian Journal of Remote Sensing*, *41*(5), 440–457. https://doi.org/10.1080/07038992.2015.1104637

van der Sanden, J. J., Short, N. H., & Drouin, H. (2018). InSAR Coherence for Automated Lake Ice Extent Mapping : TanDEM-X Bistatic and Pursuit Monostatic Results. *International Journal of Applied Earth Observation and Geoinformation*, *73*, 605–615.

https://doi.org/10.1016/j.jag.2018.08.009

Vargel, C., Royer, A., St-Jean-Rondeau, O., Picard, G., Roy, A., Sasseville, V., & Langlois, A. (2020). Arctic and Subarctic Snow Microstructure Analysis for Microwave Brightness Temperature Simulations. *Remote Sensing of Environment*, *242*(March), 111754. https://doi.org/10.1016/j.rse.2020.111754

Venier, G. O., & Cross, F. R. (1975). *An Airborne Linear-Sweep FM Radar System for Measuring Ice Thickness*.

Verpoorter, C., Kutser, T., Seekell, D. A., & Tranvik, L. J. (2014). A Global Inventory of Lakes Based on High-Resolution Satellite Imagery. *Geophysical Research Letters*, *41*, 6396–6402. https://doi.org/10.1002/2014GL060641.Received

Wakabayashi, H., Jeffries, M. O., & Weeks, W. F. (1994). C-Band Backscatter Variation and Modelling for Lake Ice in Northern Alaska. *Journal of The Remote Sensing Society of Japan*, *14*(3), 220–229. https://doi.org/10.11440/rssj1981.14.220

Wakabayashi, H., Nishio, F., & Jeffries, M. (1999). C-Band Backscattering Characteristics of Lake Ice in Northern Alaska During Spring Thaw Period. *Journal of The Remote Sensing Society of Japan*, *19*(4), 333–341. https://doi.org/10.11440/rssj1981.19.333

Wang, J., Duguay, C. R., Clausi, D. A., Pinard, V., & Howell, S. E. L. (2018). Semi-Automated Classification of Lake Ice Cover Using Dual Polarization RADARSAT-2 Imagery. *Remote Sensing*, *10*(1727), 1–27. https://doi.org/10.3390/rs10111727

Wang, L., Scott, K. A., Xu, L., & Clausi, D. A. (2016). Sea Ice Concentration Estimation During Melt From Dual-Pol SAR Scenes Using Deep Convolutional Neural Networks : A Case Study. *IEEE Transactions on Geoscience and Remote Sensing*, *54*(8), 4524–4533. https://doi.org/10.1109/TGRS.2016.2543660

Warne, C. P. K., McCann, K. S., Rooney, N., Cazelles, K., & Guzzo, M. M. (2020). Geography and Morphology Affect the Ice Duration Dynamics of Northern Hemisphere Lakes Worldwide. *Geophysical Research Letters*, *47*(12), 1–10. https://doi.org/10.1029/2020GL087953

Weeks, W. F., Fountain, A. G., Bryan, M. L., & Elachi, C. (1978). Differences in Radar Return From Ice-Covered North Slope Lakes. *Journal of Geophysical Research*, *83*(C8), 4069–4073.

https://doi.org/10.1029/JC083iC08p04069

Weeks, W. F., Gow, A. J., & Schertler, R. J. (1981). *Ground-Truth Observations of Ice-Covered North Slope Lakes Imaged by Radar No. CRREL-81-19*.

Weeks, W. F., Sellmann, P., & Campbell, W. J. (1977). Interesting Features of Radar Imagery of Ice Covered North Slope Lakes. *Journal of Glaciology*, *18*(78), 129–136. https://doi.org/10.3189/S0022143000021572

Wegmüller, U., & Mätzler, C. (1999). Rough Bare Soil Reflectivity Model. *IEEE Transactions on Geoscience and Remote Sensing*, *37*(3), 1391–1395. https://doi.org/10.1109/36.763303

Wendleder, A., Wessel, B., Roth, A., Breunig, M., Martin, K., & Wagenbrenner, S. (2013). TanDEM-X Water Indication Mask: Generation and First Evaluation Results. *IEEE Journal of Selected Topics in Applied Earth Observations and Remote Sensing*, *6*(1), 171–179. https://doi.org/10.1109/JSTARS.2012.2210999

White, D. M., Prokein, P., Chambers, M. K., Lilly, M. R., & Toniolo, H. (2008). Use of Synthetic Aperture Radar for Selecting Alaskan Lakes for Winter Water Use. *Journal of the American Water Resources Association*, *44*(2), 276–284. https://doi.org/10.1111/j.1752-1688.2007.00160.x

Wickert, J., Cardellach, E., Martin-Neira, M., Bandeiras, J., Bertino, L., Andersen, O. B., Camps, A., Catarino, N., Chapron, B., Fabra, F., Floury, N., Foti, G., Gommenginger, C., Hatton, J., Hoeg, P., Jaggi, A., Kern, M., Lee, T., Li, Z., … Zuffada, C. (2016). GEROS-ISS: GNSS REflectometry, Radio Occultation, and Scatterometry Onboard the International Space Station. *IEEE Journal of Selected Topics in Applied Earth Observations and Remote Sensing*, *9*(10), 4552–4581. https://doi.org/10.1109/JSTARS.2016.2614428

World Meteorological Organization. (2022). *The 2022 GCOS ECVs Requirements (GCOS 245)*. https://library.wmo.int/index.php?lvl=notice_display&id=22135#.Y0bua3bMKUk

Wu, Y., Duguay, C. R., & Xu, L. (2021). Assessment of Machine Learning Classifiers for Global Lake Ice Cover Mapping from MODIS TOA Reflectance Data. *Remote Sensing of Environment*, *253*(May 2020), 112206. https://doi.org/10.1016/j.rse.2020.112206

Xiao, M., Rothermel, M., Tom, M., Galliani, S., Baltsavias, E., Schindler Photogrammetry, K., Sensing, R., & Zürich, E. (2018). Lake Ice Monitoring with Webcams. *ISPRS Annals of the Photogrammetry,*

Remote Sensing and Spatial Information Sciences, *IV–2*(June 2018), 311–317. https://doi.org/10.5194/isprs-annals-IV-2-311-2018

Yan, Q., & Huang, W. (2020). Sea Ice Thickness Measurement Using Spaceborne GNSS-R: First Results with TechDemoSat-1 Data. *IEEE Journal of Selected Topics in Applied Earth Observations and Remote Sensing*, *13*, 577–587. https://doi.org/10.1109/JSTARS.2020.2966880

Yankielun, N. E., Ferrick, M. G., & Weyrick, P. B. (1993). Development of an Airborne Millimeter-Wave FM-CW Radar for Mapping River Ice. *Canadian Journal of Civil Engineering*, *20*(6), 1057–1064. https://doi.org/10.1139/l93-136

Yu, Q., & Clausi, D. A. (2008). IRGS: Image Segmentation Using Edge Penalties and Region Growing. *IEEE Transactions on Pattern Analysis and Machine Intelligence*, *30*(12), 2126–2139. https://doi.org/10.1109/TPAMI.2008.15

Zakharova, E., Agafonova, S., Duguay, C., Frolova, N., & Kouraev, A. (2020). River Ice Phenology and Thickness from Satellite Altimetry. Potential for Ice Bridge Road Operation. *The Cryosphere Discussions*, 1–31. https://doi.org/10.5194/tc-2020-325

Zambrano-Bigiarini, M. (2017). *hydroGOF* (0.3-10). https://cran.r-project.org/web/packages/hydroGOF/hydroGOF.pdf

Zhang, T., & Jeffries, M. O. (2000). Modeling Interdecadal Variations of Lake Ice Thickness and Sensitivity to Climatic Change in Northernmost Alaska. *Annals of Glaciology*, *31*, 339–347. https://doi.org/10.3189/172756400781819905

Zhu, J., Tan, S., King, J., Derksen, C., Lemmetyinen, J., & Tsang, L. (2018). Forward and Inverse Radar Modeling of Terrestrial Snow Using SnowSAR Data. *IEEE Transactions on Geoscience and Remote Sensing*, *56*(12), 7122–7132. https://doi.org/10.1109/TGRS.2018.2848642